# Label-Free Tracking and Mass Measurement of Single Protein Complexes on Lipid Bilayers


Eric Dylan Benjamin Foley

St Hugh's College

University of Oxford

A thesis submitted for the degree of

*Doctor of Philosophy in Physical and Theoretical Chemistry*

8th August, 2022

# Acknowledgements

My time in Oxford has been an exciting experience thanks to my wonderful colleagues, friends, and family. I am also grateful to the Clarendon Fund, St Hugh's College, and the Oxford-Nottingham Biomedical Imaging CDT for providing the financial support that allowed me to study here.

Firstly, I would like to thank my supervisor, Philipp Kukura, for his continuous support and guidance during my research projects. His exciting ideas, advice, patience, and understanding helped me find my way through many challenging road blocks, especially during the initial COVID lockdowns. I would also like to thank Weston Struwe for his advice and supervision during my work on the HIV project.

The Kukura group as a whole has been a thoroughly enjoyable working environment. Everyone was always happy to discuss ideas and to help other members, which created a friendly and collaborative atmosphere. In particular, I would like to thank Fabian Soltermann, Samuel Tusk, Stephen Thorpe, Manish Kushwah, and Roi Asor. Fabian helped me settle into the group and to get past the steep learning curve. With Sam and Steve I have had many discussion that helped me define the direction of my research projects, particularly in my first two years. Manish deserves a special mention because he supported me throughout the entirety of my degree and taught me many things, especially in the lab. Together with Roi, we frequently discussed new experiments and analyses, which often resulted in exciting new ideas, particularly in my final year. As a whole, the collaborative nature and friendliness of the group always ensured that I enjoyed my work.

Apart from my colleagues, I have the Oxford University Table Tennis Club to thank, where I spent most of my free time. I have met many Incredible individuals during my time there, and made valuable long-lasting friendships. In particular, I am grateful to Abe, Jef, Emi, and Ali for the many fun dinners and movie nights that provided welcome distractions from work.

I am also grateful to my friends Sophie, Bryan, and Varan. Over the past years, I have made many valuable experiences with each of them, and I am happy we managed to continuously stay in touch, even when we could not visit each other.

Finally, I would like to thank my parents, my brother, Kim, and my partner, Kritica. They have always supported and encouraged me in my endeavours. Even when we were separated across half the globe, they provided me with valuable advice both in scientific and personal matters. Without them, I would not be where I am today and words cannot express the level of gratitude I feel for each of their roles in my life.

# Statement of Originality

The research described in this thesis was carried out by the author between October 2019 and August 2022. It is presented in the form of an integrated thesis, as approved by the sub-department of Physical and Theoretical Chemistry, and is a hybrid of a published scientific paper (Chapter 4) and conventional chapters (Chapters 1-3, 5-6). The presented work includes nothing which is the outcome of work done in collaboration, except where specifically indicated in the text. The use of the first person plural is strictly a matter of style in keeping with standard scientific convention.

# List of Publications

The work carried out by the author between October 2019 and August 2022 led to the following publications:

1. F. Soltermann, **E.D.B. Foley**, V. Pagnoni, M. Galpin, J.L.P. Benesch, P. Kukura, W.B. Struwe, Quantifying protein-protein interactions by molecular counting with mass photometry, *Angewandte Chemie International Edition*, 2020, **59**, 10774-10779.

2. **E.D.B. Foley***, M.S. Kushwah*, G. Young, P. Kukura, Mass photometry enables label-free tracking and mass measurement of single proteins on lipid bilayers, *Nature Methods*, 2021, **18**, 1247-1252.

3. **E.D.B. Foley***, R. Asor*, M.S. Kushwah, F. Soltermann, S. Burnap, A. Oleryinova, W.B. Struwe, P. Kukura, Quantification of protein-protein interactions and cross-linking of viral spike proteins by mass photometry, in preparation.

4. M.S. Kushwah, **E.D.B. Foley**, P. Kukura, Specific pull-down of single proteins from complex mixtures with mass photometry, in preparation.

5. M.S. Kushwah, **E.D.B. Foley**, R. Asor, P. Kukura, Understanding dynamin polymerization by single-molecule counting and particle tracking using mass photometry, in preparation.

*These authors contributed equally.

# Abstract

Protein-protein interactions are essential for biological processes, but can display a level of polydispersity that is difficult to study with bulk measurements. Recently, mass photometry, a label-free single molecule imaging technique, has been used to quantify protein-protein interactions by measuring the mass of single proteins. So far, however, measurements are limited to solution-based systems and nM concentrations. Here, we aim to expand the applications of mass photometry to proteins on lipid bilayers, and to increase the concentration range of solution-based measurements.

We implement a surface passivation protocol that reduces non-specific binding by up to four orders of magnitude, and apply further surface functionalisation strategies aimed at accessing measurements at µM concentrations. Next, we develop a mass photometry-based method for tracking individual protein complexes on lipid bilayers, thereby demonstrating quantification of oligomer-dependent kinetics and mobilities. We then extend this method to interactions of the HIV-1 envelope glycoprotein (Env) with broadly neutralising antibodies. Using our assay, we resolve polydisperse anitbody-induced cross-linking and quantify the corresponding binding affinities. We show that lipid bilayers give access to mass photometry measurements at µM protein concentrations, and demonstrate specific pull-down of target proteins from complex mixtures. Finally, we discuss aspects of the data analysis for these assays with a specific focus on systematic errors in the diffusion and mass measurements, and outline strategies for their correction.

# Contents

# List of Figures

# List of Abbreviations

| | |
|---|---|
| $K_d$ | dissociation constant |
| $k_{off}$ | dissociation rate constant |
| $k_{on}$ | association rate constant |
| bnAb | broadly neutralising antibody |
| BSA | bovine serum albumin |
| bt | biotin |
| CMOS | complementary metal oxide semiconductor |
| DOPC | 1,2-dioleoyl-sn-glycero-3-phosphocholine |
| DOPE | 1,2-dioleoyl-sn-glycero-3-phosphoethanolamine |
| DOPS | 1,2-dioleoyl-sn-glycero-3-phospho-l-serine |
| Env | HIV-1 envelope glycoprotein |
| FWHM | full width at half maximum |
| HIV | human immunodeficiency virus |
| IgG | immunoglobulin G |
| IMP | integral membrane protein |
| iSCAT | interferometric scattering microscopy |
| MAP | membrane-associated protein |
| MP | mass photometry |
| PDF | probability density function |
| PEG | polyethylene glycol |

| | |
|---|---|
| PSF | point spread function |
| SEM | standard error of the mean |
| SLB | supported lipid bilayer |
| SNR | signal-to-noise ratio |
| SOSIP | BG505 SOSIP.664 |
| SPR | surface plasmon resonance |
| SPT | single-particle tracking |
| StrAv | streptavidin |
| Tfn | human apo-transferrin |
| Tfn-IgG | anti-human transferrin antibody |
| WT | wild-type dynamin-1 |

# Chapter 1

# Introduction

Proteins fulfill an incredible diversity of functions central to life. The human proteome alone contains over 500,000 different proteins, an estimated 80% of which engage in protein-protein interactions,[1] thereby forming intricate functional networks. As part of these networks, a single protein can on average engage in at least six different interactions with other proteins, and this number can vary case by case from one to over one hundred interacting partners for a single protein.[2,3] The timescales involved can range from a few milliseconds to more than a year,[4,5] and often rely on homo- and hetero-oligomerisation, i.e. the formation of protein complexes composed of either several copies of the same protein or multiple different proteins.

Protein-protein interactions play key roles in signalling and regulatory processes, such as membrane trafficking,[6] and the neutralisation of pathogens.[7] The malfunction of these interactions can have drastic consequences, e.g. neurodegenerative diseases[8] and cancers.[9] As a result, the development of therapeutic interventions targeting these processes has become an area of interest,[10] and the number of drugs relying on protein-protein interactions to reach their target are rapidly increasing.[11]

There are several cases where identifying and studying specific protein-protein interactions and their underlying mechanisms has resulted in new

therapeutic strategies.[12–14] Thus, quantification of the associated biophysical parameters may further aid in this process. In this context, the complexity, heterogeneity, and sheer amount of protein-protein interactions are significant hurdles both to identifying potential binding partners, and studying and quantifying the underlying interactions. Two types of systems that currently present challenges to this field are the study of polydisperse interactions, and studying interactions in and on membranes.

Polydisperse interactions often involve the dynamic (dis)assembly and co-existence of different oligomeric states of the same protein, different proteins, or both, which makes them difficult to accurately study with many existing biophysical methods. For example, structural techniques such as cryo-electron microscopy[15] only provide a snapshot of these interactions, which makes following entire processes in real time challenging. On the other hand, many solution-based methods, e.g. surface plasmon resonance,[16] rely on averaging the signal obtained from many individual protein molecules, which means that resolving co-existing species or oligomeric states is either difficult or infeasible.

Interactions in and on cell membranes present an additional challenge in that studying them requires measurements either in vivo or with membrane mimetic systems, such as supported lipid bilayers (SLBs) or lipid nanodiscs.[17,18] Both options are technically challenging, but crucial to pursue because membrane proteins comprise ∼25% of the human proteome and 60% of drug targets.[19]

A particularly difficult case arises when the system to be studied involves membrane proteins and exhibits polydisperse properties, e.g. in amyloid-β aggregation, and cross-linking of viral spike proteins.[20–22] To address these challenges both individually and in combination, single-molecule microscopy methods have become pivotal.[23] For one, these techniques allow for stoichiometric analysis of the composition of individual protein complexes. Additionally,

single protein complexes can be localised and tracked in space and/or time and in and on membranes in vivo and in vitro. As a result, researchers have gained valuable insights into polydisperse processes, such as membrane protein clustering[24] and the monomer-dimer equilibrium of G-protein coupled receptors.[25] In particular, the extension of single molecule imaging to spatiotemporal tracking of single molecules, known as single-particle tracking (SPT), has enabled the study of highly transient interactions on membranes that could be of functional importance.[4] However, most single-molecule imaging techniques rely on labelling of the analyte to visualise it, which imposes challenges,[26–30] especially in resolving mixtures of co-existing species and stoichiometries.[31]

In this work, we aim to address some of these challenges with mass photometry (MP), a recently developed label-free single-molecule microscopy technique. MP is primarily used to detect and measure the mass of protein complexes as they bind from solution non-specifically to a glass coverslip. Over the last four years, it was demonstrated that MP can be used to determine the distribution of protein complexes in solution,[32] quantify protein-protein interactions,[33,34] and is well-suited for polydisperse systems.[32,35,36] Importantly, these capabilities could potentially be translated to SPT of protein complexes on SLBs, making MP a promising approach for resolving co-existing species both in solution and on membranes. However, conventional solution-based MP measurements are restricted to nM concentrations,[33] which prevents the characterisation of weak interactions in solution. Additionally, reports of MP measurements on SLBs are rare and MP-based spatiotemporal tracking of proteins had not been reported.

Overcoming these two limitations is the aim of this thesis. We begin by briefly reviewing examples of biophysical techniques used to quantify protein-protein interactions in Chapter 2, with a particular focus on tracking single

proteins on membranes. Finally, we discuss current challenges surrounding these techniques and introduce MP as a potential tool to address them.

Chapter 3 focuses on MP measurements in solution and increasing the range of accessible protein concentrations. We implement a surface passivation protocol to reduce non-specific binding of proteins to glass coverslips. These surfaces are then further functionalised with the aim of introducing specificity and to control the number of binding events of target analyte.

In Chapter 4, we present an approach termed dynamic MP to simultaneously track and measure the mass of individual membrane-bound protein complexes on SLBs. The capabilities of this method are highlighted by measuring the oligomeric distributions of membrane-bound dynamin-1 complexes, and quantifying oligomer-dependent mobilities and membrane affinities.

In Chapter 5, we use MP to study protein-protein interactions of the HIV-1 envelope glycoprotein (Env). By developing an assay based on dynamic MP, we investigate the binding of broadly neutralising antibodies and cell receptors to SLB-bound Env. We demonstrate robust resolution and characterisation of polydisperse mixtures of the resulting protein complexes on the lipid bilayer, with a particular focus on inter-Env cross-linking. In the course of this work, we achieve measurements in the presence of high nM to low µM protein concentrations and quantify the corresponding binding affinities.

Our measurements at high concentrations suggested that dynamic MP assays may have scope for isolating target proteins along with their interacting partners from complex mixtures. In Chapter 6, we explore this aspect by investigating the passivating properties of SLBs and whether biofunctionalised SLBs can be used to specifically recruit target proteins from complex media.

Finally, the contents of this thesis are summarised in Chapter 7, and dynamic MP is discussed in terms of future applications and improvements.

# Chapter 2

# Studying Protein-Protein Interactions by Tracking Single Molecules

## 2.1 Introduction

Studying a protein's interactions in detail requires the interplay of multiple approaches ranging from techniques for identifying potential binding partners to quantitative methods for extracting key biophysical parameters.[1,37–39] Quantifying parameters such as the interaction stoichiometries, binding affinity, and kinetics, i.e. association and dissociation rate constants, can provide valuable insights into the underlying mechanism.[40] However, this process is often complicated by the fact that proteins interact with each other and oligomerise to various degrees and in different settings, such as in the cytosol and in, on and across lipid bilayers. Some processes can involve all of these settings simultaneously, e.g. interactions occurring near cell membranes (Fig. 2.1), and are particularly challenging to characterise.

To identify a protein's binding partners, one has the choice between several existing methods, many of which are based on high-throughput screening using affinity tags fused to the protein of interest.[1,39,41] The target protein is

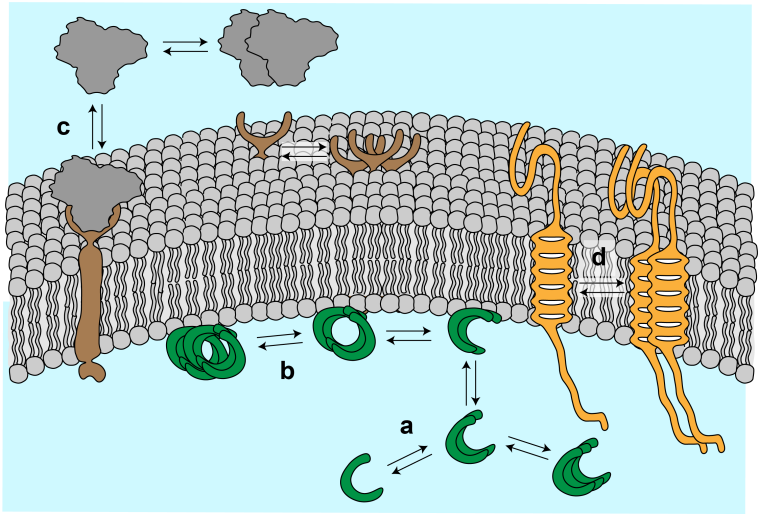


**Figure 2.1: Protein-protein interactions at cell membranes.** Cell membranes consist of a bilayer of phospholipids with a hydrophylic surface and hydrophobic core and several other components (not displayed). Interactions include oligomerisation of proteins in solution (**a**) and bound to the surface of the membrane (**b**), binding of soluble proteins to membrane receptors (**c**), and oligomerisation/clustering of proteins embedded in the membrane (**d**).

expressed with a genetically fused tag that specifically binds to compounds used in the purification step, thereby selectively isolating the target protein. For example, in His pull-down assays, the protein of interest, i.e. the bait protein, is expressed with a polyhistidine tag. The cell lysate is then incubated with $Ni^{2+}$ beads, which specifically bind the polyhistidine tag, thereby allowing for selective purification of the bait protein and its associated binding partners.[41] Isolated proteins can then be identified by an appropriate technique, e.g. mass spectrometry, provided the interactions are sufficiently long-lived to stay intact during the purification process.[42]

Further characterisation and quantification of the identified interactions is often done separately, and with recombinantly expressed binding partners to obtain enough sample. The complexity of the cellular environment can pose challenges to the quantification of some key biophysical parameters, e.g. rate constants. As such, these measurements are often performed in vitro, which

simplifies the experimental approach, decreases noise sources, and improves throughput. For this step, a huge range of available in vitro techniques can be chosen from.[41,43] Methodologies include in-solution techniques, such as microscale thermophoresis,[44] techniques that analyse interactions by separating the resulting protein complexes, e.g. analytical ultracentrifugation,[45] and methods that characterise binding by measuring adsorption to a surface, such as surface plasmon resonance.[16] However, even with this abundance of available in vitro techniques, polydisperse interaction and some aspects of interactions involving membrane proteins remain challenging to study.

A systematic review of available in vitro methods for quantifying protein-protein interactions is beyond the scope of this thesis and is available elsewhere.[41,43] Instead, we will begin this chapter by touching on one of the most popular and widespread methods, surface plasmon resonance (SPR) in Section 2.2. This technique shows parallels to mass photometry, the focus of this work, in that it is surface-based, carried out in vitro, and label-free. We will use SPR to showcase what is achievable with most ensemble-based methods, i.e. methods that average the signal from many individual protein complexes. Key limitations are highlighted, particularly in studying polydisperse interactions, and interactions taking place in and on membranes. To address these challenges, we discuss single-molecule methods with a focus on single-particle tracking in Section 2.3, and highlight recent developments in this area. Finally, in Section 2.4, we introduce mass photometry (MP) as a method to overcome the limitations of existing single-molecule techniques. We highlight recent work surrounding mass photometry, its use for characterising polydisperse systems in solution and its potential for tracking protein complexes on SLBs.

## 2.2 Quantifying Protein-Protein Interactions

The simplest case of a protein-protein interaction consists of two proteins binding to each other in a 1:1 ratio to form a single protein complex. In the analysis of this process, a common assumption is reversibility, i.e. the complex is able to dissociate back into the two constituent proteins. Association of the two proteins and dissociation of the complex have corresponding rate constants that, along with the concentrations of each species, determine the rates of these processes:

$$P_f + Q_f \underset{k_{off}}{\overset{k_{on}}{\rightleftharpoons}} PQ, \tag{2.1}$$

where $P_f$ and $Q_f$ are the free (unbound) proteins, $PQ$ is the complex formed between $P$ and $Q$, and $k_{on}$ and $k_{off}$ are the association and dissociation rate constants, respectively. When this interaction is at equilibrium, the degree to which two proteins assemble into a complex at a given concentration can be expressed by the dissociation constant, $K_d$:

$$K_d = \frac{k_{off}}{k_{on}} = \frac{[P_f][Q_f]}{[PQ]}, \tag{2.2}$$

where terms in square brackets indicate the concentration of that species at equilibrium. As such, the lower the $K_d$ the higher the binding affinity between two proteins. Both the analysis of the thermodynamic parameter, $K_d$, and the kinetic parameters, $k_{on}$ and $k_{off}$, can provide essential insights into underlying reaction mechanisms.[46,47] For example, the $K_d$ is equal to the concentration of free $P$ and $Q$ at which half of the total molecules have associated into the complex $PQ$. Thus, when looking at the binding of an antibody-based drug to its target protein, the $K_d$ is related to the dosage required to achieve the desired effect. On the other hand, the inverse of $k_{off}$ indicates how long the antibody remains bound to its target, i.e. the half-life of the interaction.

Current biophysical techniques employ a variety of strategies to quantify these parameters. For example, techniques such as surface plasmon resonance (SPR) are based on attaching the target protein to a surface and monitoring changes in the properties of the surface due to binding of other species. In a typical SPR experiment,[16,48] the surface of a thin gold film on a glass substrate is functionalised with a protein or other biosensing molecules, and put in contact with analyte solution containing the binding partners of interest. The interface of the functionalised gold film and the analyte solution is then illuminated at the so-called SPR angle, where the beam is reflected with significantly lower intensity due to the excitation of surface plasmons in the gold film (Fig. 2.2a). Binding of the analyte to the functionalised surface results in small changes to the refractive index of the interface, which alters the SPR angle. These changes are proportional to the amount of analyte adsorbed to the surface, and quantified in terms of response units (RU).

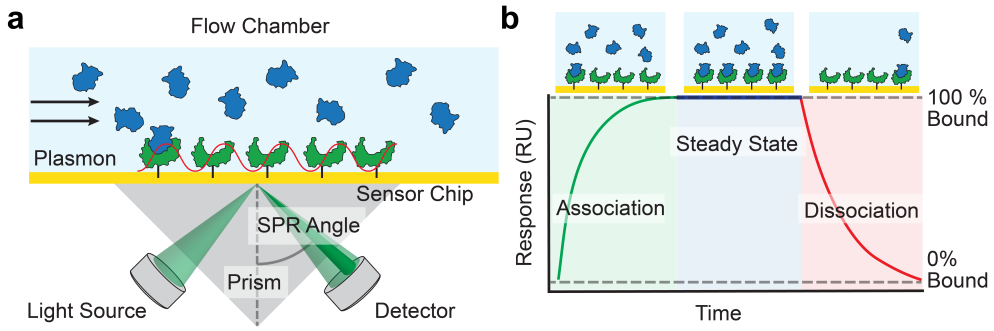


**Figure 2.2: Principle of surface plasmon resonance for quantifying protein-protein interactions.** **a**) Schematic of a typical SPR experiment showing a biofunctionalised surface in contact with analyte solution. **b**) Diagram of the typical data output from an SPR experiment showing an increase in response units during the binding phase, a plateau during the steady state, and decrease in the dissociation phase. Adapted from reference 43 (open access).

Typically, the RU are monitored during binding of the analyte until steady-state conditions have been reached indicated by a plateau in RU vs time. At this point, the analyte solution is replaced with buffer and dissociation of the

interaction is monitored via a decrease in RU (Fig. 2.2b). By fitting appropriate models to the association and dissociation portion of the data, the $k_{on}$ and $k_{off}$ of the underlying interaction can be determined, which gives access to the $K_d$. Alternatively, the $K_d$ can be determined directly from the steady-state signal by conducting multiple experiments at different concentrations.[49]

In more complex interactions where several copies of one protein form a complex with the target protein, SPR can be used to extract the stoichiometry by fitting advanced biophysical models to the data.[50] However, as with other ensemble-based methods, SPR struggles in studying interactions where multiple binding stoichiometries and oligomeric states co-exist.[43] For example, the functions of some cytoskeletal proteins, e.g. actin[51] and tubulin,[52] rely on dynamic changes in the relative amounts of several co-existing oligomeric states. A detailed and accurate mechanistic understanding of such polydisperse systems requires the ability to resolve and quantify distinct species, and studying the $K_d$ and rate constants as a function of oligomeric state and stoichiometry.

### 2.2.1 Studying the Interactions of Membrane Proteins

Another challenge many biophysical techniques face is the study of protein-protein interactions in or on cell membranes. Membrane proteins can be divided into integral membrane proteins (IMPs), which are inserted in the cell membrane, and membrane-associated proteins (MAPs) that bind to cell membranes via non-covalent protein-lipid or electrostatic interactions. IMPs are composed of hydrophobic domains, which are buried in the hydrophobic core of the cell membrane, and hydrophilic domains that extend out of the membrane into the cytosol. Consequently, they can interact with other IMPs within the membrane and also with soluble proteins in the cytosol, and play key roles in processes such as cell signalling and membrane trafficking.

In contrast, MAPs are soluble in aqueous media and often engage in interactions both in solution and while bound to the cell membrane. Some MAPs can self-assemble dynamically into higher order structures on membranes, as is commonly encountered in cell transport and cytoskeletal proteins such as dynamins[53] and septins,[54] or bind to IMPs, e.g. G-proteins in cell signalling.[55] For example, the MAP dynamin-1, which facilitates endocytosis, is thought to exist predominantly as a tetramer in the cytosol but displays dimer-based assembly into higher order helices on cell membranes in areas where membrane fission is occurring.[56]

The requirement of a cell membrane to study membrane protein interactions imposes technical difficulties, and is either not compatible with many biophysical techniques or severely limiting. As a result, researchers have developed membrane mimetic strategies for in vitro studies. For example, IMPs can be extracted from native cell membranes by using suitable detergents. After purification, one can obtain the IMPs of interest encapsulated in detergent micelles (Fig. 2.3a). Alternative approaches aim to isolate IMPs in more native environments, e.g. nanodiscs[18] and lipid particles.[57] These constructs consist of either IMPs surrounded by phospholipid assemblies contained by a membrane scaffold protein or IMPs surrounded by nanoscopic sections of the cell membrane contained by amphiphatic copolymers (Fig. 2.3b-c). Overall, these approaches enable the study of native oligomeric states, interactions with lipids and soluble binding partners, and the activity of IMPs.[58–61]

In recent years it has become increasingly clear that the composition of cell membranes is highly heterogeneous on the nano- and mesoscale,[62,63] and that not only MAP but also IMP function can involve the dynamic and transient assembly into larger complexes.[4,25,63] In these processes the intrinsic fluidity of cell membranes allows for IMPs and MAPs to diffuse laterally, thereby

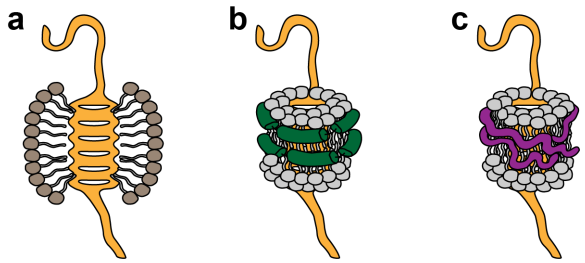


**Figure 2.3: Membrane mimetic systems for solubilising IMPs. a**) Schematic of an IMP in a detergent micelle, **b**) in phospholipids assembled by a membrane scaffold protein (lipid nanodisc), and **c**) in a section of a native cell membrane contained by an amphiphatic copolymer.

facilitating these transient interactions,[62] which is difficult to reproduce when IMPs are encased by nanoscopic membrane mimetic containers. Therefore, it is important to also study these protein-protein interactions in a setting that can facilitate lateral diffusion and the resulting dynamic interactions, and to characterise them as a function of space and time.[64,65]

The ideal approach to studying protein-protein interactions around cell membranes would be in vivo. However, this is experimentally challenging in many aspects, especially for quantitative analyses of kinetics and binding affinities. Supported lipid bilayers (SLBs) constitute a set of alternative membrane mimetic systems that can facilitate the spatiotemporal analysis of protein-protein interactions surrounding cell membranes in vitro.[66] SLBs consist of a lipid bilayer formed on a solid support using phospholipid compositions similar to those of cell membranes.[17] The bottom layer of SLBs is separated from the solid support by a thin 1-2 nm aqueous layer, which supports the lateral mobility of lipids and bound MAPs on the nano- and mesoscale (Fig. 2.4a).[17] However, in conventional SLBs, the hydration layer is too thin to separate outer membrane domains of IMPs from the solid support, rendering these proteins immobile when inserted into SLBs.[67] Although experimentally more challenging, some mobility can be retained in these cases by incorporating a cushion between the SLB and solid support (Fig. 2.4b).[67,68]

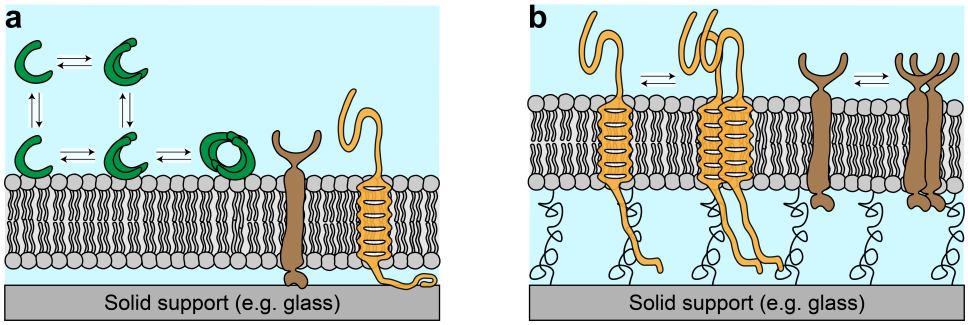


**Figure 2.4: Supported lipid bilayers for studying membrane proteins. a**) Conventional SLB with a thin hydration layer that supports phospholipid mobility and is suitable for the study of MAPs. **b**) Tethered SLB with greater separation to the solid support that can accommodate hydrophilic domains of IMPs and conserve their mobility.

SLBs are compatible with several ensemble-based biophysical techniques based on surface adsorption, such as SPR.[69] However, these methods are typically only sensitive to changes in the amount of biomolecules adsorbed to the surface, and cannot observe dynamic interactions between surface-bound proteins. Additionally, the inherent averaging of signals from distinct protein complexes remains a problem. In this regard, single-molecule microscopy methods have proven extraordinarily valuable.[70] These approaches are compatible with SLBs, allow for imaging of individual protein complexes, and can be used to determine their subunit compositions, i.e. stoichiometries, and spatial distribution both in vitro and in vivo.[23,71–73] Imaging single protein complexes immobilised to a surface as a function of time can also be used to quantify both kinetic and stoichiometric details simultaneously.[40]

Single-molecule microscopy methods are promising tools for overcoming both the challenge posed by quantifying polydisperse protein-protein interactions and those of membrane proteins. Here, we will focus on a subset of single-molecule imaging techniques, collectively known as single-particle tracking, that combine the characterisation of individual mobile protein complexes as a function of both space and time.[74] These methods can in principle provide

simultaneous quantification of oligomeric states and kinetic parameters of a variety of protein-protein interactions, including interactions on membranes, and are thus particularly promising.

## 2.3 Single-Particle Tracking

Single-particle tracking (SPT) is based on imaging, localising and tracking individual molecules via optical microscopy techniques.[74] The resulting molecular trajectories can be analysed individually or as ensembles, which gives access to information at the single-molecule level with spatiotemporal resolution. To date, SPT-based methods have played crucial roles in revealing and studying transient homo- and hetero-oligomerisation processes around cell membranes.[4,25,75,76] As a result, the scientific community has put significant effort into developing advanced experimental methods and algorithms aimed at improving the capabilities of SPT.[74,77,78]

Visualising the target molecule against the imaging background typically requires attaching a nanoscopic label to the molecule of interest. A series of images is then collected in which sparsely distributed target molecules are visible as diffraction-limited spots (Fig. 2.5a). For sub-diffraction objects, the shape of these spots is determined by the point spread function (PSF) of the microscope. The PSF typically exhibits a full width at half maximum (FWHM) of 200-300 nm depending on the wavelength of light used and the numerical aperture, i.e. the range of angles of photons that can be collected. A model of the PSF can then be fitted to these signals to determine the position of the label and thereby the target molecule within a few nm or less in each image. Subsequently, the location and signal intensity of individual analytes can be linked into particle trajectories throughout the time series of images by using

suitable algorithms.[74] This workflow allows for the extraction and tracking of the signal intensity and the diffusion coefficient of the analyte in both time and space with typical localisation precisions and temporal resolutions ranging from 1 to 50 nm and tens of µs to 100 ms, respectively.

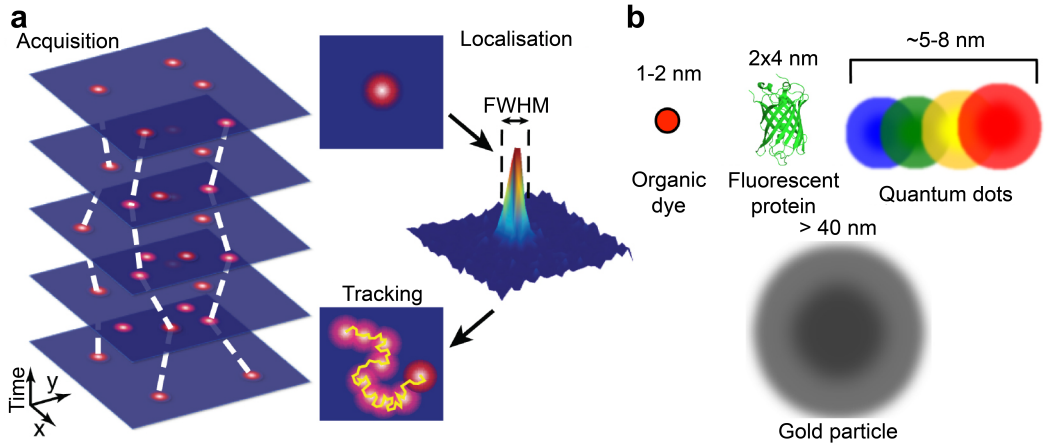


**Figure 2.5: Concept of SPT and labelling methods. a**) Workflow of SPT. In the acquisition step a series of images is taken, containing a small number of labelled molecules (red spots). Typical movies contain between hundreds to thousands of images recorded with a high-speed camera. In the localisation step, the image at a given time is analysed to retrieve the positions of the particles. The positional accuracy ultimately depends on the full width at half maximum (FWHM) of the PSF, the number of photons collected from the emitter and the different sources of noise from the experiment. After repeating the localisation step on a time series of images, the positions are linked to generate trajectories that track the motion and the signal of the particle. **b**) Labelling choices include organic dyes, fluorescent proteins, quantum dots and gold nanoparticles. The approximate size of these different labels is given in the picture. Panels **a** and **b** adapted from reference 74 with permission from IOP Publishing Ltd.

The precision with which individual molecules can be localised depends on the signal-to-noise ratio (SNR). In an ideal experiment, the achievable SNR is limited by stochastic fluctuations in the number of photons collected to form the image, known as shot noise. In the absence of other background fluctuations, the SNR scales as $\sqrt{N}$, where $N$ is the number of collected photons. The chosen imaging speed directly impacts how many photons can be collected, and often a compromise has to be reached between the desired temporal resolution

and localisation precision. Ultimately, the achievable spatiotemporal resolution is tied to the photon flux arising from the chosen nanoscopic label, whereby possible choices vary in size and rely on either light scattering (e.g. gold nanoparticles) or fluorescence (e.g. organic dyes, quantum dots, fluorescent proteins) as a contrast mechanism (Fig. 2.5b). In addition to high photon flux, the ideal label should be photochemically stable to allow for continuous imaging, and should not impact the function or mobility of the target molecule to result in optimal performance.

### 2.3.1 Fluorescence-Based Methods

The first report of detecting a single fluorescent molecule at room temperature dates back to 1993.[79] Since then this field has rapidly expanded and found many promising applications. Using optical filters to detect only wavelengths in the emission spectrum of the target fluorophore efficiently rejects background signal, such that single proteins with attached or genetically fused fluorescent labels can be imaged in vitro and in vivo. Additionally, using multiple fluorophores with different emission spectra enables simultaneous observation of multiple different species,[80] and can also allow for probing of conformational details in protein-protein interactions.[81]

Single-molecule fluorescence microscopy has provided valuable quantitative insights into protein-protein interactions, such as the subunit compositions of protein complexes,[82] the distribution of stoichiometries in the interactions between different proteins,[83] and corresponding binding affinities[84] and kinetic parameters.[40] Obtaining this information at the single-molecule level has enabled researchers to resolve subtle details, such as kinetic differences during different stages of the formation of a protein complex.[83] It can also provide biophysical parameters as a function of co-existing stoichiometries and species.[40]

Importantly, these capabilities can be translated to fluorescence-based SPT, which allows for resolving co-existing oligomeric states and associated differences in their mobility in and on membranes.[20] Fluorescence-based SPT has also given access to studying short-lived interactions of proteins in and on membranes, such as transient dimerisation of membrane proteins, on ms timesales.[4,75] However, the reliance on fluorescent labels results in limitations both for resolving co-existing interaction stoichiometries and for SPT.

To determine the composition of single protein complexes, researchers have developed several methods for counting individual subunits. A widely used approach relies on stepwise photobleaching of the fluorophores attached to a protein complex.[85] After a certain time period of fluorophore excitation, light-induced structural changes lead to the irreversible loss of fluorescence, known as photobleaching. Given a set of protein subunits each labelled with a fluorophore, the total number of subunits in a protein complex can be determined by counting the discrete drops in fluorescence intensity due to the bleaching of each fluorophore (Fig. 2.6a-b).

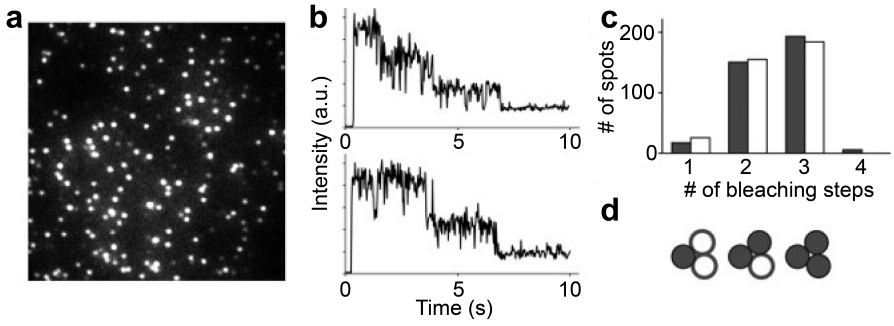


**Figure 2.6: Single-molecule subunit counting based on photobleaching. a**) A movie of single molecules in/on the membrane or at the coverslip is recorded. The density needs to be low enough to separate individual protein complexes. **b**) From each fluorescent spot, the intensity is calculated and bleaching steps are counted. **c**) The histogram of experimentally observed bleaching steps (filled bars) can be fitted by a binomial distribution (empty bars). Here, a distribution for n = 3 fits best. **d**) The oligomeric state of the protein is deduced. Figure adapted from reference 85 with permission from John Wiley and Sons.

A disadvantage of this approach, is that it requires complete photobleaching of all fluorophores in each protein complex to extract reliable results, which in some cases demanded immobilisation of the target protein complexes to ensure sufficient observation time.[85] An alternative subunit counting approach relies on the calibration of the fluorescent signal of a protein complex against the signal expected from a single fluorophore.[66,86] In principle, this approach enables the direct conversion of the fluorescent signal of a single protein complex to the number of constituent subunits. Although this method circumvents the need to observe complete photobleaching, it is still subject to limitations shared by both approaches.

Each subunit of the target protein complexes has a specific probability of having been labelled with a fluorophore and of that fluorophore being active. For a set of exclusively trimeric protein complexes, these effects result in a binomial distribution of counted subunits, which can be fitted to extract the most likely number (Fig. 2.6c). However, for a protein that exists as a mixture of several oligomeric states, as is often encountered in self-assembling proteins,[51–54] this approach will result in the convolution of several binomial distributions.[31] In these cases, it is extremely challenging, if not infeasible, to accurately quantify the abundances of different protein complexes and corresponding biophysical parameters. Thus, there is a need for more robust techniques to accurately quantify oligomeric states and associated biophysical parameters.

In the context of SPT, fluorescent labels introduce several challenges. In shot noise-limited experiments, the precision in localising a labelled protein is determined by the number of photons collected during imaging and can be approximated by $\sigma/\sqrt{N}$, where $N$ is the number of collected photons and $\sigma$ is the standard deviation of the PSF.[87] For a single fluorophore, the photon flux is limited by the fluorescence lifetime, which results in achievable spatiotemporal

resolutions of roughly 1 nm/Hz$^{1/2}$.[88] For example, at 100 Hz, the routinely achievable localisation precision is about 10 nm, and at 1 kHz decreases to about 30 nm. As a result, there is an intrinsic limit in the accessible timescales of protein-protein interactions by fluorescence-based SPT (without compromising localisation precision), and in some cases the temporal resolution is insufficient to resolve individual steps in protein oligomerisation.[31] Additionally, several other caveats are introduced by photophysical effects, such as photobleaching and photoblinking. Photobleaching places an inherent limit on the achievable observation times in SPT. On the other hand, photoblinking, i.e. the intrinsic switching between bright and dark states of fluorophores,[29,30] complicates the tracking and quantification of fluorescent signals. Finally, introducing fluorescent labels can impact protein function and introduce other artefacts,[26–28] and simultaneously tracking more than two distinct species is challenging due to the spectral overlap of different fluorophores. Cumulatively, these effects pose a significant experimental and analytical challenge to extracting quantitative information from fluorescence-based SPT both in vivo and in vitro.

### 2.3.2 Interferometric Scattering Microscopy

Many of the issues encountered with fluorescent labels can be avoided by instead relying on light scattering as a contrast mechanism. Light scattering is universal to nanoscopic objects and the achievable photon flux, and thus the achievable SNR, is in principle only limited by the incident illumination. In fact, relatively simple scattering-based optical setups can reach $< 10$ µs temporal resolutions with localisation precisions of 1-2 nm or less,[89] thereby exceeding what is routinely achievable in fluorescence-based SPT.[88,90]

The scattering amplitude of a spherical nanoscopic object can be written as:

$$s = \epsilon_m \pi \frac{d^3}{2} \frac{\epsilon_p - \epsilon_m}{\epsilon_p + 2\epsilon_m}, \tag{2.3}$$

where $\epsilon_m$ and $\epsilon_p$ are the permittivities of the medium and scatterer, respectively, and $d$ is the scatterer's diameter.[90] Therefore, any object with a refractive index distinct from that of the surrounding medium will produce a scattering signal. This signal scales with the square of the scattering amplitude, i.e. the sixth power of the object's diameter. In principle, the scattering signal from objects as small as a single atom can be imaged.[91] However, in purely scattering-based SPT methods, e.g. dark-field microscopy, the drastic drop in signal with decreasing object size introduces practical limitations. For objects as small as single proteins, the background fluctuations due to scattering from the sample environment and reflections from optical elements overwhelm the signal of interest, and are difficult to sufficiently suppress. Thus, purely scattering-based SPT typically requires labelling of the protein of interest with gold nanoparticles on the order of 30-40 nm to track single molecules.[74,88]

Using labels in this size range risks introducing artefacts in the system under observation caused, for instance, by steric hindrance, potential cross-linking between the label and multiple biomolecules,[92] and by the motion of the label itself.[93] Therefore, using smaller labels, or measuring completely label-free, is desirable. In this context, interferometric scattering microscopy (iSCAT) has become an area of interest.[90] In iSCAT setups, a coherent light source is directed onto a glass coverslip in contact with aqueous sample (Fig. 2.7a). At the glass-water interface, a small portion of the incident illumination ($E_i$) is reflected ($E_r$) and collected by the objective lens along with light scattered by the sample ($E_s$). The interference of $E_r$ and $E_s$ produces an image on the camera (Fig. 2.7b).

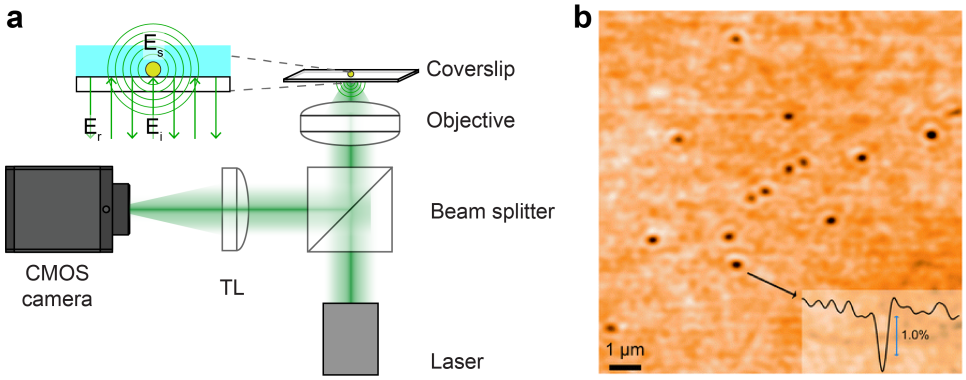


**Figure 2.7: Principle of interferometric scattering microscopy. a**) Diagram of an iSCAT setup. The interface between a glass coverslip and analyte solution is illuminated by a coherent light source. At the interface, part of the incident illumination ($E_i$) is reflected. The interference of the reflected light ($E_r$) and the light scattered by the analyte ($E_s$) forms the image on the camera. **b**) Image of 15 nm gold nanoparticles spin coated onto the surface of a clean glass coverslip immersed in water obtained by illumination at $\lambda = 532$ nm with iSCAT. Variations in the background correspond to scattering signal contributions from tiny imperfections in the glass surface. A cross section of the image is shown to indicate the extinction in the signal produced by a single gold nanoparticle compared to the glass surface roughness. Panel **b** adapted from reference 88 with permission from RSC.

In this imaging scheme, the interference of scattered and reflected light yields the following detected intensity:

$$I_d = |E_i|^2[r^2 + |s^2| + 2r|s|\cos(\phi)], \tag{2.4}$$

where $I_d$ is the detected intensity, $r^2$ the reflectivity of the interface, $s$ the scattering amplitude of the nanoscopic object (Eq. 2.3), and $\phi$ the phase difference between scattered and reflected light. For weak scatterers, where $r \gg s$, $|s|^2$ becomes negligible compared to the interference term $r|s|\cos(\phi)$.[94] As a result, the interferometric signal scales with the third power of the scatterer's diameter, which results in less drastic drops in signal with decreasing object size compared to purely scattering-based methods.[88,90] This improved scaling enables the use of smaller labels in SPT, while still achieving similar spatiotemporal resolutions. For example, using 20 nm gold nanoparticles as labels, iSCAT-based SPT has been used to track protein-lipid interactions on

membranes with 20 µs temporal resolution and 2 nm localisation precision.[93] Applications have also extended to in vivo, although these experiments are more challenging due to the high scattering background in cells, and require labelling with gold nanoparticles of at least 20-40 nm in size.[95,96]

As a consequence of these findings, iSCAT showed promise in complementing fluorescence-based approaches by providing previously inaccessible details. For example, in 2015, iSCAT was used to track the molecular motor myosin 5a with 1 ms temporal resolution and 4 nm localisation precision (labelled with a 20 nm gold nanoparticle), as it moved in 74 nm steps along actin filaments.[97] This spatiotemporal resolution allowed the authors to identify and characterise a transient state during each step, which had a lifetime of only ∼20 ms (Fig. 2.8). Combined with further experiments, these findings led to new insights into how this molecular motor achieves consistently unidirectional motion along actin filaments.

By relying on light scattering as a contrast mechanism, iSCAT also avoids complications encountered in fluorescence-based SPT, e.g. photoblinking and photobleaching, which results in simplified data analysis and improved observation times. However, for observing and quantifying dynamic interactions between several proteins, such as oligomerisation, the use of labels that are up to one order of magnitude larger than the target proteins is a source of concern. Ideally, these processes should be studied label-free to minimise any potential artefacts in the interaction and resulting effects on quantitative analyses.

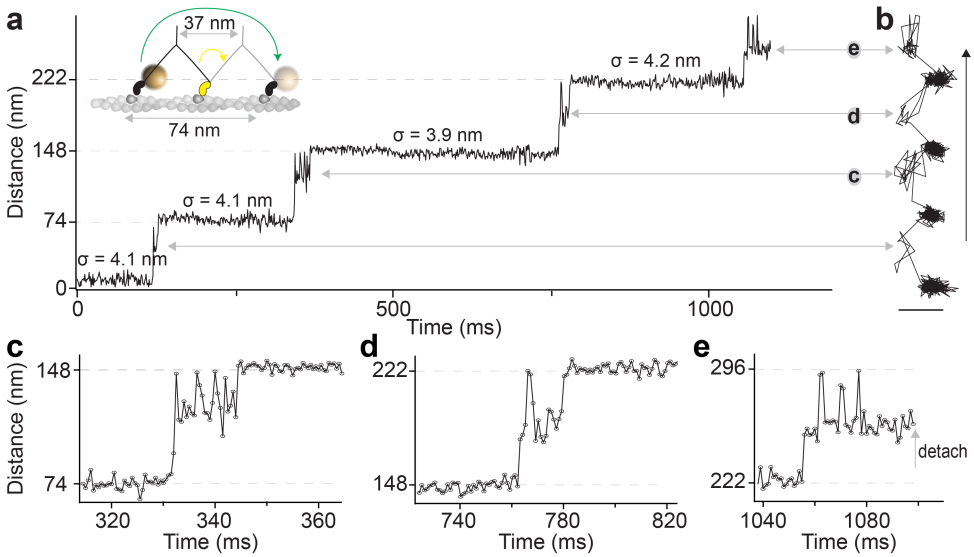


**Figure 2.8: High-speed nanometric tracking of myosin 5a with iSCAT. a**) Distance travelled as a function of time for a single myosin 5a molecule biotinylated at the N-terminus and labelled with a 20 nm streptavidin-functionalised gold particle. The lateral localisation precision, $\sigma$, defined as the standard deviation of the positional fluctuations of the label while bound to actin is given above each of the actin-attached periods. Inset, schematic of gold-labelled myosin 5 stepping along actin. **b**) Corresponding 2D-trajectory with the arrow indicating the direction of movement. **c-e**) Close-up of the transient states indicated in **a** and **b**. Scale bar, 50 nm. Adapted from reference 97 (open access, no copyright).

### 2.3.3 Label-free Single-Particle Tracking

As previously discussed, in the shot noise-limited case, the SNR of the imaged analyte scales with $\sqrt{N}$. It is clear that at least in principle, single biomolecules can be imaged based on light scattering given sufficient incident photons ($N$). The difficulty lies in actually achieving shot noise-limited detection. In iSCAT, the improved scaling in signal with decreasing object size compared to purely scattering-based methods reduces the impact of background signal such as spurious reflections.[88] However, the interferometric signal from a single biomolecule is still several orders of magnitude smaller than the signal from the surface roughness of the glass coverslip. Thus, one key challenge for label-free imaging by iSCAT was the efficient removal of this background signal.

Label-free in vitro SPT of individual biomolecules based on iSCAT was initially demonstrated on processes involving large macromolecules in the MDa range, e.g. interactions of viruses with viral receptors on SLBs or the disassembly of microtubules.[98,99] Notably, in 2014 label-free SPT of a single 500 kDa protein complex, myosin 5a, was achieved with a temporal resolution and localisation precision of 40 ms and 5 nm, respectively.[100] Here, the authors took advantage of the mobility of myosin 5a on actin filaments to continuously subtract static background features (Fig. 2.9a-c), resulting in shot noise-limited detection. With sufficient temporal averaging, this approach achieved a detection limit on the order of 60 kDa (Fig. 2.9d).

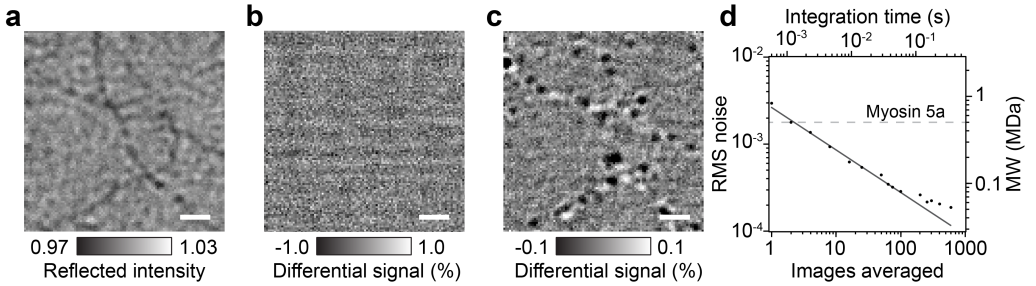


**Figure 2.9: Label-free tracking of single myosin 5a complexes by iSCAT.** **a**) Raw iSCAT image of myosin 5a on actin filaments. **b**) Corresponding image after subtracting static background features. **c**) Time-averaged background-subtracted image, where shot noise is sufficiently reduced to reveal mobile myosin 5a molecules. **d**) Background noise as a function of the number of averaged images. Solid line indicates shot noise behavior. A second vertical axis was added corresponding to the molecular weight (MW) detectable at an SNR of 1 as a function of integration time. In the case of myosin 5a, this number corresponds to 1 ms. The dashed grey line represents the molecular weight of myosin 5a. Scale bars, 1 µm. Individual panels adapted from reference 100; copyright 2014 American Chemical Society.

The results on myosin 5a were encouraging and suggested that the label-free detection and tracking of smaller proteins by iSCAT may be possible. Indeed, in the following years the combined findings from three research groups demonstrated the label-free tracking of single 500 kDa protein complexes and detection of immobilised proteins as small as 60 kDa.[32,100–103]

## 2.4 Mass Photometry

Several innovations to iSCAT resulted in increased sensitivity and precision by improving the imaging contrast and reducing background fluctuation. Ultimately, this led to the application of iSCAT as an in vitro technique for detecting and measuring the mass of immobilised biomolecules completely label-free,[32] which later became known as mass photometry (MP). MP was demonstrated to show robust scaling of the detected interferometric contrast of single biomolecules with their molecular weight across a wide range of proteins.[32] Consequently, by monitoring the mass of individual protein complexes, protein-protein interactions could be quantified at the single-molecule level completely label-free. In particular, different co-existing oligomeric states could be resolved robustly. MP also shows potential for use as an SPT technique, by localising individual protein complexes on the detection surface, thereby enabling the quantification of protein-protein interactions on SLBs.

### 2.4.1 Development and Principle of Mass Photometry

Based on Eq. 2.4 the imaging contrast of small scatterers, e.g. proteins, can be written as:

$$\frac{I_d}{I_b} = 1 + \frac{2|s|\cos(\phi)]}{r}, \tag{2.5}$$

where $I_d$ and $I_b$ are the light intensities detected in the presence and absence of the scatterer, respectively.[103] In conventional iSCAT setups, this relationship resulted in imaging contrasts of approximately 0.4% $MDa^{-1}$ for single proteins relative to the background signal.[100,101] The background fluctuations were largely governed by shot noise, resulting in baseline noise of $\sqrt{N}/N$ relative to the number of detected photoelectrons, $N$.[103]

The majority of commercially available cameras could detect up to $\sim 10^5$ photoelectrons per pixel, which, in an ideal experiment, translated to background fluctuations in interferometric contrast of 0.3% or roughly the signal from an 800 kDa protein (without temporal averaging). Thus, the robust detection of proteins $\ll$ 500 kDa, without having to resort to extensive temporal averaging, required cameras with full-well depths $> 10^5$. Additionally, the weak interferometric signal in raw images made determining the optimal focus position of the microscope challenging.[103] To circumvent these issues, a new optical design was implemented, in which the reflected light was selectively attenuated, while leaving scattered light largely unaffected. This effectively decreased $r$ (Eq. 2.5), which resulted in increased interferometric contrast.[103]

Scattered and reflected light originating from the illuminated glass-water interface travel at intrinsically different angles with respect to the sample. The reflected light is captured by the objective lens in regions associated with low numerical aperture, while small scatterers distribute photons to regions of high numerical aperture. Thus, by placing a partial reflector in the centre region of the back focal plane of the objective, the reflected light could be selectively attenuated (Fig. 2.10). The resulting increase in contrast did not inherently increase the SNR due to the reduced total number of photons reaching the detector. However, this approach allowed for the use of commercially available CMOS cameras with low full-well depths, high read-out speeds and high quantum efficiencies, ultimately benefiting the detection process.[103]

The authors applied their improved experimental setup to a landing assay, in which analyte solution was put in contact with the glass coverslip, resulting in proteins non-specifically binding to the glass-water interface. To detect the relatively weak signal from individual landing events compared to the interferometric signal from the roughness of the glass surface, the authors

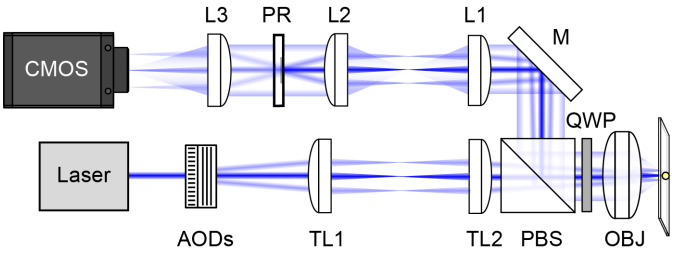


**Figure 2.10: Schematic of an iSCAT setup for mass photometry.** The experimental setup is based on acousto-optic (AOD) scanning of a collimated beam using a telecentric imaging setup (TL1/2). The combination of a $\lambda/4$ waveplate (QWP) and polarising beam splitter (PBS) separates incident from scattered and reflected light. Two lenses (L1/2) create an image of the back focal plane of the microscope objective (OBJ) where the partial reflector (PR) attenuates the back-reflected beam while leaving scattered light effectively unchanged. A final lens (L3) forms an image on the CMOS camera. Figure adapted from reference 103; copyright 2017 American Chemical Society.

applied a background subtraction algorithm.[103] For each raw image, $i$, an average of the images $i$ to $i + N$ was calculated and divided by the average of the $N$ preceding images. By repeating this computation throughout a series of images, the authors obtained ratiometric movies, in which static features were continuously removed leaving only dynamic features visible, e.g. individual proteins binding to the surface (Fig. 2.11a-b). This routine resulted in the signal from single proteins gradually fading in until they reached their maximum contrast value at the time when binding occurred, and then gradually disappearing as part of the static background (Fig. 2.11c). Thus, the time of binding and thereby the interferometric contrast of single proteins could be reliably determined, avoiding fluctuations caused by binding events occurring at different times during the acquisition of an image (Fig. 2.11d).[32,103]

Overall, these innovations enabled the detection of proteins as small as 50 kDa with precise and accurate quantification of their interferometric contrasts,[32] which had important implications for studying protein-protein interactions. A protein's contrast is a function of its refractive index and scales linearly with volume (Eqs. 2.3-2.5). As such, a protein's contrast should scale loosely with

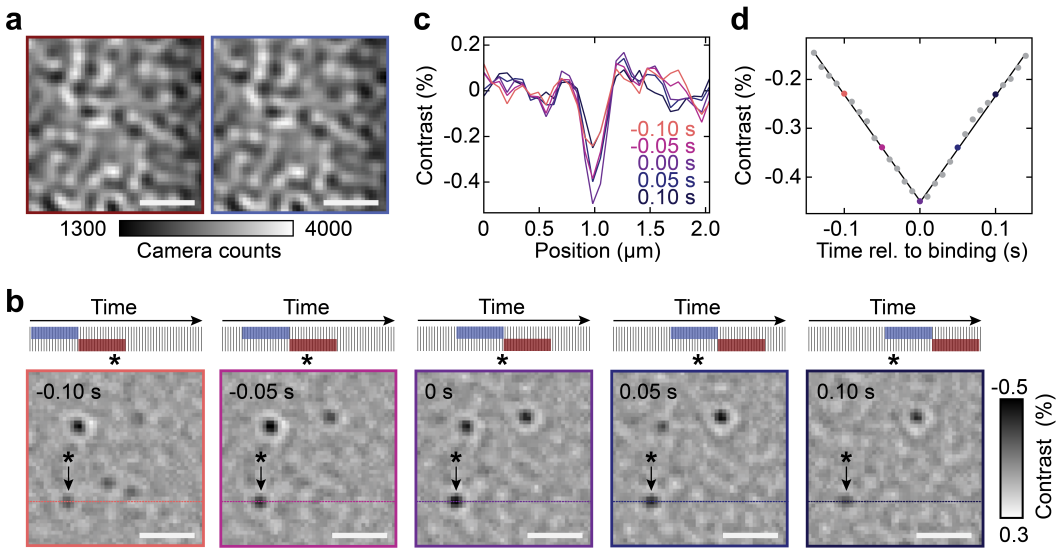


**Figure 2.11: Ratiometric background subtraction in mass photometry.** **a**) Raw camera images before and after the landing event in **b-d** showing image contrast due to coverslip roughness. **b**) Illustration of the image averaging and ratiometric imaging approach. The asterisk marks a landing event. Individual images are averaged into two consecutive blocks (blue and red), which are normalised and divided to provide ratiometric contrast. The mid-point is scanned in time, meaning that the signal from stochastic landing events grows and fades, as indicated by the black arrow. Scale bars, 1 µm. **c**) Corresponding cross-sections for the particle highlighted in **b**. **d**) Corresponding signal magnitudes extracted by a fit to the PSF and fit (black). Figure adapted from reference 32; reprinted with permission from AAAS.

its mass, which had been reported to hold by several groups at this point.[100–102] More recently, Young et al.[32] showed that based on the amino acid sequence of proteins from six different genomes, the refractive indices and specific volumes of proteins only varied by approximately 1% (Fig. 2.12a). This distribution, combined with the outlined improvements to iSCAT, enabled the detection and mass measurement of single unlabelled protein complexes with a sensitivity of ∼40 kDa, an average mass accuracy of 2% (Fig. 2.12b), and a mass resolution of ∼20 kDa. Thus, the mass and subunit composition of individual protein complexes in an analyte solution could be determined by converting contrast to mass with a suitable calibration, which later became known as MP.

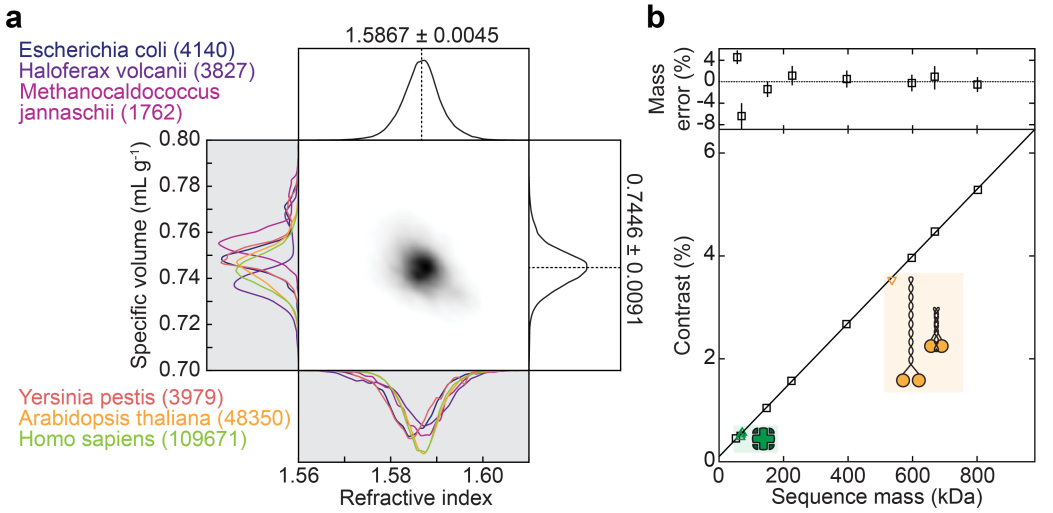


**Figure 2.12: Mass accuracy, precision, and dependence on molecular shape and identity.** **a**) Two-dimensional distributions of refractive index and specific volume for all proteins in six genomes, as calculated from the amino acid sequences. The top, right, and middle panels show the combined data from all genomes. The left and bottom panels show the respective normalised distributions for the separate genomes. **b**) Contrast versus molecular mass, including for proteins used for mass calibration (black), characterisation of shape dependence (yellow) and protein-ligand binding (green). Mass error (upper panel) is given as a percentage of the sequence mass relative to the given linear fit. Both panels adapted from reference 32; reprinted with permission from AAAS.

### 2.4.2 Characterisation of Protein-Protein Interactions

Within the limits of its mass accuracy and resolution, MP enabled the quantification of different co-existing protein complexes and stoichiometries via single-molecule counting. Young et al. demonstrated these capabilities on a solution of bovine serum albumin (BSA, 66 kDa) in contact with the glass coverslip on the MP setup.[32] The authors were able to detect and confidently resolve individual oligomeric complexes ranging from monomeric to tetrameric BSA, as they bound to the glass coverslip (Fig. 2.13a-c). Plotting all detected binding events in a histogram (Fig. 2.13d) yielded an oligomeric distribution from which the relative abundances could be extracted by integrating over the area of each oligomeric peak.

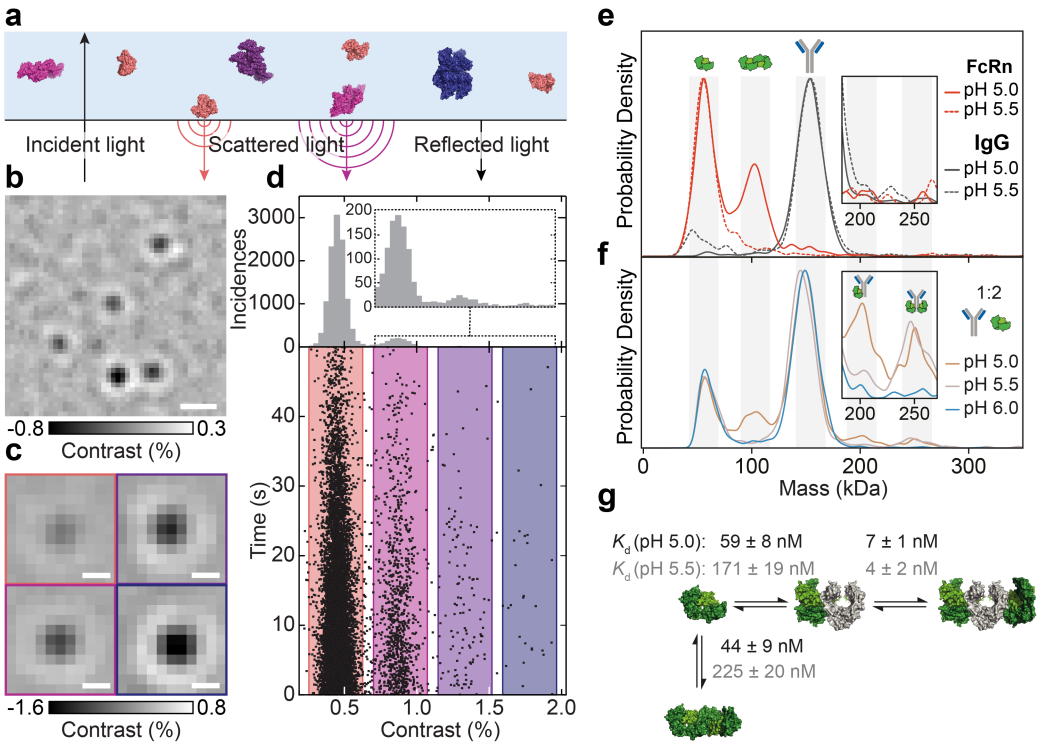


**Figure 2.13: Quantifying protein-protein interactions by MP. a**) Schematic of the experimental approach relying on immobilisation of individual molecules near a refractive index interface. Oligomeric states are coloured differently for clarity. **b)** Ratiometric image of BSA. Scale bar, 0.5 µm. **c**) Representative images of monomers (top left), dimers (bottom left), trimers (top right), and tetramers (bottom right) of BSA. Scale bars, 200 nm. **d**) Scatter plot of single-molecule binding events and their contrasts for 12 nM BSA from 14 movies (lower panel). Corresponding histogram with a zoomed-in view of the region for larger species (upper panel). **e**) Self-assembly of FcRn dimers at pH 5 (red) and 5.5 (dotted red) and equivalent pH measurements of IgG at pH 5 (grey) and 5.5 (dotted grey). **f**) IgG-FcRn complexes (1:1 mixture) at pH 5, 5.5 and 6. **g**) Associated pH-dependent $K_d$ of each complex revealing cooperativity in FcRn binding. Panels **a-d** adapted from reference 32; reprinted with permission from AAAS. Panels **e-g** adapted from reference 33 (open access).

Quantifying the abundances of distinct protein complexes at the single-molecule level based on their mass yielded a relatively simple method for determining solution-based binding affinities (Eq. 2.2). This proved particularly valuable in systems that exhibited multivalent binding or several oligomeric states.[33,34] For example, a recent study applied MP to the interaction between an immunoglobulin G antibody (IgG) and the neonatal fc receptor (FcRn), which regulates the half-life of IgGs in serum. The measurements revealed

dimerisation of FcRn and binding to IgG in 1:1 and 2:1 stoichiometries, whereby all species could be resolved, which enabled the quantification of the $K_d$ of each species as a function of pH (Fig. 2.13e-f).

Young et al. also demonstrated that MP could be used to follow assembly mechanisms of higher order protein complexes and to quantify the associated kinetics. The authors used SLBs to observe the formation of individual immobile α-synuclein aggregates, which have been implicated in Parkinson's disease,[104] as a function of concentration. As a result, aggregation rates and first-order assembly kinetics could be extracted (Fig. 2.14a-b). Moreover, the same study demonstrated tracking of the growth of individual actin filaments immobilised on coverslips and quantified the mass gain associated with individual growth steps (Fig. 2.14c-e).

Overall, these results clearly demonstrated the ability of MP to resolve different co-existing protein complexes, quantify corresponding binding affinities and kinetics as a function of oligomeric state or stoichiometry, and to handle polydisperse systems. A crucial point remains that the absence of labels avoided label-induced artefacts, which greatly simplifies the experimental approach and data analysis, in particular the quantification of the abundances of different protein complexes. The demonstrated compatibility of MP with SLBs also holds promise for the development of MP-based SPT. Thus, MP shows great potential in charcterising polydisperse systems and in translating these capabilities to studying membrane proteins on SLBs, thereby complementing and verifying insights from single-molecule fluorescence-based approaches.

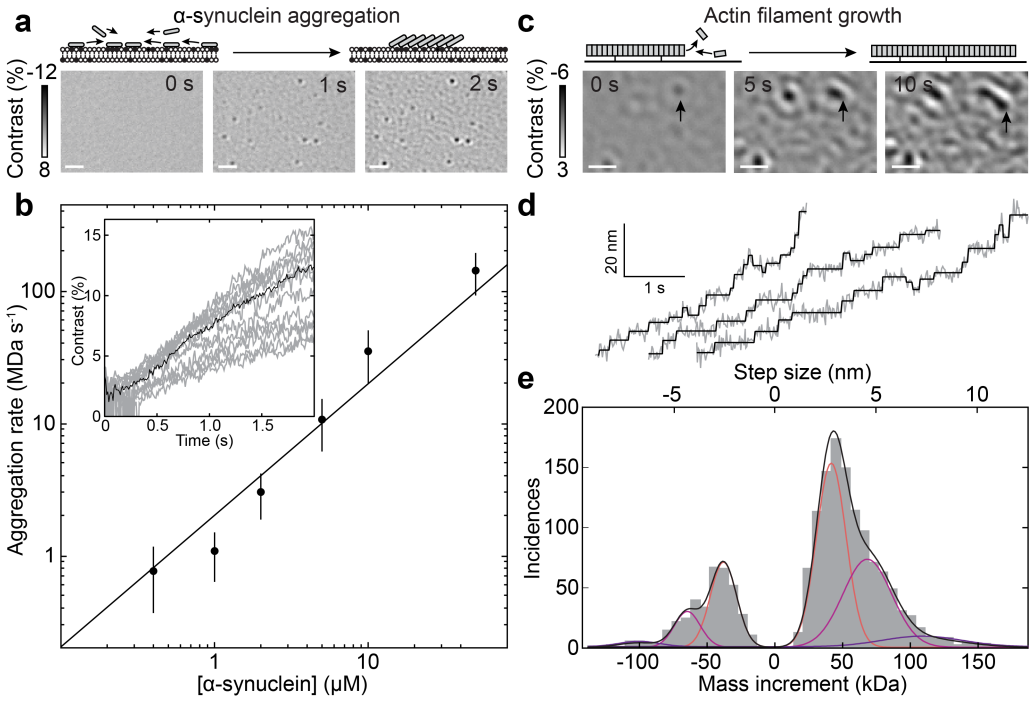


**Figure 2.14: Quantifying aggregation and self-assembly at the single-molecule level. a**) Schematic and MP images of α-synuclein (1 µM) aggregation on a negatively charged SLB. **b**) Initial growth rate versus α-synuclein concentration, shown with the best fit assuming first-order kinetics. Error bars denote SEM for different particles. Inset, individual (gray) and average (black) growth trajectories for 21 particles from **a**. **c**) Schematic and MP images of actin polymerisation. The arrow highlights a growing filament. **d**) Representative traces of actin filament tip position (gray) and corresponding detected steps (black). **e**) Step and mass histogram from 1523 steps and 33 filaments, including a fit to a Gaussian mixture model (black) and individual contributions. Scale bars, 1 µm. In these experiments, background correction involved removal of the static background before acquisition, rather than ratiometric imaging. Figure adapted from reference 32; reprinted with permission from AAAS.

### 2.4.3 Current Limitations and Outlook

The aim of this thesis is to capitalise on the benefits of MP to facilitate the quantification of polydisperse protein-protein interactions and membrane protein interactions, thereby complementing the shortcomings of other techniques, such as single-molecule fluorescence. In this context, there are important limitations to address and explore both for studying solution-based systems and for extending MP to SPT of protein complexes on membranes.

First, we will consider limitations associated with solution-based MP measurements, known as landing assays. In an MP landing assay, buffer solution is placed on a glass coverslip and held in place by a silicone gasket. Typically, analyte solution is introduced with a micropipette and proteins in solution immediately begin to bind to the glass coverslip non-specifically (Fig. 2.15a). After generating ratiometric images, these binding events are detected and quantified to extract the interferometric contrast of each protein molecule. Contrast is then converted to mass using an external calibration. A typical measurement lasts 60-90 s during which the proteins are depleted from the solution and the number of binding events rapidly decays (Fig. 2.15b). In the context of this thesis, it is important to realise that landing assays rely on proteins remaining stationary immediately after binding to the surface to robustly measure their mass.

This experimental approach imposes limitations on the accessible concentration range. Below 1 nM, insufficient binding events are recorded to extract statistically significant information before the protein in solution is depleted. At concentrations $\gg$ 100 nM, the non-specific binding events are too dense to resolve the signal from individual proteins (Fig. 2.15c-d). Moreover, the ratiometric background subtraction algorithm also reveals signals from proteins unbinding from the glass coverslip, which can lead to additional crowding of images. While Young et al. reported the adsorption of proteins to be largely irreversible at the investigated concentrations of 5 - 10 nM, at higher concentrations, the surface of the glass coverslip becomes increasingly crowded and unbinding events become more likely (Fig. 2.15d, white signals). Ultimately, the inability to resolve individual landing events poses an issue for accurate molecular counting and subsequent quantification of oligomeric abundances and binding affinities.

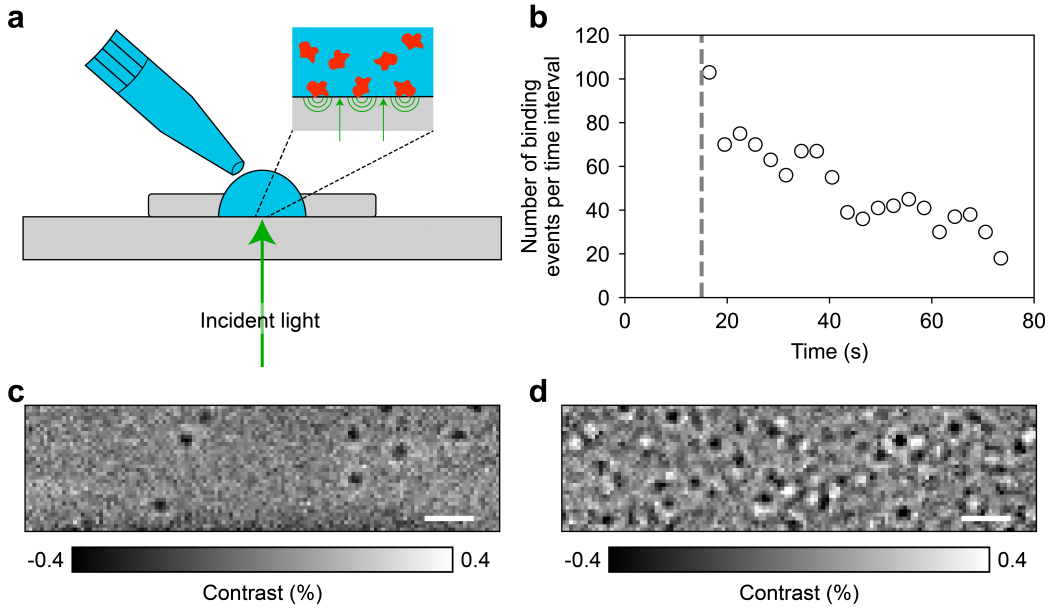


**Figure 2.15: MP landing assays and concentration limitations. a**) Analyte solution is added to a buffer droplet held in place by a silicone gasket on a glass coverslip illuminated by the MP laser. Proteins in solution then rapidly bind to the surface, generating the interferometric signal. **b**) Decay of protein binding events over time in a gasket-based MP experiment. The number of binding events decreases over 60-90 s until most protein has been depleted from the droplet or until the surface is saturated with protein. The grey line represents the 15 s delay between introduction of the protein solution and start of the measurement. **c-d**) Ratiometric images of apo-transferrin (80 kDa) at 25 and 200 nM, respectively. Scale bars, 1 µm.

In the context of developing an MP-based SPT assay to study interactions on SLBs, the main hurdle is the lack of knowledge to which degree the capabilities of MP in solution can be translated to tracking laterally mobile protein complexes. While Young et al. used MP to quantify changes in the mass of largely immobile protein aggregates on SLBs, SPT of mobile proteins with the improved performance of MP compared to conventional iSCAT had not been demonstrated. Furthermore, while laterally mobile protein complexes will generate local changes in the refractive index of the interface, and thus remain in principle detectable, there was no custom or commercial software for the detection and analysis of this type of data. As such, realising MP-based SPT requires further exploration of the compatibility of SLBs with MP and the

development of suitable custom software. A key question is to which degree the sensitivity, mass accuracy, and mass resolution achievable in landing assays can be translated to SPT, while still obtaining spatiotemporal resolution on par with or superior to single-molecule fluorescence-based methods.

As it stands, the narrow range of protein concentrations compatible with MP landing assays drastically limits the solution-based protein-protein interactions we can study. In particular, the upper limit of a total particle concentration of ∼100 nM, prevents the application of MP to weak and transient processes, which often have a $K_d > 1$ µM, and represent the majority of protein-protein interactions.[105] As MP has already provided valuable insights for interactions in the nM range,[33,106] accessing higher concentrations could be transformative for this technology. At the same time, the successful translation of the capabilities of MP landing assays to SPT on SLBs would provide access to a completely new realm for quantifying protein-protein interactions on membranes, particularly in the context of resolving and tracking different co-existing protein complexes. Both of these methodological advancements would be of great value to the scientific community and should be pursued.

We begin in Chapter 3 by exploring to which degree the accessible concentration ranges in MP landing assays can be extended with the aim of making measurements in µM concentrations feasible. We then transition to focusing on the development of MP-based SPT in Chapter 4 and explore the achievable sensitivity, mass accuracy, mass resolution and spatiotemporal resolution. The remainder of this thesis focuses on combining these two aims and enabling MP measurements at µM concentrations on SLBs.

# Chapter 3

# Expanding the Concentration Range of Solution-Based Mass Photometry

The work in this chapter was started prior to the outbreak of the COVID-19 pandemic, and therefore was cut short in March 2020, when research facilities closed down for several months.

A small portion of this chapter (section 3.2.1, Figs. 3.3-3.4) has been partially adapted from the following publication: F. Soltermann, E.D.B. Foley, V. Pagnoni, M. Galpin, J.L.P. Benesch, P. Kukura, W.B. Struwe, Quantifying protein-protein interactions by molecular counting with mass photometry, *Angewandte Chemie International Edition*, 2020, **59**, 10774-10779.[33] Reprint permitted under the terms of the Creative Commons Attribution 4.0 International License. Specifically, my contributions to this publication were the development of the continuous-flow setup, experiments to measure monomer:dimer ratios of 2G12 (Fig. 3.3-3.4), and, in collaboration with Fabian Soltermann, data analysis of these experiments.

## 3.1 Introduction

As outlined in Chapter 2, MP shows promise in complementing the shortcomings of other single-molecule methods. However, MP relies on proteins binding non-specifically to a glass coverslip to detect and measure their mass, which restricts current solution-based measurements to ∼1-100 nM, and thus limits MP to measuring strong protein-protein interactions. Measuring at $< 1$ nM is simply a matter of increasing statistics, either by increasing the imaging area or by continuously replenishing analyte solution to allow for longer measurements. In contrast, accessing concentrations $> 100$ nM is more challenging due to crowding of the MP images, which interferes with the detection of single binding events. Other techniques, such as single-molecule fluorescence microscopy, partially avoid this problem by labelling only a fraction of the analyte,[23] which is not compatible with MP. Therefore, enabling MP measurements at $> 100$ nM requires an approach to directly control the number of binding events.

The non-specific adsorption of proteins is more generally referred to as biofouling, and presents a challenge to a range of other biophysical techniques that rely on surface interactions. For example, in SPR, non-specific binding to the detection surface results in increased background fluctuations, which decreases sensitivity.[107] To address these issues, the scientific community has developed several types of antifouling coatings. Amongst the available options, polyethylene glycol (PEG)-based surface modifications are a popular choice due to their simple implementation and excellent performance.[108] By immobilising PEG on a surface to form a hydrated monolayer, proteins approaching the surface encounter energetic penalties from penetrating the hydration layer and from steric repulsion from PEG chains.[109,110] The result is a passivated detection surface that reduces non-specific binding events (Fig. 3.1a).[111]

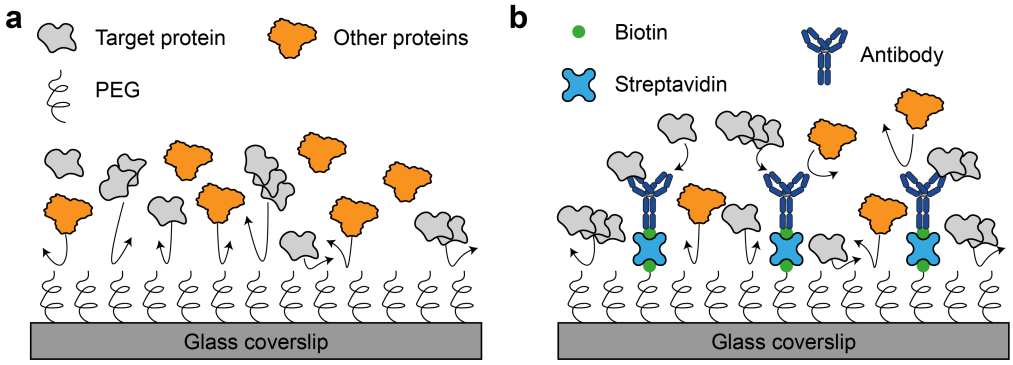


**Figure 3.1: Principle of antifouling coatings and biofunctionalisation.** **a**) Schematic of a glass surface coated in polyethylene glycol (PEG) to prevent non-specific binding of proteins in solution to the surface. **b**) Schematic of a biofunctionalised PEGylated glass surface. A small portion of PEG with biotinylated head groups is incorporated. Streptavidin binds to these headgroups, which allows for further functionalisation with a biotinylated antibody that specifically binds only the target protein.

By incorporating PEG chains with functionalised headgroups, passivated surfaces can be further modified to introduce specificity towards target analyte. This strategy is often used in single-molecule fluorescence microscopy to selectively immobilise target proteins on the detection surface, thereby minimising background signal or other artefacts due to non-specific interactions.[40,111,112] In this context, a common choice is the biotin-streptavidin system. Streptavidin (StrAv) is a 60 kDa protein with four binding sites for biotin (bt) and the resulting interaction is one of the strongest non-covalent bonds found in nature, with a half-life $> 30$ h.[113,114] By incorporating a small fraction of bt-PEG in the coating, followed by incubation with StrAv (or one of its analogues), the resulting surface becomes specific to bt and bt-containing proteins. As most proteins can be biotinylated via exposed lysine residues, this method allows for immobilisation of a wide range of biomolecules, e.g. antibodies, that can be used to specifically bind the target protein (Fig. 3.1b).[40,111]

The preparation of passivated biofunctionalised surfaces presents a potential route to increasing the accessible concentrations in MP. In particular, by

controlling the amount of biofunctionalised PEG on the surface, it should be possible to directly control the number of binding events in MP landing assays. In the past, some iSCAT-based studies have utilised PEG-based surfaces to minimise non-specific binding events at high solution concentrations, while studying the assembly of single protein complexes attached to the coverslip.[115] Although Young et al. employed a similar surface functionalisation strategy to study actin filament growth at 1 µM,[32] the degree to which non-specific binding of different proteins can be reduced in MP experiments remains unexplored. Additionally, reports of MP measurements relying on biofunctionalised surfaces are rare.

In this chapter, we investigate approaches aimed at increasing the accessible concentrations for solution-based MP measurements. First, we make use of a simple microfluidic setup to continuously replenish analyte solution and enable measurements at $< 1$ nM. Subsequently, we benchmark the accuracy of molecular counting by MP as a function of concentration. Next, we implement a PEG-based surface passivation protocol to reduce non-specific interactions of a range of proteins with glass coverslips. We explore limitations in the pasivation performance, and further functionalise the PEG surfaces with biotin and streptavidin to introduce specificity.

## 3.2 Results and Discussion

### 3.2.1 Molecular Counting and Concentration Range

To first highlight the limitations in the concentration range accessible in MP landing assays, we recorded measurements of the largely monomeric protein human apo-transferrin (Tfn; 80 kDa) at 2-200 nM (Fig. 3.2). At concentrations $< 50$ nM, the number of binding events was proportional to the concentration

of Tfn, as one might intuitively expect. However, at concentrations above 50 nM, this proportionality began to break down due to the high density of binding events, resulting in neighbouring binding events overlapping and therefore not being detected. As MP experiments measure local changes in the refractive index of the glass coverslip, signals due to protein unbinding from the surface are also detected and quantified (appearing as white particles with negative mass), which can increase the complexity of the data analysis. The amount of unbinding events sgnificantily increased above 50 nM Tfn, which indicated that the glass coverslips became mostly saturated with protein at these concentrations. Both the overlap of binding events and increased unbinding resulted in decreased mass resolution (increased peak width) at high concentrations (Fig. 3.2d).

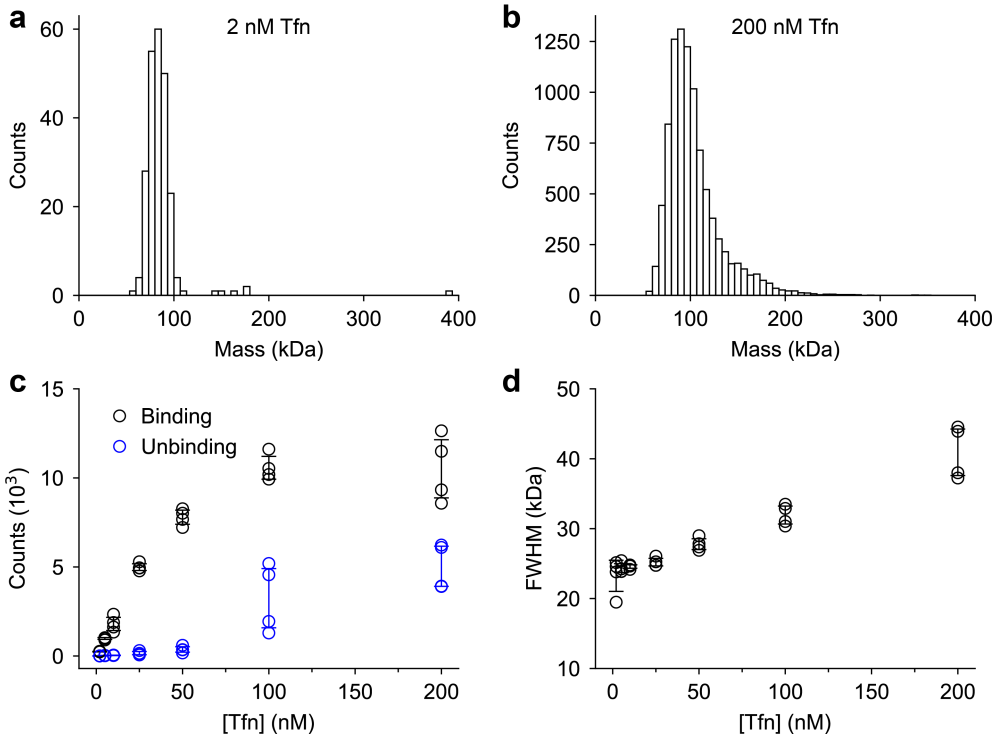


**Figure 3.2: Effect of protein concentration on MP landing assays. a-b**), Mass histograms obtained from MP landing assays of Tfn solutions at 2 nM and 200 nM, respectively. **c**) Number of binding and unbinding events detected in 60 s MP landing assays vs concentration of Tfn. **d**) Full width at half maximum (FWHM) of the mass distribution of detected Tfn binding events.

These effects have direct consequences on the quantification of relative abundances of different proteins in solution and the extraction of parameters such as the $K_d$. Thus, we benchmarked the performance of MP in accurately quantifying the abundances of different proteins in solution. We used the HIV-1 neutralising antibody 2G12 (150 kDa) in its monomeric and dimeric form, which showed no interaction with each other, and monomer did not transition into dimer or vice versa on the timescales relevant to our experiments. Measuring mixtures of these two species by MP resulted in mass distributions with two peaks corresponding to 2G12 monomer and dimer, and their abundances could be readily quantified (Fig. 3.3). Therefore, a titration of 1:1 mixtures of these species (determined by UV-visible spectroscopy) served as a robust method to check whether quantification of the relative abundances of these species by MP yields accurate results.

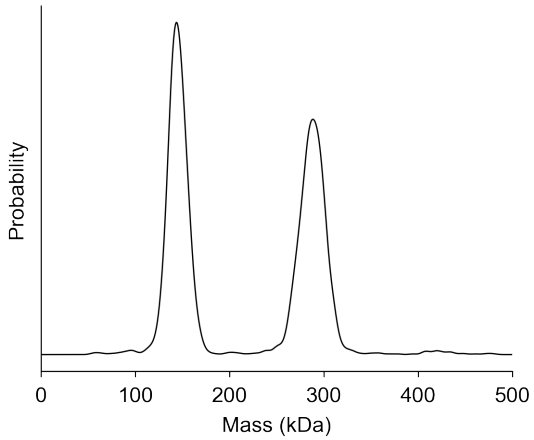


**Figure 3.3: Mass distribution of 2G12 monomer and dimer mixture.** Representative mass distribution of a 1:1 mixture of 2G12 monomer:dimer measured by MP in a silicone gasket at 10 nM. Integrating the areas of both peaks resulted in a measured monomer:dimer ratio of 1.05.

To access concentrations as low as 100 pM, we implemented a simple microfluidic system that continuously replenished the protein solution. This microfluidic setup allowed for longer measurements and more binding events to

be recorded compared to gasket-based MP experiments. Combined with gasket-based measurements, this approach enabled us to quantify the abundances of 2G12 monomer and dimer in 1:1 mixtures ranging from 100 pM to 50 nM (Fig. 3.4).

Overall, these measurements yielded 2G12 monomer:dimer ratios in good agreement with the expected 1:1 ratio. However, the microfluidic experiments from 0.1-1 nM showed bias towards the monomer. This effect could be successfully corrected for by accounting for the expected differences in the diffusion coefficients of 2G12 monomer and dimer based on their molecular weights. Additionally, at concentrations $> 10$ nM we systematically detected more dimer than expected, and this bias became more pronounced with increasing concentration. We attribute this effect to the increased overlap of neighbouring binding events with increasing concentration. When binding events overlap, the particle detection and fitting algorithm often favours the larger signal, which resulted in proportionately more 2G12 dimer being detected in these measurements. While this bias towards large particles only introduced an error of 20% at 50 nM, at higher concentrations one should be mindful of this effect and characterise it thoroughly when using MP to measure abundances of proteins with significantly different mass.

The extension of the concentration range down to 100 pM enabled the investigation of protein-protein interactions with a $K_d < 1$ nM, which were previously inaccessible by MP. For example, in our recent publication, we used the microfluidic setup to characterise the binding of the antibody trastuzumab to soluble domains of IgG Fc receptors revealing a $K_d$ of 50 pM and 1 nM for glycosylated and deglycosylated trastuzumab, respectively.[33] Nevertheless, MP measurements at total particle concentrations of 100 nM and higher remained challenging due to the high frequency of non-specific binding events. Therefore,

our next step was to implement a passivation protocol in MP landing assays with the aim of then modifying this surface to introduce specificity towards target proteins, which should make studying protein-protein interactions in the µM range and in complex mixtures possible.

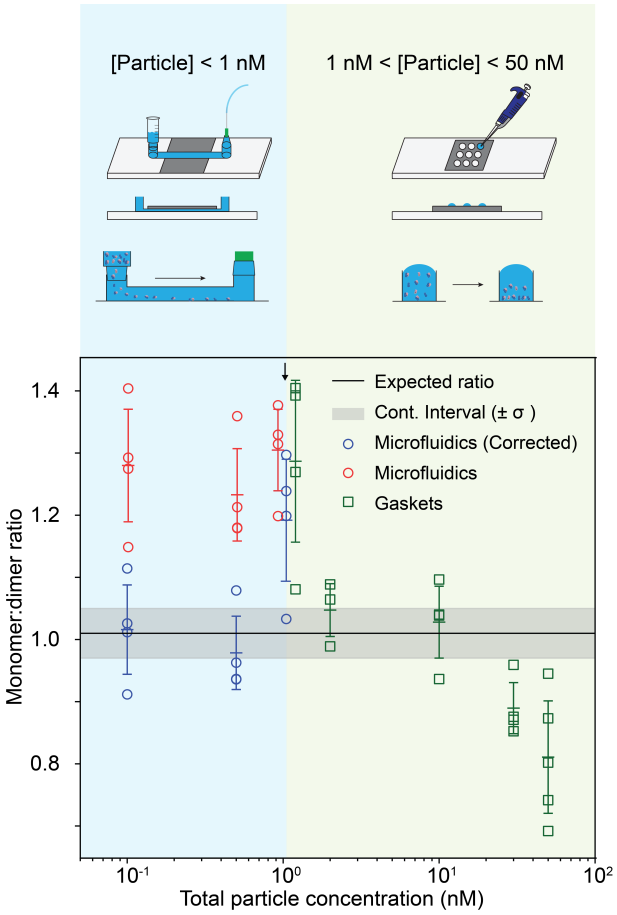


**Figure 3.4: Dynamic range of MP landing assays for accurate molecular counting.** Experimental setup for microfluidic chambers (top, left) and silicone gaskets (top, right). MP ratio measurements of a 1:1 mixture of 2G12 monomer and dimer at different dilutions (0.1, 0.5, 1, 1, 2, 10, 30, 50 nM). The three results for 1 nM solutions were separated horizontally (arrow) to improve readability. Diffusion-corrected microfluidic ratios (blue) were obtained by normalising monomer and dimer counts to their corresponding molecular weight dependent factor in the diffusion coefficient ($MW^{-1/3}$). The expected ratio (1.04 ± 0.05, black) was determined from UV-VIS measurements of concentrated (µM) stock solution of the pure monomer and dimer. Figure adapted from reference 33 (open access).

### 3.2.2 Surface Passivation for Mass Photometry

To date, surface passivation methods have rarely been employed in MP experiments and it is unclear how well their performance translates from other biophysical methods. Here, we implemented and benchmarked a polyethylene glycol (PEG)-based surface passivation protocol for single-molecule imaging.[111] In brief, glass coverslips were treated with an aminosilane followed by an aqueous solution of PEG with N-hydroxysuccinimide groups to obtain glass coverslips densely connected to PEG chains via amide bonds (Fig. 3.5).

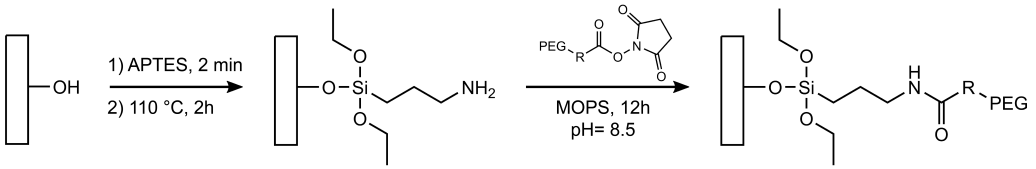


**Figure 3.5: PEGylation protocol for mass photometry coverslips.** Plasma cleaned glass slides are treated with 2% (3-aminopropyl)tryethoxysilane (APTES) in acetone, followed by incubation at 110 °C in a dry oven. The coverslips are then incubated with 50 mg $mL^{-1}$ polyethylene glycol (PEG) containing N-hydroxysuccinimide headgroups that react with the exposed amine groups on the glass to form stable amide bonds, yielding glass coverslips with attached PEG chains.

Importantly, the PEGylation did not significantly change the surface roughness (Fig. 3.6a-b), and resulting MP movies of PEGylated glass with buffer showed similar background fluctuations compared to bare glass. Moreover, the resulting surfaces demonstrated a significant reduction in binding events for all proteins tested in this study (Fig. 3.6c). Compared to MP landing assays on bare glass (Fig. 3.2), the PEGylated coverslips enabled a reduction in binding events of at least two to four orders of magnitude in all cases. Generally, the number of binding events for all proteins tested on PEGylated slides equalled the number of unbinding events, which indicated that far fewer proteins irreversibly bound to the surface compared to bare glass (Fig. 3.2).

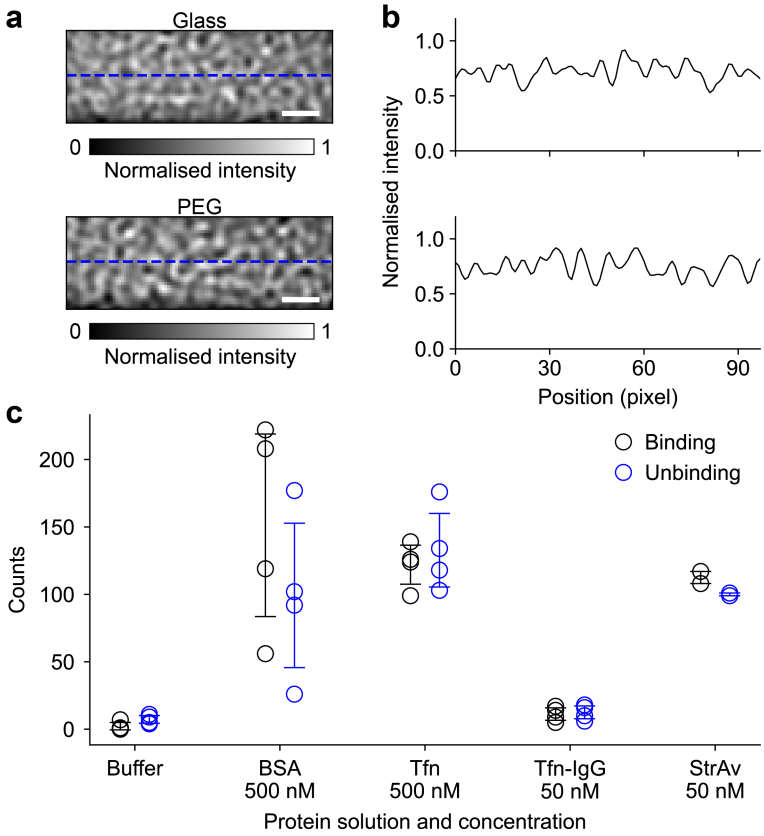


**Figure 3.6: Performance of PEGylated coverslips in mass photometry.** **a-b**) MP images of a glass coverslip (top) and a PEGylated glass coverslip (bottom) with corresponding plots of the measured pixel intensity vs pixel position along the blue dotted line. **c**) Binding and unbinding events detected during MP landing assays with buffer and various protein concentrations. Error bars represent the mean ± s.d. of the individually plotted data points. BSA: bovine serum albumin, Tfn: transferrin, Tfn-IgG: anti-human transferrin antibody, StrAv: Streptavidin. Scale bars, 1 µm.

Although this passivation protocol successfully minimised non-specific binding events, at concentrations $> 1$ µM we observed increased background fluctuations compared to buffer. At 5 µM, these background fluctuations reached a level where they would be expected to interfere with the detection of 100-200 kDa proteins (Fig. 3.7). We attribute this effect to an increased number of proteins residing near the surface but in solution, rather than binding to the surface, with increasing concentration. We expect that the magnitude of these fluctuations is dependent on a combination of protein size and concentration.

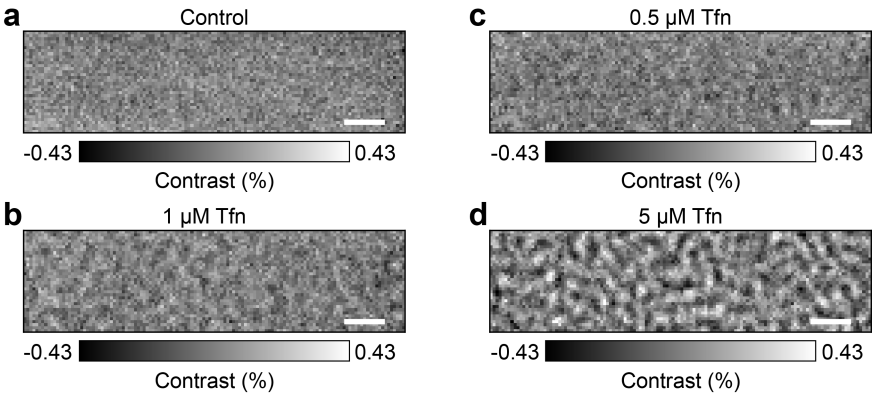


**Figure 3.7: Background fluctuations with PEGylated coverslips at high protein concentrations. a-d**), Representative background-subtracted images of MP experiments performed with buffer, 500 nM, 1 µM, and 5 µM Tfn, respectively. A contrast of 0.43% corresponds to a ∼100 kDa protein under these imaging conditions. Scale bar, 1 µm.

At this point, we wondered if it was possible to control the number of binding events recorded at a specific concentration by varying the amount of PEG attached to the coverslips, i.e. by changing the concentration of PEG used to treat the coverslips. If successful, this approach would avoid the need for biofunctionalisation steps. Indeed, testing 500 nM bovine serum albumin (BSA) and 500 nM Tfn on coverslips incubated with different PEG concentrations revealed a clear trend of decreasing binding events with increasing PEG concentration (Fig. 3.8a-b). Thus, in principle, it was possible to optimise the number and frequency of binding events for MP experiments. However, we observed a significant difference in the mass distribution of BSA obtained on bare glass compared to PEGylated glass (Fig. 3.8c-d). On bare glass, we obtained a distribution of oligomeric species ranging from monomeric to tetrameric BSA, as previously observed.[32] On PEGylated glass, the mass distributions were dominated by monomeric BSA and thus not representative of the solution distribution.

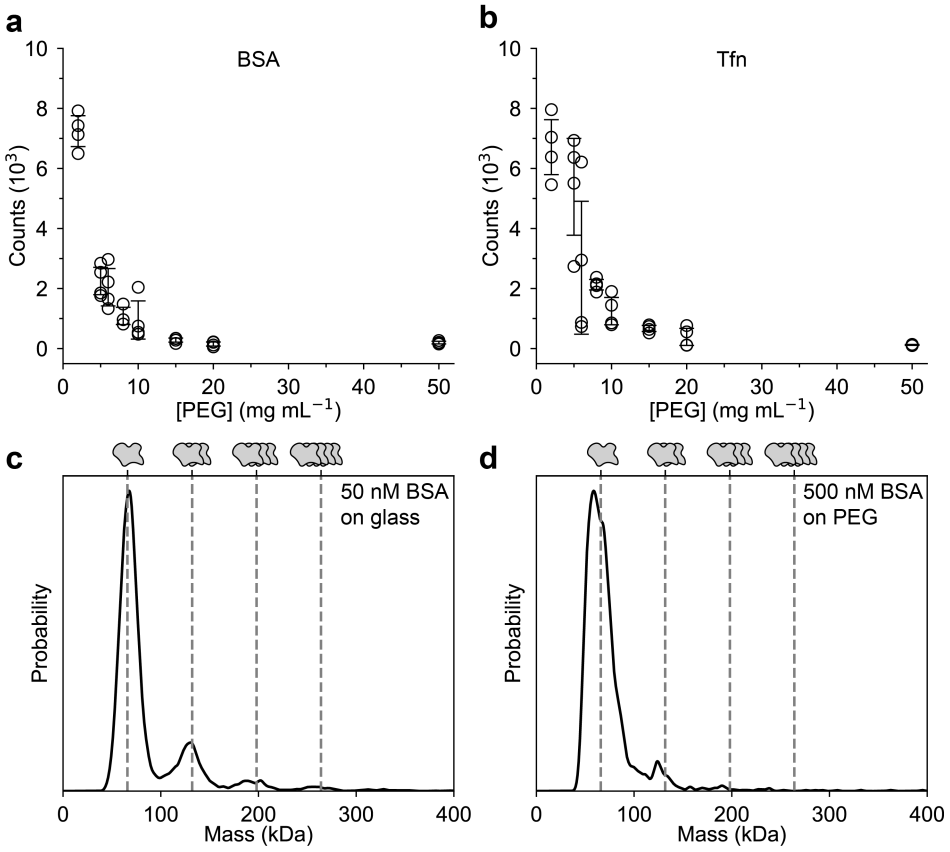


**Figure 3.8: Effect of PEG concentration on non-specific binding events.** **a-b**), Number of binding events recorded in MP landing assays with 500 nM BSA and Tfn, respectively, vs concentration of PEG used to prepare the coverslips. Error bars represent the mean ± s.d. **c-d**) Representative mass distributions recorded with 50 nM BSA on bare glass and with 500 nM BSA on coverslips treated with 6 mg mL$^{-1}$ PEG, respectively. Grey dotted lines indicate the expected mass of BSA monomer, dimer, trimer, and tetramer.

Nevertheless, the implemented passivation protocol successfully reduced the number of non-specific binding events and resulted in acceptable background fluctuations for protein concentrations $< 5$ µM. As controlling the number of binding events by changing the amount of PEG attached to the coverslips was impractical, we moved on to explore biofunctionalisation of the PEG surface. Provided the passivation performance could be retained when introducing these modifications, this approach showed great promise in being applied to study protein-protein interactions at concentrations up to 5 µM by MP.

### 3.2.3 Introducing Specificity via Surface Modifications

To introduce specificity to the PEGylated coverslips, we opted for a strategy based on biotin (bt; 0.25 kDa) and streptavidin (StrAv; 60 kDa).[111] We chose this system due to its effectiveness in other single-molecule microscopy studies, and because it allows for immobilisation of a wide range of biomolecules via biotinylation of lysine residues.

By mixing 1% of bt-PEG into the PEG solution, we were able to produce coverslips that specifically bound StrAv, while retaining their passivating properties (Fig. 3.9a). However, compared to bare glass coverslips, we observed an increase in the relative number of unbinding events. Moreover, when bt-PEG slides were incubated with StrAv, thoroughly rinsed, and placed with buffer on the mass photometer, we recorded a large number of unbinding events (negative mass) and some binding events (positive mass) with mean masses of -58 and 59 kDa, respectively (Fig. 3.9b), suggesting that StrAv was rapidly unbinding during MP measurements. When we added a solution of 15 nM biotinylated Tfn to bt-PEG slides pre-incubated with StrAv, we observed a shift in binding events to 70 kDa consistent with an unresolved mixture of StrAv and bt-Tfn (60 and 80 kDa, respectively). However, we also observed a polydisperse distribution of unbinding events with one peak at -59 kDa corresponding to StrAv, and a second peak at -115 kDa, which only appeared in the presence of both StrAv and bt-Tfn. These results indicated that the StrAv-incubated bt-PEG slides could specifically bind bt-Tfn, but StrAv was rapidly unbinding from the surface during MP measurements ($>$ 2000 unbinding events in 60 s).

The unbinding of StrAv from the bt-PEG surface was inherently problematic, as it resulted in crowding of the MP movies. Therefore, we next investigated potential causes. As StrAv clearly remained bound to bt-PEG during the

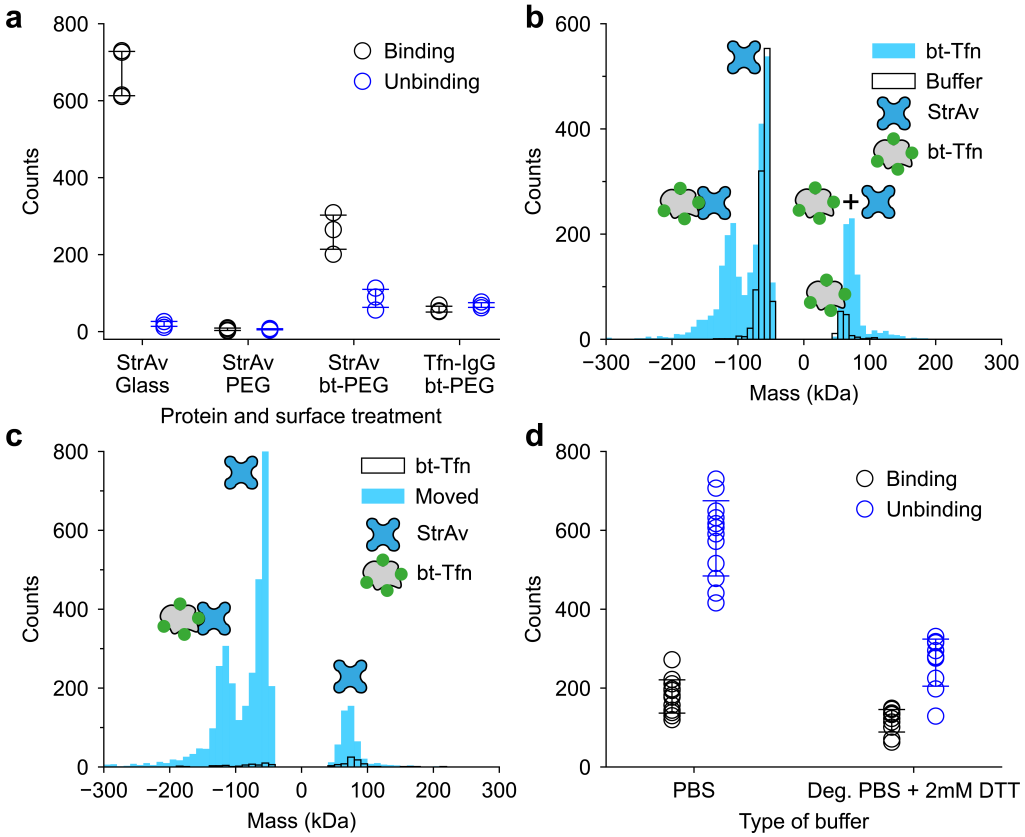


**Figure 3.9: Performance of biotin-PEG coverslips.** **a**) Number of binding and unbinding events recorded with 5 nM StrAv on glass coverslips, PEG coverslips and bt-PEG coverslips, and of 100 nM Tfn-IgG (anti-human transferrin antibody) on bt-PEG coverslips (f.l.t.r.). **b**) Mass histograms recorded on StrAv-incubated bt-PEG coverslips with buffer solution (black, hollow histogram) or 15 nM biotinylated Tfn (bt-Tfn, light blue histogram). Counts at negative mass correspond to unbinding events. **c**) Mass histograms recorded on StrAv-incubated bt-PEG coverslips with 15 nM bt-Tfn after exposing the coverslip area to the MP illumination laser (with intermittent rinsing steps) until unbinding of StrAv had ceased (black, hollow histogram), and after subsequently moving the same coverslip to a different area (light blue histogram). **d**) Unbinding and binding events recorded on avidin- and bt-Tfn-incubated bt-PEG coverslips with regular buffer or degassed buffer solution with 2 mM dithiothreitol.

thorough rinsing process, we first tested whether these unbinding events were triggered by the laser illumination of the MP setup. We incubated bt-PEG coverslips with StrAv followed by thorough rinsing and placed the coverslips with buffer solution on the MP setup. After illuminating the same area of the coverslips while intermittently replacing the buffer until unbinding had largely ceased, we recorded a measurement in the presence of bt-Tfn. The

resulting mass histogram (Fig 3.9c; black, howllow histogram) showed almost no binding and unbinding events compared to the data in Fig. 3.9b, which indicated that most StrAv had unbound from the bt-PEG surface. When the same coverslip was then moved to bring a different area into contact with the MP laser, the number of recorded events increased significantly (Fig. 3.9c; lightblue histogram) and we obtained a mass histogram more similar to the data in Fig. 3.9b. This result indicated that areas of the coverslip that had not been exposed to the MP laser still contained surface-bound StrAv and could bind bt-Tfn. Furthermore, we observed similar unbinding events when using avidin instead of StrAv and also determined that conducting measurements in degassed buffer under reducing conditions decreased the number of unbinding events (Fig. 3.9d). These results suggested that illumination of the coverslips by the MP laser was responsible for the observed unbinding of StrAv from the bt-PEG surface and pointed to photo-induced oxidative damage as a possible cause.

While clearly caused by illumination by the MP laser, it was not obvious whether the unbinding events were a result of breaking of the non-covalent bond between biotin and StrAv, photodamage to the bt headgroups, or entire bt-PEG chains attached to StrAv unbinding from the glass coverslips. In the absence of StrAv, unbinding of bt-PEG would not be detectable due to its low molecular weight of 5 kDa. However, PEG unbinding due to exposure to the MP laser should, over time, result in the deterioration of passivation performance. Similarly, damage to the bt head group over time should result in a decreased ability of the surface to bind StrAv.

To investigate whether damage to the bt-PEG surface was the cause of StrAv unbinding from the coverslips, we compared the passivating properties of PEGylated coverslip areas before and after illumination by the MP laser for 5

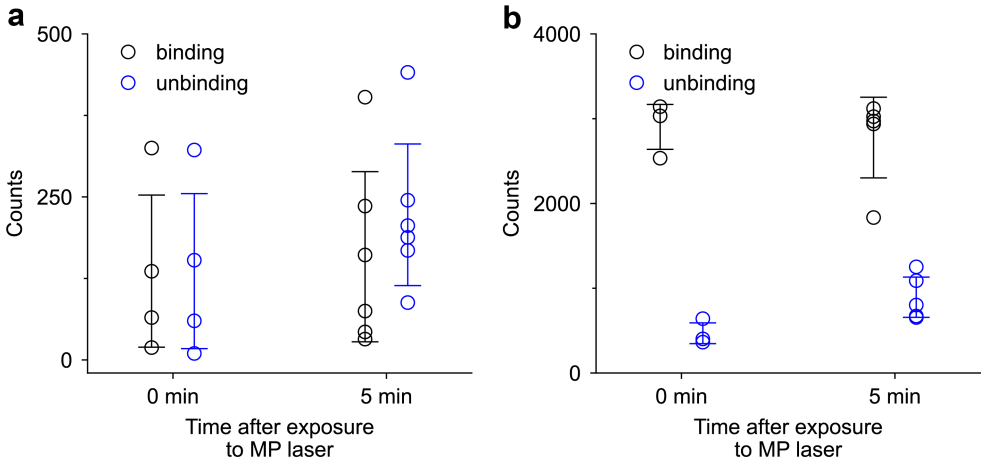


**Figure 3.10: Effect of MP illumination on surface functionalisation. a-b**) Binding and unbinding events recorded during MP measurements of 100 nM TFn-IgG and 15 nM StrAv, respectively, on bt-PEG coverslips before and after illuminating the measurement area of the coverslips with the MP laser.

min (Fig 3.10a). Additionally, we compared the ability of an area of a bt-PEG surface to bind StrAv to the same area after 5 min of illumination by the MP laser (Fig 3.10b). In both cases, we did not find any significant differences, suggesting that the bt-PEG chains and their connection to the glass surface remained largely intact during extended laser illumination.

Overall, our results point towards the breaking of the non-covalent bt-StrAv as the cause for the observed unbinding events and that this behaviour can be partially suppressed by conducting the experiments in degassed buffer under reducing conditions. However, StrAv unbinding from the surface remained a challenge for our approach to facilitate MP measurements at high concentration.

## 3.3 Conclusion

We demonstrated that concentrations as low as 100 pM can be accessed in MP landing assays by implementing a simple microfluidic system, and that abundances of different proteins in solution can be accurately quantified with this setup. To enable MP measurements above 100 nM, we investigated a PEG-based approach for surface passivation of the coverslips. Surface passivation resulted in a reduction of non-specific binding events by up to four orders of magnitude, and the baseline noise remained similar up to low µM concentrations. Subsequent attempts to introduce specificity towards target proteins via bt-StrAv-based surface functionalisation proved difficult. We consistently observed laser-induced unbinding of StrAv from the bt-PEG surface, which made MP measurements challenging and prevented further modifications with biotinylated proteins or antibodies. Nevertheless, this work demonstrates that, in principle, MP measurements at low µM solution concentrations are feasible, provided the passivated surface can be robustly biofunctionalised.

As our results suggested that the MP laser was triggering unbinding of StrAv from bt, opting for covalent over non-covalent surface modifications may lead to a more successful approach. For example, PEG surfaces with exposed maleimide or N-hydroxysuccinimide groups can form covalent bonds with cysteine and lysine amino acid residues, respectively.[116] Using these approaches would enable the to covalent attachment of antibodies to the PEG surface, which could then be used to specifically bind target proteins, while potentially avoiding unbinding of surface modifications.

At this point, the COVID-19 pandemic caused our facilities to shut down for several months, preventing further work on this chapter. In the meantime, a promising alternative emerged. Two of our postdoctoral researchers collected

preliminary data indicating that mobile protein complexes could be detected on supported lipid bilayers (SLBs) via MP. SLBs display strong passivating properties against a variety of proteins.[117,118] Additionally, proteins that do bind to the SLB via protein-lipid interactions diffuse laterally with the lipids, which we can take advantage of. A protein diffusing on a surface will generate a local change in refractive index as a function of its position, thereby continuously generating changes in the interferometric signal. Thus, by attaching molecular probes, e.g. antibodies, specific to target proteins to SLBs, we can generate surfaces on which these probes continuously remain visible due to their mobility. Therefore, an SLB-based approach to MP experiments will easily facilitate the distinction between transient non-specific binding events to the SLB from specific binding events to SLB-bound molecular probes.

So far, SLB-based experiments showed promise on two key avenues: 1) they could enable a robust approach to conducting MP experiments at high concentration or in complex mixtures, and 2) they could enable the quantification of membrane protein interactions on lipid bilayers, which aligned excellently with the aims of this thesis. Therefore, our efforts shifted to developing an analytical pipeline and, when facilities reopened, an experimental protocol for SLB-based MP measurements, which we present in Chapter 4. We will revisit our aim of enabling MP measurements at high concentration in Chapters 5 and 6.

## 3.4 Methods

### 3.4.1 Materials and Sample Storage

Human apo-transferrin (Tfn), bovine serum albumin (BSA), streptavidin (StrAv), avidin and biotin-labelled human apo-transferrin (bt-Tfn) were obtained from Sigma Aldrich. 2G12 monomer and dimer were expressed and purified as described previously.[33,119] The anti-human transferrin antibody (Tfn-IgG) was purchased from Medix Biochimica (Anti-h Transferrin 3104 SPTN-5). Concentrations were determined by UV-visible spectroscopy (DeNovix DS-11+). The polyethylene glycol reagents for functionalisation of the glass coverslips were obtained from Laysan Bio Inc: PEG-SVA-5000 (mPEG-Succinimidyl Valerate, MW = 5000 Da, Item# MPEG-SVA-5000-1g) and biotin-PEG-SVA-5000 (MW = 5000 Da, Item# Biotin-PEG-SVA-5000-100mg). All proteins were dissolved or buffer exchanged in phosphate-buffered saline (Gibco® DPBS) and stored at 4 °C for use for up to two weeks or at -80 °C for long-term storage. Anti-human transferrin was stored at 4 °C for long-term use (up to 18 months). The PEG reagents were aliquoted as dry powders and stored at -20 °C under nitrogen and defrosted before use.

### 3.4.2 Functionalisation of Glass Coverslips

The protocol for PEGylation and surface functionalisation was adapted from Chandradoss et al.[111]

*Aminosilation.* Glass coverslips (24 mm × 50 mm, Menzel Gläser, VWR 630-2603) were cleaned by sequential sonication in 2% Hellmanex in MilliQ-water, Milli-Q water, isopropanol, and Milli-Q water for 5 min each in an ultrasonic bath. The coverslips were dried with a stream of nitrogen and treated with

oxygen plasma (Zepto plasma cleaner, Diener Electronics) for 8 min. The plasma cleaned coverslips were briefly immersed in acetone and then swirled in a 2% APTES ((3-aminopropyl)-triethoxysilane, Sigma Aldrich) solution in acetone for 2 min. Next, the coverslips were briefly immersed in acetone again to remove excess APTES and placed in an oven at 110 °C for 2 h. After cooling to room temperature the coverslips were cleaned by sonication in acetone for 10 min, rinsed with Milli-Q water and dried with a stream of nitrogen.

*PEGylation and biofunctionalisation.* Aminosilanised coverslips were incubated with 50 mg $mL^{-1}$ PEG-SVA-5000 in 50 mM MOPS (Sigma Aldrich) buffer (pH 8.0) overnight in a humidity chamber by sandwiching 60 µL of PEG solution between two coverslips. PEGylated coverslips were rinsed with Milli-Q water and dried under nitrogen before use. PEG solutions were prepared immediately before use to minimise hydrolysis. Improved passivation was observed with additional treatments with PEG solution and minimised exposure to air via sandwiching of the coverslips. For surface functionalisation via bt-StrAv, 1% (mole fraction) biotin-PEG-SVA-5000 was included in the PEG solution. After PEGylation, silicone gaskets (3 mm × 1 mm, GBL103250, Grace Bio-Labs) were rinsed sequentially with Milli-Q water, isopropanol and Milli-Q water, dried under a stream of nitrogen and placed on the coverslips. For further surface functionalisation, bt-PEG coverslips were incubated with 20-100 nM StrAv or avidin in silicone gaskets for at least 20 min followed by thorough rinsing with Milli-Q water. For the data presented in Fig. 3.9d, incubation with avidin and rinsing was followed by incubation with 20 nM bt-Tfn for at least 20 min followed by further rinsing with Milli-Q water.

### 3.4.3 Mass Photometry Data Acquisition

Coverslips were cleaned as described previously.[32] Briefly, borosilicate coverslips were cleaned in an ultrasonicator bath sequentially with Milli-Q water, isopropanol and Milli-Q water, and then dried under a stream of nitrogen. Next, silicone gaskets were rinsed sequentially with Milli-Q water, isopropanol and Milli-Q water, dried under a stream of nitrogen and placed on the cleaned coverslips. Unless otherwise stated, MP data was acquired as follows. 30 µL of DPBS was placed into a gasket to find the optimal focus position on the coverslip surface. After locking in the focus position, 25 µL of buffer was removed and replaced with the sample solution. Data acquisition was started ∼15 s (5 s for the data in Fig. 3.4) after adding sample to the gasket. Microfluidic experiments were carried out as described previously.[33,119] Plastic flow chambers (sticky-Slide VI 0.4, Ibidi) were placed onto cleaned coverslips, filled with 150 µL of buffer and connected to a syringe-pump system (World Precision Instruments AL-1000, Fig. 3.4) and sample reservoir via flexible tubing, taking care not to introduce any air bubbles to the flow chamber. Next, the flow chamber was positioned on the mass photometer such that the MP laser was directed closely to the inlet of the flow chamber. The syringe pump was run at 90 µL $min^{-1}$ until the sample reservoir was almost empty, during which the focus was optimised and locked in. Next, analyte solution was introduced to the sample reservoir and after the focus had restabilised, acquisition was started. We note that at particle concentrations $> 1$ nM the surface of the coverslip quickly becomes saturated, resulting in rapid binding and unbinding of additional protein introduced via continuous flow. Therefore, use of this system should be restricted to concentrations $< 1$ nM.

Data was acquired on a Refeyn OneMP mass photometer at a frame rate of 1 kHz in a 10.8 µm x 2.9 µm field of view with 5-fold frame binning (200 Hz effective frame rate) and 4 x 4 pixel binning (final pixel size = 84.4 nm) for 60 s for gasket-based measurements (30 s for the data in Fig. 3.4), and 240 s for microfluidic measurements. For experiments quantifying the number of unbinding events on bt-PEG surfaces (Fig. 3.9), the coverslip was moved slightly immediately before starting data acquisition, to ensure the MP laser was hitting a new area of the coverslip, unless otherwise stated (Fig. 3.9c, 3.10).

### 3.4.4 Data Analysis

Acquired movies were processed and analysed using DiscoverMP (Refeyn Ltd) with the following settings: navg = 5; PSF parameters $a_{12}$ = -5.398947, $w$ = 2.308575 , $s$ = 5.281672; filter 1 = 0.7 and filter 2 = 0.25. The resulting contrast histograms were converted to mass histograms via calibration with an in-house mass standard (containing species at 90, 180, 360, 540, 720, 900 kDa).

The full width at half maximum of the data presented in Fig. 3.2 was extracted by fitting a single Gaussian to the mass histogram recorded with different concentrations of Tfn. Unless otherwise stated, all successfully detected and fitted events at positive mass and negative mass were summed to yield the number of binding and unbinding events, respectively. In Fig. 3.9d local regions with high binding and unbinding densities were excluded from the analysis. In Fig. 3.4 2G12 monomer:dimer ratios were extracted from the mass histograms as previously described.[33,119]

# Chapter 4

# Mass Photometry Enables Label-Free Tracking and Mass Measurement of Single Proteins on Lipid Bilayers

This chapter has been adapted from the following publication: E.D.B. Foley, M.S. Kushwah, G. Young, P. Kukura, Mass photometry enables label-free tracking and mass measurement of single proteins on lipid bilayers, *Nature Methods*, 2021, **18**, 1247-1252.[120] Reprint permitted under the terms of the Creative Commons Attribution 4.0 International License. The only modifications made are conversion to British spelling, shortening of figure captions, and reformatting to fit the general format of this thesis. The referenced Extended Data and Supplementary Information are provided in Appendices A-B.

Overall, E.D.B.F. and M.S.K. contributed equally to this publication. More specifically, M.S.K., G.Y. and P.K. conceived the study, and all of the authors contributed to the methodology. E.D.B.F. and G.Y. wrote the software. M.S.K., E.D.B.F. and G.Y. carried out the investigation, and E.D.B.F. and G.Y. did the formal analysis. E.D.B.F., M.S.K. and P.K. wrote the original draft, which was then reviewed and edited by all of the authors. E.D.B.F., M.S.K. and P.K. created the Figures; P.K. supervised the study.

## 4.1 Introduction

Integral membrane and membrane-associated proteins (IMPs and MAPs) are essential for a number of cellular processes such as signalling and vesicular trafficking, and this makes them important therapeutic targets.[121,122] Their function often relies on homo- and hetero-oligomerisation,[123,124] and this complexity, combined with the need for lipid bilayers, makes it particularly challenging to accurately characterise the stoichiometries and kinetics of the biomolecular interactions underlying IMP and MAP function and regulation. Advances in single molecule fluorescence-based microscopy methods[125,126] have enabled in vivo and in vitro investigations of IMP interactions, such as dimerisation of G-protein-coupled receptors[4,81] and nano-clustering,[24] and MAP interactions, such as the coordination of Min proteins during bacterial cell division,[127] and the mechanism of amyloid-β plaque formation on cell membranes, which is associated with Alzheimer's disease.[20]

The main challenges to fluorescence-based methods, however, arise from quantitative uncertainties caused by incomplete labelling of the sample, photochemical and photophysical effects such as photoblinking, photobleaching and quenching, and the distinct labelling required to detect multiple species simultaneously. These limitations have made it challenging to accurately quantify processes such as membrane (un)binding of MAPs and the dynamics and stoichiometries of protein–protein interactions for both MAPs and IMPs. Although numerous approaches aimed at molecular subunit counting exist,[66,71,128] the analysis and interpretation of the resulting oligomeric distributions is complicated and the number of heterogeneous species that can be detected simultaneously remains limited. Given the critical functional importance of homo- and hetero-oligomeric interactions for membrane-associated processes,

there is an urgent need for a quantitative and dynamic approach that is capable of complementing the information accessible from existing methods.

Mass photometry (MP) is a label-free method that detects single biomolecules in solution and measures their mass with an overall mass accuracy and resolution of 2% and 20 kDa, respectively.[32] These capabilities enable the quantification of protein–protein interactions in solution with sufficient sensitivity to accurately determine stoichiometry and rate of reactions.[33] As such, MP could be ideally suited to address the shortcomings of existing fluorescence-based techniques for in vitro applications to studying IMPs and MAPs. Existing implementations of MP rely on the stationary binding of individual molecules to a surface, usually a glass coverslide. By averaging images taken before a binding event and subtracting them from averaged images taken after a binding event, the signal due to glass surface roughness is removed and the shot noise is lowered sufficiently to detect individual molecules binding to the surface.[101,103,129] When molecules remain mobile after binding to the surface, however, the resulting signals are a convolution of the positions of the molecules over the averaged time frame, which makes their detection and quantification difficult. Here, by implementing a new background processing methodology, we show that the capabilities of MP can be extended to in vitro studies of individual protein complexes diffusing on supported lipid bilayers (SLBs).

To explore the suitability of MP to study processes on an SLB, we chose the 100 kDa MAP wild-type dynamin-1 (WT) on a 60–40 1,2-dioleoyl-sn-glycero-3-phosphocholine (DOPC)– 1,2-dioleoyl-sn-glycero-3-phospho-l-serine (DOPS) bilayer, in line with previous in vitro investigations.[56,130–137] Dynamin is a multi-domain, large GTPase that can catalyse membrane fission during clathrin-mediated endocytosis.[53] Its role in membrane constriction and fission relies on its (dis)assembly on lipid bilayers, with our current understanding of the underlying

molecular mechanisms of dynamin polymerisation based predominantly on structural information and bulk behaviour.[138] Single molecule fluorescence studies on dynamin have struggled to resolve oligomeric distributions,[31,139] making dynamin a particularly attractive system for MP. By applying an alternative background-removal approach to MP, referred to as dynamic MP, to images of dynamin diffusing on an SLB, we achieve sufficient sensitivity to track individual dynamin oligomers while simultaneously measuring their mass. Due to the label-free nature of MP, the observation time of individual molecules is limited only by the time in which they remain bound to the SLB and/or in the field of view. Furthermore, we achieve sub-50 kDa mass resolution while also enabling quantification of oligomer-specific diffusion coefficients and membrane affinities, making dynamic MP a powerful method for studying membrane-associated biomolecular processes.

## 4.2 Results and Discussion

### 4.2.1 Label-Free Imaging of Mobile Dynamin Oligomers

Raw MP images of dynamin on an SLB exhibited an optical background caused by the roughness of the microscope coverslip (Fig. 4.1a, raw images). By implementing a sliding median background subtraction,[100] we obtained a nearly shot noise-limited imaging background, revealing diffraction-limited features arising from individual WT complexes diffusing on the SLB (Extended Data Fig. 1 and Supplementary Video 1). The sliding median background subtraction involves estimating the static imaging background from the temporal median of a series of frames around each frame of interest (see Methods). Importantly, this approach avoids the convolution of scattering contrast and particle motion inherent in the background subtraction used in standard MP, and reduces the

imaging background at equivalent imaging speeds due to the larger number of frames contributing to the background image (Extended Data Fig. 1 and Supplementary Fig. 1).

For the chosen system, the detected particles exhibited clearly differing signal intensities (Fig. 4.1a, filtered images, and Supplementary Video 1). Filtering for trajectories that remained bound to the SLB for at least 50 frames, corresponding to a residence time of 151 ms (Supplementary Fig. 2), and plotting the mean contrast of the remaining 425 trajectories revealed a contrast distribution with equally spaced peaks, as expected for different oligomeric states (Fig. 4.1b). The contrast values of these particles increased linearly with mass (Fig. 4.1c) and matched well with the expected contrasts of WT dimers, tetramers, hexamers and octamers based on standard MP measurements (Extended Data Fig. 2a-b and Supplementary Table 1), demonstrating that dynamic MP can simultaneously image, track and measure the mass of diffusing biomolecular complexes on SLBs. Additionally, the oligomeric distribution of WT on the SLB displayed a shift to higher oligomeric states compared with the solution distribution measured using standard MP (Extended Data Fig. 2c-d).

### 4.2.2 Localisation Precision and Effect of Imaging Speed

Localisation precision and imaging speed are key performance parameters for single-particle tracking and contribute decisively to the type of information that can be extracted from individual trajectories. The nature of the sliding median background subtraction prevented the assessment of localisation precision by repeated measurement of the location of surface-immobilised particles, as is commonly done in fluorescence-based methods.[140] Nevertheless, we could estimate the localisation precision by extracting the error of our point spread

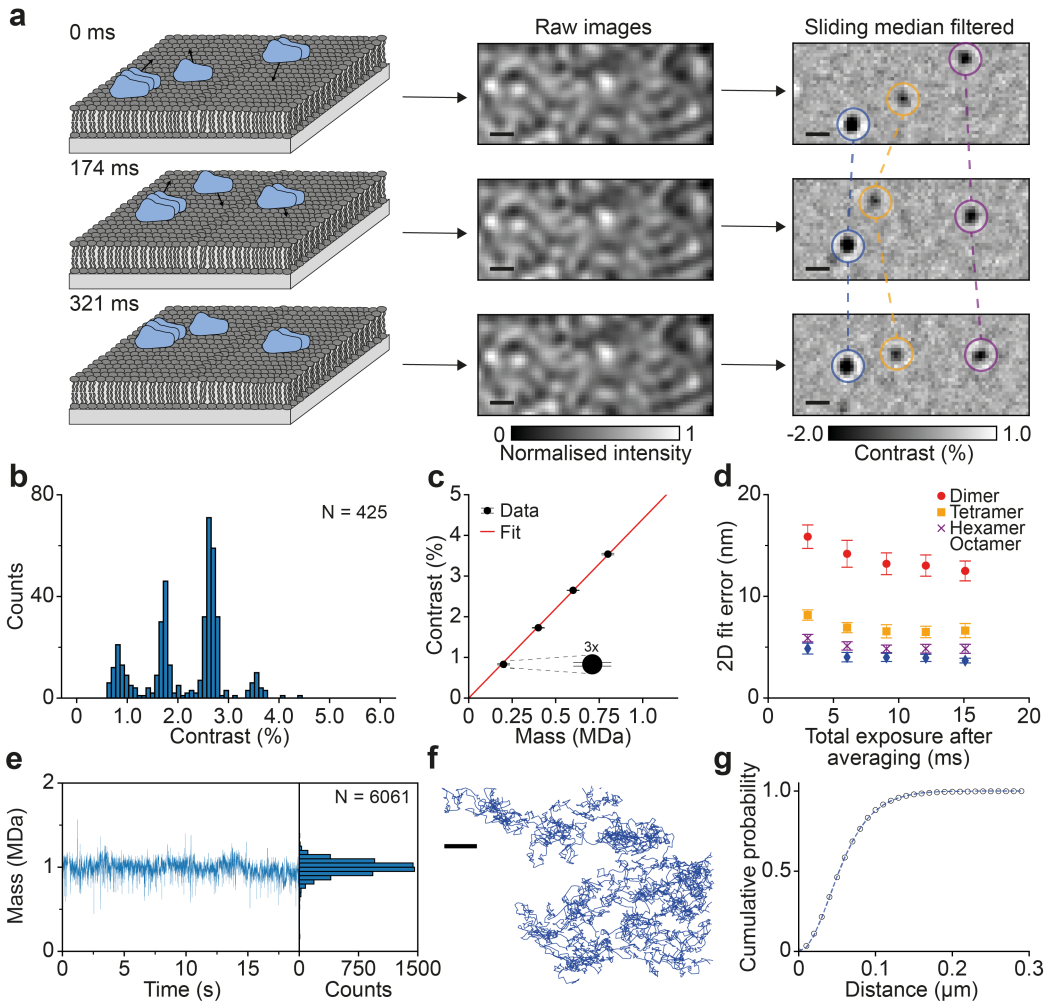


**Figure 4.1: Principle and performance of dynamic MP. a**) Schematic diagram of dynamic MP of protein complexes diffusing on an SLB. The images were acquired at 331 Hz and processed with a sliding median filter, which showed individual protein complexes on the bilayer as diffraction-limited spots. **b**) Histogram of mean trajectory contrasts detected in a dynamic MP movie of WT diffusing on an SLB (considering only trajectories of at least 151 ms in length). **c**) Contrast–mass calibration curve of the dynamic MP measurement shown in **b** yielding a contrast to mass ratio of 4.40% $MDa^{-1}$. Error bars represent the mean contrast ± s.e.m. of each oligomeric species. **d**) 2D localisation error of our PSF-fitting procedure of WT dimers, tetramers, hexamers and octamers plotted as a function of effective exposure time. Data are given as the mean localisation errors in 2D ± the combined s.d. of the mean errors in x and y of particle trajectories detected during the dynamic MP movie in b (n = 1 movie, 4 min), processed with different amounts of frame averaging. **e**) Mass trace and histogram of a WT decamer trajectory. **f**) Corresponding particle trajectory. **g**) Corresponding cumulative probability of particle displacements during 1 frame ($t$ = 3 ms) and the fits to a two-component model (Eq. 4.4). Scale bars, 500 nm.

function (PSF)-fitting procedure (Fig. 4.1d). At the imaging speed of 331 Hz (3 ms total exposure time), the fit error for WT dimers (200 kDa particles) was 16 nm, which compares well with the localisation precision in single-molecule fluorescence imaging at similar speeds (18 nm),[90] and improved with increasing mass (8, 6 and 5 nm for WT tetramers, hexamers and octamers, respectively).

Localisation errors improved by up to 20% when lowering the effective imaging speed to 110 Hz, beyond which there was no further improvement. On average, we found that the slope of the contrast–mass calibration curve in dynamic MP was 8% lower than in standard MP, in which particles are stationary. This drop in contrast matched well with the contrast decrease expected from particle movement during image acquisition, i.e. motion blur (Extended Data Fig. 3 and Supplementary Tables 1–3). This trend became more pronounced as we lowered the effective imaging speed from 331 Hz to 66 Hz, resulting in a drop in contrast precision of 20% and a further 15% decrease in particle contrast (Extended Data Fig. 4). As such, we attribute these effects to motion blurring of the PSFs, which results in decreased particle contrast and diminished improvements in localisation precision at lower imaging speeds. We thus chose to image at 331 Hz to minimise the effects of motion blurring. As a result, however, we were unable to detect WT monomers on the SLB, and in some cases it was difficult to distinguish WT dimers from background noise. We therefore excluded dimeric particles from the mobility and membrane affinity analysis.

### 4.2.3 Quantifying Oligomer-Specific Mobility and Membrane Affinity

Given that dynamic MP is not subject to photobleaching, the time limit on observing particle trajectories is in principle determined only by how long the

particles remain bound to the membrane and/or within the field of view. The longest trajectory we could identify lasted more than 6,000 frames with robust localisation precision and mass measurement (Fig. 4.1e-f and Supplementary Video 2). From these data, we could compute the diffusion coefficient by fitting multiple-mobility models to the cumulative probability distribution of particle displacement (Supplementary Fig. 4a) during a defined lag time, $t$ (Eqs. 4.3-4.5).[125] For the WT decamer particle in Fig. 4.1e-f, a two-component fit was determined to be the most suitable (see Methods), and produced major and minor diffusion coefficients of $D_1 = 0.58$ µm$^2$ s$^{-1}$ and $D_2 = 0.22$ µm$^2$ s$^{-1}$ with relative weightings of 0.56 and 0.44, respectively, using $t = 3$ ms (Fig. 4.1g).

Applying this approach to 20 nM WT, a concentration chosen to achieve a suitable particle density for single-molecule measurements, we were able to measure the diffusion coefficients of different oligomeric species, resulting in a mass resolution of $< 50$ kDa (Fig. 4.2a). More than 95% of species exhibited only one type of diffusive behavior (Supplementary Figs. 4b and 5), as expected for simple Brownian motion. Further repeat measurements with WT (Extended Data Fig. 5, Supplementary Figs. 6-7 and Supplementary Table 4) and its 90 kDa mutant, ΔPRD (Fig. 4.2b, Supplementary Figs. 8-9 and Supplementary Table 5), which is more oligomerisation-prone than WT,[56] revealed a reproducible inverse proportionality of the diffusion coefficient with the number of oligomeric subunits. Given that the diffusion of membrane-bound proteins has been reported to depend primarily on their contact area with the SLB and the number of bound lipids,[141–143] our results suggest that the contact between the SLB and the oligomers of WT and ΔPRD in the range observed here increases linearly with oligomeric state. Additionally, we observed an increase in calculated diffusion coefficients of all oligomeric species when

increasing the lag time from 3 to 12 ms (Extended Data Fig. 6), most probably caused by the dynamic error originating from a combination of the relatively fast particle motion with nanometer localisation precision.[144] At longer lag times there was little change in the diffusion coefficients, again confirming that dynamin undergoes Brownian motion on the timescales relevant to this study.

We were also able to quantify the residence times of dynamin species bound to the SLB (a measure of the affinity of dynamin to the SLB) and their dependence on oligomeric state. We found that the distribution of residence times of both the WT and ΔPRD oligomers was well described by an exponential model (Fig. 4.2c), as expected for a first-order process, from which we could extract the dissociation rate for each oligomeric species (Supplementary Figs. 10 and 11). The majority of trajectories lasted less than 300 ms and, similarly to the diffusive behavior, the dissociation constants were inversely proportional to the number of subunits (Fig. 4.2d, Extended Data Fig. 7 and Supplementary Tables 4 and 5), i.e. to oligomeric mass, suggesting that SLB contact increases linearly with oligomeric state. Additionally, we found instances of dynamin oligomers dissociating into subunits on the SLB (Fig. 4.2e and Supplementary Video 3) and vice versa (Fig. 4.2f and Supplementary Video 4). Such events were rarely observed in our experiments (in less than 0.1% of trajectories), suggesting that they tend to happen on timescales longer than the SLB residence times for dynamin in its apo state ($<$ 200 ms on average). Upon the addition of GTP, which is essential to dynamin function and disassembly from the membrane, we found that the overall particle density of WT immediately decreased (Fig. 4.2g and Supplementary Fig. 12). Addition of the non-hydrolysable analogue 5'-guanylyl imidodiphosphate (GMPPNP) had the same effect (Extended Data Fig. 8), suggesting that GTP binding triggers a decrease in the SLB affinity of dynamin oligomers.

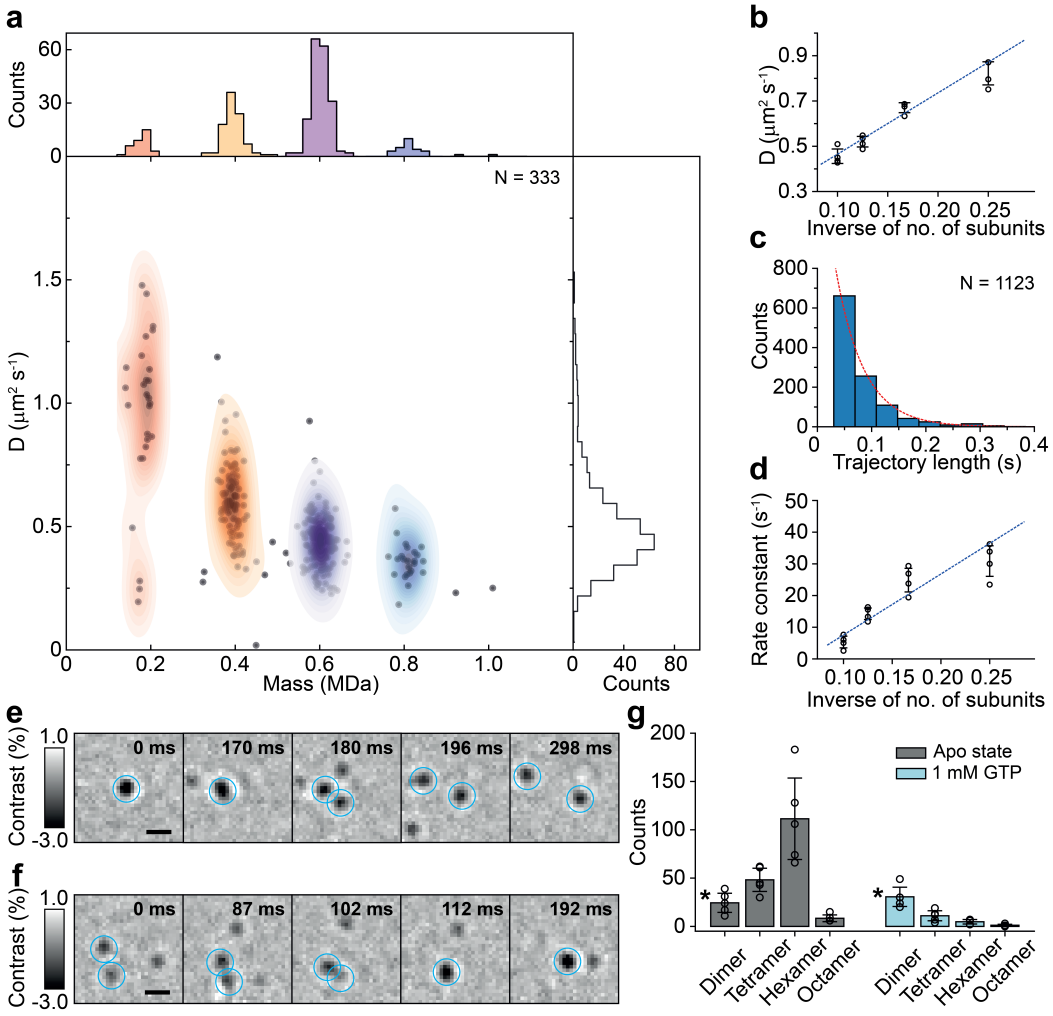


**Figure 4.2: Oligomeric properties and dynamics of dynamin diffusing on an SLB. a**) Major diffusion components versus mean trajectory mass for a dynamic MP movie of WT (20 nM). **b**) Major diffusion components of each oligomeric species of ΔPRD (10–20 nM) vs the inverse of the number of oligomeric subunits, and a corresponding weighted linear fit (blue dashed line). Error bars represent the mean ± s.d. **c**) Histogram of SLB residence times of ΔPRD hexamer trajectories from one of the dynamic MP movies with a fit to a 1-component exponential distribution (appropriately scaled here for display) yielding a dissociation rate constant of 19.4 $s^{-1}$. **d**) Dissociation rate constants of each oligomeric species of ΔPRD versus the inverse of the number of oligomeric subunits (10–20 nM) and a corresponding weighted linear fit (blue dashed line). Error bars represent the mean ± s.d. **e-f**) Examples of a dissociation event and an association event, respectively. **g**) Effect of GTP addition on the oligomeric distribution of 10–20 nM WT (5 independent replicates of 1 min dynamic MP movies before and after GTP addition). Data are given as mean ± s.d. *WT dimer partially overlapped with background noise and could not always be reliably identified. Scale bars, 500 nm.

## 4.3 Conclusion

We have demonstrated accurate and resolved mass measurement of proteins diffusing on supported lipid bilayers at the single-molecule level without extrinsic labels. We were able to quantify key parameters such as oligomeric distribution, residence times (i.e. membrane affinity) and diffusion coefficients, and observed (dis)association events all at a temporal resolution of 3 ms. The ability to quantify mass, diffusion coefficients and membrane affinities also allowed us to validate our observation of dynamin dimers, tetramers, hexamers, octamers and decamers on the SLB, suggesting that dynamin oligomerisation proceeds by dimer addition, in agreement with fluorescence and structural-based studies,[31,56,133,145] instead of being based on exclusively tetrameric subunits, which is the predominant species in solution.[146] As such, our results suggest that single-molecule studies could further our understanding of the importance of tetrameric particles in the dynamics of dynamin polymerisation. Our observation of decreased membrane affinity caused by GTP binding is intriguing considering that dynamin can tubulate membranes effectively both in the apo and GTP-bound states.[134,145] A possible explanation for this observation could be that GTP binding-induced conformational change[147,148] imparts curvature sensitivity to dynamin oligomers, leading to their dissociation from flat, supported bilayers, although further experiments on curved membranes are necessary to validate this hypothesis. To examine the mechanism of dynamin assembly in more detail, comparison of the oligomeric (dis)assembly of dynamin-1 and of the mutants that affect dynamin assembly,[149] along with disease-associated mutants,[150–152] on SLBs containing phosphatidylinositol 4,5-bisphosphate (PIP2), which specifically recruits dynamin,[131,153] could provide extremely valuable insights. Similarly, these experiments would benefit from

the quantification of oligomeric distributions in a more physiologically relevant setting such as curved membranes, although we would expect the kinetics, not the mechanism of the assembly, to be affected given that the rates of dynamin polymerisation are controlled by membrane curvature.[131]

The potential shortcomings of our approach include a limitation on the concentration range, i.e. to reliably resolve and quantify single molecules the particle densities on the SLB should be $< 1$ µm$^{-2}$. Currently, the need for SLBs excludes studies of integral membrane proteins due to the unavoidable interaction with the supporting glass substrate. In the future, we expect that the use of cushioned, suspended or tethered lipid bilayers[154] will expand the demonstrated capabilities to include integral membrane proteins. This advance will enable quantitative and stoichiometric studies of homo- and heterotypic interactions of IMPs and MAPs with each other and with other soluble proteins, and the effect of therapeutics in near native environments. Currently, the detection limit and the mass resolution of dynamic MP are limited by background fluctuations and particle-like features present on the SLB (Extended Data Fig. 9). As such, further improvements in SLB formation will result in improved mass sensitivity and resolution, and provide access to the majority of protein–protein interactions in and on lipid membranes. More generally, we expect that single-protein detection and mass measurement on lipid bilayers will prove powerful for the specific, label-free detection of biomolecules in complex mixtures, and has the potential for further improvements in the capabilities of MP through prolonged observation of individual molecules.

## 4.4 Methods

### 4.4.1 Stocks, Reagents, and Instruments

For the list of stocks, reagents and instruments that were used in this study and their suppliers, as well as how the buffer stocks were prepared, please refer to the Materials section in the Supplementary Information (Appendix B).

### 4.4.2 Protein Expression and Purification

For details on the expression of WT and ΔPRD, purification, size-exclusion chromatography and storage conditions, please refer to the Supplementary Information (Appendix B).

### 4.4.3 Supported Lipid Bilayer Preparation

Liposomes were prepared by dissolving DOPC (Avanti Polar Lipids; 850375P) and DOPS (sodium salt) (Avanti Polar Lipids; 840035P) in chloroform and mixing them in a clean glass tube at a 60–40 molar ratio (500 µM total lipid concentration). The mixture was then dried under a constant nitrogen stream via rotary evaporation, and further dried under vacuum for 1 h at room temperature (22–23 °C). A total of 500 µL HKS-150 (20 mM HEPES, pH 7.4, 150 mM KCl; see buffer preparation in the Supplementary Information) was added to the dried lipids and the mixture was covered with parafilm, incubated at 50 °C in a water bath for 1 h, briefly vortexed, and stored overnight at room temperature. The resulting liposome mixture was transferred into a 1.5 ml Eppendorf tube and kept in ice-water and sonicated using a 3 mm probe at 25% amplitude with a 1 s on–3 s off sonication cycle (Sonics & Materials) for 10 min (i.e. 40 min in total). Sonicated liposomes were then spun at 20,000 ×

g for 30 min at 4 °C and the supernatant was collected in an Eppendorf tube, stored at 4 °C, and used within 3 d.

To prepare fluid SLBs, glass coverslips (24×50 mm, Menzel Gläser, VWR 630-2603) were cleaned by sonication in Milli-Q water for 5 min, isopropanol for 5 min, and Milli-Q water again for 5 min in an ultrasonic bath, dried using a nitrogen stream and stored in a dry place until use. Before SLB preparation, coverslips were treated with oxygen plasma for at least 8 min using a Zepto plasma cleaner (Diener eletronic) at maximum power. Silicone gaskets (6 mm × 1 mm, GBL103280, Grace Bio-Labs) were rinsed sequentially with Milli-Q water, isopropanol and Milli-Q water, dried under a nitrogen stream, and placed on the freshly plasma-cleaned coverslips along with 30 µL freshly reconstituted HKS-150 containing 1.7 mM $MgCl_2$. A total of 20 µL sonicated liposomes was then added to the gasket, followed by mixing with a micropipette and incubation at room temperature for at least 30 min. Before use of the SLBs for measurements, 15 µL fresh HKS-M (20 mM HEPES, pH 7.4, 150 mM KCl, 1 mM $MgCl_2$) was added to the gasket to account for the loss of volume due to evaporation. Unfused vesicles were washed away with HKS-M and then with reaction buffer (20 mM HEPES, pH 7.4, 100 mM KCl, 1 mM $MgCl_2$).

### 4.4.4 MP Setup

All data except for the trajectories in Figs. 4.1a,e–g and 4.2e-f were acquired on a Refeyn OneMP mass photometer with a 10.8 × 2.9 µm$^2$ (128 × 35 pixels) field of view. The microscope used to acquire the data in Figs. 4.1a,e–g and 4.2e-f was custom-built with a 9.4 × 6.2 µm$^2$ field of view (138 × 88 pixels with a binned pixel size of 70.3 nm) and is similar to that described previously.[103] The custom-built setup is illustrated in Supplementary Fig. 15 and the differences to the setup used in our previous work are highlighted in the figure caption.

### 4.4.5 Data Acquisition

*Dynamic MP.* To acquire dynamic MP movies, the SLBs were placed on the sample stage to optimise the focus of the microscope. After locking the focus of the microscope, WT or ΔPRD was added to the SLB by replacing 3–6 µL buffer from the silicone gasket with 3–6 µL (total volume, 60 µL) 200 nM WT or ΔPRD (in reaction buffer) solution and mixing well with a micropipette to achieve a final concentration of 10–20 nM. Data acquisition was started 10 s after the addition of protein. Images were collected at 994 Hz and saved after the binning of pixels into blocks of 4 × 4 and the binning of frames into groups of 3, resulting in an effective frame rate of 331 Hz and a final pixel size of 84.4 nm (for the data used in Extended Data Figs. 2, 3, 8 and Supplementary Figs. 3 and 13 the pixel size was 77.4 nm).

Data acquisition was briefly paused (∼5–10 s) once every minute (20,000 frames) to readjust the microscope focus to account for drift over time before resuming acquisition. This resulted in sets of multiple 1 min movies for each SLB and sample combination. For experiments on the effect of GTP, 3–4 movies of WT (10–20 nM) were recorded as described above, after which image acquisition was briefly paused and 1.2 µL GTP (50 mM) was added (total gasket volume, 60 µL), followed by mixing to obtain a final concentration of ∼1 mM before the resumption of acquisition. For the data shown in Extended Data Fig. 8, GTP or GMPPNP was added at the beginning of the measurement together with WT (20 nM), i.e. each sample condition was measured on a separate SLB. The number of replicate measurements is indicated in figure captions and corresponds to the number of sets of movies that were taken for each sample. We used the same purified batch of WT and ΔPRD for all data collected on the OneMP setup.

*Standard MP.* Unless otherwise stated, standard MP measurements (landing assays) were carried out in silicone gaskets (3 mm × 1 mm, GBL103250, Grace Bio-Labs) on microscopy slides that had been cleaned by consecutive sonication in Milli-Q water, isopropanol, and Milli-Q water. Protein solutions (20 µL) were added to the gaskets containing 4 µL buffer and images were acquired for 60 s at 331 Hz, except for the data in Supplementary Fig. 14c, which were acquired at 250 Hz. Landing assays were analysed using DiscoverMP (Refeyn Ltd) to extract particle contrasts.

### 4.4.6 Data Processing

*Background subtraction.* Dynamic MP movies were processed by treating each frame with a sliding median background subtraction algorithm. In brief, each frame was divided by its local median, i.e. the median of a pre-defined frame interval (here, 201 frames or 607 ms) centred around the frame of interest, to calculate the background-subtracted frames, $F$:

$$F_i = \frac{x_i}{X_{i-100:i+100}}, \tag{4.1}$$

where $x_i$ is the current raw frame and $X_{i100:i+100}$ represents the median pixel values of raw frames, from $i-100$ up to (and including) $i+100$. Each background-subtracted frame was then additionally treated with a two-dimensional (2D)-median noise filter to remove any large dynamic background sources (e.g. fluctuations in illumination), if present. The window size of 201 frames for the sliding median algorithm was chosen because it was the smallest window size that did not detrimentally affect particle contrast or contrast precision (Extended Data Fig. 10). For smaller window sizes, particle contrast values and contrast precision decreased significantly, especially for larger particles that were less mobile, while larger window sizes increased processing times

without an additional increase in sensitivity or performance. We anticipate that for slower moving particles ($D < 0.3$ µm$^2$ s$^{-1}$ ), it may be necessary to further increase the window size to avoid detrimental effects on performance. Moreover, the sliding median filter may have detrimental effects on the mass resolution at high particle densities, e.g. $\gg 0.4$ µm$^{-2}$ (Supplementary Fig. 3 and Supplementary Table 2). We also found that, contrary to theoretical shot noise calculations, increasing the sliding median window size resulted in increasing baseline noise from 44 kDa at the minimum window size to 52 kDa at a window size of 201 frames, where it plateaued (Extended Data Fig. 9a). This trend is most likely a result of the background noise in dynamic MP movies appearing as small particle-like features, which are subtracted out by the sliding median filter at small window sizes (along with particles of interest) but not at large window sizes. In practice, this particle-like background noise resulted in a quantitative detection limit of  150 kDa (Extended Data Fig. 9b-c), which prevented us from reliably quantifying dimeric particles of WT and ΔPRD. At present we have not yet identified the origin of these background features.

*Particle detection.* Particle candidates were identified by treating each processed frame with a Laplacian of Gaussian filter that matched the size of the PSFs in our MP setups (Supplementary Fig. 16). From this filtered image two binary maps were constructed by applying a manually set threshold (0.0011 for all data except the data in Extended Data Figs. 2, 3, 8 and Supplementary Figs. 3 and 13, for which the threshold was set to 0.0014), and applying a local maximum filter. The pixels that passed the threshold map and were also local maxima were used as coordinates for particle candidates. For each pair of candidate coordinates, a 13 × 13 pixel region of interest was constructed with the candidate pixel at the centre, and this region of interest was passed through our PSF-fitting procedure to quantify particle contrast and location.

If a particle candidate was too close to an edge of the field of view to construct a 13 × 13 region of interest, i.e. within 6 pixels of an edge, it was discarded. In some cases, background noise features were identified as particle candidates and this could lead to the PSF fit converging onto a nearby particle in the region of interest, which resulted in duplicate fits. To avoid problems with trajectory linking, only the first instance of a fitted particle was retained and duplicates were deleted.

*Particle quantification and the point spread function model.* The location and contrast of the particle candidates were quantified through least-squares minimisation of the residual between the 13 × 13 region of interest and our PSF model (for details on how the fitting error in particle locations was extracted please refer to the Supplementary Information). Due to the interferometric nature of dynamic MP, we based our PSF model on the shape of a jinc function[155] rather than its square, which is more commonly used in fluorescence-based techniques:

$$I(r) = \left( a_1 jinc\left(\frac{r}{w_1}\right) + a_2 jinc\left(\frac{r}{w_2}\right)\right) e^{-\left(\frac{r}{2\sigma}\right)^2}, \tag{4.2}$$

The first jinc function models the light scattered by a small particle, which is clipped by the circular objective aperture, where $r$ is the distance from the PSF centre, $w$ the width of the jinc function and $a$ its amplitude. In MP setups a partial reflector positioned in the back focal plane helps to increase particle contrast by attenuating the light reflected by the coverslip,[103] which we account for by including a second jinc function. This combination of two jinc functions is then multiplied by a Gaussian with standard deviation $\sigma$, which is an empirical adjustment to reflect the appearance of the PSFs in our setups, which appear to have weaker outer lobes than we can account for with jinc functions alone. We calibrated this PSF model using standard

MP landing assays that were carried out $\leq$ 2 h before or after the dynamic MP experiments. We then extracted and saved the ratio of the amplitudes of the two jinc functions ($a_1/a_2$), the width of the first jinc function $w_1$ and the standard deviation of the Gaussian $\sigma$. The width of the second jinc function ($w_2$) is calculated using prior knowledge of the dimensions of the back aperture and partial reflector (here, $w_2$=2.27$w_1$). The analysis of these landing assays was carried out using DiscoverMP (Refeyn Ltd), and the extracted parameters used for each measurement are supplied with the raw data.

*Trajectory linking.* The successfully fitted particles were linked into trajectories using the open-source Python package trackpy.[156] More specifically, we used the trackpy.link_df function with a maximum search distance of 4 pixels from frame to frame and a 'memory' of 3 frames. The memory parameter refers to the maximum number of frames during which a feature can vanish (as a result of unsuccessful PSF fitting, for example) and reappear and still be considered the same particle. Due to this memory parameter, our linked trajectories can contain gaps of up to 3 frames in length each. To obtain accurate trajectory lengths, the missing frames were treated as trajectory points at which the contrast and position could not be determined.

### 4.4.7 Trajectory Analysis

Unless otherwise stated, linked trajectories were processed as described here. Only trajectories that lasted at least 151 ms (50 frames) were used for analysis, given that this effectively reduced the amount of background noise features and incorrect linking, and improved contrast resolution (Supplementary Fig. 2), while also providing sufficient data points to calculate diffusion coefficients with high confidence. Additionally, particle trajectories that had coordinates that were within 5 pixels of the edge of the field of view were discarded to

avoid artificial trajectory shortening caused by particles leaving (and sometimes re-entering) the field of view. Next, we constructed a contrast histogram for each trajectory and applied a Gaussian fit to extract the mean and standard deviation of the contrast of each trajectory. These mean trajectory contrasts were then filtered by their standard deviation to further eliminate poorly linked or noisy trajectories (Supplementary Fig. 17). For this filtering step, we used a contrast versus standard deviation trend obtained from a standard MP landing assay of ΔPRD on the same instrument with eight-fold frame averaging (Supplementary Fig. 17a), and applied it with an appropriate contrast offset to the trajectories obtained after length filtering (Supplementary Fig. 17b). This offset was identified by inspection to account for the additional variation caused by operating at a faster frame rate compared with standard MP (offset, 0.0015 at 331 Hz). Examples of trajectories that were kept and rejected based on this filtering step are shown in Supplementary Fig. 17d-e. After these two filtering steps, the mean trajectory contrasts were plotted in histograms for WT and ΔPRD. We then used Gaussian fitting to the resulting contrast distribution to extract the mean contrast of each oligomeric species and self-calibrated the data to convert contrast to mass, and then allocated particle trajectories to the oligomeric states (i.e. a trajectory was identified as belonging to a particular oligomer if its mean mass was within 2 s.d. of the mean mass of one of the oligomeric species; see Supplementary Figs. 6, 8 and 12 for examples of this selection range).

### 4.4.8 Diffusion Analysis

For each trajectory that passed the filtering steps, the cumulative probability distribution of a particle's displacement during a lag time of 4 frames ($t = 12$ ms) was calculated (except in Fig. 2a and Supplementary Fig. 4a, where $t$

= 3 ms was used to resolve multiple mobility components, if present). This lag time was chosen to reduce the influence of motion blurring, which is often referred to as a dynamic measurement error,[144] on our measurements of particle displacement. This dynamic error results in an underestimation of particle displacements at short lag times, which we observed at lag times below 12 ms (Extended Data Fig. 6). To calculate diffusion coefficients we fitted the following one-, two-, and three-component models to the calculated cumulative probability distribution, $P(r,t)$.[125]

$$P\left(r,t\right) = 1 - e^{-\frac{r^2}{4Dt+2\sigma^2}}, \tag{4.3}$$

$$P\left(r,t\right) = 1 - we^{-\frac{r^2}{4D_1t+2\sigma^2}} - \left(1-w\right)e^{-\frac{r^2}{4D_2t+2\sigma^2}}, \tag{4.4}$$

$$P\left(r,t\right) = 1 - w_1e^{-\frac{r^2}{4D_1t+2\sigma^2}} - w_2e^{-\frac{r^2}{4D_2t+2\sigma^2}} - \left(1-w_1-w_2\right)e^{-\frac{r^2}{4D_2t+2\sigma^2}}, \tag{4.5}$$

where $r$ represents particle displacement during the chosen lag time, $t$; $D_1$, $D_2$ and $D_3$ represent the diffusion coefficients and $w_1$ and $w_2$ represent their weightings (with boundary conditions set so that the exponential weightings sum to 1); $\sigma$ represents the 2D localisation error (Fig. 4.1d), which is included here to avoid overestimation of particle motion at short lag times. The data in Fig. 4.1g and Supplementary Fig. 4a were not corrected for the localisation error because corrections were found to be negligible in this case. A trajectory was characterised as having more than one mobility component if adding an additional component improved the mean squared residual of the fit by more than one order of magnitude. Using this criterion, $< 5\%$ of trajectories measured in this study displayed two mobility components and none displayed three mobility components at $t$ = 3 ms or 12 ms (Supplementary Figs. 4a and 5). Trajectories that satisfied at least one of the following three criteria were excluded from diffusion analysis: more than 20% of the trajectory points were gaps; the mean of all contrast values of a trajectory differed by more than

20% from the value determined by Gaussian fitting; and the trajectory was too stationary (characterised by having a fast and slow mobility component and a weighting factor of $< 0.3$ for the fast component). For example, in the WT dataset shown in Fig. 2a, of 343 trajectories used in the analysis, six trajectories had too many gaps (criterion 1), two trajectories had mean contrasts that differed significantly from the trajectory contrast determined by Gaussian fitting (criterion 2), and two were too stationary (criterion 3). These criteria helped eliminate trajectories that were strongly influenced by background fluctuations or were a result of incorrect trajectory linking (Supplementary Fig. 18). Using this approach, histograms of the diffusion coefficients were plotted for each oligomeric species (Supplementary Figs. 4b, 7 and 9) and the mean diffusion coefficient of each oligomer was calculated by fitting a Gaussian to these distributions. For the small number of trajectories that displayed two diffusion components, only the major component was included in these histograms. The number of histogram bins was determined using the Freedman–Diaconis rule.

### 4.4.9 Residence Time Analysis

To calculate the dissociation rate constants of each oligomeric species from the SLB, we slightly modified the trajectory filtering procedure described above (Supplementary Information). After filtering the detected trajectories, contrast histograms (70 bins) were plotted and trajectories were sorted by oligomeric species as described above. The distribution of trajectory lengths of a given oligomeric species was fitted to the probability density function of a 1-component exponential distribution and the rate parameter was optimised by maximum likelihood estimation. To correct for the threshold of 33 ms (10 frames) that was applied in prior filtering steps, it was necessary to scale the

probability density function by incorporating the threshold as an additional parameter:

$$p\left(k|t,t_d\right) = ke^{-k(t-t_d)}, \tag{4.6}$$

where $k$ is the dissociation rate constant from the membrane, $t_d$ is the time threshold applied during filtering, and $t$ is the trajectory length. This process was repeated for each oligomeric species detected in the dynamic MP measurements of WT (7 repeats) and ΔPRD (4 repeats) taken at 10–20 nM (Supplementary Figs. 10 and 11).

### 4.4.10 GTP Analysis

For details on how the data examining the effect of GTP and GMPPNP on the oligomeric distribution of WT were analysed (e.g. modified trajectory filtering), please refer to the Supplementary Information (Appendix B).

### 4.4.11 Simulations of Dynamic MP Movies

For details on how simulations of dynamic MP movies were carried out, please consult the Supplementary Information (Appendix B).

# Chapter 5

# Characterisation of Protein-Protein Interactions of HIV-1-Env with Label-Free Single-Particle Tracking

The broadly neutralising antibodies and CD4 construct studied in this chapter were provided by the NIH AIDS Reagent Program and Katie Doores (King's College London). 2G12 and gp120 were expressed and purified by Weston B. Struwe (Kavli Institute for NanoScience Discovery, Oxford) and Fabian Soltermann (Physical and Theoretical Chemistry, Oxford). BG505 SOSIP.664 was expressed and purified by Snezena Vasiljevic (Oxford Glycobiology Institute, Oxford) and purified by Fabian Soltermann. The solution-based data presented in Fig. 5.2a-b was collected by Fabian Soltermann. The thermodynamic modelling presented in Fig. 5.6 was carried out by Roi Asor (Kavli Institute for NanoScience Discovery, Oxford). The thermodynamic model for cross-linking interactions is still being developed by Roi Asor, and the corresponding results shown in Fig. 5.6f are preliminary. We plan to submit the work in this chapter for publication in combination with other work carried out in our group.

## 5.1 Introduction

A recent report by UNAIDS estimated that over 35 million individuals currently carry the human immunodeficiency virus (HIV-1), which has resulted in over 30 million deaths since 1990.[157] Despite the prevalence of this virus, the past decades have yielded limited effectiveness of prophylactic treatments and no available vaccine. This seemingly slow progress in HIV treatment has been attributed to several properties of the virus that aid it in evading humoral immune responses. Firstly, HIV displays extraordinarily high rates of genetic mutations, which increase the diversity of the antigens targeted by the host's immune system.[13,158] Secondly, the production of the HIV-1 envelope glycoprotein (Env) involves extensive glycosylation by the host cell, which results in a glycan shield that appears as belonging to the host cell and impedes the recognition by antibodies.[159] Thirdly, the sparse density of Env on the viral surface is thought to impair B cell activation[160] and limit the neutralisation potency of antibodies.[22] Finally, it has been shown that key functional epitopes on Env are conformationally or sterically shielded.[161,162]

Nevertheless, a subset of infected individuals were found to develop broadly neutralising antibodies (bnAbs) that either bind to or penetrate Env's glycan shield. These antibodies are capable of neutralising a range of HIV-1 strains, albeit with varying efficacy, and were demonstrated as effective prophylactic agents.[163,164] Moreover, the continuing discovery of bnAbs guides vaccine design with the aim of producing a vaccine candidate that elicits bnAbs with high neutralisation breadth,[13,165] e.g. by mimicking structural aspects of Env.[166]

Env is a non-covalent trimer of heterodimers formed between the glycoprotein gp120 and the transmembrane glycoprotein gp41. When not engaged to target cell receptors, Env assumes a tightly closed conformation, which is the

primary target of bnAbs.[167] Upon engaging its target cell receptor, CD4, Env undergoes rearrangement into an open state (Fig. 5.1a-b).[168] This rearrangement allows Env to simultaneously bind to its coreceptor, which ultimately leads to fusion and cell entry.[169] This structural and comformational complexity in Env and its interactions with cell receptors present a significant challenge to the production of proteins closely resembling its structure.

Nevertheless, in 2013, researchers were able to engineer and isolate stabilised soluble native-like trimers that mimicked the closed conformation of Env (Fig. 5.1c).[170] This construct was termed BG505 SOSIP.664 (SOSIP; strain BG505 with C-terminus at position 664) and showed high reactivity with bnAbs and low reactivity with non-neutralising antibodies.[170] These properties enabled researchers to obtain high resolution structures of SOSIP bound to bnAbs and its solubilised target receptors.[171,172] Inclusion of a polyhistidine tag at the C-terminus of SOSIP also facilitated the biophysical characterisation of protein-protein interactions surrounding Env by techniques such as surface plasmon resonance (SPR) and biolayer interferometry (BLI).[170,173]

To date, studying interactions between Env and bnAbs has suggested potential drug targets and inspired the design of small-molecule drugs.[13,14] However, studying these interactions is a complex task. Due to the trimeric configuration of Env, bnAbs can have 1-3 target epitopes on a single Env, which gives rise to several possible binding stoichiometries and mechanisms. A prominent example of this complexity is the binding of CD4 to Env, which was recently demonstrated to exhibit mechanistic differences depending on how many CD4 molecules have already bound to Env.[83] Moreover, bivalent bnAbs can in principle result in highly heterogeneous interactions such as intra- and inter-Env cross-linking, the latter of which is particularly challenging to characterise due to the high degree of polydispersity.

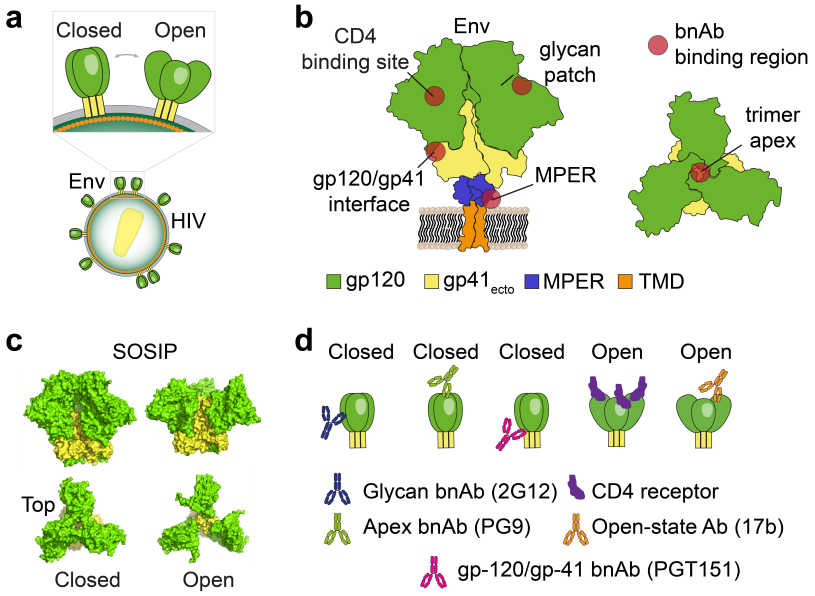


**Figure 5.1: Structure of HIV-1 Env and epitopes targeted by broadly neutralising antibodies.** **a**) Env is embedded in the viral membrane and sparsely distributed with 7-10 Env molecules per virion. The cartoon highlights the differences between the closed and open conformation of Env. **b**) Schematic of Env and its subunits displaying gp120, gp41, the membrane-proximal external region (MPER), and its transmembrane domain (TMD). Epitopes of bnAbs and the CD4 receptor are higlighted in red. **c**) Structure of the engineered Env-mimicking construct, SOSIP (MPER and TMD are absent in this construct). **d**) Schematic of bnAbs and receptors investigated in this chapter and their target binding sites. Figure adapted from reference 119 with permission.

Multivalent cross-linking in bnAb-virus interactions is a topic of high interest, as it results in increased avidity and neutralisation potency, as observed in influenza.[174,175] However, in the HIV-1 field, the possibility of cross-linking is a point of contention. Intra-Env cross-linking has strict geometric constraints that cannot be fulfilled by most bnAbs,[22,168,176] and inter-Env cross-linking is considered unlikely due to the low surface density[177] and low mobility of Env on the viral and cell membranes (D = 0.002-0.02 $\mu m^2$ $s^{-1}$).[21,178] Additionally, some bivalent bnAbs have shown similar neutralisation potencies (often reported as half maximal inhibitory concentrations: $IC_{50}$) compared to their monovalent fragments, which suggests limited scope for avidity via inter-Env cross-linking.[22] On the other hand, several studies have reported that Env arranges into clusters

on mature virions,[21,177,179] which could increase the likelihood of inter-Env cross-linking compared to randomly distributed Env. There have also been examples in the literature where increased avidity or cross-linking was achieved by increasing the valency of antibodies and soluble receptor molecules.[161,180–184]

The bnAbs target a number of different epitopes on Env (Fig. 5.1d), resulting in many distinct combinations of stoichiometric and geometric constraints on inter-Env cross-linking. Moreover, frequently employed in vitro ensemble-based techniques such as SPR and BLI are not equipped to characterise highly polydisperse processes or resolve co-existing stoichiometries and corresponding biophysical parameters. Additionally, these methods are typically based on immobilising SOSIP, which allows for interactions between SOSIP and proteins in solution, but not between multiple SOSIP molecules on the surface. Therefore, the inherent complexity of Env's interactions with bnAbs combined with the lack of accessible techniques that can readily detect, resolve and quantify cross-linked oligomeric complexes may in part be responsible for the debate in the literature. Consequently, there is a need for studying the interactions between Env and bnAbs at the single molecule level to resolve subtle mechanistic details, similar to the recent findings on CD4,[83] and to address the questions surrounding inter-Env cross-linking. These investigations have the potential to reveal crucial information, such as potential relationships between $IC_{50}$-values of bnAbs and co-existing binding stoichiometries, cross-linking, and associated kinetics. These insights could be highly beneficial to the design of drugs and more effective bnAbs.

In this regard, mass photometry (MP) is uniquely positioned to deliver new information. MP is a label-free technique that images single proteins in solution as they bind non-specifically to a glass coverslip (referred to as landing assays). The signal generated from these binding events has been shown

to be proportional to the mass of the protein, resulting in a mass accuracy and resolution of 2% and 20 kDa, respectively.[32] To date, several studies have demonstrated that MP assays are well-suited for studying a variety of polydisperse systems and resolving co-existing stoichiometries.[32,33,35,36,120,185,186]

MP-based experiments should allow us to study and quantify the interactions between bnAbs, Env, and its target receptors and investigate inter-Env cross-linking. In particular, our recent application of MP to single protein complexes diffusing on supported lipid bilayers (SLBs), termed dynamic MP,[120] could provide valuable new information by characterising the interactions between SLB-bound SOSIP molecules in the presence of bnAbs. Importantly, the inverse scaling of diffusion with the number of lipid anchors of SLB-bound proteins[120,141–143] means that cross-linking should be easy to identify through shifts to lower diffusion coefficients. At the same time, dynamic MP provides a more physiologically relevant platform compared to other techniques based on static surface immobilisation.

Here, we use a combination of MP landing assays and dynamic MP-based assays to characterise the interactions of Env with the bnAbs 2G12, PG9, PGV04, PGT151 and 17b, which each target different epitopes on Env (Fig. 5.1d). By using SLB-bound SOSIP as a proxy system for Env on the surface of virions, this experimental approach readily facilitates the resolution and quantification of binding stoichiometries, and provides an accessible method to determine whether specific bnAbs can cause inter-Env cross-linking in vitro. We also demonstrate the quantitative capabilities of our assay by extracting binding affinities via thermodynamic modelling and investigate the interactions between SOSIP and its solubilised target receptor, CD4.

## 5.2 Results and Discussion

### 5.2.1 Characterisation of Binding Stoichiometries by MP Landing Assays

The bnAbs we chose to investigate covered different target epitopes on Env and varying binding stoichiometries (Fig. 5.1d). PG9, PGT151, and PGV04 contain two variable fragments (Fabs) per molecule that can engage Env. PG9's target epitope is situated on the gp120 subunits at the apex of Env's trimeric structure. Consequently, one PG9 antibody can asymmetrically engage two epitopes simultaneously, yielding a 1:1 binding stoichiometry of PG9:Env complexes.[187] PGT151 targets the gp120-gp41 interface, whereby the first two binding events trigger a conformational change that prevents binding to the third interface, resulting in a maximum PGT151:Env stoichiometry of 2:1.[188] PGV04 binds to Env's CD4 binding site on gp120, allowing for a maximum 3:1 binding stoichiometry of PGV04:Env.[189] Finally, 2G12 presents a special case in that its domain-exchanged architecture results in an inter-locked dimeric arrangement of its Fabs, which binds to the glycan shield on gp120.[190] Thus, 2G12 is a monovalent antibody with a maximum 3:1 binding stoichiometry.

Due to the diversity of expected binding behaviours of our bnAbs, we first benchmarked the specificity and stoichiometry of their interactions with Env's gp120 subunit, which contains the epitopes of 2G12, PG9 and PGV04. We prepared 1:1 mixtures at 2-3 µM of each bnAb (∼150 kDa by MP) with gp120 (∼85 kDa by MP), diluted to 15 nM, and then used MP landing assays to measure the distribution of protein complexes. This approach allowed us to rapidly determine that 2G12, PG9 and PGV04 indeed bound to gp120 with high specificity and the expected stoichiometries: 1:1 for monovalent 2G12,

and 1:2 bnAb:gp120 for bivalent PG9 and PGV04 (Fig. 5.2a). Meanwhile, PGT151 showed no binding due to the absence of the gp120-gp41 interface, which confirmed that all bnAbs interacted with gp120 as reported. The binding affinities appeared to be in the pM-nM range, although quantification of these values was problematic because it was not clear if the measured distributions had re-equilibrated from µM to nM concentrations. Nevertheless, these results showed that MP could be used to characterise the stoichiometries and potentially also the binding affinities between bnAbs and SOSIP.

Next, we expanded our approach to the trimeric construct, SOSIP, which mimics the structure of Env in its closed conformation. As for the experiments with gp120, we measured mixtures of SOSIP (330 kDa by MP) with each bnAb by MP landing assays. For 2G12 and PG9, we observed the expected stoichiometries of 3:1 and 1:1 (bnAb:SOSIP), respectively (Fig. 5.2b). On the other hand, incubation of SOSIP with PGV04 or PGT151 resulted in a complete lack of SOSIP particles in the mass distributions. In principle, the bivalency and low nM $K_d$ of these bnAbs[191] combined with their expected 3:1 and 2:1 binding stoichiometries could cause inter-SOSIP cross-linking. At µM mixing concentrations, these factors could lead to a high degree of cross-linking and ultimately precipitation of large cross-linked bnAb:SOSIP particles, thereby causing SOSIP to disappear from our mass distributions. Indeed, incubating SOSIP with PGT151 at nM concentrations revealed several species $>$ 700 kDa. These mass distributions were in good agreement with cross-linked PGT151:SOSIP complexes with an expected maximum of 2 PGT151 binding sites on each SOSIP molecule (Fig. 5.2c-d). The abundance of cross-linked compared to non-cross-linked SOSIP particles increased with increasing concentration (Fig. 5.2e), which confirmed the postulated high degree of cross-linking and precipitation when incubating at µM concentrations.

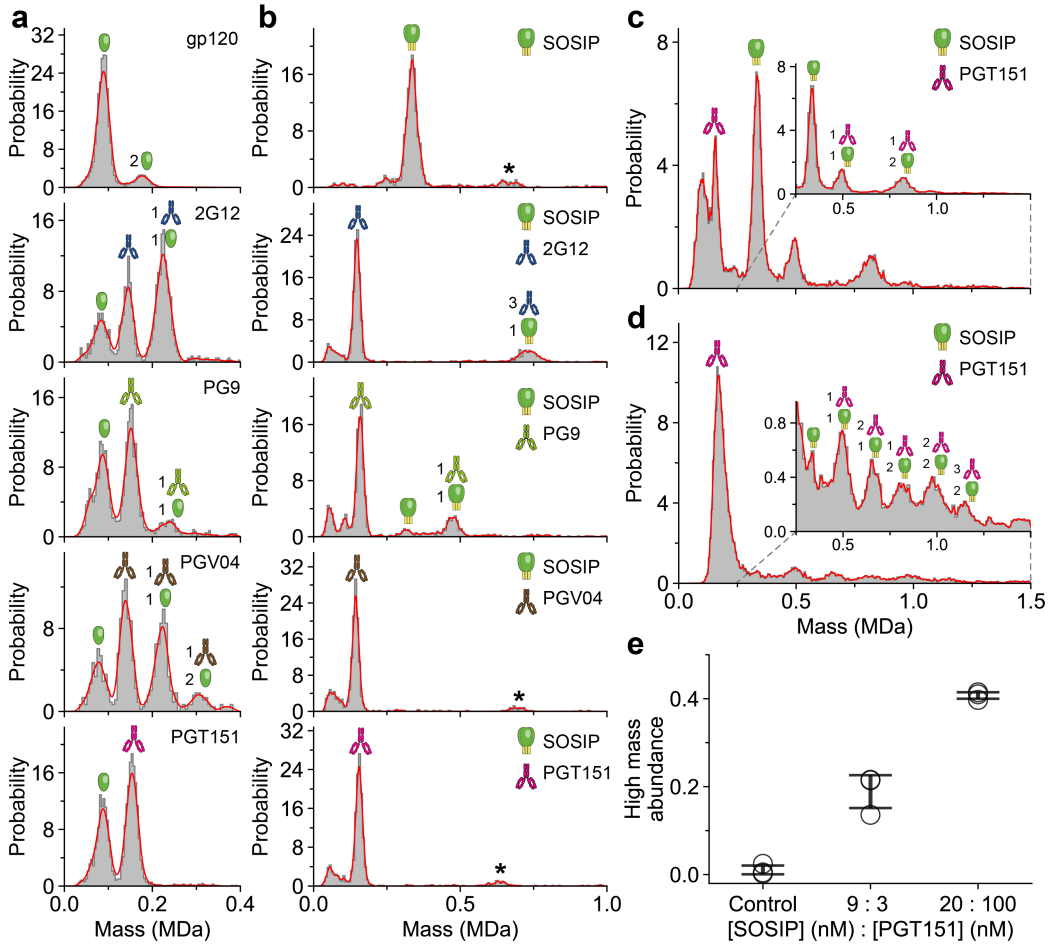


**Figure 5.2: Characterisation of gp120 and SOSIP interactions with broadly neutralising antibodies by MP landing assays. a-b**) Mass histograms (grey) and corresponding probability distributions (red) of mixtures of bnAbs with gp120 and SOSIP, respectively. Mixtures were incubated at 1:1 (bnAb:gp120) and 4:1 (bnAb:SOSIP) molar ratios at 2-3 µM and diluted to 15 nM total concentrations before measurement. **c**) Mass histogram (grey) and corresponding probability distribution (red) of 8 nM SOSIP incubated with 3 nM PGT151 for 30 min and diluted 2-fold immediately before measurement. **d**) Same as **c** but with 20 nM SOSIP and 100 nM PGT151 diluted 10-fold immediately before measurement. Insets, mass distributions from 0.25-1.5 MDa. **e**) Abundance of particles $> 0.75$ MDa relative to low mass particles ($> 0.25$ MDa and $< 0.75$ MDa). The smallest cross-linked state (1:2 PGT151:SOSIP) is expected to appear at 0.81 MDa and the largest non-cross-linked state is expected to appear at 0.63 MDa (2:1 PGT151:SOSIP). The cartoons indicate the bnAb:gp120 and bnAb:SOSIP stoichiometries of each mass peak. *Impurity present in SOSIP sample.

### 5.2.2 Quantification of SOSIP-bnAb Interactions on Lipid Bilayers

The results from MP landing assays showed that the SOSIP construct and its interactions with bnAbs were functional and thus comparable to in vivo.[170] While we identified cross-linking, the quantification of this process by MP landing assays is subject to several complications. Firstly, in solution, SOSIP can encounter bnAbs in many different orientations (Fig. 5.3a), which are not necessarily accessible in vivo, where Env is anchored in the viral membrane. Secondly, MP landing assays rely on counting non-specific binding events of proteins to the coverslip to obtain solution-based mass distributions (Fig. 5.3b). Consequently, high protein concentrations ($> 50$ nM) can lead to crowding in MP movies, which decreases mass resolution and can affect the accuracy of quantitative analyses.[33] Here, this aspect is highlighted in Fig. 5.2d, where the large number of PGT151 landing events impaired mass resolution.

To address these limitations, we developed a dynamic MP[120] assay, in which SOSIP was bound to an SLB, allowing it to freely diffuse and interact with other proteins in solution and on the SLB. By preparing SLBs containing lipids with a nitrilotriacetic acid (NTA) headgroup on glass coverslips, we were able to specifically recruit SOSIP to the SLBs via the polyhistidine tags (8-His) at its C-terminus (Fig. 5.3c) in an orientation similar to that in vivo.[170] As SOSIP contains one 8-His tag on each of its three subunits, it can in principle bind to 12 NTA lipids simultaneously (one lipid per set of two histidine residues), resulting in an extremely stable interaction.[170] At the same time, the passivating properties of SLBs[117] should ensure that bnAbs can only interact with the detection surface by binding specifically to SOSIP, avoiding challenges with high bnAb concentrations. Furthermore, measuring the diffusion coefficient

of SLB-bound SOSIP should simplify the characterisation of inter-SOSIP cross-linking, as diffusion is inversely proportional to the number of bound phospholipids.[120,141–143] Thus, any cross-linked SOSIP complexes should diffuse markedly slower compared to non-cross-linked complexes.

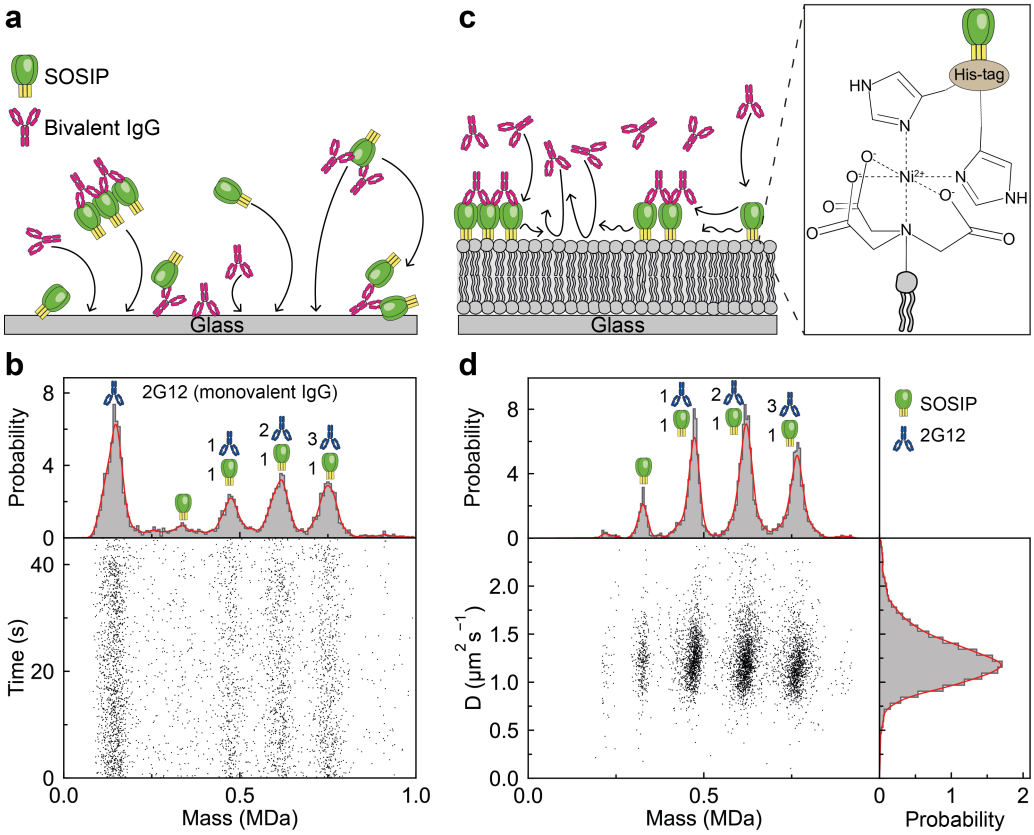


**Figure 5.3: Dynamic MP for studying bnAb-SOSIP interactions.** **a**) Schematic of an MP landing assay of a solution mixture of SOSIP and a bnAb, in which proteins non-specifically bind to the detection surface. **b**) Corresponding data obtained from an MP landing assay of 15 nM SOSIP incubated with 45 nM 2G12 and diluted 5-fold immediately before measurement. **c**) Schematic of a dynamic MP measurement of SOSIP bound to an SLB in contact with bnAb solution. The inset shows how SOSIP is attached to the SLB via its C-terminal His-tags. **d**) Mean mass vs diffusion coefficient of trajectories detected after incubating SLB-bound SOSIP with 10 nM 2G12, presented with histograms (grey) of mass (top) and diffusion (right) and corresponding probability densities (red). The cartoons indicate the 2G12:SOSIP stoichiometries of each mass peak.

For simplicity, we trialled this assay by exposing SLB-bound SOSIP to a 10 nM solution of the non-cross-linking bnAb 2G12. We were able to simultaneously measure the mass and diffusion of individual 2G12:SOSIP complexes,

whereby the observation time was only limited by how long complexes remained in the field of view of the mass photometer. From this information we constructed two-dimensional mass-diffusion distributions in which each data point corresponds to the mean mass and diffusion coefficient of a single 2G12:SOSIP complex. This data revealed a mixture of binding states with a maximum of three 2G12 molecules bound to SOSIP (Fig. 5.3d), which suggested a $K_d$ in the low nM range.[170,191] As expected, we did not observe any evidence of non-specific interactions between the SLB and 2G12, and the lack of cross-linking resulted in similar diffusion coefficients for all 2G12:SOSIP complexes centred around 1.2 $\mu m^2$ $s^{-1}$.

Having established an experimental approach, we next investigated the response of SLB-bound SOSIP to 100 nM solutions of each bnAb, and continuously monitored the resulting mass-diffusion distributions as a function of time (Fig. 5.4a-f). At first glance, the results with dynamic MP were in line with expectations based on the data obtained from landing assays (Fig. 5.2). We confirmed the expected stoichiometries and apparent $K_d$s in the low nM range. Importantly, we were able to detect PGT151- and PGV04-mediated inter-SOSIP cross-linking, resulting in mass shifts to the 1-2 MDa range and significantly decreased diffusion coefficients.

The dynamic MP assays also revealed several more subtle details. We identified a low abundance species corresponding to a 4:1 2G12:SOSIP complex (expected mass ∼930 kDa, Fig. 5.4b). This peak most likely occurs due to 2G12 binding to an additional epitope on SOSIP, and may correspond to the µM interactions that have occasionally been reported in the literature.[191] The results with PG9 showed a small cluster of trajectories corresponding to two SOSIP molecules cross-linked by one PG9 molecule, which could be confidently assigned due to the combination of the mass shift and drop in

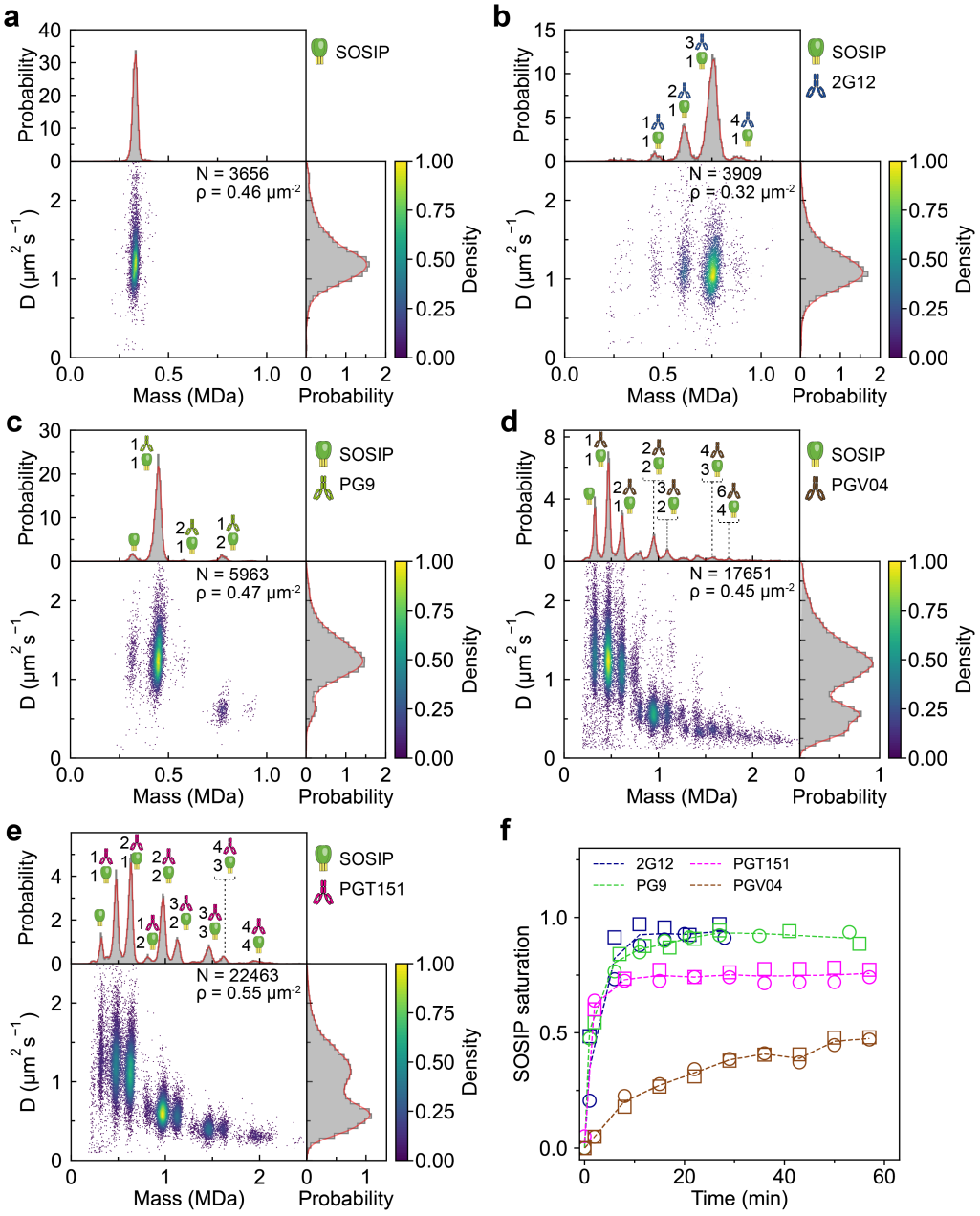


**Figure 5.4: Characterisation of bnAb-SOSIP interactions by dynamic MP. a-e**) Mean mass vs diffusion coefficients of trajectories of SOSIP alone and SOSIP with 100 nM of 2G12, PG9, PGV04 and PGT151, respectively, presented with histograms (grey) of mass (top) and diffusion (right) and corresponding probability densities (red). The cartoons indicate the bnAb:SOSIP stoichiometries of each mass peak and ρ the particle density on the SLB. **f**) SOSIP saturation vs time after addition of bnAb solution to the SLB. Saturation is given as a fraction of occupied binding sites of all detected SOSIP complexes, assuming 3, 1, 3 and 2 maximum binding sites on SOSIP for 2G12, PG9, PGV04 and PGT151, respectively.

diffusion coefficient relative to the other species. Finally, the PGT151 and PGV04 datasets revealed an unexpectedly high abundance of 2:2 bnAb:SOSIP complexes compared to other species. These results suggested that PGT151 and PGV04 may be able to cross-link SOSIP molecules into ring-like structures, where both Fabs of two bnAb molecules interconnect the same two SOSIP molecules, resulting in increased avidity compared to branched structures.

Our assay design offered two other benefits. Firstly, continuously monitoring the same SLBs during bnAb-SOSIP binding allowed us to compare association rates (Fig. 5.4f). Similarly to previous measurements by SPR,[191] 2G12 and PGT151 bound to SOSIP the fastest, followed by PG9, all of which reached a steady state within sixty minutes. In contrast, PGV04 bound to SOSIP markedly slower, most likely due to its less accessible target epitope (CD4 binding site).[161] Secondly, the high number of possible PGV04:SOSIP complexes resulted in partial overlap of different complexes in the mass distribution (Fig. 5.4d), which was challenging to disentangle based on mass alone. As expected, we observed robust scaling of the mean diffusion coefficient of bnAb:SOSIP complexes with the inverse of the number of cross-linked SOSIP molecules. More precisely, complexes containing two SOSIP molecules diffused two times slower compared to non-crosslinked complexes, and complexes containing three SOSIP molecules diffused three times slower (Fig. 5.5a). Therefore, by filtering the obtained trajectories by their diffusion coefficient, we were able to resolve species with similar mass, but different cross-linking states (Fig. 5.5b).

Our results enabled us to confidently resolve different co-existing stoichiometries and cross-linked states, which allowed for quantification of the relative abundances of different bnAb:SOSIP complexes. At the same time, continuously monitoring the formation of bnAb:SOSIP allowed us to verify steady-state binding conditions (Fig. 5.4f), which meant that binding affinities could be

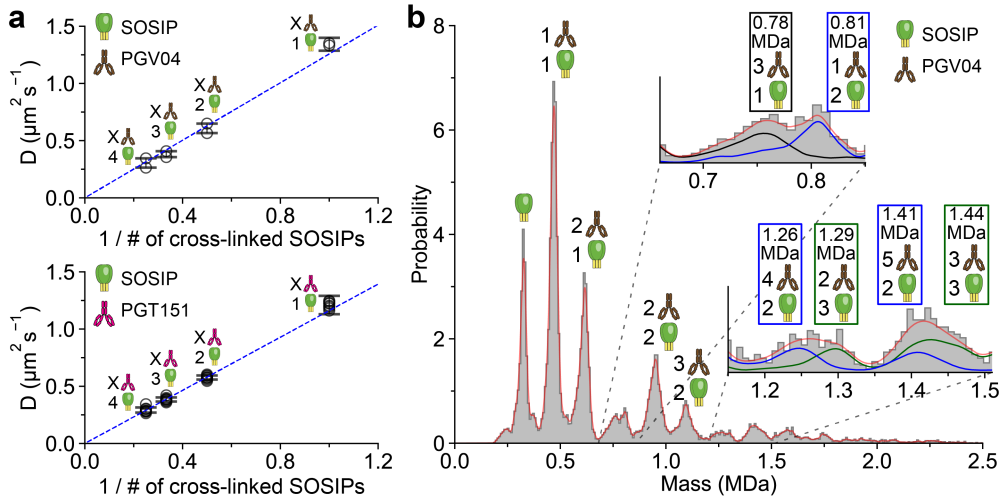


**Figure 5.5: Diffusion measurements enhance resolution. a**) Mean diffusion coefficient of bnAb:SOSIP complexes vs the inverse of the number of SOSIP molecules in each complex. The data was obtained from two replicates with PGV04 (top) and eight replicates of PGT151 (bottom). The dashed blue lines represent corresponding linear fits. **b**) Mass histogram (grey) and corresponding probability distribution (red) of SLB-bound SOSIP with 100 nM PGV04 from Fig. 5.4d. Insets, mass distributions before and after separating trajectories by their diffusion coefficients. Using the data in **a-b**, trajectories were classified as containing one SOSIP molecule (black: $D > 0.85$ μm$^2$ s$^{-1}$), two (blue: 0.45 μm$^2$ s$^{-1}$ $< D <$ 0.85 μm$^2$ s$^{-1}$) or three (green: $D <$ 0.45 μm$^2$ s$^{-1}$) and plotted as separate probability distributions. The expected masses of the resolved complexes are printed above their cartoons.

determined by applying a thermodynamic model. Thus, we next performed titration series with the bnAbs to quantify their binding affinities to SOSIP.

Starting with five different concentrations of 2G12 in contact with SLB-bound SOSIP, we obtained mass distributions based on 2-5 replicates each (Fig. 5.6a). The measured abundances of 2G12:SOSIP stoichiometries agreed well with those predicted by a fit to a thermodynamic model (Fig. 5.6b), yielding observed $K_d$s of 1.3 ± 0.3 nM, 3.8 ± 0.8 nM and 11.5 ± 2.3 nM for the first, second and third 2G12 molecule binding to SOSIP. These values were in excellent agreement with previous measurements by SPR and isothermal titration calorimetry (ITC), where $K_d$s ranged from 1-16 nM.[170,191] The weaker fourth binding event could also be quantified with a $K_d$ of 1.6 ± 0.3 μM, demonstrating the improved dynamic range compared to MP landing assays.

We applied a similar approach to a series of three PG9 concentrations (Fig. 5.6c). In line with a simple 1:1 Langmuir adsorption model, plotting the ratio of the 1:1 PG9:SOSIP complex to SLB-bound SOSIP against concentration of PG9 resulted in a linear trend (Fig. 5.6d) with a $K_d$ of 8.0 ± 4.0 nM, also in good agreement with previous measurements by SPR ($K_d$ = 5-11 nM).[170,191] Additionally, another $K_d$ corresponding to the cross-linking of SOSIP by PG9 could be quantified as 0.33 ± 0.20 µm$^{-2}$ (Fig. 5.6e). However, the cross-linking interaction depends on the density of SOSIP on the SLB and therefore should be examined at a range of different SOSIP densities in addition to those used in these measurements (0.15-0.40 µm$^{-2}$) to obtain more reliable results.

Finally, we examined the interactions between SLB-bound SOSIP and PGT151 at four different concentrations of PGT151 (Fig. 5.6f). Similarly to the 2G12 data, fitting a thermodynamic model to the measured abundances of PGT151:SOSIP stoichiometries, resulted in observed $K_d$s of 19.1 ± 3.9 nM and 57 ± 12 nM for the first and second PGT151 molecule binding to SOSIP (Fig. 5.6g). Again, these values were in good agreement with previously reported values by SPR, BLI and ITC ($K_d$ = 0.3-130 nM).[191–193] Expanding the thermodynamic model to include a cross-linking interaction for forming branched SOSIP structures and one for forming ring-like structures, resulted in a fit in good agreement with the experimentally obtained abundances of all observed PGT151:SOSIP stoichiometries (Fig. 5.6h). While these modelling results for cross-linked stoichiometries are still in the preliminary stage, the inclusion of an interaction for forming ring-like structures adequately explained the unexpectedly high abundance of the 2:2 PGT151:SOSIP complex.

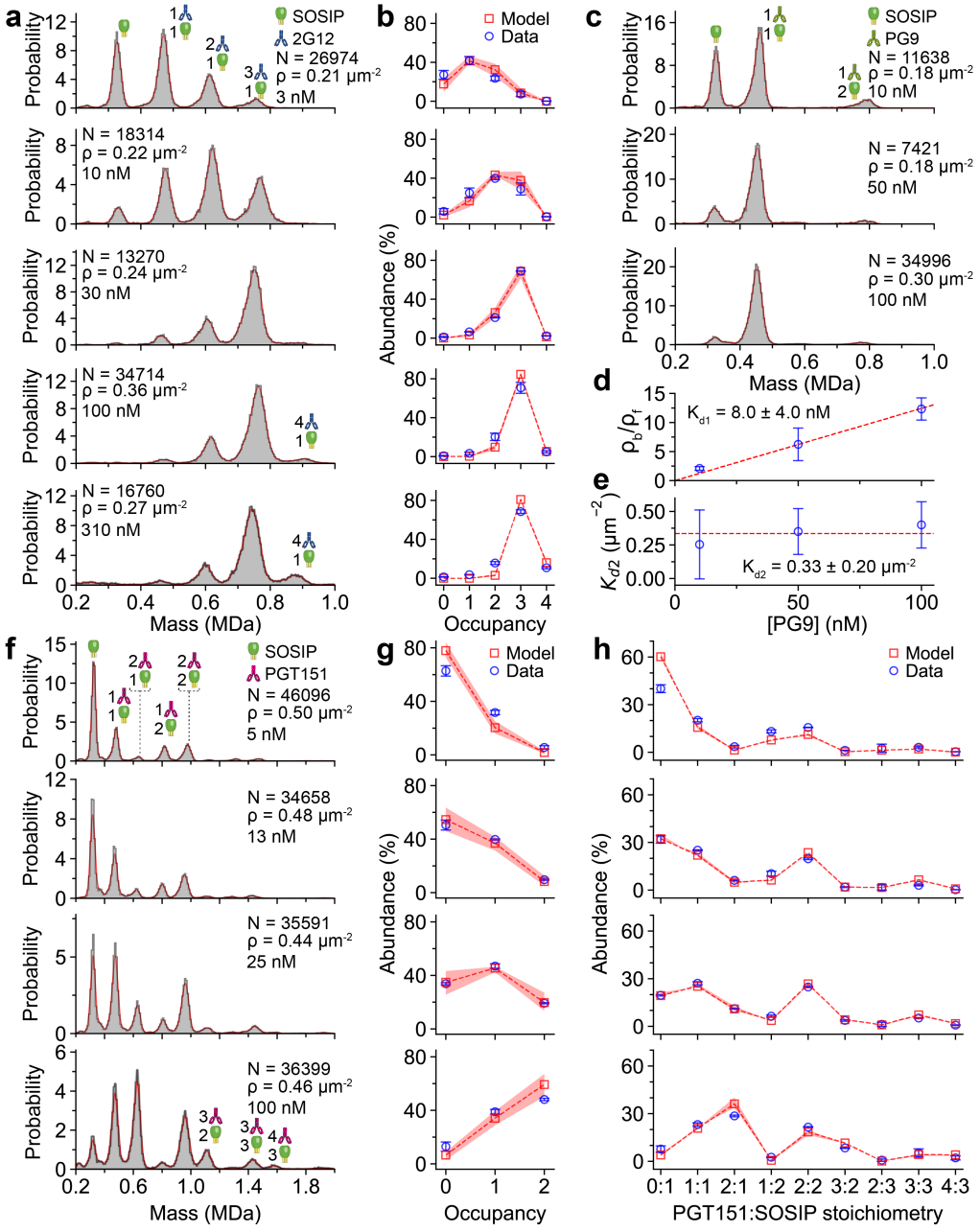


**Figure 5.6: Quantification of bnAb-SOSIP interactions.** **a**) Mass distributions of SLB-bound SOSIP obtained from titrations with 2G12. **b**) Abundances of 2G12 occupancies on SOSIP from experiments (blue) and from fitting a thermodynamic model (red). **c**) Same as **a** but with PG9. **d**) Ratio of the particle densities of the 1:1 PG9:SOSIP complex to free SOSIP vs PG9 concentration and fit. **e**) $K_{d2}$ for the PG9 cross-linking interaction at different PG9 concentrations. The red line is the average $K_{d2}$. **f-g**) Same as **a-b** but for PGT151. Only 0:1, 1:1 and 2:1 PGT151:SOSIP complexes were considered in **f**. **h**) Abundances of all PGT151:SOSIP complexes from measurements (blue) and from fitting a cross-linking model (red). Mass distributions are averages of 2-5 replicates, error bars the corresponding mean ± s.d and ρ the particle density. The red area in **b**, **g-h** is the error in the model (see Methods).

Overall, the reproducibility of these titrations clearly highlighted the robustness of dynamic MP-based assays, which was emphasised by the close agreement of this data with predictions from thermodynamic models and previously reported $K_d$s. Furthermore, the ability to model and quantify cross-linking interactions will enable direct comparison of the cross-linking potencies of different bnAbs, which could yield important insights for a variety of virus-antibody interactions.

### 5.2.3 Interactions of SOSIP with the CD4 Receptor

The interactions between Env and CD4 mark the first stage of cell entry of HIV virions. This process has been shown to involve asymmetric binding of individual CD4 molecules,[194] resulting in a 3:1 CD4:Env complex with an open conformation.[195] Due to variations in sequential CD4 binding events, this interaction was recently examined using single-molecule fluorescence. SOSIP was immobilised on a surface and individual CD4 molecules were labelled with a single fluorescent dye, such that stoichiometries could be identified and counted via photobleaching.[83] In line with previous reports, the authors observed mainly 3:1 CD4:SOSIP complexes, but also small amounts of 1:1 and 2:1 complexes, ultimately concluding that the transition from the 1:1 to 2:1 state is disfavoured. However, it was not clear whether photoblinking and inactive fluorophores were accounted for as potential sources of the observed 2:1 and 1:1 complexes. Additionally, this experimental approach did not allow for quantification of the abundances of free and bound SOSIP molecules and statistics were limited to about 100 molecules per experiment, which introduced uncertainty in the data. Therefore, we aimed to investigate this interaction with our dynamic MP-based approach to complement previous reports and to provide additional information.

To study the interactions of CD4 with SOSIP, we chose the construct sCD4-183, a solubilised truncated version of CD4 consisting of the 183 N-terminal amino acids (sequence mass = 20 kDa), which has previously been used to study CD4-SOSIP interactions in solution.[173] We first determined whether we could detect CD4-SOSIP interactions by incubating SLB-bound SOSIP with 2 µM sCD4-183. As a result, we observed the formation of a new peak in SOSIP's mass distribution at 385 kDa with similar diffusion coefficients to free SOSIP (Fig. 5.7a). This 55 kDa mass shift indicated the formation of a 3:1 sCD4-183:SOSIP complex, which we confirmed by adding 50 nM of the antibody 17b (150 kDa), which selectively binds to the open state of Env. This step resulted in the formation of several peaks corresponding to up to three 17b molecules binding to each sCD4-183:SOSIP complex, as well as cross-linking, and no binding of 17b to free SOSIP (Fig. 5.7b). These observations confirmed the 3:1 stoichiometry and transition into an open SOSIP confirmation.

Next, we examined the effects of sCD4-183 concentration on this interaction. Increasing sCD4-183 concentrations from 0.5 to 2 µM resulted in gradually higher abundances of the 3:1 complex (Fig. 5.7c), but we found little evidence indicating the presence of 1:1 or 2:1 complexes. While resolving the 1:1 complex from free SOSIP is challenging due to the similar diffusion coefficients and mass, binding of a single sCD4-183 should result in a mass shift and broadening of the free SOSIP peak. We did not find convincing evidence of a shift in mass, and the separation between the peaks corresponding to free SOSIP and the 3:1 complex remained similar across all concentrations (Fig. 5.7d). Finally, the mass distributions on the SLB took at least 6 h to reach a steady state, and remained effectively unchanged for several hours after removal of the sCD4-183 solution (Fig. 5.7e). This behaviour suggested a half-life of at least 6-8 h, which implied a slow $k_{off}$ for the 3:1 complex on the order of 1-3 * $10^{-5}$ $s^{-1}$.

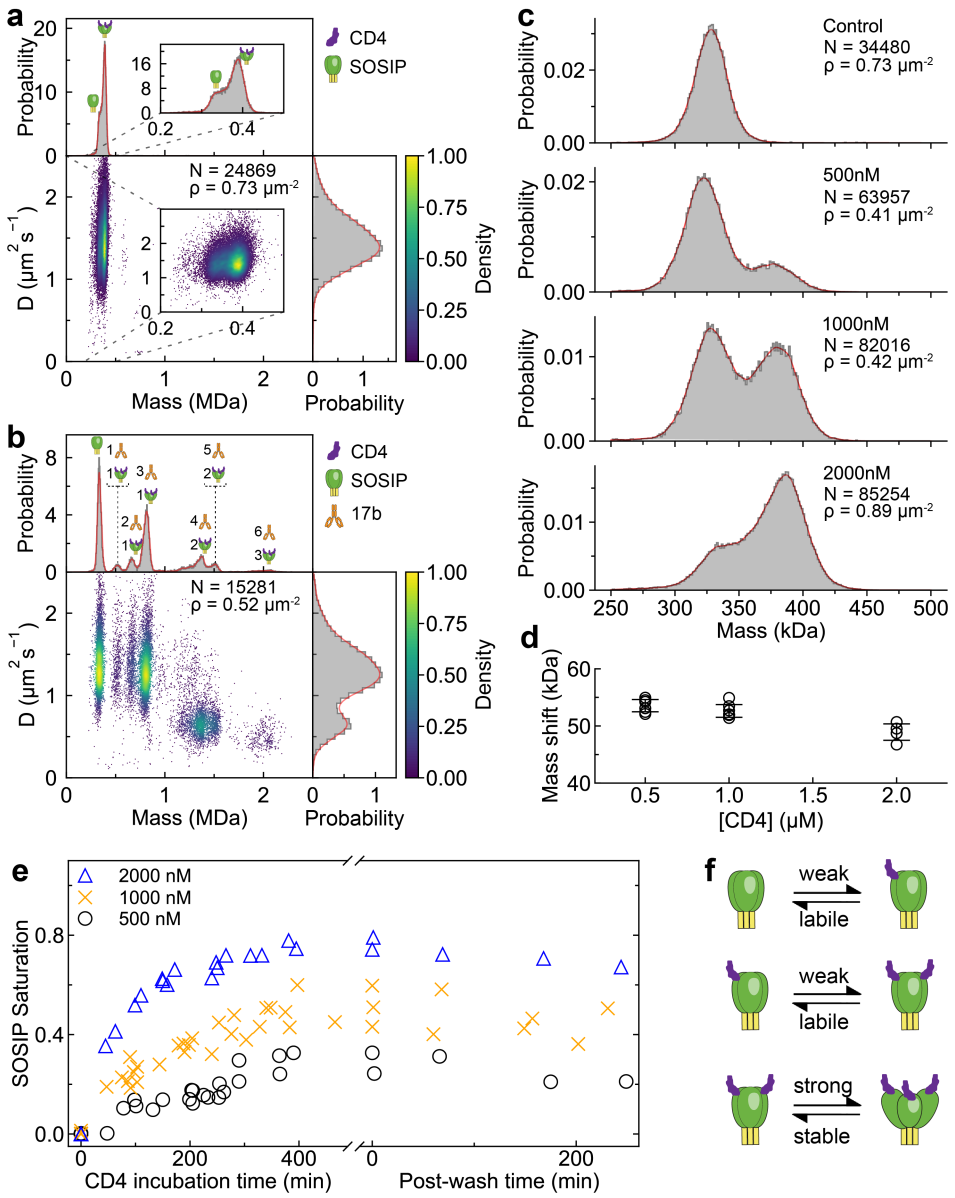


**Figure 5.7: Interactions of SOSIP with CD4.** **a**) Mean mass vs diffusion coefficient of SOSIP trajectories after incubation for 5 h with sCD4-183 (2 µM), presented with histograms (grey) of mass (top) and diffusion (right) and corresponding probability densities (red). **b**) Same as **a** after addition of 17b (50 nM) to the same SLB. The cartoons indicate the bnAb:SOSIP stoichiometries of each mass peak and ρ the particle density on the SLB. **c**) Average mass histograms (grey) and corresponding probability distributions (red) of SLB-bound SOSIP after incubation with different concentrations of sCD4-183 for 4-6 h. **d**) Corresponding difference in average mass of the two peaks in the mass distributions. **e**) Saturation of SOSIP binding sites vs time after addition of sCD4-183, and after replacing the sCD4-183 solution with buffer. **f**) Insights into the binding mechanism of CD4 and SOSIP from the data. The data in **c**-**e** was obtained from 5-7 replicates at each concentration.

The absence of both the 1:1 and 2:1 stoichiometries and relatively slow formation of the 3:1 complex suggested that binding of the third CD4 molecule is strongly favoured compared to the first two binding events, most likely due to the favourable change in conformation (Fig. 5.7f). In this context, our results are in good agreement with the single-molecule fluorescence study and the lack of isolated structures showing 2:1 and 1:1 stoichiometries.[83] Importantly, our approach allowed us to sample significantly more sCD4-183:SOSIP complexes (over 30,000-80,000 trajectories per sCD4-183 concentration), thereby increasing the confidence in our results compared to those from single-molecule fluorescence. Additionally, the lack the 1:1 and 2:1 complexes in our data indicate that these states are short-lived, with far higher $k_{off}$s compared to the 3:1 complex. Thus, two sCD4-183 molecules must bind to SOSIP in quick succession to result in the formation of the 3:1 complex. For soluble monomeric CD4 molecules, this condition is less likely to be fulfilled compared to multimeric CD4 constructs, which provides a clear explanation for the drastically enhanced avidity of CD4 multimers.[161,196] The previously observed clustering of CD4 on cell membranes[197] will have a similar effect, allowing Env to attach to target cells, while providing protection against neutralisation by soluble CD4 mimics.

## 5.3 Conclusion

We have demonstrated a single-molecule platform for quantifying several types of bnAb-SOSIP interactions by combining screening experiments via MP landing assays with dynamic MP measurements of SLB-bound SOSIP. Importantly, the label-free nature of these methods greatly simplifies the experimental approach and is well-suited for quantifying cross-linking and other complex distributions at the single-molecule level. We used our method to characterise

subtleties in the interactions of SOSIP with the bnAbs 2G12, PG9, PGV04 and PGT151, such as the potential formation of ring-like structures in inter-SOSIP cross-linking. In the case of the bnAb 17b, it was also possible to directly infer conformational changes in SOSIP via 17b binding. Furthermore, our measurements of SLB-bound SOSIP in the presence of its solubilised target receptor CD4 contributed valuable insights to existing knowledge of the mechanism of this interaction. In the future, applying a kinetic model to the CD4-SOSIP data will help to extract even more details on the binding mechanism by providing robust quantitative insights.

Dynamic MP assays provided several advantages for our investigations. Firstly, the ability to continuously monitor proteins attached to a surface simplified time-resolved measurements of the same sample over several hours, and allowed for confirmation of steady-state binding conditions. Secondly, the passivating properties of the SLBs allowed us to perform measurements in the presence of up to 2 µM protein, which is significantly higher than the accessible concentrations in MP landing assays. As a result, we were able to observe a fourth binding event between 2G12 and SOSIP with a $K_d$ of 1.6 µM, which was the first time that a binding affinity in this range could be quantified by MP. Thirdly, the combination of mass and diffusion measurements allowed us to resolve bnAb:SOSIP complexes with similar mass but different degrees of cross-linking. Finally, the translation of MP experiments from glass onto SLBs provided a more physiologically meaningful approach to studying interactions between viral spike proteins and bnAbs or target receptors. Cummulatively, these advancements facilitated the quantification of binding affinities as a function of bnAb:SOSIP stoichiometry and with increased dynamic range compared to MP landing assays.

A key argument against the possibility of inter-Env cross-linking in vivo is its low density and mobility on the surface of HIV-1. Although the estimated density of Env on virions (∼300 µm$^{-2}$)[177] is about 3 orders of magnitude higher than in our experiments (0.1-0.6 µm$^{-2}$), Env's mobility in vivo is approximately three magnitudes lower than in our experiments.[21] As such, whether cross-linking of HIV-1 Env by bnAbs is possible in vivo remains open for debate. Nevertheless, we demonstrated a method for determining whether bnAbs can, in principle, cross-link neighbouring Env molecules based purely on geometric, steric and affinity-based restraints without having to resort to more complex structural approaches such as cryo-EM. In combination with the quantitative insights gained by applying thermodynamic models, these experiments may in the future help to narrow down what aspects make bnAbs more potent. In particular, we envisage that applying dynamic MP to other virus-antibody interactions where cross-linking is more likely to occur due to increased density of spike proteins, e.g. influenza,[174,175] will deliver valuable insights.

In the future, the scope of dynamic MP assays can be enhanced by further exploring the dynamic range in accessible protein concentrations and optimising SLB compositions to achieve greater surface passivation. In principle, potential applications include determining rate constants for association and dissociation of different protein complexes similar to techniques such as surface plasmon resonance, but at the single-molecule level. Such measurements will be simplified by expanding the accessible imaging area to increase statistics over shorter time periods, and will likely also require the integration of microfluidics to eliminate potential mass transport limitations. Nevertheless, these improvements are completely feasible and bear the promise of significantly enhancing the capabilities of dynamic MP.

## 5.4 Methods

### 5.4.1 Materials and Sample Storage

HEPES (H3375), KCl(P9541) and Chloroform (288306) were obtained from Merck Life Science UK Limited. The plasma cleaner was purchased from Diener electronic and the ultrasonicator from Sonics & Materials. All buffers were stored at 4 °C.

The phospholipids used in the supported lipid bilayer preparation were obtained from Avanti Polar Lipids(DOPC, 1,2-dioleoyl-snglycero-3-phosphocholine, 850375P; DOPS, 1,2-dioleoyl-snglycero3-phospho-L-serine (sodium salt), 840035P; DGS-NTA, 1,2-dioleoyl-sn-glycero-3-[(N-(5-amino-1-carboxypentyl)iminodiacetic acid)succinyl] (nickel salt), 790404P). The lipid powders were kept at -80 °C and aliquots were stored in chloroform at -20 °C for up to one year.

CD4 (sCD4-183; 2-domain soluble construct from *e. coli*), PG9 and 17b were obtained from the NIH AIDS Reagent Program, and PGV04 and PGT151 were obtained from Katie Doors, King's College London. 2G12,[33] gp120,[198] and SOSIP[199] were expressed and purified as described previously. All antibodies were buffer-exchanged into phosphate-buffered saline (Gibco® DPBS), and stored at 4 °C for long-term use. SOSIP, gp120 and CD4 were kept in DPBS at -80 °C for long-term storage and at 4 °C for short-term use. Concentrations were determined by UV-visible spectroscopy (DeNovix DS-11+), using $\epsilon_{max}$ = 68,505 $M^{-1}$ $cm^{-1}$ for gp120, $\epsilon_{max}$ = 335,175 $M^{-1}$ $cm^{-1}$ for SOSIP, $\epsilon_{max}$ = 18,240 $M^{-1}$ $cm^{-1}$ for sCD4-183, and $\epsilon_{max}$ = 200,000 $M^{-1}$ $cm^{-1}$ for the bnAbs (due to lack of sequence information).

### 5.4.2 Supported Lipid Bilayer Preparation

Liposomes were prepared at a total lipid concentration of 500 µM composed of 89:10:1 molar ratios of DOPC:DOPS:DGS-NTA. The protocol used for liposome preparation was the same as previously described,[120] with the exception that they were prepared in HKS-100 (20 mM HEPES, pH 7.4, 100 mM KCl). Liposomes were stored at 4 °C and used for up to five days.

For SLB preparation, coverslips were sonicated as described in Chapter 4, and treated with oxygen plasma using a Zepto plasma cleaner (13.56 MHz generator, 30% power, 0.5 mbar) for 3 min. Cleaned silicone gaskets (6 mm x 1 mm) were placed on the plasma cleaned coverslips, and 30 µL of HKS-100 with 2 mM $MgCl_2$ was added together with 20 µL of liposomes. After 15 min, the gaskets were rinsed with HKS-100 followed by DPBS to remove unfused vesicles.

### 5.4.3 MP Landing Assays

For MP landing assays, borosilicate coverslips (24 mm x 50 mm, Menzel Gläser, VWR 630-2603) were sequentially sonicated in 50:50 isopropanol:Milli-Q water and then Milli-Q water for 5 min each, and blow-dried with a stream of nitrogen. Silicone gaskets (3 mm x 1 mm) were then cleaned, placed on the coverslips and filled with buffer to find the optimal focus positon on the mass photometer, as described in Chapter 3.

*Data acquisition.* Mixtures of bnAbs with gp120 and SOSIP were prepared at 1:1 and 4:1 molar ratios, respectively, at total concentrations ranging from 2-3 µM, and incubated for 2 h at room temperature. These mixtures were diluted to a final total concentration of 15 nM and measured by MP within a few minutes of dilution. Data was acquired on a Refeyn OneMP mass photometer

(10.8 µm x 2.9 µm, 1 kHz raw frame rate), with the exception of the data shown in 5.2c-e, where a Refeyn TwoMP mass photometer (16.9 µm x 12.0 µm, 540 Hz raw frame rate) was used. Images were saved with 5-fold frame averaging and 4 x 4 pixel binning.

*Data analysis.* Acquired movies were analysed using DiscoverMP (Refeyn Ltd). The obtained contrast distributions were converted to mass distributions using an in-house mass standard.

### 5.4.4 Dynamic MP

For dynamic MP measurements, 0.5-3 nM of SOSIP was added to the prepared SLBs, and particle densities were monitored on the mass photometer until they had reached a suitable level (∼0.1-0.5 µm$^{-2}$ for non-cross-linking bnAbs and ∼0.8-1.2 µm$^{-2}$ for cross-linking bnAbs). Once a suitable density of SOSIP molecules on the SLB had been reached (usually within 2-3 min), the SLBs were rinsed with DPBS.

When replacing the solution in the gaskets, at least 15 µL must remain in contact with the SLB at all times to prevent exposure of the SLB to air. Thus, CD4 and bnAbs were added to the SLBs by preparing dilutions of the desired concentration. We then exchanged 40 µL of these solutions with the solution on the SLBs five times, resulting in final concentrations within $< 1\%$ of the prepared dilution and a total volume of 60 µL in the gasket. This process was repeated every 90 min to ensure bnAb concentrations remained constant.

Dynamic MP movies were acquired on a Refeyn OneMP mass photometer (9.9 µm x 6.3 µm, 540 Hz raw frame rate) and saved with 2-fold frame averaging and 4 x 4 pixel binning resulting in a final pixel size of 77.4 nm (128 x 81 pixels) and effective frame rate of 270 Hz, with the following exceptions: two 2G12 dataset (3 nM), five PG9 datasets (10 nM and 100 nM), and one PGV04

dataset (100 nM), which were recorded at 540 Hz (no significant differences in the measured mass-diffusion distributions were observed). Every 60-90 s data acquisition was paused to readjust the focus of the mass photometer. In this fashion, datasets were recorded over 2-5 min. For all PGT151 and PGV04 measurements, the same area of the SLB was monitored over 1 h to ensure consistent particle densities over this time frame. In these cases, 15 µL of PBS was added to the gasket after 30 min of measuring to account for evaporation.

*Data analysis.* Dynamic MP movies were processed and analysed as described previously.[120] We used a sliding median background subtraction window of 2.23 s, a threshold for particle detection of 0.0015, and the following PSF-fitting parameters: $a_{12}$ = -5.5206591676, $w$ = 2.1900907038 , $s$ = 5.4573928577. Before linking fitted particles into trajectories as previously described,[120] particles with a fitted contrast of 0.002 or less (∼50 kDa), and particles where the fitted location diverged more than two pixels from where the particle was detected were removed. Trajectory linking was performed with a maximum search radius of 5 pixels and 3 pixels for movies acquired at 270 Hz and 540 Hz, respectively, and a memory parameter of 1 frame. After linking, the total particle density was determined by dividing the average number of trajectories in each image by the effective imaging area (9.1 µm x 5.5 µm to account for the exclusion of particles near the edge of the images in the fitting procedure).

Linked trajectories were filtered by length (minimum trajectory length = 30 frames). A single Gaussian distribution was then fitted to the contrast measurements of each trajectory to extract the mean trajectory contrast. We then filtered remaining trajectories according to the standard deviation of the Gaussian fit to their contrast measurements. We used a linear fit to a standard deviation vs contrast trend obtained from three landing assays of our in-house mass calibrant. We applied y-offset to this trend equal to the median plus half

the interquartile range of the standard deviation of all trajectories identified in a given set of movies; this line served as the upper limit for the filter.

Next, we determined the diffusion coefficient of each trajectory as described previously,[120] with the addition of a correction factor to account for motion blur caused by the particles' movement during image acquisition:[200]

$$P\left(r,t\right)=1-\exp\left(-\frac{r^2}{4Dt(1-\frac{t_0}{3t})+2\sigma^2}\right), \tag{5.1}$$

where $r$ is the particle displacement during the chosen lag time (1 frame; $t$ = 3.7 ms or 1.9 ms depending on the frame rate), $t_0$ is the exposure time used for image acquisition (set to 1/frame rate), and $D$ and $\sigma$ represent the particle's diffusion coefficient and 2D localisation error, respectively. Less than 3% of particles had a second mobility component and none had a third. The final diffusion coefficients are given as the weighted average of the two components.

After determining the diffusion coefficients, we converted the mean trajectory contrasts to mass using a contrast vs mass calibration from MP landing assays of our in-house mass calibrant. Motion blur resulted in a systematic underestimation of each trajectory's mass. As such, we corrected the mass of each trajectory based on the expected degree of blur, which we obtained from simulations similar to those described in Chapter 4. This process is described in more detail in Chapter 6. Trajectories with a diffusion coefficient $< 0.1$ μm$^2$ s$^{-1}$ or where the mean trajectory contrast differed from the median contrast by more than 20% were excluded.

### 5.4.5 Thermodynamic Model for bnAb-SOSIP Interactions

To extract $K_d$s for the interactions between SLB-bound SOSIP and bnAbs, we applied appropriate thermodynamic models. These models relied on comparing

the relative abundances of bnAb:SOSIP stoichiometries obtained from the titration series (Fig. 5.6a,c,f) to the expected behaviour of the model. In all cases, the relative abundance of each bnAb:SOSIP stoichiometry at a given antibody concentration was determined by fitting a sum of Gaussian functions to the mass distributions obtained from individual dynamic MP measurements (Fig. 5.6). The resulting abundances of each stoichiometry were normalised by the sum of the lengths of all trajectories belonging to each stoichiometry. The modelled datasets consisted of 2 replicates per concentration for PG9, 2-5 replicates per concentration of 2G12, and 2 replicates per concentration of PGT151. Replicates were obtained on separate SLBs. In all cases, we verified steady-state binding conditions, as demonstrated in Fig. 5.4f.

*PG9 modelling.* We considered the binding of PG9 from solution to SLB-bound SOSIP and the binding of the SLB-bound 1:1 PG9:SOSIP to free SLB-bound SOSIP (cross-linking) as two separate interactions. PG9 binding to SOSIP was modelled using a simple 1:1 Langmuir adsorption model:

$$\frac{\rho_{Sb}}{\rho_{Sf}} = \frac{[Ab]}{K_{d1}}, \tag{5.2}$$

where $\rho_{Sf}$ and $\rho_{Sb}$ denote the particle density (in $\mu m^{-2}$) of free SOSIP and SOSIP bound to one PG9 molecule ($Ab$), respectively, $K_{d1}$ is the dissociation constant (Eq. 2.2), $[Ab]$ is the steady-state concentration PG9. As PG9 was in vast excess compared to SLB-bound SOSIP, the steady-state concentration of PG9 was set equal to the initial solution concentration in the experiments. The ratio $\rho_{Sb}/\rho_{Sf}$ was calculated from the relative abundances of these species obtained from the dynamic MP measurements. Plotting this ratio against the three investigated concentrations of PG9 yielded a line of best fit with a slope equal to $1/K_{d1}$. The error in $K_{d1}$ was calculated from the relative standard deviations in $\rho_{Sb}/\rho_{Sf}$ obtained from individual dynamic MP measurements.

The $K_d$ of PG9-mediated cross-linking of SLB-bound SOSIP ($K_{d2}$) was calculated as a simple 1:1 interaction on the SLB:

$$K_{d2} = \frac{\rho_{Sf}\rho_{Sb}}{\rho_{Sc}}, \tag{5.3}$$

where $\rho_{Sc}$ denotes the particle density of cross-linked SOSIP (2:1 PG9:SOSIP complex) on the SLB. The particle densities were calculated by multiplying the relative abundance of each species obtained from dynamic MP measurements by the total particle density on the SLB. The $K_{d2}$ (in µm$^{-2}$ relative to the standard reference particle density of 1 µm$^{-2}$) was calculated at the three investigated concentrations of PG9 to obtain an average estimate. The error in $K_{d2}$ was calculated from the relative standard deviations in the values of $\rho_{Sf}\rho_{Sb}/\rho_{Sc}$ obtained from individual dynamic MP measurements.

*Non-cross-linking multivalent binding.* We applied the same general model to 2G12 and the first two binding events (non-cross-linked stoichiometries) of PGT151. For a reaction between an SLB-bound SOSIP molecule and $n$ bnAb moleucles we can write the following reaction with equilibrium constant, $K_n$:

$$Ab_n + S \overset{K_n}{\rightleftharpoons} Ab_nS, \tag{5.4}$$

$$K_n = \frac{\rho_{Ab_nS}}{\rho_S[Ab]^n} = \frac{\exp(-\Delta\mu_n)}{(c^{\mathrm{o}})^n}, \tag{5.5}$$

where $S$ is SOSIP, $Ab$ is a bnAb molecule, terms in square brackets denote concentration and $\rho$ the particle density on the SLB, $c^{\mathrm{o}}$ is the standard reference concentration (1 M) and $\Delta\mu_n$ denotes the total difference in the chemical potential of reagents and products, i.e. the total change in free energy associated with this process (in units of $k_BT$, where $k_B$ is the Boltzmann constant and $T$ is the temperature in K). $\Delta\mu_n$ is composed of the following terms:

$$\Delta\mu_n = \Delta\mu_n^{\mathrm{o}} - \omega_n, \tag{5.6}$$

Here, $\Delta\mu_n^o$ denotes the change in the standard chemical potentials (free energy) and $\omega_n$ is a contribution accounting for the different degeneracies of a given bnAb:SOSIP stoichiometry. The expressions for $\Delta\mu_n^o$ and $\omega_n$ depend on the individual bnAb:SOSIP stoichiometries, such that:

$$\Delta\mu_n^o = \sum_i^n \epsilon_i, \tag{5.7}$$

$$\omega_n = \log\left(m^n\right) + \log\left(\frac{N!}{n!(N-n)!}\right), \tag{5.8}$$

where $\epsilon_i$ is the change in standard free energy associated with the $ith$ bnAb molecule binding to a single binding site on SOSIP, $m$ is the valency of the bnAb molecules and $N$ is the number of available binding sites on SOSIP. The first logarithmic term accounts for degenerate binding states arising from the possible combinations in which the $m$ binding sites of $n$ bnAb molecules can combine with SOSIP. The second logarithmic term accounts for further degeneracies due to different combinations of SOSIP binding sites that can be occupied by $n$ bnAb molecules.

Thus, using Eqs. 5.6-5.8, Eq. 5.5 can be rewritten in terms of the ratio ($R(n)$) of the abundances of each bnAb:SOSIP stoichiometry relative to free SOSIP, from which the relative abundances ($p_n$) of all stoichiometries can be calculated and compared to the experimental data:

$$R(n) = \frac{\rho_{Ab_nS}}{\rho_S} = \exp\left(-\sum_i^n(\epsilon_i) + \omega_n + n\log\frac{[Ab]}{c^o}\right), \tag{5.9}$$

$$p_n = \frac{R(n)}{\sum_0^{n_{max}} R(n)}, \tag{5.10}$$

where $n_{max}$ is the maximum number of bnAb molecules bound to a single SOSIP molecule.

*2G12 modelling.* For the interactions between 2G12 and SLB-bound SOSIP, we set the number of available binding sites on SOSIP to $N = 3$, the valency

of 2G12 to $m = 1$, and assumed that the first three bnAb molecules binding to a single SOSIP site result in the same change in standard free energy ($\epsilon_{1-3} = \epsilon_1 = \epsilon_2 = \epsilon_3$). We also included an additional free energy parameter ($\epsilon_4$) to account for the weaker fourth binding events, for which we set the number of available sites on SOSIP to 1. Setting $\epsilon_{1-3}$ and $\epsilon_4$ as variable parameters, we fit the modelled $p_n$s of the bnAb:2G12 stoichiometries to the experimentally determined values obtained from the dynamic MP experiments across all five 2G12 concentrations (Fig. 5.6a; 2-5 replicates per concentration). Optimising the fit by minimising the reduced chi-squared statistic yielded $\epsilon_{1-3}$ = -19.4 and $\epsilon_4$ = -13.4 both in units of $k_BT$. From these values, the observed $K_d$s for each binding event could be calculated from Eqs. 5.5-5.8:

$$Ab + S \overset{K_{d1}}{\rightleftharpoons} AbS + Ab \overset{K_{d2}}{\rightleftharpoons} Ab_2S + Ab \overset{K_{d3}}{\rightleftharpoons} Ab_3S + Ab \overset{K_{d4}}{\rightleftharpoons} Ab_4S, \quad (5.11)$$

$$K_{d1} = \exp(\epsilon_{1-3} - \omega_1)c^{\circ} = 1.3 \pm 0.3 \text{ nM}, \quad (5.12)$$

$$K_{d2} = \exp(\epsilon_{1-3} + \omega_1 - \omega_2)c^{\circ} = 3.8 \pm 0.8 \text{ nM}, \quad (5.13)$$

$$K_{d3} = \exp(\epsilon_{1-3} + \omega_2 - \omega_3)c^{\circ} = 11.5 \pm 2.3 \text{ nM}, \quad (5.14)$$

$$K_{d4} = \exp(\epsilon_4)c^{\circ} = 1.6 \pm 0.3 \text{ µM}, \quad (5.15)$$

where $\omega_1 = \omega_2 = \log 3$, and $\omega_3 = \omega_4 = 0$. The $K_{ds}$ were calculated with $\epsilon \pm 0.2$ to obtain the error from the resulting upper and lower bounds. Relative abundances were recalculated with an error in binding energies of 0.2 (units of $k_BT$) and a 10% error in bnAb concentrations to obtain upper and lower bounds, which are indicated by the red shaded areas in Fig. 5.6b,g-h.

*PGT151 modelling.* For the interactions between PGT151 and SLB-bound SOSIP, we modelled the non-cross-linking binding events (0:1, 1:1, and 2:1 PGT151:SOSIP) in similar fashion as 2G12. We set the number of available binding sites on SOSIP to $N = 3$, the valency of PGT151 to $m = 2$, and

assumed that a maximum of two PGT151 molecules can bind to SOSIP with identical changes in standard free energy. Fitting the modelled $p_n$s to the experimental data obtained from four PGT151 concentrations (Fig. 5.6f; 2 replicates each) yielded $\epsilon_{1-2}$ = -16.0 ± 0.2 (in units of $k_BT$). As with 2G12, the observed $K_ds$ were then calculated from Eqs. 5.5-5.8:

$$Ab + S \overset{K_{d1}}{\rightleftharpoons} AbS + Ab \overset{K_{d2}}{\rightleftharpoons} Ab_2S, \tag{5.16}$$

$$K_{d1} = \exp\left(\epsilon_{1-2} - \omega_1\right)c^{\mathrm{o}} = 19.1 \pm 3.9 \text{ nM}, \tag{5.17}$$

$$K_{d2} = \exp\left(\epsilon_{1-2} + \omega_1 - \omega_2\right)c^{\mathrm{o}} = 57 \pm 12 \text{ nM}, \tag{5.18}$$

where $\omega_1 = \log 6$ and $\omega_2 = \log 12$. Errors were obtained as described for 2G12.

Modelling of the cross-linking interactions is still in development and the results presented in Fig. 5.6h are preliminary. Thus, a detailed explanation of this model is not provided here. Briefly, the results were obtained with a similar model to that applied to the non-cross-linking interactions of PGT151 and 2G12M, but with significantly increased complexity. As SLB-bound SOSIP molecules can interact and bind to each other, both the chemical potential of bnAb in solution and SOSIP on the SLB must be included in the model. Additionally, the number of existing degeneracies is significantly higher and varies with cross-linked state, which expands the $\omega$ terms in the model.[201] The current version of the model assumes the existence of one binding energy for PGT151 binding to SLB-bound SOSIP from solution, a cross-linking energy to form branched structures, and a distinct cross-linking energy for forming ring-like structures to explain the high abundance of 2:2 and 3:3 PGT151:SOSIP.

# Chapter 6

# Specific Pull-Down of Single Proteins from Complex Mixtures with Mass Photometry

## 6.1 Introduction

In principle, the ability to use mass photometry to quantify mass, stoichiometry and oligomeric states could be useful for identifying and studying protein-protein interactions in complex mixtures, in similar fashion to a pull-down assay or affinity purification.[1,41] These methods are generally based on immobilising antibodies or bait proteins on a solid support, which then act as a biosensor for target proteins. This surface is then exposed to a complex mixture of species, such as cell lysate, that contain the analyte, which specifically binds to the bio-functionalised surface. Subsequent washing of the surface removes non-specific interactions and enables the detection and/or isolation ("pull-down") of the target protein and any associated proteins, which can be used, for instance, to identify new protein-protein interactions and for diagnostics.[1,202] Most of these methods are ensemble-based, which poses a challenge for systems where the protein of interest is involved in multiple complexes with different compositions.[42] On the other hand, single-molecule fluorescence-based approaches

are subject to label-induced artefacts and complications, particularly when the analyte exists as a mixture of complexes and oligomeric states.

While MP is well-suited to overcome these challenges, its conventional implementation relies on detecting proteins when they bind to a surface, after which they become part of the static background and are subtracted out.[32] Consequently, this approach is not compatible with the usual pull-down methodology of exposing the surface to a complex mixture, washing, and investigating the resulting signal. An MP-based pull-down approach requires either the direct measurement in complex media or an approach to visualise the analyte after it has bound and the surface has been washed, while minimising any signal arising from non-specific interactions.

In Chapter 3 we demonstrated that surface passivation via polyethylene glycol successfully reduced the detected signal from non-specific interactions in MP landing assays. However, we also showed that measurements in the presence of µM protein concentrations resulted in increased background fluctuations in MP. This effect decreased the quality of measurements to a point where they may become infeasible at higher concentrations. In contrast, our work on dynamic MP in Chapters 4-5 clearly demonstrated the necessary requirements for a pull-down assay: 1) proteins are bound to functionalised supported lipid bilayers (SLBs), which means they remain mobile and continuously visible after binding has taken place,[120] and 2) the SLB significantly reduces unwanted non-specific interactions. Dynamic MP enables us to resolve co-existing protein complexes and their stoichiometries by both mass and diffusion, which will become particularly useful for identifying distinct protein-protein interactions in complex systems. Additionally, measuring the mass of bound complexes may in some cases serve to identify previously unknown binding partners without using any additional approaches, such as mass spectrometry.[1] Therefore, this

method has great potential as a platform for single-molecule pull-down assays, provided the passivation performance of the SLBs can be translated to higher concentrations and different media.

Here, we explore the potential of dynamic MP as a platform for the specific pull-down of single proteins from complex mixtures. As a proof of concept we investigate the passivation performance of SLBs against bovine serum albumin (BSA). We then demonstrate functionalisation of the SLBs with monoclonal antibodies and selectively recruit proteins from high background concentrations of BSA. As accurate and precise measurements of mass and diffusion are critical to capitalise on the benefits of dynamic MP, we next outline systematic errors in measurements by dynamic MP and how to correct for these.

## 6.2 Results and Discussion

### 6.2.1 Lipid Bilayer Passivation and Functionalisation

We decided to start with a relatively simple assay design to investigate whether dynamic MP could be used to specifically pull single molecules down from complex mixtures. Our strategy was based on attaching monoclonal antibodies to SLBs as biosensors and then exposing this surface to a solution containing antigen, which should then bind specifically to the SLB-bound antibodies. The passivating properties of the SLB should minimise non-specific interactions of the antigen and other proteins in solution, and allow for these to be removed through washing steps (Fig. 6.1a-b). SLB-bound antibodies should be large enough to be detected by dynamic MP ($\sim$150 kDa), and thus will remain visible due to the lateral diffusion of their phospholipid anchors. After washing, bound antigen can be identified by a shift in the mass distribution of the antibodies without being adversely affected by high background concentrations of protein.

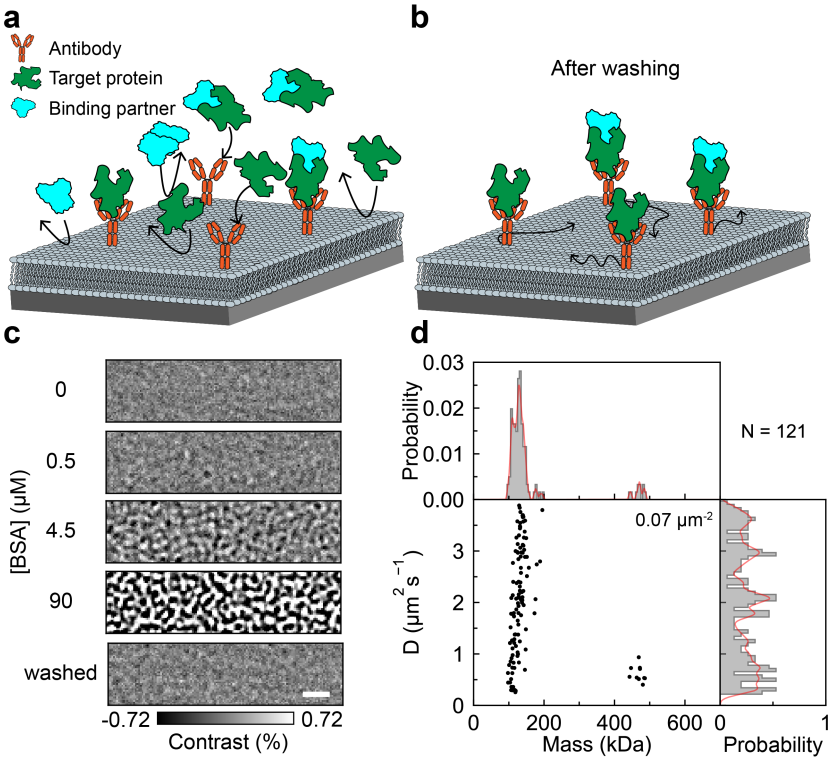


**Figure 6.1: Principle of specific pull-down by dynamic MP. a-b**) Schematic of SLB-bound antibodies in contact with analyte solution and after washing away non-specific interactions. The lateral mobility of the antibodies enables their continuous detection. **c**) Dynamic MP images of an SLB in contact with increasing concentrations of BSA and after washing. **d**) Corresponding mean mass vs diffusion coefficient of trajectories detected on the SLB after washing, with histograms (grey) of mass (top) and diffusion (right) and corresponding probability densities (red). The particle density on the SLB is printed on the scatter plot. Scale bar, 1 µm.

For simplicity, we decided to use the interaction between streptavidin (StrAv; 60 kDa) and biotin (bt; 0.25 kDa) to functionalise SLBs with biotinylated antibodies. Biotinylated phospholipids are commercially available and can be doped into the SLB composition in small amounts to yield a bt-containing SLB. Antibodies can then be biotinylated via lysine residues to recruit them to SLBs via StrAv. It should be noted that a lysine-based biotinylation protocol results in multiple bt groups per antibody molecule, which can result in cross-linking of multiple StrAv molecules to one antibody. Nevertheless, we decided that this protocol should suffice here as a proof of concept.

A key question central to the success of this approach was whether the passivating properties of bt-containing SLBs could withstand protein concentrations in the mid to high µM range. To this end, we incubated an SLB consisting of a molar ratio of 89.99:10:0.01 PC:PS:bt-DOPE with increasing concentrations of BSA up to 90 µM (Fig. 6.1c). The resulting dynamic MP movies showed little to no diffusing protein complexes or increases in background fluctuations at nM BSA concentrations. In line with our results with PEG in Chapter 3, µM BSA concentrations resulted in high background fluctuations, but could almost entirely be removed by washing the SLB with buffer (Fig. 6.1d). Crucially, the most remaining trajectories were short-lived ($<$ 10 frames residence time on the SLB) and had a mean mass $<$ 200 kDa and should therefore only minimally overlap with the expected mass of a StrAv-antibody complex bound to the SLB. Thus, these results demonstrated sufficiently suppressed non-specific interactions to continue with the development of our protocol.

Next, we functionalised the SLBs with a bivalent monoclonal antibody that had been biotinylated via its exposed lysine residues. For this step, we chose anti-human transferrin antibody (Tfn-IgG; 150 kDa), as it was a system we were familiar with and its interaction with human apo-transferrin (Tfn; 80 kDa) has a commercially reported $K_d$ of 0.3 nM. We incubated bt-containing SLBs with 2 nM StrAv (60 kDa), followed by washing, and incubation with Tfn-IgG. Dynamic MP measurements of the resulting SLBs yielded largely monodisperse distributions of SLB-bound molecules (190-200 kDa with $D$ ~2 µm$^2$ s$^{-1}$) corresponding to one Tfn-IgG bound to the SLB via a one StrAv molecule (Fig. 6.2a). These trajectories displayed longer dwell times ($>$ 50 frames) than those recorded after exposure to BSA (Fig. 6.1d), which allowed for their confident distinction from background signal. Our data also revealed a small amount of larger species with slower diffusion coefficients, most likely

corresponding to one Tfn-IgG molecule bound to two StrAv molecules. Exposing these SLBs to 20 nM Tfn for as little as 5 min resulted in a mass distribution with peaks corresponding to free Tfn-IgG and Tfn-IgG bound to one and two Tfn molecules (Fig. 6.2b). Importantly, this assay produced similar results when exposing the functionalised SLBs to 20 nM Tfn in the presence of 50 µM BSA followed by washing, whereby the abundances of different species varied depending on the incubation time of the SLB with Tfn solution (Fig. 6.2c).

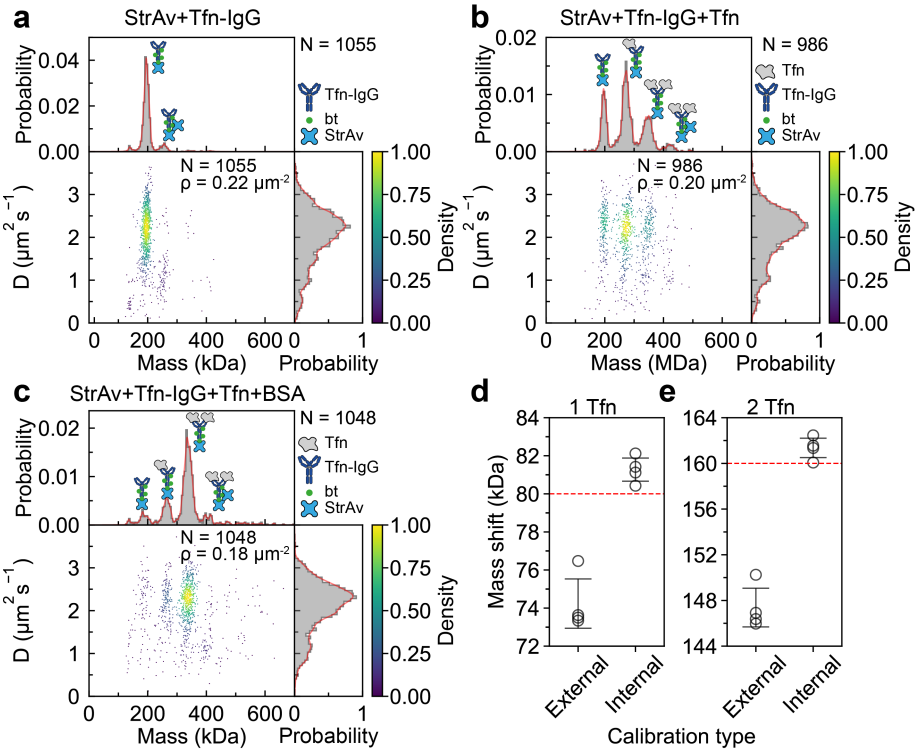


**Figure 6.2: Antibody attachment and specific binding.** **a**) Mean mass vs diffusion coefficient of trajectories detected on an SLB (89.99:10:0.01 DOPC:DOPS:bt-DOPE) functionalised with Tfn-IgG via bt-StrAv interactions. The plot is presented with histograms (grey) of mass (top) and diffusion (right) and corresponding probability densities (red) **b-c**) Same as **a** after exposing functionalised SLBs to 20 nM Tfn in buffer and in 50 µM BSA, respectively. The cartoons indicate the bnAb:SOSIP stoichiometries of each mass peak and ρ the particle density on the SLB. **d-e**) Mean mass shifts (4 replicates) of Tfn-IgG bound to one and two Tfn molecules, respectively, relative to the measured mass of free SLB-bound Tfn-IgG. Red lines indicate the expected mass shift. External calibrations were performed via landing assays and internal calibration were performed using the ratio of the expected to measured mass of free SLB-bound Tfn-IgG prior to exposure to Tfn.

In general, the measured masses of SLB-bound species were slightly lower than expected, with SLB-bound Tfn-IgG appearing at 190-200 kDa (expected mass for a 1:1 StrAv:Tfn-IgG complex: 210 kDa), and mass shifts due to binding of Tfn of 73-76 kDa (expected mass: 80 kDa). These systematic errors in mass were undesirable for pull-down assays, as they could impair the identification of bound proteins and associated stoichiometries. To this end, a key benefit of this assay is the fact that free SLB-bound Tfn-IgG complexes remain continuously visible and have a known mass (here from MP landing assays), which means they can act as an internal calibrant. By scaling the measured masses of all species by the ratio of the expected mass of free SLB-bound Tfn-IgG to its measured mass, we obtained Tfn-induced mass shifts close to the expected values and with lower standard deviations between replicates (Fig. 6.2d-e).

These initial results marked the first example of an MP measurement involving protein concentrations well into the µM range, and showed promise for using dynamic MP as a platform for single-molecule pull-down assay. In particular, the ability to calibrate mass internally is an attractive aspect, as it removes the need for external calibrations via MP landing assays. Additionally, internal calibrations are likely to help remove variations between measurements stemming from inconsistent focusing of the mass photometer or sample drift, thereby increasing the reproducibility and precision of the assay.

An aspect we have thus far not mentioned, is the number of antibodies bound to the SLB, i.e. the particle density, which directly determines to which extent the target protein population in solution can be sampled. Depending on the polydispersity of this population, it will be necessary to vary and control the number of antibodies on the SLB. In the data presented thus far, we observed significant variations in particle density of SLB-bound Tfn-IgG from 0.05-0.4 $\mu m^{-2}$, corresponding to approximately 1-10 particles in the field of view at any

given time. The obtained particle densities varied with StrAv concentration and incubation time, and were difficult to estimate before the recruitment of Tfn-IgG because the mass of StrAv on its own is below the detection limit of dynamic MP. Thus, we instead aimed to control the Tfn-IgG density via the proportion of biotinylated phospholipids in the SLB. We expected that limiting the number of bt binding sites should allow us to obtain reproducible Tfn-IgG densities by adding an excess of StrAv to functionalise the SLB. This approach should eliminate the dependence of particle densities on StrAv concentration and incubation time.

Assuming an average area per phospholipid molecule of approximately 70 $Å^2$,[203] the optimal amount of bt-DOPE in the SLB should be on the order of 0.0001 - 0.00001% to obtain particle densitites suitable for our assays. In line with these calculations, reducing the amount of bt-DOPE by a factor of 10 to 0.001% and incubating with 10 nM StrAv followed by bt-Tfn-IgG still resulted in excessive particle densities ($\gg$ 0.5 $\mu m^{-2}$) and with significant variations. Additionally, the StrAv:Tfn-IgG complexes now existed as a heterogeneous mixture of 1:1, 2:1 and 3:1 stoichiometries. Addition of Tfn further complicated the mass-diffusion distributions with several species overlapping (Fig. 6.3a-b). Further attempts to control particle densities by reducing the amount of bt-DOPE by up to four orders of magnitude were unsuccessful. We determined that even in the complete absence of bt-DOPE, incubation of SLBs with 10 nM StrAv resulted in similar particle densities after recruitment of Tfn-IgG (Fig. 6.3c). Similar results were obtained with SLBs that contained only DOPC and DOPE-PEG (Fig. 6.3d). In both cases, we were unable to remove particles from the SLB by washing, which suggested StrAv may be able to bind directly to non-biotinylated phospholipids in our assays.

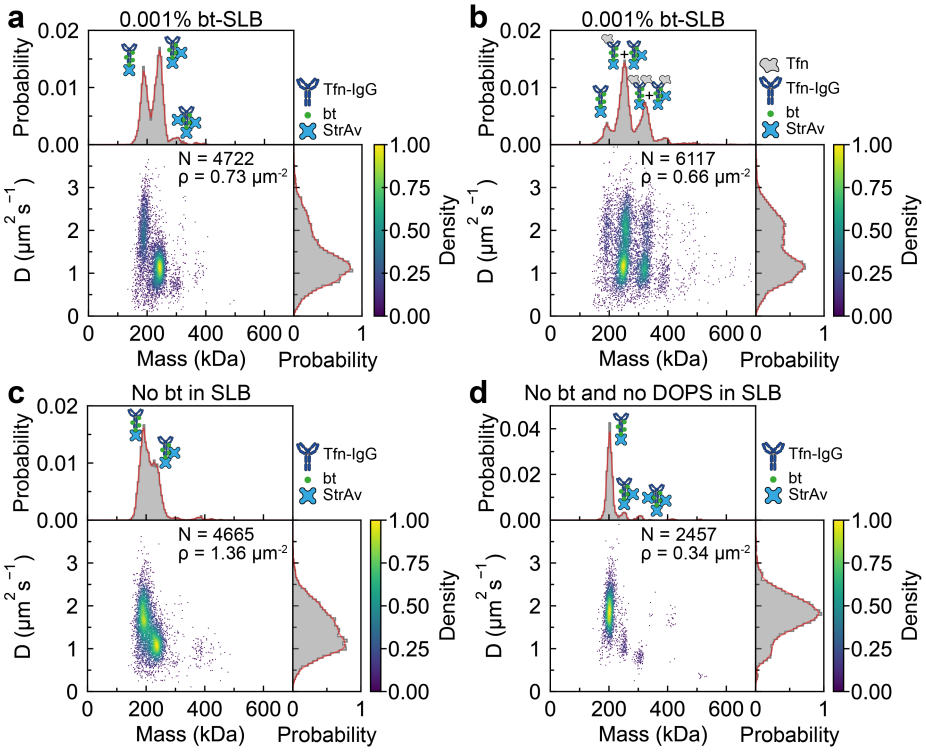


**Figure 6.3: Streptavidin cross-linking and aggregation. a**) Mean mass vs diffusion coefficient of trajectories detected on an SLB functionalised with Tfn-IgG via bt-StrAv interactions but prepared with 10 times less bt and 5 times higher concentration of StrAv compared to Fig. 6.2. The plot is presented with histograms (grey) of mass (top) and diffusion (right) and corresponding probability densities (red). **b**) Same as **a** after exposing the SLB to 20 nM Tfn. **c-d**) Same as **a** but with SLBs without bt consisting of 90:10 DOPC:DOPS and 98.6:1.4 DOPC:DOPE-PEG, respectively. The cartoons indicate the bnAb:SOSIP stoichiometries of each mass peak and ρ the particle density on the SLB.

The lack of precise control over particle densities will present a challenge in the long term. Additionally, while the detection of cross-linked StrAv:Tfn-IgG complexes highlights the ability of dynamic MP to resolve different species, it needlessly complicates the obtained data. Fortunately, many alternative approaches for biofunctionalising SLBs have been developed,[204,205] which means overcoming these challenges should simply be a matter of exploring other protocols and SLB compositions. The demonstration of pull-down of Tfn from 50 µM BSA remains a promising result and shows the potential of dynamic MP for pull-down assays.

### 6.2.2 Data Analysis and Limitations

Maximising mass accuracy and precision is paramount for the success of dynamic MP in single-molecule pull-down. When imaging particles that are laterally mobile, their signal is affected by motion blur. The continuous movement of particles during image acquisition results in broadening of the PSF, which translates to a decrease in amplitude, and thus a decrease in the mass observed by dynamic MP. The magnitude of this mass drop depends on the exposure time used for imaging and the diffusion coefficient of the particles. Long exposure times and fast diffusion result in lower observed particle mass and vice versa. Here, this effect on our measurements was demonstrated by simulating raw images containing diffusing particles (∼250 kDa) and then processing them with the same pipeline used for dynamic MP measurements (Fig. 6.4a).

In principle, this mass drop can be corrected for if the diffusion coefficient can be accurately measured. The observed diffusion coefficient is subject to two types of systematic errors. Firstly, in our imaging routine, each frame shows the particle's position throughout the exposure time, rather than its instantaneous position, resulting in underestimation of particle motion.[200] More precisely, when the diffusion coefficient is calculated based on the particle's displacement during a defined lag time (Eqn. 5.1) the observed diffusion coefficient scales by a factor of 1 - $t_0/3t$, where $t$ is the chosen lag time and $t_0$ the exposure time of the acquired images (Fig. 6.4b). Implementing this factor in our diffusion calculations allowed us to correct for this systematic error and yielded measured diffusion coefficients close to the values we simulated (Fig. 6.4c).

The small systematic offset that remained in this data was a consequence of the second systematic error, the achievable precision in the measurement of each particle's location. The two-dimensional localisation error ($\sigma = \sqrt{\sigma_x^2 + \sigma_y^2}$)

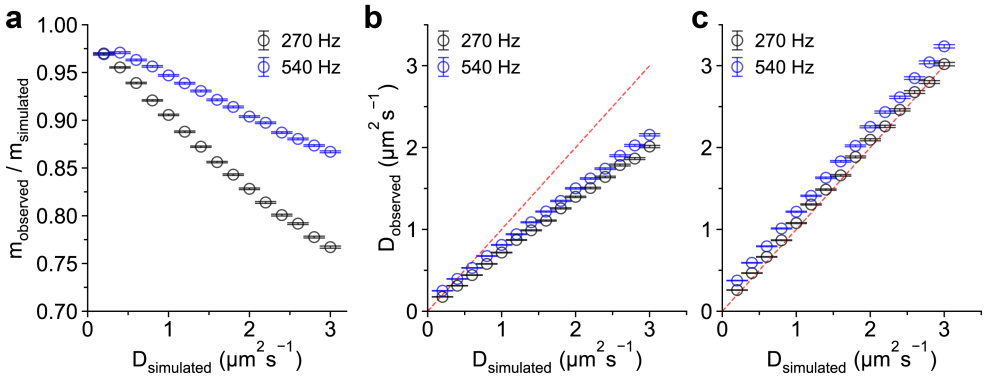


**Figure 6.4: Effect of motion blur on dynamic MP measurements.** **a**) Ratio of observed to simulated trajectory mass vs simulated diffusion coefficient obtained from simulated dynamic MP movies at 270 Hz (black) and 540 Hz (blue). **b**) Observed vs simulated diffusion coefficients at 270 Hz (black) and 540 Hz (blue) in the absence of any corrections. **c**) Same as **b** but with corrections to the diffusion coefficients to account for motion blur, highlighting the remaining offset due to unaccounted localisation errors. The red lines are drawn with slope = 1 for visual aid. Data points are presented as mean ± SEM obtained from fitting a Gaussian curve to the mass and diffusion distributions of the analysed trajectories (∼600 per data point).

results in an overestimation of the mean squared displacement of each particle by $2\sigma^2$ and thus an overestimation of its diffusion coefficient.[144] The magnitude of this error depends on the SNR of each particle, whereby the signal depends on a combination of particle mass and mobility. The background noise depends largely on the frame rate of the measurement, which is why the observed diffusion coefficients in Fig. 6.4c appeared higher at 540 Hz than at 270 Hz.

In Chapter 4 we accounted for this effect by extracting the mean localisation error directly from the covariance of the parameters of our PSF-fitting operation.[120] Since then, we have investigated the localisation errors of our measurements more thoroughly via simulated dynamic MP movies. By processing simulated movies with the same pipeline used for dynamic MP measurements, we were able to compare the measured positions of all particles to their simulated ground truth. Repeating this for movies containing particles with different simulated masses and diffusion coefficients allowed us to systematically evaluate

localisation errors at different frame rates (Fig. 6.5a-b). It is worth noting that this data showed an impact, albeit small, of diffusion on our ability to localise particles at 270 Hz, but this effect was negligible at 540 Hz.

Next, we interpolated this data to achieve higher resolution for different particle masses and diffusion coefficients (Fig. 6.5c-d). This three dimensional dataset could then be used to assign a localisation error to any particle's trajectory based on its measured mass and expected diffusion coefficient. Incorporating these assigned localisation errors in our diffusion calculations combined with the corrections for motion blur yielded observed diffusion coefficients in excellent agreement with the simulated values (Fig. 6.5e). Overall, the impact of the localisation error on the observed diffusion coefficient was lower compared to motion blur effects, and basically negligible at particle sizes above 300-400 kDa. For example, the localisation error of a 200 kDa particle with a diffusion coefficient of 1.0 $\mu m^2$ $s^{-1}$ resulted in overestimation of its diffusion coefficient of 6% and 23% at 270 Hz and 540 Hz, respectively, when using a lag time of 1 frame. For a particle twice the size, these numbers dropped to 1% and 5%, respectively. Nevertheless, both errors should be accounted for to increase the performance of dynamic MP, especially when working at frame rates $> 540$ Hz.

Access to accurate diffusion coefficients of SLB-bound particles allowed for the robust correction for the inherent underestimation of particle mass. This procedure is demonstrated here on a dataset of SLB-bound SOSIP (330 kDa by MP) in contact with 2G12 antibodies (150 kDa by MP) acquired at 270 Hz as part of the work undertaken in Chapter 5. Using an external mass calibration and in the absence of any corrections for motion blur, the SOSIP peak appeared at approximately 290 kDa, with mass shifts of 130 kDa for each bound 2G12 molecule, and diffusion coefficients centred around 0.8 $\mu m^2$ $s^{-1}$ (Fig. 6.6a). Additionally, the mass-diffusion distributions of each species

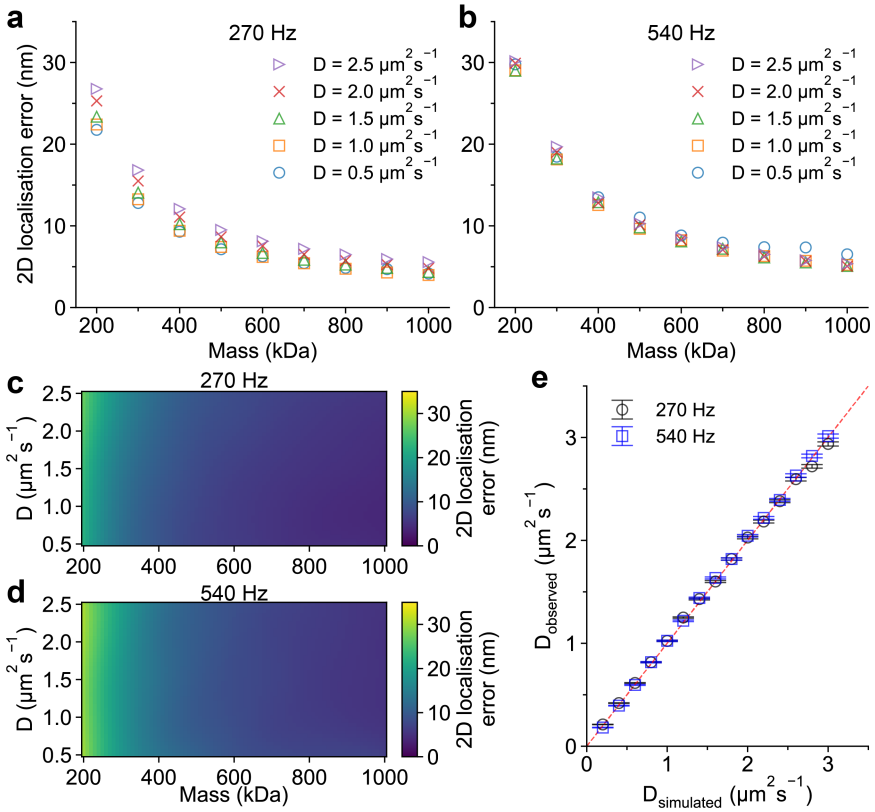


**Figure 6.5: Estimation of localisation errors and corrections. a-b**) Mean two-dimensional localisation error vs particle mass obtained from simulated dynamic MP movies at 270 and 540 Hz, respectively, and for different diffusion coefficients of the simulated trajectories. Relative standard deviations were on the order of 10% and are not shown for visibility. **c-d**) Corresponding maps of localisation errors as a function of diffusion coefficient and mass, up-scaled by a factor of 10 by interpolation. **e**) Observed vs simulated diffusion coefficients at 270 Hz (black) and 540 Hz (blue) after correcting for both motion blur and localisation errors. The red line is drawn with slope = 1 for visual aid. Data points are presented as mean ± SEM obtained from fitting a Gaussian function to the mass and diffusion distributions of the analysed trajectories.

appeared sloped, such that the underlying particle trajectories appeared to have lower mass the higher their diffusion coefficient. Applying the outlined corrections to the calculations of the diffusion coefficients shifted the centre of the distribution to 1.2 $\mu m^2\ s^{-1}$. We could then use the resulting diffusion coefficients to extract the expected mass drop of each trajectory from Fig. 6.4a and correct the mean mass of all individual trajectories accordingly (Fig. 6.6b). This procedure significantly improved the mass accuracy and also resulted in

slight improvements to mass resolution, i.e. a decrease in the full width at half maximum (FWHM) of each mass peak relative to its mean mass (Fig. 6.6c). On average, the mass accuracy improved from underestimating the mass by 15.1 ± 2.2% to 1.8 ± 2.0%, and mass resolutions improved by 8.5 ± 5.3 % relative to the resolution in the absence of corrections.

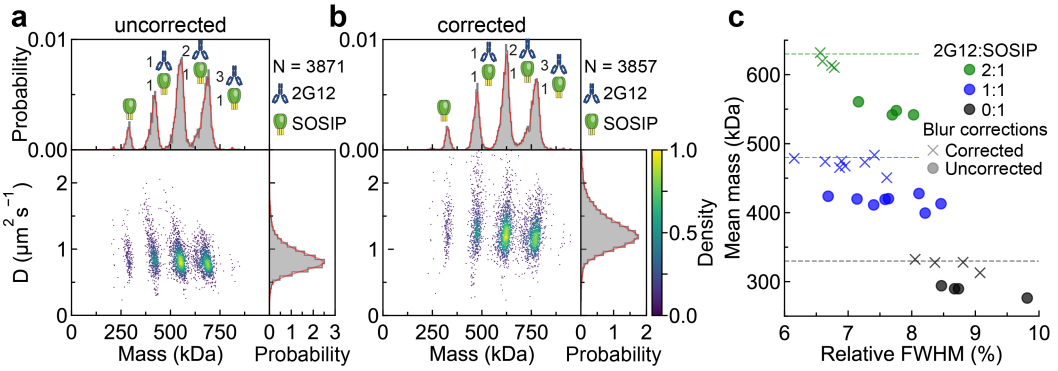


**Figure 6.6: Effect of diffusion and mass corrections.** **a**) Uncorrected mean mass vs diffusion coefficients of trajectories of SLB-bound SOSIP (330 kDa) incubated with 10 nM 2G12 (150 kDa; see Chapter 5), presented with histograms (grey) of mass (top) and diffusion (right) and corresponding probability densities (red). **b**) Same as **a** but after correcting all diffusion coefficients for localisation errors and motion blur, and correcting the mean mass of each trajectory according to the expected mass drop based on its diffusion coefficient. **c**) Mean mass vs full width at half maximum (FWHM) relative to the mean mass of different stoichiometries of SLB-bound 2G12:SOSIP. Dashed lines represent the expected mass of SOSIP (black), 1:1 2G12:SOSIP (blue) and 2:1 2G12:SOSIP (green) complexes. Data was obtained by Gaussian fitting applied to eight dynamic MP measurements, whereby only the two most abundant species in each measurement were examined to avoid effects caused by statistical limitations.

The slight enhancement in mass resolution was particularly encouraging in that it demonstrated scope for further performance improvements. Increasing both mass and diffusion resolution is essential to realising the full potential of dynamic MP-based pull-down assays in resolving complex mixtures of species bound to the SLB. The FWHM of the mass and diffusion distribution of a protein complex depends on the precision to which the mass and diffusion coefficients of individual trajectories can be determined. According to the central limit theorem, the standard deviation in the mean mass and diffusion of

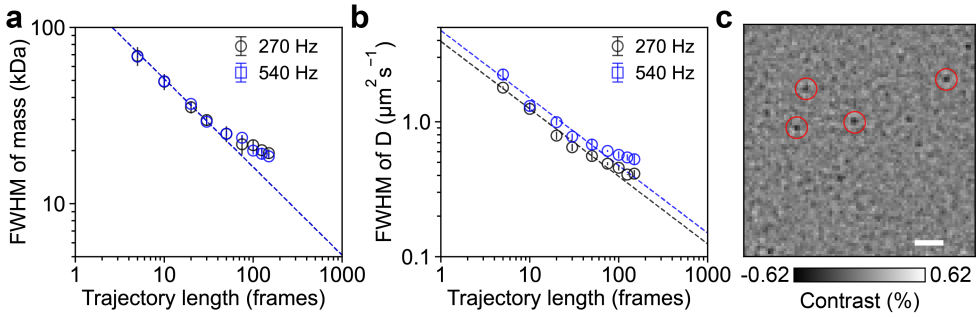


**Figure 6.7: Effect of observation time on resolution in dynamic MP. a-b**) FWHM of the mass and diffusion distribution vs trajectory length of all free SOSIP particles (330 kDa) obtained from dynamic MP measurements at 270 Hz (black) and 540 Hz (blue) presented as log-log plots. Dashed lines correspond to a fit of the data to the expected trend FWHM = $\mathrm{FWHM}_0/\sqrt{N}$, where $N$ is the trajectory length and $\mathrm{FWHM}_0$ the FWHM obtained from a single mass or displacement measurement. Data is shown as mean ± s.d. from three repeat measurements on separate SLBs for each frame rate (6 SLBs total; 300 trajectories each). **c**) 9.9 µm x 9.9 µm image of an SLB functionalised with Tfn-IgG via bt-StrAv interactions (acquired at 360 Hz). A subset of signals corresponding to StrAv-Tfn-IgG complexes are circled in red. Scale bar, 1 µm.

a trajectory should be inversely proportional to the square root of the number of individual measurements, i.e. the number of frames the trajectory could be observed for. By examining our dynamic MP measurements on SOSIP, we found that our data was in close agreement with this predicted trend, which translates to a straight line with slope -1/2 on the log-log plot in Fig. 6.7a-b. While the experimentally observed mass resolutions begin to deviate from the theoretical limit at trajectory lengths > 50, the experimental trend still indicates scope for further improvements by going to longer trajectory lengths. Therefore, extending the observation times of single particles on the SLB should result in further improvements to both mass and diffusion resolution.

In our pull-down experiments, trajectory lengths were mainly limited by the relatively small field of view of the commercial mass photometer (10.8 µm x 2.9 µm), which we chose due to limitations on the frame rate for larger fields of view. These limitations have since been fixed, allowing us to expand the field of view by a factor of three, while acquiring images at 360 Hz. These imaging

conditions still allowed for the robust detection of SLB-bound StrAV-Tfn-IgG molecules (Fig. 6.7c). Therefore, it should be possible to increase the imaging area even further and maintain similar frame rates via a custom-built mass photometer. These innovations should improve trajectory sampling and thereby enhance mass and diffusion resolution.

## 6.3 Conclusion

The work in this chapter is the first example of MP measurements with solutions with a total protein concentration well into the µM range. Furthermore, we demonstrated that dynamic MP is a suitable platform for single-molecule pull-down assays by functionalising SLBs with monoclonal antibodies, and that these surfaces exhibit passivation against up to 90 µM BSA. Importantly, this approach yields accurate mass measurements with current mass resolutions on the order of 20-50 kDa depending on the achievable trajectory length and the mass of the protein complexes under investigation.

The combination of mass and diffusion measurements of single particles also enabled the identification of different species bound to the SLB, such as different stoichiometries of StrAv:Tfn-IgG complexes, highlighting the potential of this method in dealing with complex protein distributions on the SLB. However, the scope of dynamic MP-based pull-down assays is currently limited by the protocol for surface functionalisation, as the binding of StrAv to bt-free phospholipids can complicate mass-diffusion distributions unnecessarily. The issues encountered with StrAv binding also showed that the passivating properties of SLBs are not universal, and it is likely that pull-down from different complex media will require careful optimisation of the SLB composition and solution conditions.

Regarding data analysis, our corrections to the calculation of diffusion coefficients successfully eliminated the impact of localisation errors and motion blur on dynamic MP measurements. Of course, a similar effect could have been achieved by simply increasing the lag time used to calculate diffusion coefficients, which would minimise these two errors. However, being able to obtain accurate diffusion coefficients while using the minimum lag time possible comes with important benefits, such as narrower distributions of diffusion coefficients[206] and maximised temporal resolution.

Robust diffusion measurements also allowed us to improve the mass accuracy and resolution of dynamic MP. Nevertheless, use of an external calibration still resulted in a systematic underestimation of mass on the order of 1-4% for our SOSIP measurements and 5-10% for the pull-down experiments relative to MP landing assays. It is not clear what caused this systematic underestimation of mass. A possible reason could be the increased distance of the SLB-bound proteins to the glass surface, i.e. to the focus position of the mass photometer, compared to MP landing assays. The increased distance would change the phase difference between the light scattered by the protein complexes and the reflected light (Eq. 2.5). For the systems in question, this distance should be on the order of 10-30 nm,[207,208] depending on surface orientation of the protein complexes and SLB composition, and could thus translate to a 1-10% decrease in measured contrast.[209] Nevertheless, in most cases, this performance suffices to confidently identify different species on SLBs. Furthermore, we have shown that use of an internal calibration can offer improvements in cases where increased mass accuracy is required. At this point, we note that it is important to apply internal calibrations in combination with motion blur corrections to mass, particularly in cases where different species on the SLB exhibit distinct distributions of diffusion coefficients. A mixture of such mobilities will result

in varying observed mass drops for each species, which an internal calibration based on the mass of a single species alone cannot account for.

Overall, we envisage further improvements to the experimental design by implementing alternative surface functionalisation protocols and expanding the accessible imaging area of the mass photometer. In light of the problems we encountered with bt-StrAv on PEGylated surfaces in Chapter 3 and on SLBs in this chapter, a protocol based on covalent modifications may be preferable. For example, using click chemistry for SLB functionalisation provides a robust route for the selective attachment of biomolecules.[210] Additionally, using antibodies with a single site for SLB attachment, instead of the lysine-based biotinylation used here, will help to avoid issues regarding cross-linking. Combined with improvements promised by custom-built mass photometers optimised for single particle tracking, these modifications will result in greatly enhanced scope for measuring complex distributions of proteins on SLBs.

## 6.4 Methods

### 6.4.1 Materials and Sample Storage

Anti-human transferrin antibody (Tfn-IgG) was obtained from Medix Biochimica (Anti-h Transferrin 3104 SPTN-5). Streptavidin (StrAv), bovine serum albumin (BSA), human apo-transferrin (Tfn), and dimethyl sulfoxide (DMSO) were obtained from Sigma Aldrich. All phospholipids were purchased from Avanti Polar Lipids (bt-DOPE, 1,2-dioleoyl-sn-glycero-3-phosphoethanolamine-N-(cap biotinyl) (sodium salt), 870273; DOPE-PEG, 1,2-dioleoyl-sn-glycero-3-phosphoethanolamine-N-[methoxy(polyethylene glycol)-2000] (ammonium salt), 880130). Tfn-IgG was biotinylated via its lysine residues with biotin conjugated with N-hydroxysuccinimide. Briefly, 99 µL Tfn-IgG (16 µM; PBS,

pH 7.2) was mixed with 10 µL of 2.33 mM bt-NHS in DMSO (EZ-Link$^{TM}$ NHS-Biotin, Thermo Fisher Scientific, 20217) and incubated for 4 h on ice. The mixture was then buffer exchanged into PBS 6 times to remove excess biotin, and stored at 4 °C for further use.

### 6.4.2 Supported Lipid Bilayer Preparation

Liposomes and supported lipid bilayers (SLBs) were prepared as described in Chapter 5, except that SLBs were prepared in flow channels consisting of a small coverslip (24 mm x 24 mm, No. 1.5, VWR) stuck to a large coverslip (24 mm x 50 mm), both of which were plasma cleaned.[32] All SLBs used for functionalisation contained 0.01% bt-PE (mole fraction) unless otherwise stated. For surface functionalisation, cleaned SLBs were incubated with 2 nM StrAv for 20 min, washed by flushing twice with 200 µL HKS-100 (20 mM HEPES, pH 7.4, 100 mM KCl) through the channel, followed by incubation with 100 nM bt-Tfn-IgG for 10 min, and again washed twice with 200 µL HKS-100. The same washing procedure was used to remove BSA from SLBs (Fig. 6.1). To remove excess StrAv bound to SLBs in the absence of bt, we tried sequential washes with HKS-100 and the same buffer with 600 mM KCl, but were unsuccessful. Functionalised SLBs were used immediately for measurements.

### 6.4.3 Dynamic MP

*Data acquisition.* Dynamic MP movies were recorded as described in Chapter 4 (10.8 µm x 2.9 µm, 994 Hz raw frame rate unless otherwise stated), with 3-fold frame averaging and 4 x 4 pixel binning resulting in an effective frame rate of 331 Hz and a final pixel size of 77.4 nm (140 x 37 pixels). For specific pull-down of Tfn, SLBs were incubated with 20 nM Tfn in PBS or 20 nM Tfn in 50 µM BSA for 5-20 min followed by washing twice with 200 µL HKS-100.

*Data analysis.* The data processing and analysis of dynamic MP movies was carried out as described in Chapters 4 and 5. We used a sliding median background subtraction window of 201 frames for all data, which translated to 607 and 558 ms for the small and large (9.9 µm x 9.9 µm, 360 Hz) detection areas, respectively. The particle detection threshold was set to 0.0011 and 0.0010 for the small and large detection areas, respectively. When the fitted location of a particle diverged more than two pixels from the pixel where it was initially detected, the particle was excluded from further analysis. Additionally, particles with a fitted contrast of 0.002 or less (∼50 kDa) were removed.

For trajectory linking, the maximum search radius was set to 5 pixels and the memory parameter to 3 frames in line with the faster diffusion and smaller mass of the particles analysed in this chapter, compared to Chapters 4 and 5. After linking, the total particle density was determined by dividing the average number of trajectories in each image by the effective imaging area (10.1 µm x 2.1 µm to account for the exclusion of particles near the edge of the images in the fitting procedure). The resulting trajectories were then filtered by their length with a minimum trajectory length of 50 frames (10 frames for the data in Fig. 6.1d) and then filtered by the standard deviation in their contrast measurements. The diffusion coefficient (lag time = 1 frame; $t = 3$ ms) and mean mass of each trajectory were determined as described in Chapter 5. Trajectories with a diffusion coefficient $< 0.1$ µm$^2$ s$^{-1}$ or where the mean trajectory contrast differed from the median contrats by more than 20% were excluded. Unless otherwise stated, we applied corrections for motion blur and localisation error to the diffusion calculations, and the mean mass of individual trajectories was corrected based on the expected mass drop caused by motion blur at the corresponding effective frame rate (Fig. 6.4a). The SOSIP data in Fig. 6.6 and Fig. 6.7, were processed as described in Chapter 5.

### 6.4.4 Dynamic MP Simulations

All simulated dynamic MP movies were generated as described previously.[120] Briefly, point spread functions (PSFs) were added to raw images of an SLB in contact with buffer acquired at 270 and 540 Hz (9.9 µm x 6.3 µm field of view). PSFs were generated according to the model used for particle fitting (Chapter 4) with appropriate scaling to obtain the desired contrast. To simulate diffusion and motion blur particle trajectories were generated at 5 kHz for 270 Hz movies and 10 kHz for 540 Hz movies. PSFs were moved incrementally according to the simulated displacements in x and y positions, which were randomly sampled from identical Gaussian distributions with mean and variance equal to 0 and $2Dt$, respectively. The amplitude of the PSFs was scaled according to the time spent at each position relative to the time span of a single frame, which resulted in a blurred average position of the PSFs for each frame. The resulting raw images were then run through the background subtraction procedure (sliding median window size of 601 frames).

*Effect of motion blur.* To quantify the effect of motion blur on the observed trajectory mass and diffusion, movies were simulated with PSFs with a contrast of 0.95% (∼250 kDa) and diffusion coefficients ranging from 0.2 to 3.0 $\mu m^2$ $s^{-1}$. The resulting movies were processed and analysed in the same way as the experimental data (detection threshold of 0.0011, filtered with a minimum trajectory length of 30 frames) to extract the mean mass and diffusion coefficient of each trajectory (∼600 trajectories for each simulated diffusion coefficient).

*Localisation error.* To quantify the localisation error of particles in dynamic MP, we simulated movies containing only one particle per image (trajectory length = 50 frames, starting at the centre of the image with 9800 images per movie). This process was repeated for contrasts ranging from 0.72% (∼200

kDa) to 3.6% (∼1000 kDa) and diffusion coefficients ranging from 0.5 to 2.5 $\mu m^2\ s^{-1}$, resulting in approximately 200 simulated trajectories with 50 data points each for every mass-diffusion combination.

The dynamic MP movies (sliding median window size = 201 frames) were then analysed by creating a 17 x 17 pixel area around each simulated particle and applying our PSF-fitting procedure to extract the measured positions of the trajectories in each image. We then determined the median of the Euclidean distances between the measured positions of each trajectory and the simulated ground truth. Fitting a Gaussian function to the resulting distribution of median localisation errors yielded the mean localisation error of each mass-diffusion combination. It is worth noting that the resulting localisation errors are represented as a function of mass, which is based on the current performance of the mass photometer (contrast-to-mass slope = 3.6 * $10^{-3}$ % $kDa^{-1}$ for a detection area of 9.9 µm x 6.3 µm). Therefore, this calibration should be updated if there are significant differences in the performance of the mass photometer over time or compared to the instrument used here.

# Chapter 7

# Summary and Outlook

The most significant innovation in this work was the development of a mass photometry-based SPT assay, termed dynamic MP. This method allows for simultaneous quantification of mass and diffusion coefficient of protein complexes bound to supported lipid bilayers. As a result, mixtures of different oligomeric states or distinct protein complexes originating from interactions of SLB-bound proteins with each other or with proteins in solution can readily be resolved and analysed completely label-free. Dynamic MP also represents a significant enhancement to the range of the possible single-molecule biophysical studies with mass photometry. The combination of solution-based measurements on glass surfaces and SLB-based assays facilitates more functionally relevant studies of membrane proteins, especially membrane-associated proteins, which fulfill functions in both media. Additionally, we showed that the passivating properties of SLBs increased the dynamic range of MP and allowed for measurements in more complex mixtures, such as protein concentrations in the high µM range. As a result we were able to quantify binding affinities as a function of co-existing stoichiometries, with $K_d$s ranging from low nM up to low µM. Crucially, these capabilities come without many of the experimental and analytical complications introduced by relying on fluorescent labels, making these measurements accessible to non-experts.

Initially, we focused on improving the capabilities of solution-based MP experiments, specifically to increase the accessible concentration range of MP and to study interactions in the µM range. We implemented a surface passivation protocol based on attaching polyethylene glycol (PEG) to glass coverslips, which reduced non-specific binding to the surface by up to four orders of magnitude. Next, we attempted to functionalise these surfaces via the biotin-streptavidin system to introduce specificity towards target proteins. At this stage, we encountered complications due to what we concluded was unbinding of streptavidin from biotin, which seemed to be triggered by the MP illumination source. We were forced to abandon further investigations into alternative surface functionalisation protocols due to laboratory closures caused by the COVID-19 pandemic.

Instead, we focused on the development of SPT by MP. At this point, the key hurdle in developing these experiments into a functional assay was the lack of custom software to process and analyse this type of data. Thus, we first developed software to detect and track single protein complexes on SLBs by MP, and developed an analytical pipeline to extract the corresponding masses and diffusion coefficients. We applied our technique, termed dynamic MP, to the self-assembling protein dynamin-1. In this study, we were able to quantify key biophysical parameters of dynamin-1, such as the distribution of oligomeric states and oligomer-dependent diffusion coefficients and rate constants of dissociation from the SLB. These results provided insights into dynamin's mechanism of polymerisation on membranes that had remained elusive for several decades and continue to be an active area of investigation. At a simlar time, a study was published[185] in which the authors applied the same technique to the bacterial MinDE proteins, highlighting the breadth of potential applications of this method.

The passivating properties of SLBs combined with the commercial availability of phospholipids tailored for covalent or non-covalent biofunctionalisation protocols indicated that SLBs could act as a more promising substitute for the PEG-based surface functionalisation. Additionally, the combination of mass and diffusion measurements on SLBs suggested potential for improved resolution compared to MP landing assays, especially in more complex protein-protein interactions, such as cross-linking in antibody-virus interactions. Therefore, we next developed a dynamic MP-based assay aimed at characterising and quantifying protein-protein interactions in HIV-1. By using SOSIP, a protein engineered to mimic the HIV-1 envelope glycoprotein (Env), as a model system, we were able to gain valuable insights into its interactions with bnAbs. We accurately determined binding stoichiometries, protein conformations, the extent of cross-linking of SOSIP by bivalent bnAbs, quantified binding affinities as a function of stoichiometry, and delivered qualitative insights into the kinetics of these processes. Importantly, our investigations into SOSIP's interactions with its target cell receptor, CD4, revealed intricate details in the binding mechanism, while avoiding the demanding requirements of single-molecule fluorescence-based assays.

Our work on Env demonstrated that dynamic MP could be used to simultaneously quantify interactions between protein complexes bound to SLBs and with proteins in solution. It was also the first example of MP-based quantification of a $K_d$ in the µM range. These findings suggested that SLB-based surface functionalisations may enable MP measurements in more complex mixtures, which could provide a single-molecule platform for pull-down assays without relying on labels as a detection mechanism. This motivated us to dedicate the final chapter to exploring the possibility of detecting protein-protein interactions in complex mixtures. We successfully showed proof of concept by

functionalising SLBs with monoclonal antibodies and specifically recruiting human apo-transferrin (Tfn; 20 nM) from a solution of 50 µM BSA. Finally, we highlighted possible pitfalls and limitations in analysing dynamic MP data and introduced corrections that robustly account for systematic errors in the mass and diffusion measurements. This approach yielded accurate mass and diffusion values, which showed its potential in identifying unknown binding partners of target proteins.

Overall, we have demonstrated several applications of dynamic MP, ranging from membrane-associated proteins and protein-protein interactions surrounding viruses, to biosensing. The breadth of these topics, combined with the relatively straightforward methodology compared to other single-molecule methods, clearly highlights the potential for the more widespread adoption of dynamic MP. A particularly exciting aspect is the potential of dynamic MP to be applied to integral membrane proteins in SLBs, although this will require use of cushioned or suspended SLBs to retain protein mobility.

We have identified and discussed several potential improvements to dynamic MP that should aid in its future development. For one, our work was conducted on commercial mass photometers, in which the field of view and acquisition speeds are designed for MP landing assays, rather than SPT experiments. Thus, a custom-built instrument with an optimised combination of large field of view and fast acquisition speeds promises to increase observation times and statistics. In theory, increasing observation times to 1,000 images per trajectory could yield mass and diffusion resolutions as low as 5 kDa and 0.1 $\mu m^2\ s^{-1}$, respectively (Fig. 6.7a-b). Increased sampling statistics could also allow for the observation of protein association and dissociation events on the SLB in real-time and quantification of the corresponding rate constants. Another area that bears potential is improvements to the trajectory linking algorithm, which

is currently done via the open-source Python software trackpy.[156] So far we have not explored alternative options, which means benchmarking different linking algorithms including machine learning-based methods is bound to result in further benefits.

In terms of the design of pull-down assays, we have merely scratched the surface in this work. There are a plethora of options of different phospholipids for SLB functionalisation and labelling methods for the attachment of antibodies or bait proteins, leaving plenty of room for improvements. Establishing robust control over attachment methods and the resulting particle densities will be enormously beneficial. Together with the potential advancement in resolution, it may even become possible to design SLBs with multiple types of biosensing molecules with distinct and resolved diffusion populations, thereby allowing for multiplexed measurements. The solution media to which these assays can be applied to will depend on the passivation performance of the SLBs, which should be explored further to include more complex media such as cell lysates and serum. Similarly, the sensitivity in terms of analyte concentration in the media remains to be investigated.

This work has established and demonstrated the methodology of dynamic MP, explored some of the current limitations, and given an overview of what is likely merely a subset of future applications. With commercial mass photometers becoming more widespread in laboratories around the world, MP-based tracking experiments will increase in their accessibility. We believe that the future of this technique is bright and are excited to see what applications and insights evolve from it.

# References


[1] T. Berggård, S. Linse and P. James, Methods for the detection and analysis of protein–protein interactions, *Proteomics*, 2007, **7**, 2833–2842.

[2] K. Luck *et al.*, A reference map of the human binary protein interactome, *Nature*, 2020, **580**, 402–408.

[3] U. Stelzl *et al.*, A human protein-protein interaction network: a resource for annotating the proteome, *Cell*, 2005, **122**, 957–968.

[4] R. S. Kasai *et al.*, The class-A GPCR dopamine D2 receptor forms transient dimers stabilized by agonists: detection by single-molecule tracking, *Cell Biochemistry and Biophysics*, 2018, **76**, 29–37.

[5] B. H. Toyama *et al.*, Identification of long-lived proteins reveals exceptional stability of essential cellular structures, *Cell*, 2013, **154**, 971–982.

[6] W. Cho and R. V. Stahelin, Membrane-protein interactions in cell signaling and membrane trafficking, *Annual Review of Biophysics and Biomolecular Structure*, 2005, **34**, 119–151.

[7] L. L. Lu, T. J. Suscovich, S. M. Fortune and G. Alter, Beyond binding: antibody effector functions in infectious diseases, *Nature Reviews Immunology*, 2018, **18**, 46–61.

[8] L. L. Blazer and R. R. Neubig, Small molecule protein–protein interaction inhibitors as CNS therapeutic agents: current progress and future hurdles, *Neuropsychopharmacology*, 2009, **34**, 126–141.

[9] A. W. White, A. D. Westwell and G. Brahemi, Protein–protein interactions as targets for small-molecule therapeutics in cancer, *Expert Reviews in Molecular Medicine*, 2008, **10**, e8.

[10] D. E. Scott, A. R. Bayly, C. Abell and J. Skidmore, Small molecules, big targets: drug discovery faces the protein–protein interaction challenge, *Nature Reviews Drug Discovery*, 2016, **15**, 533–550.

[11] A. Beck, L. Goetsch, C. Dumontet and N. Corvaïa, Strategies and challenges for the next generation of antibody–drug conjugates, *Nature Reviews Drug Discovery*, 2017, **16**, 315–337.

[12] H. Lu *et al.*, Recent advances in the development of protein–protein interactions modulators: mechanisms and clinical trials, *Signal Transduction and Targeted Therapy*, 2020, **5**, 213.

[13] D. R. Burton, P. Poignard, R. L. Stanfield and I. A. Wilson, Broadly neutralizing antibodies present new prospects to counter highly antigenically diverse viruses, *Science*, 2012, **337**, 183–186.

[14] T. Xiao *et al.*, HIV-1 fusion inhibitors targeting the membrane-proximal external region of Env spikes, *Nature Chemical Biology*, 2020, **16**, 529–537.

[15] J. Frank, Single-particle imaging of macromolecules by cryo-electron microscopy, *Annual Review of Biophysics and Biomolecular Structure*, 2002, **31**, 303–319.

[16] M. Malmqvist, Surface plasmon resonance for detection and measurement of antibody-antigen affinity and kinetics, *Current Opinion in Immunology*, 1993, **5**, 282–286.

[17] L. K. Tamm and H. M. McConnell, Supported phospholipid bilayers, *Biophysical Journal*, 1985, **47**, 105–113.

[18] I. G. Denisov and S. G. Sligar, Nanodiscs for structural and functional studies of membrane proteins, *Nature Structural and Molecular Biology*, 2016, **23**, 481–486.

[19] J. P. Overington, B. Al-Lazikani and A. L. Hopkins, How many drug targets are there?, *Nature Reviews Drug Discovery*, 2006, **5**, 993–996.

[20] P. Narayan *et al.*, Single molecule characterization of the interactions between amyloid-β peptides and the membranes of hippocampal cells, *Journal of the American Chemical Society*, 2013, **135**, 1491–1498.

[21] J. Chojnacki *et al.*, Envelope glycoprotein mobility on HIV-1 particles depends on the virus maturation state, *Nature Communications*, 2017, **8**, 545.

[22] J. S. Klein and P. J. Bjorkman, Few and far between: how HIV may be evading antibody avidity, *PLOS Pathogens*, 2010, **6**, e1000908.

[23] F. Luo, G. Qin, T. Xia and X. Fang, Single-molecule imaging of protein interactions and dynamics, *Annual Review of Analytical Chemistry*, 2020, **13**, 337–361.

[24] F. Baumgart *et al.*, Varying label density allows artifact-free analysis of membrane-protein nanoclusters, *Nature Methods*, 2016, **13**, 661–664.

[25] R. S. Kasai *et al.*, Full characterization of GPCR monomer–dimer dynamic equilibrium by single molecule imaging, *Journal of Cell Biology*, 2011, **192**, 463–480.

[26] J. B. Grimm and L. D. Lavis, Caveat fluorophore: an insiders' guide to small-molecule fluorescent labels, *Nature Methods*, 2022, **19**, 149–158.

[27] J. Enderlein, E. Toprak and P. R. Selvin, Polarization effect on position accuracy of fluorophore localization, *Optics Express*, 2006, **14**, 8111–8120.

[28] M. Dehghani, S. M. Gulvin, J. Flax and T. R. Gaborski, Systematic evaluation of PKH labelling on extracellular vesicle size by nanoparticle tracking analysis, *Scientific Reports*, 2020, **10**, 9533.

[29] J. P. Hoogenboom *et al.*, Power-law blinking in the fluorescence of single organic molecules, *ChemPhysChem*, 2007, **8**, 823–833.

[30] M. F. Garcia-Parajo *et al.*, Real-time light-driven dynamics of the fluorescence emission in single green fluorescent protein molecules, *Proceedings of the National Academy of Sciences*, 2000, **97**, 7237–7242.

[31] E. Cocucci, R. Gaudin and T. Kirchhausen, Dynamin recruitment and membrane scission at the neck of a clathrin-coated pit, *Molecular Biology of the Cell*, 2014, **25**, 3595–3609.

[32] G. Young *et al.*, Quantitative mass imaging of single biological macromolecules, *Science*, 2018, **360**, 423–427.

[33] F. Soltermann *et al.*, Quantifying protein–protein interactions by molecular counting with mass photometry, *Angewandte Chemie International Edition*, 2020, **59**, 10774–10779.

[34] D. Wu and G. Piszczek, Measuring the affinity of protein-protein interactions on a single-molecule level by mass photometry, *Analytical Biochemistry*, 2020, **592**, 113575.

[35] A. Sonn-Segev *et al.*, Quantifying the heterogeneity of macromolecular machines by mass photometry, *Nature Communications*, 2020, **11**, 1772.

[36] A. Olerinyova *et al.*, Mass photometry of membrane proteins, *Chem*, 2021, **7**, 224–236.

[37] R. B. Russell *et al.*, A structural perspective on protein–protein interactions, *Current Opinion in Structural Biology*, 2004, **14**, 313–324.

[38] M. Zhou, Q. Li and R. Wang, Current experimental methods for characterizing protein–protein interactions, *ChemMedChem*, 2016, **11**, 738–756.

[39] E. M. Phizicky and S. Fields, Protein-protein interactions: methods for detection and analysis, *Microbiological reviews*, 1995, **59**, 94–123.

[40] Y. Lu *et al.*, Substrate degradation by the proteasome: a single-molecule kinetic analysis, *Science*, 2015, **348**, 1250834.

[41] C. L. Meyerkord and H. Fu, *Protein-protein interactions: methods and applications*, Humana Press, New York, 2nd edn., 2015.

[42] A.-C. Gingras, M. Gstaiger, B. Raught and R. Aebersold, Analysis of protein complexes using mass spectrometry, *Nature Reviews Molecular Cell Biology*, 2007, **8**, 645–654.

[43] F. Soltermann, W. B. Struwe and P. Kukura, Label-free methods for optical in vitro characterization of protein-protein interactions, *Physical Chemistry Chemical Physics*, 2021, **23**, 16488–16500.

[44] M. Jerabek-Willemsen *et al.*, MicroScale thermophoresis: interaction analysis and beyond, *Journal of Molecular Structure*, 2014, **1077**, 101–113.

[45] J. Lebowitz, M. S. Lewis and P. Schuck, Modern analytical ultracentrifugation in protein science: A tutorial review, *Protein Science*, 2002, **11**, 2067–2079.

[46] A. C. Pan, D. W. Borhani, R. O. Dror and D. E. Shaw, Molecular determinants of drug–receptor binding kinetics, *Drug Discovery Today*, 2013, **18**, 667–673.

[47] P. L. Kastritis and A. M. J. J. Bonvin, On the binding affinity of macromolecular interactions: daring to ask why proteins interact, *Journal of the Royal Society, Interface*, 2012, **10**, 20120835.

[48] Y. Tang, X. Zeng and J. Liang, Surface plasmon resonance: an introduction to a surface spectroscopy technique, *Journal of chemical education*, 2010, **87**, 742–746.

[49] R. Karlsson, A. Michaelsson and L. Mattsson, Kinetic analysis of monoclonal antibody-antigen interactions with a new biosensor based analytical system, *Journal of Immunological Methods*, 1991, **145**, 229–240.

[50] E. S. Day *et al.*, Determining the affinity and stoichiometry of interactions between unmodified proteins in solution using Biacore, *Analytical Biochemistry*, 2013, **440**, 96–107.

[51] V. Okreglak and D. G. Drubin, Loss of Aip1 reveals a role in maintaining the actin monomer pool and an in vivo oligomer assembly pathway, *Journal of Cell Biology*, 2010, **188**, 769–777.

[52] A. Akhmanova and M. O. Steinmetz, Control of microtubule organization and dynamics: two ends in the limelight, *Nature Reviews Molecular Cell Biology*, 2015, **16**, 711–726.

[53] S. L. Schmid and V. A. Frolov, Dynamin: functional design of a membrane fission catalyst, *Annual Review of Cell and Developmental Biology*, 2011, **27**, 79–105.

[54] B. L. Woods and A. S. Gladfelter, The state of the septin cytoskeleton from assembly to function, *Current Opinion in Cell Biology*, 2021, **68**, 105–112.

[55] S. L. Ritter and R. A. Hall, Fine-tuning of GPCR activity by receptor-interacting proteins, *Nature Reviews Molecular Cell Biology*, 2009, **10**, 819–830.

[56] P. Zhang and J. E. Hinshaw, Three-dimensional reconstruction of dynamin in the constricted state, *Nature Cell Biology*, 2001, **3**, 922–926.

[57] T. J. Knowles *et al.*, Membrane proteins solubilized intact in lipid containing nanoparticles bounded by styrene maleic acid copolymer, *Journal of the American Chemical Society*, 2009, **131**, 7484–7485.

[58] M. Frick and C. Schmidt, Mass spectrometry—A versatile tool for characterising the lipid environment of membrane protein assemblies, *Chemistry and Physics of Lipids*, 2019, **221**, 145–157.

[59] M. T. Marty, K. K. Hoi and C. V. Robinson, Interfacing membrane mimetics with mass spectrometry, *Accounts of Chemical Research*, 2016, **49**, 2459–2467.

[60] B. Liang and L. K. Tamm, NMR as a tool to investigate the structure, dynamics and function of membrane proteins, *Nature Structural and Molecular Biology*, 2016, **23**, 468–474.

[61] C. Bechara *et al.*, A subset of annular lipids is linked to the flippase activity of an ABC transporter, *Nature Chemistry*, 2015, **7**, 255–262.

[62] M. F. Garcia-Parajo *et al.*, Nanoclustering as a dominant feature of plasma membrane organization, *Journal of Cell Science*, 2014, **127**, 4995–5005.

[63] S. K. Saka *et al.*, Multi-protein assemblies underlie the mesoscale organization of the plasma membrane, *Nature Communications*, 2014, **5**, 4509.

[64] L. Dehmelt and P. I. H. Bastiaens, Spatial organization of intracellular communication: insights from imaging, *Nature Reviews Molecular Cell Biology*, 2010, **11**, 440–452.

[65] Y. Cui *et al.*, Single-particle tracking for the quantification of membrane protein dynamics in living plant cells, *Molecular Plant*, 2018, **11**, 1315–1327.

[66] C.-C. Chang *et al.*, Interactions of amyloid-β peptides on lipid bilayer studied by single molecule imaging and tracking, *Biochimica et Biophysica Acta (BBA) - Biomembranes*, 2018, **1860**, 1616–1624.

[67] M. L. Wagner and L. K. Tamm, tethered polymer-supported planar lipid bilayers for reconstitution of integral membrane proteins: silane-polyethyleneglycol-lipid as a cushion and covalent linker, *Biophysical Journal*, 2000, **79**, 1400–1414.

[68] D. L. Floyd *et al.*, Single-particle kinetics of influenza virus membrane fusion, *Proceedings of the National Academy of Sciences*, 2008, **105**, 15382–15387.

[69] M. Beseničar, P. Maček, J. H. Lakey and G. Anderluh, Surface plasmon resonance in protein–membrane interactions, *Chemistry and Physics of Lipids*, 2006, **141**, 169–178.

[70] A. Ishijima and T. Yanagida, Single molecule nanobioscience, *Trends in Biochemical Sciences*, 2001, **26**, 438–444.

[71] F. Fricke, J. Beaudouin, R. Eils and M. Heilemann, One, two or three? Probing the stoichiometry of membrane proteins by single-molecule localization microscopy, *Scientific Reports*, 2015, **5**, 14072.

[72] C. E. Perez and J. Gonzalez, Ruben L., In vitro and in vivo single-molecule fluorescence imaging of ribosome-catalyzed protein synthesis, *Current opinion in chemical biology*, 2011, **15**, 853–863.

[73] C. Joo *et al.*, Advances in single-molecule fluorescence methods for molecular biology, *Annual Review of Biochemistry*, 2008, **77**, 51–76.

[74] C. Manzo and M. F. Garcia-Parajo, A review of progress in single particle tracking: from methods to biophysical insights, *Reports on Progress in Physics*, 2015, **78**, 124601.

[75] R. S. Kasai and A. Kusumi, Single-molecule imaging revealed dynamic GPCR dimerization, *Current Opinion in Cell Biology*, 2014, **27**, 78–86.

[76] K. G. Suzuki *et al.*, GPI-anchored receptor clusters transiently recruit Lyn and Gα for temporary cluster immobilization and Lyn activation: single-molecule tracking study 1, *Journal of Cell Biology*, 2007, **177**, 717–730.

[77] A. Kusumi *et al.*, Tracking single molecules at work in living cells, *Nature Chemical Biology*, 2014, **10**, 524–532.

[78] H. Shen *et al.*, Single particle tracking: from theory to biophysical applications, *Chemical Reviews*, 2017, **117**, 7331–7376.

[79] E. Betzig and R. J. Chichester, Single molecules observed by near-field scanning optical microscopy, *Science*, 1993, **262**, 1422–1425.

[80] E. C. Arnspang, J. R. Brewer and B. C. Lagerholm, Multi-color single particle tracking with quantum dots, *PLOS ONE*, 2012, **7**, e48521.

[81] W. B. Asher *et al.*, Single-molecule FRET imaging of GPCR dimers in living cells, *Nature Methods*, 2021, **18**, 397–405.

[82] S. K. Das *et al.*, Membrane protein stoichiometry determined from the step-wise photobleaching of dye-labelled subunits, *ChemBioChem*, 2007, **8**, 994–999.

[83] P. Agrawal *et al.*, Stoichiometric analyses of soluble CD4 to native-like HIV-1 envelope by single-molecule fluorescence spectroscopy, *Cell Reports*, 2019, **29**, 176–186.e4.

[84] J. R. Wayment and J. M. Harris, Biotin−avidin binding kinetics measured by single-molecule imaging, *Analytical Chemistry*, 2009, **81**, 336–342.

[85] R. J. Arant and M. H. Ulbrich, Deciphering the subunit composition of multimeric proteins by counting photobleaching steps, *ChemPhysChem*, 2014, **15**, 600–605.

[86] V. C. Coffman and J.-Q. Wu, Counting protein molecules using quantitative fluorescence microscopy, *Trends in Biochemical Sciences*, 2012, **37**, 499–506.

[87] R. E. Thompson, D. R. Larson and W. W. Webb, Precise nanometer localization analysis for individual fluorescent probes, *Biophysical journal*, 2002, **82**, 2775–2783.

[88] J. Ortega-Arroyo and P. Kukura, Interferometric scattering microscopy (iSCAT): new frontiers in ultrafast and ultrasensitive optical microscopy, *Physical Chemistry Chemical Physics*, 2012, **14**, 15625–15636.

[89] H. Ueno *et al.*, Simple dark-field microscopy with nanometer spatial precision and microsecond temporal resolution, *Biophysical Journal*, 2010, **98**, 2014–2023.

[90] G. Young and P. Kukura, Interferometric scattering microscopy, *Annual Review of Physical Chemistry*, 2019, **70**, 301–322.

[91] E. W. Streed, A. Jechow, B. G. Norton and D. Kielpinski, Absorption imaging of a single atom, *Nature Communications*, 2012, **3**, 933.

[92] F. Reina *et al.*, Complementary studies of lipid membrane dynamics using iSCAT and super-resolved fluorescence correlation spectroscopy, *Journal of physics D: Applied physics*, 2018, **51**, 235401–235401.

[93] K. M. Spillane *et al.*, High-speed single-particle tracking of GM1 in model membranes reveals anomalous diffusion due to interleaflet coupling and molecular pinning, *Nano Letters*, 2014, **14**, 5390–5397.

[94] K. Lindfors, T. Kalkbrenner, P. Stoller and V. Sandoghdar, Detection and spectroscopy of gold nanoparticles using supercontinuum white light confocal microscopy, *Physical Review Letters*, 2004, **93**, 037401.

[95] R. W. Taylor *et al.*, Interferometric scattering microscopy reveals microsecond nanoscopic protein motion on a live cell membrane, *Nature Photonics*, 2019, **13**, 480–487.

[96] G. de Wit, D. Albrecht, H. Ewers and P. Kukura, Revealing compartmentalized diffusion in living cells with interferometric scattering microscopy, *Biophysical Journal*, 2018, **114**, 2945–2950.

[97] J. Andrecka *et al.*, Structural dynamics of myosin 5 during processive motion revealed by interferometric scattering microscopy, *eLife*, 2015, **4**, e05413.

[98] H. Ewers *et al.*, Label-free optical detection and tracking of single virions bound to their receptors in supported membrane bilayers, *Nano Letters*, 2007, **7**, 2263–2266.

[99] J. Andrecka *et al.*, Label-free imaging of microtubules with sub-nm precision using interferometric scattering microscopy, *Biophysical Journal*, 2016, **110**, 214–217.

[100] J. Ortega Arroyo *et al.*, Label-free, all-optical detection, imaging, and tracking of a single protein, *Nano Letters*, 2014, **14**, 2065–2070.

[101] M. Piliarik and V. Sandoghdar, Direct optical sensing of single unlabelled proteins and super-resolution imaging of their binding sites, *Nature Communications*, 2014, **5**, 4495.

[102] M. Liebel, J. T. Hugall and N. F. van Hulst, Ultrasensitive label-free nanosensing and high-speed tracking of single proteins, *Nano Letters*, 2017, **17**, 1277–1281.

[103] D. Cole *et al.*, Label-free single-molecule imaging with numerical-aperture-shaped interferometric scattering microscopy, *ACS Photonics*, 2017, **4**, 211–216.

[104] C. Galvagnion *et al.*, Lipid vesicles trigger (α)-synuclein aggregation by stimulating primary nucleation, *Nature Chemical Biology*, 2015, **11**, 229–234.

[105] M. Y. Hein *et al.*, A human interactome in three quantitative dimensions organized by stoichiometries and abundances, *Cell*, 2015, **163**, 712–723.

[106] A. Fineberg, T. Surrey and P. Kukura, Quantifying the monomer–dimer equilibrium of tubulin with mass photometry, *Journal of Molecular Biology*, 2020, **432**, 6168–6172.

[107] H. Vaisocherová *et al.*, Ultralow fouling and functionalizable surface chemistry based on a zwitterionic polymer enabling sensitive and specific protein detection in undiluted blood plasma, *Analytical Chemistry*, 2008, **80**, 7894–7901.

[108] I. Banerjee, R. C. Pangule and R. S. Kane, Antifouling coatings: recent developments in the design of surfaces that prevent fouling by proteins, bacteria, and marine organisms, *Advanced Materials*, 2011, **23**, 690–718.

[109] S. Chen, L. Li, C. Zhao and J. Zheng, Surface hydration: principles and applications toward low-fouling/nonfouling biomaterials, *Polymer*, 2010, **51**, 5283–5293.

[110] S. I. Jeon, J. H. Lee, J. D. Andrade and P. G. De Gennes, Protein—surface interactions in the presence of polyethylene oxide: I. Simplified theory, *Journal of Colloid and Interface Science*, 1991, **142**, 149–158.

[111] S. D. Chandradoss *et al.*, Surface passivation for single-molecule protein studies, *JoVE*, 2014, e50549.

[112] I. Rasnik, S. A. McKinney and T. Ha, Surfaces and orientations: much to FRET about?, *Accounts of Chemical Research*, 2005, **38**, 542–548.

[113] V. H. Pérez-Luna *et al.*, Molecular recognition between genetically engineered streptavidin and surface-bound biotin, *Journal of the American Chemical Society*, 1999, **121**, 6469–6478.

[114] U. Piran and W. J. Riordan, Dissociation rate constant of the biotin-streptavidin complex, *Journal of Immunological Methods*, 1990, **133**, 141–143.

[115] R. F. Garmann, A. M. Goldfain and V. N. Manoharan, Measurements of the self-assembly kinetics of individual viral capsids around their RNA genome, *Proceedings of the National Academy of Sciences of the United States of America*, 2019, **116**, 22485–22490.

[116] F. Rusmini, Z. Zhong and J. Feijen, Protein immobilization strategies for protein biochips, *Biomacromolecules*, 2007, **8**, 1775–1789.

[117] F. Persson *et al.*, Lipid-based passivation in nanofluidics, *Nano Letters*, 2012, **12**, 2260–2265.

[118] M.-L. Visnapuu, D. Duzdevich and E. C. Greene, The importance of surfaces in single-molecule bioscience, *Molecular BioSystems*, 2008, **4**, 394–403.

[119] F. Soltermann, Biophysical characterization of protein-protein interactions with mass photometry, *Ph.D. thesis*, University of Oxford, 2020.

[120] E. D. B. Foley, M. S. Kushwah, G. Young and P. Kukura, Mass photometry enables label-free tracking and mass measurement of single proteins on lipid bilayers, *Nature Methods*, 2021, **18**, 1247–1252.

[121] S. Tan, H. T. Tan and M. C. M. Chung, Membrane proteins and membrane proteomics, *Proteomics*, 2008, **8**, 3924–3932.

[122] A.-C. Durieux, B. Prudhon, P. Guicheney and M. Bitoun, Dynamin 2 and human diseases, *Journal of Molecular Medicine*, 2010, **88**, 339–350.

[123] J. R. Bolla, M. T. Agasid, S. Mehmood and C. V. Robinson, Membrane protein–lipid interactions probed using mass spectrometry, *Annual Review of Biochemistry*, 2019, **88**, 85–111.

[124] J. A. Marsh and S. A. Teichmann, Structure, dynamics, assembly, and evolution of protein complexes, *Annual Review of Biochemistry*, 2015, **84**, 551–575.

[125] G. J. Schütz, H. Schindler and T. Schmidt, Single-molecule microscopy on model membranes reveals anomalous diffusion, *Biophysical Journal*, 1997, **73**, 1073–1080.

[126] M. Vrljic, S. Y. Nishimura and W. E. Moerner, in *Lipid Rafts*, ed. T. J. McIntosh, Humana Press, Totowa, NJ, 2007, pp. 193–219.

[127] M. Loose *et al.*, Min protein patterns emerge from rapid rebinding and membrane interaction of MinE, *Nature Structural and Molecular Biology*, 2011, **18**, 577–583.

[128] X. Wang *et al.*, Single-molecule fluorescence imaging to quantify membrane protein dynamics and oligomerization in living plant cells, *Nature Protocols*, 2015, **10**, 2054–2063.

[129] P. Kukura *et al.*, High-speed nanoscopic tracking of the position and orientation of a single virus, *Nature Methods*, 2009, **6**, 923–927.

[130] M. Leonard, B. Doo Song, R. Ramachandran and S. L. Schmid, Robust colorimetric assays for dynamin's basal and stimulated GTPase activities, *Methods in Enzymology*, 2005, **404**, 490–503.

[131] P. V. Bashkirov *et al.*, GTPase cycle of dynamin is coupled to membrane squeeze and release, leading to spontaneous fission, *Cell*, 2008, **135**, 1276–1286.

[132] R. Deo *et al.*, ATP-dependent membrane remodeling links EHD1 functions to endocytic recycling, *Nature Communications*, 2018, **9**, 5187.

[133] J. S. Chappie *et al.*, A pseudoatomic model of the dynamin polymer identifies a hydrolysis-dependent powerstroke, *Cell*, 2011, **147**, 209–222.

[134] L. Kong *et al.*, Cryo-EM of the dynamin polymer assembled on lipid membrane, *Nature*, 2018, **560**, 258–262.

[135] A. C. Sundborger *et al.*, A dynamin mutant defines a superconstricted prefission state, *Cell Reports*, 2014, **8**, 734–742.

[136] A. Kadosh *et al.*, The tilted helix model of dynamin oligomers, *Proceedings of the National Academy of Sciences*, 2019, **116**, 12845–12850.

[137] A. Colom *et al.*, Dynamic remodeling of the dynamin helix during membrane constriction, *Proceedings of the National Academy of Sciences*, 2017, **114**, 5449–5454.

[138] B. Antonny *et al.*, Membrane fission by dynamin: what we know and what we need to know, *The EMBO Journal*, 2016, **35**, 2270–2284.

[139] L. Wang *et al.*, Dynamin 2 mutants linked to centronuclear myopathies form abnormally stable polymers, *Journal of Biological Chemistry*, 2010, **285**, 22753–22757.

[140] A. Yildiz *et al.*, Myosin V walks hand-over-hand: single fluorophore imaging with 1.5-nm localization, *Science*, 2003, **300**, 2061–2065.

[141] J. D. Knight *et al.*, Single molecule diffusion of membrane-bound proteins: window into lipid contacts and bilayer dynamics, *Biophysical Journal*, 2010, **99**, 2879–2887.

[142] B. P. Ziemba and J. J. Falke, Lateral diffusion of peripheral membrane proteins on supported lipid bilayers is controlled by the additive frictional drags of (1) bound lipids and (2) protein domains penetrating into the bilayer hydrocarbon core, *Chemistry and Physics of Lipids*, 2013, **172-173**, 67–77.

[143] L. K. Tamm, Lateral diffusion and fluorescence microscope studies on a monoclonal antibody specifically bound to supported phospholipid bilayers, *Biochemistry*, 1988, **27**, 1450–1457.

[144] T. Savin and P. S. Doyle, Static and dynamic errors in particle tracking microrheology, *Biophysical Journal*, 2005, **88**, 623–638.

[145] Y.-J. Chen, P. Zhang, E. H. Egelman and J. E. Hinshaw, The stalk region of dynamin drives the constriction of dynamin tubes, *Nature Structural and Molecular Biology*, 2004, **11**, 574–575.

[146] T. F. Reubold *et al.*, Crystal structure of the dynamin tetramer, *Nature*, 2015, **525**, 404–408.

[147] E. Solomaha and H. C. Palfrey, Conformational changes in dynamin on GTP binding and oligomerization reported by intrinsic and extrinsic fluorescence, *Biochemical Journal*, 2005, **391**, 601–611.

[148] S. Srinivasan *et al.*, Identification and function of conformational dynamics in the multidomain GTPase dynamin, *The EMBO Journal*, 2016, **35**, 443–457.

[149] R. Ramachandran *et al.*, The dynamin middle domain is critical for tetramerization and higher-order self-assembly, *The EMBO Journal*, 2007, **26**, 559–566.

[150] J. A. Kenniston and M. A. Lemmon, Dynamin GTPase regulation is altered by PH domain mutations found in centronuclear myopathy patients, *The EMBO Journal*, 2010, **29**, 3054–3067.

[151] N. Sambuughin *et al.*, Adult-onset autosomal dominant spastic paraplegia linked to a GTPase-effector domain mutation of dynamin 2, *BMC Neurology*, 2015, **15**, 223.

[152] N. G. James *et al.*, A mutation associated with centronuclear myopathy enhances the size and stability of dynamin 2 complexes in cells, *Biochimica et Biophysica Acta (BBA) - General Subjects*, 2014, **1840**, 315–321.

[153] R. Ramachandran and S. L. Schmid, Real-time detection reveals that effectors couple dynamin's GTP-dependent conformational changes to the membrane, *The EMBO Journal*, 2008, **27**, 27–37.

[154] S. Mashaghi and A. M. van Oijen, A versatile approach to the generation of fluid supported lipid bilayers and its applications, *Biotechnology and Bioengineering*, 2014, **111**, 2076–2081.

[155] C.-Y. Cheng and C.-L. Hsieh, Background estimation and correction for high-precision localization microscopy, *ACS Photonics*, 2017, **4**, 1730–1739.

[156] D. B. Allan, T. Caswell, N. C. Keim and C. M. van der Wel, *soft-matter/trackpy: Trackpy v0.4.2*, 2019, https://doi.org/10.5281/zenodo.3492186.

[157] *How to get to zero: Faster. Smarter. Better.*, UNAIDS World AIDS Day Report (UNAIDS, Geneva, 2011).

[158] J. M. Cuevas *et al.*, Extremely high mutation rate of HIV-1 in vivo, *PLoS biology*, 2015, **13**, e1002251.

[159] X. Wei *et al.*, Antibody neutralization and escape by HIV-1, *Nature*, 2003, **422**, 307–312.

[160] D. R. Burton and L. Hangartner, Broadly neutralizing antibodies to HIV and their role in vaccine Design, *Annual Review of Immunology*, 2016, **34**, 635–659.

[161] P. D. Kwong *et al.*, HIV-1 evades antibody-mediated neutralization through conformational masking of receptor-binding sites, *Nature*, 2002, **420**, 678–682.

[162] A. F. Labrijn *et al.*, Access of antibody molecules to the conserved coreceptor binding site on glycoprotein gp120 is sterically restricted on primary human immunodeficiency virus type 1, *Journal of Virology*, 2003, **77**, 10557–10565.

[163] J. R. Mascola *et al.*, Protection of macaques against vaginal transmission of a pathogenic HIV-1/SIV chimeric virus by passive infusion of neutralizing antibodies, *Nature Medicine*, 2000, **6**, 207–210.

[164] D. Sok and D. R. Burton, Recent progress in broadly neutralizing antibodies to HIV, *Nature Immunology*, 2018, **19**, 1179–1188.

[165] A. Escolano, P. Dosenovic and M. C. Nussenzweig, Progress toward active or passive HIV-1 vaccination, *Journal of Experimental Medicine*, 2016, **214**, 3–16.

[166] R. W. Sanders and J. P. Moore, Native-like Env trimers as a platform for HIV-1 vaccine design, *Immunological Reviews*, 2017, **275**, 161–182.

[167] R. Wyatt and J. Sodroski, The HIV-1 envelope glycoproteins: fusogens, antigens, and immunogens, *Science*, 1998, **280**, 1884–1888.

[168] J. Liu *et al.*, Molecular architecture of native HIV-1 gp120 trimers, *Nature*, 2008, **455**, 109–113.

[169] Q. Wang, A. Finzi and J. Sodroski, The conformational states of the HIV-1 envelope glycoproteins, *Trends in Microbiology*, 2020, **28**, 655–667.

[170] R. W. Sanders *et al.*, A next-generation cleaved, soluble HIV-1 Env trimer, BG505 SOSIP.664 gp140, expresses multiple epitopes for broadly neutralizing but not non-neutralizing antibodies, *PLOS Pathogens*, 2013, **9**, e1003618.

[171] D. Lyumkis *et al.*, Cryo-EM structure of a fully glycosylated soluble cleaved HIV-1 envelope trimer, *Science*, 2013, **342**, 1484–1490.

[172] J.-P. Julien *et al.*, Crystal structure of a soluble cleaved HIV-1 envelope trimer, *Science*, 2013, **342**, 1477–1483.

[173] S. W. de Taeye *et al.*, Immunogenicity of stabilized HIV-1 envelope trimers with reduced exposure of non-neutralizing epitopes, *Cell*, 2015, **163**, 1702–1715.

[174] N. S. Laursen *et al.*, Universal protection against influenza infection by a multidomain antibody to influenza hemagglutinin, *Science*, 2018, **362**, 598–602.

[175] T. Einav *et al.*, Harnessing avidity: quantifying the entropic and energetic effects of linker length and rigidity for multivalent binding of antibodies to HIV-1, *Cell Systems*, 2019, **9**, 466–474.e7.

[176] J. S. Klein *et al.*, Examination of the contributions of size and avidity to the neutralization mechanisms of the anti-HIV antibodies b12 and 4E10, *Proceedings of the National Academy of Sciences*, 2009, **106**, 7385–7390.

[177] P. Zhu *et al.*, Distribution and three-dimensional structure of AIDS virus envelope spikes, *Nature*, 2006, **441**, 847–852.

[178] N. S. Groves, M. M. Bruns and S. B. van Engelenburg, A quantitative live-cell superresolution imaging framework for measuring the mobility of single molecules at sites of virus assembly, *Pathogens*, 2020, **9**, 972.

[179] Y.-C. Chen *et al.*, Super-resolution fluorescence imaging reveals that serine incorporator protein 5 inhibits human immunodeficiency virus fusion by disrupting envelope glycoprotein clusters, *ACS Nano*, 2020, **14**, 10929–10943.

[180] R. Pejchal *et al.*, A potent and broad neutralizing antibody recognizes and penetrates the HIV glycan shield, *Science*, 2011, **334**, 1097–1103.

[181] Y. Wu *et al.*, Structural basis for enhanced HIV-1 neutralization by a dimeric immunoglobulin G form of the glycan-recognizing antibody 2G12, *Cell Reports*, 2013, **5**, 1443–1455.

[182] P. Zhu, W. C. Olson and K. H. Roux, Structural flexibility and functional valence of CD4-IgG2 (PRO 542): potential for cross-linking human immunodeficiency virus type 1 envelope spikes, *Journal of Virology*, 2001, **75**, 6682–6686.

[183] J. Dufloo *et al.*, Broadly neutralizing anti-HIV-1 antibodies tether viral particles at the surface of infected cells, *Nature Communications*, 2022, **13**, 630.

[184] L. A. Cavacini *et al.*, Effect of antibody valency on interaction with cell-surface expressed HIV-1 and viral neutralization, *The Journal of Immunology*, 1994, **152**, 2538–2545.

[185] T. Heermann *et al.*, Mass-sensitive particle tracking to elucidate the membrane-associated MinDE reaction cycle, *Nature Methods*, 2021, **18**, 1239–1246.

[186] S. S. Paul, A. Lyons, R. Kirchner and M. T. Woodside, Quantifying oligomer populations in real time during protein aggregation using single-molecule mass photometry, *bioRxiv*, 2022, 2022.06.15.496189.

[187] J.-P. Julien *et al.*, Asymmetric recognition of the HIV-1 trimer by broadly neutralizing antibody PG9, *Proceedings of the National Academy of Sciences*, 2013, **110**, 4351–4356.

[188] J. H. Lee, G. Ozorowski and A. B. Ward, Cryo-EM structure of a native, fully glycosylated, cleaved HIV-1 envelope trimer, *Science*, 2016, **351**, 1043–1048.

[189] E. Falkowska *et al.*, PGV04, an HIV-1 gp120 CD4 binding site antibody, is broad and potent in neutralization but does not induce conformational changes characteristic of CD4, *Journal of Virology*, 2012, **86**, 4394–4403.

[190] D. A. Calarese *et al.*, Antibody domain exchange is an immunological solution to carbohydrate cluster recognition, *Science*, 2003, **300**, 2065–2071.

[191] A. Yasmeen *et al.*, Differential binding of neutralizing and non-neutralizing antibodies to native-like soluble HIV-1 Env trimers, uncleaved Env proteins, and monomeric subunits, *Retrovirology*, 2014, **11**, 41.

[192] C. Blattner *et al.*, Structural delineation of a quaternary, cleavage-dependent epitope at the gp41-gp120 interface on intact HIV-1 Env trimers, *Immunity*, 2014, **40**, 669–680.

[193] P. Pugach *et al.*, A native-like SOSIP.664 trimer based on an HIV-1 subtype B env gene, *Journal of Virology*, 2015, **89**, 3380–3395.

[194] X. Ma *et al.*, HIV-1 Env trimer opens through an asymmetric intermediate in which individual protomers adopt distinct conformations, *eLife*, 2018, **7**, e34271.

[195] H. Wang *et al.*, Partially open HIV-1 envelope structures exhibit conformational changes relevant for coreceptor binding and fusion, *Cell Host and Microbe*, 2018, **24**, 579–592.

[196] M. A. G. Hoffmann *et al.*, Nanoparticles presenting clusters of CD4 expose a universal vulnerability of HIV-1 by mimicking target cells, *Proceedings of the National Academy of Sciences*, 2020, **117**, 18719–18728.

[197] Y. Yuan *et al.*, Single-molecule super-resolution imaging of T-cell plasma membrane CD4 redistribution upon HIV-1 binding, *Viruses*, 2021, **13**, 142.

[198] W. B. Struwe *et al.*, Global N-glycan site occupancy of HIV-1 gp120 by metabolic engineering and high-resolution intact mass spectrometry, *ACS Chemical Biology*, 2017, **12**, 357–361.

[199] W. B. Struwe *et al.*, Site-specific glycosylation of virion-derived HIV-1 Env is mimicked by a soluble trimeric immunogen, *Cell Reports*, 2018, **24**, 1958–1966.

[200] M. Goulian and S. M. Simon, Tracking single proteins within cells, *Biophysical Journal*, 2000, **79**, 2188–2198.

[201] R. J. Goldberg, A theory of antibody—antigen reactions. I. Theory for reactions of multivalent antigen with bivalent and univalent antibody[2], *Journal of the American Chemical Society*, 1952, **74**, 5715–5725.

[202] R. de la Rica and M. M. Stevens, Plasmonic ELISA for the ultrasensitive detection of disease biomarkers with the naked eye, *Nature Nanotechnology*, 2012, **7**, 821–824.

[203] H. I. Petrache *et al.*, Structure and fluctuations of charged phosphatidylserine bilayers in the absence of salt, *Biophysical Journal*, 2004, **86**, 1574–1586.

[204] C.-h. Yu and J. T. Groves, Engineering supported membranes for cell biology, *Medical and Biological Engineering and Computing*, 2010, **48**, 955–963.

[205] A. R. Ferhan *et al.*, Solvent-assisted preparation of supported lipid bilayers, *Nature Protocols*, 2019, **14**, 2091–2118.

[206] M. J. Saxton, Single-particle tracking: the distribution of diffusion coefficients, *Biophys J*, 1997, **72**, 1744–53.

[207] E. H. Williams *et al.*, Immobilization of streptavidin on 4H–SiC for biosensor development, *Applied Surface Science*, 2012, **258**, 6056–6063.

[208] Y. H. Tan *et al.*, A nanoengineering approach for investigation and regulation of protein immobilization, *ACS Nano*, 2008, **2**, 2374–2384.

[209] G. Young, Mass photometry: weighing single molecules with interferometric scattering microscopy, *Ph.D. thesis*, University of Oxford, 2019.

[210] B. van Lengerich, R. J. Rawle and S. G. Boxer, Covalent attachment of lipid vesicles to a fluid-supported bilayer allows observation of DNA-mediated vesicle interactions, *Langmuir*, 2010, **26**, 8666–8672.

# Appendix A

# Extended Data for Chapter 4

This section includes the Extended Data of the publication Chapter 4 was adapted from: E.D.B. Foley, M.S. Kushwah, G. Young, P. Kukura, Mass photometry enables label-free tracking and mass measurement of single proteins on lipid bilayers, *Nature Methods*, 2021, **18**, 1247-1252.[120] Reprint permitted under the terms of the Creative Commons Attribution 4.0 International License. The publication including Supplementary Videos is also available online: https://doi.org/10.1038/s41592-021-01261-w.

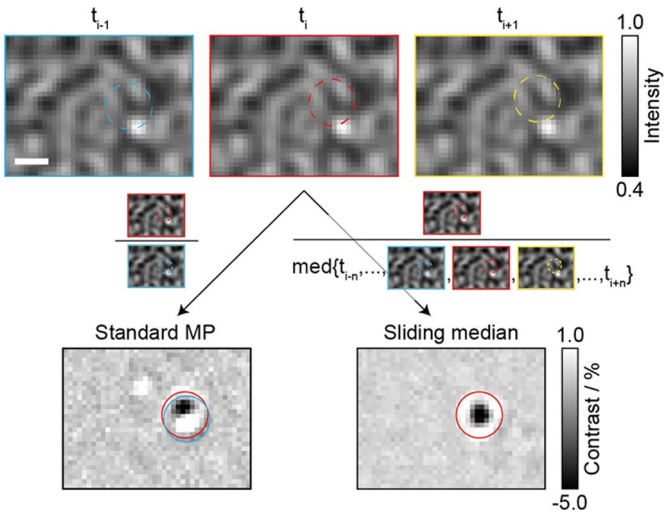


**Extended Data Fig. 1 | Background subtraction in standard mass photometry (MP) vs dynamic MP.** Zoom on three consecutive raw images from a dynamic MP movie of WT dynamin in contact with an SLB containing a particle diffusing upwards through the image (top row), which is masked by the large signal from the glass surface roughness. In standard MP (left), images are divided by preceding images to remove the large static signal due to surface roughness. This background subtraction relies on stationary binding of small particles to the surface to visualise them. When particles bind to and diffuse on the surface, the background subtraction used in standard MP results in a signal that is a convolution of the particle's position at $t_{i-1}$ and $t_i$, (blue and red, respectively), which is challenging to reliably detect and quantify. A sliding median filter (right), that is subtracting each image's temporal median background obtained from a defined window of images around the image of interest, reveals signals of only the particles in the image of interest ($t_i$, red). For further explanation see 'Data processing' in the Methods section. Scale bar = 500 nm. The effect illustrated in this figure was reproducible in all measurements shown in this study ($n > 30$).

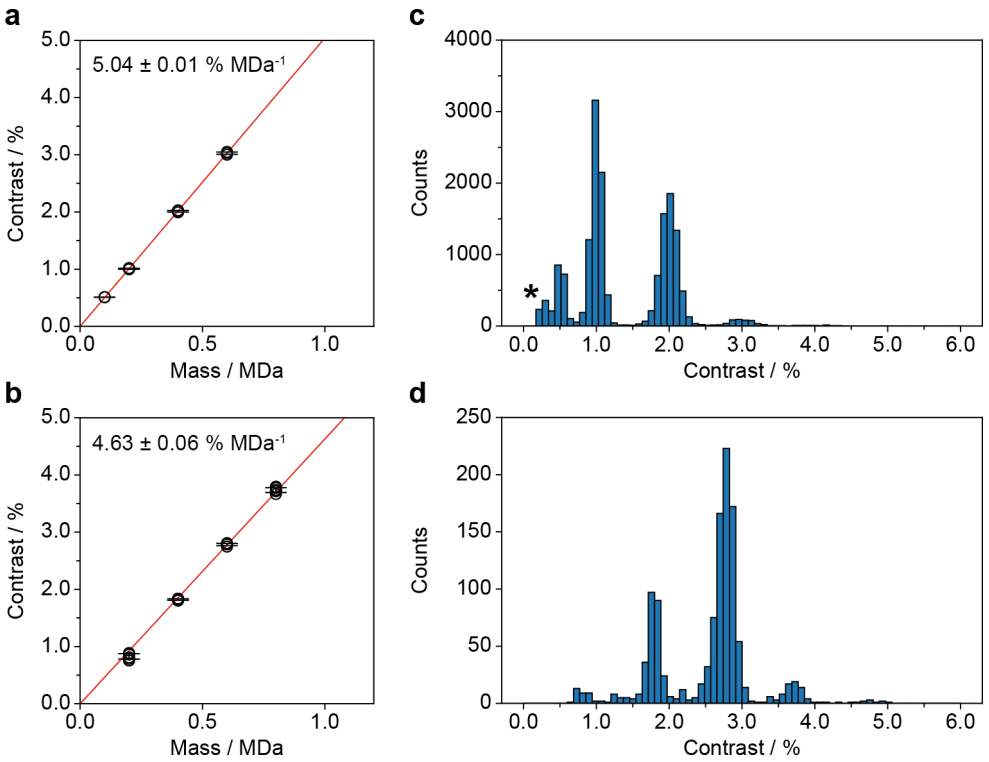


**Extended Data Fig. 2 | Comparison between WT in solution and on the SLB. (a)** Mean contrast vs mass calibrations obtained from n = 3 standard MP measurements of WT (40 nM, $n_{monomer}$ = 832, $n_{dimer}$ = 2637, $n_{tetramer}$ = 2404 and $n_{hexamer}$ = 263 particles) and **(b)** from n = 6 independent 2 min dynamic MP movies (using only trajectories that lasted at least 20 frames) of 20 nM WT on an SLB ($n_{dimer}$ = 227, $n_{tetramer}$ = 1079, $n_{hexamer}$ = 2482 and $n_{octamer}$ = 311 trajectories) acquired on the same day. The error bars in (a) and (b) represent the mean ± s.d. of the contrast of each oligomeric species from the repeat measurements. In some cases the standard deviation was less than 1% causing the contrast error bars to overlap. **(c)** Oligomeric distribution of WT (100 nM) in HKS-100 buffer measured by standard MP (n = 4 combined measurements with a total of n = 16794 particles). The peaks represent WT monomer (0.5%), dimer (1.0%), tetramer (2.0%) and hexamer (3.0%). **(d)** Oligomeric distribution of 10 nM WT in HKS-100 buffer diffusing on an SLB obtained from n = 2 combined sets of 3 min dynamic MP movies considering only trajectories that lasted at least 50 frames (n = 1187 trajectories). The contrast measured in dynamic MP movies was consistently ~8% lower than that measured in standard MP. This effect is likely a result of particle motion during image acquisition, which results in motion blurring of the PSF (Supplementary Fig. 3 and Extended Data Fig. 3). This effect increased as we increased frame averaging in dynamic MP movies (Extended Data Fig. 4). The standard MP measurements were acquired at 331 Hz and then processed at a final integration time ~24 ms (effective frame rate ~41 Hz), which enabled the detection of WT monomer. *Peak due to background noise.

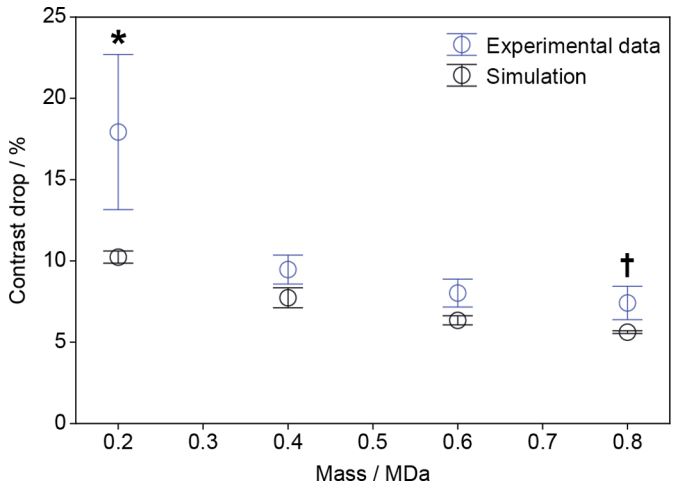


**Extended Data Fig. 3 | Contrast decrease in dynamic MP vs standard MP.** Drop in contrast of different WT oligomers (dimer, 0.2 MDa; tetramer, 0.4 MDa; hexamer, 0.6 MDa; octamer, 0.8 MDa) when comparing dynamic MP measurements to standard MP measurements (blue circles) and drop in contrast observed in simulated dynamic MP movies (Supplementary Fig. 3). For experimental data the contrast drop represents the mean reduction in the average contrast of each oligomeric species measured in n = 6 dynamic MP measurements (2 min each, considering only trajectories that lasted at least 20 frames resulting in a total of $n_{dimer} = 227$, $n_{tetramer} = 1079$, $n_{hexamer} = 2482$ and $n_{octamer} = 311$ trajectories) compared to the average contrast measured in n = 3 standard MP measurements (Supplementary Table 1, total of $n_{dimer} = 2637$, $n_{tetramer} = 2404$ and $n_{hexamer} = 263$ particles). For simulated data, the contrast drop represents the decrease in contrast of each species detected in n = 3 processed simulated movies compared to the contrast value that was used to simulate the point spread functions onto the raw images (1.00-4.00% for dimer-octamer, Supplementary Table 2, $n_{dimer} = 1780$, $n_{tetramer} = 2302$, $n_{hexamer} = 2618$ and $n_{octamer} = 2745$ trajectories). Data is presented as mean values ± s.d.. *In dynamic MP movies the contrast of dimer particles partially overlaps with that of background signal, which most likely causes underestimation of the dimer contrast and an exaggerated decrease in contrast compared to standard MP measurements. †WT octamer was not detected in standard MP measurement and the contrast was extrapolated using the contrast vs mass calibration.

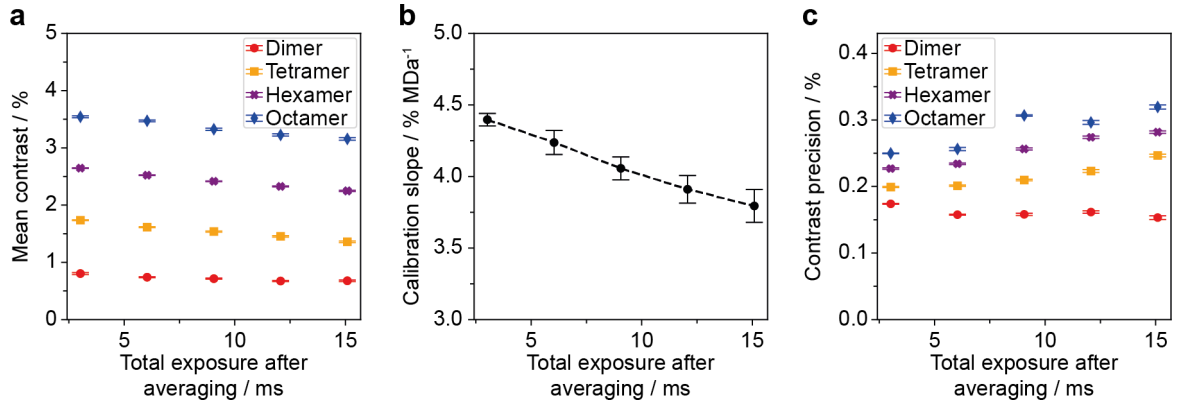


**Extended Data Fig. 4 | Effect of frame averaging on particle contrast. (a)** Mean contrast of WT dimer (red circles), tetramer (orange squares), hexamer (purple crosses) and octamer (blue diamonds) trajectories, **(b)** mean contrast vs mass calibration slope obtained from the dynamic MP movie in (a) vs single frame length after averaging and **(c)** contrast precision of our PSF-fitting procedure for each oligomer (same symbols as in (a)) all plotted vs total exposure time of 1 frame after averaging. These trends are most likely a result of particle motion during image acquisition, which becomes more pronounced as more raw images are averaged together and the frame length increases. The plots were obtained from the same movie of WT used in Figs. 1b-d and 2a (n = 1 movie (4 min) of 20 nM WT) with additional frame averaging of 1, 2, 3, 4 and 5 frames, which corresponds to frame lengths of 3.02, 6.04, 9.05, 12.07 and 15.09 ms or frame rates of 331, 166, 110, 83 and 66 Hz, respectively (see Supplementary Information). The data in (a) and (c) are presented as mean values ± s.e.m. for each oligomeric species. The data in (b) is presented as mean values ± s.d.. For these plots $n_{dimer}$ = 34, 51, 60, 52, 73, $n_{tetramer}$ = 82, 102, 98, 97, 94; $n_{hexamer}$ = 177, 229, 224, 208, 173; $n_{octamer}$ = 22, 29, 37, 38, 33 trajectories for total exposure times of 3.0, 6.0, 9.1, 12.1, 15.1 ms, respectively.

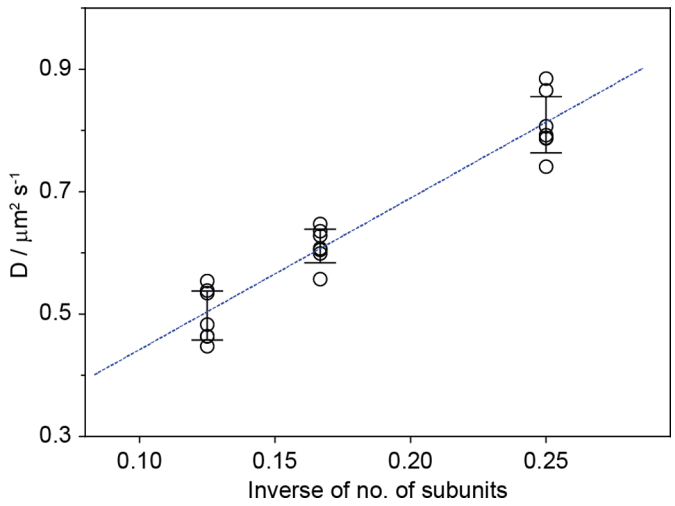


**Extended Data Fig. 5 | Diffusion coefficient vs inverse of number of subunits of WT oligomers.** Mean diffusion coefficients of each oligomeric species of WT from n = 7 independent repeat measurements ($n_{tetramer}$ = 498, $n_{hexamer}$ = 1326, $n_{octamer}$ = 156; data shown in Supplementary Fig. 6-7) vs the inverse of the number of subunits of each oligomeric species and a corresponding weighted linear fit (blue dashed line). Error bars are presented as mean values ± s.d..

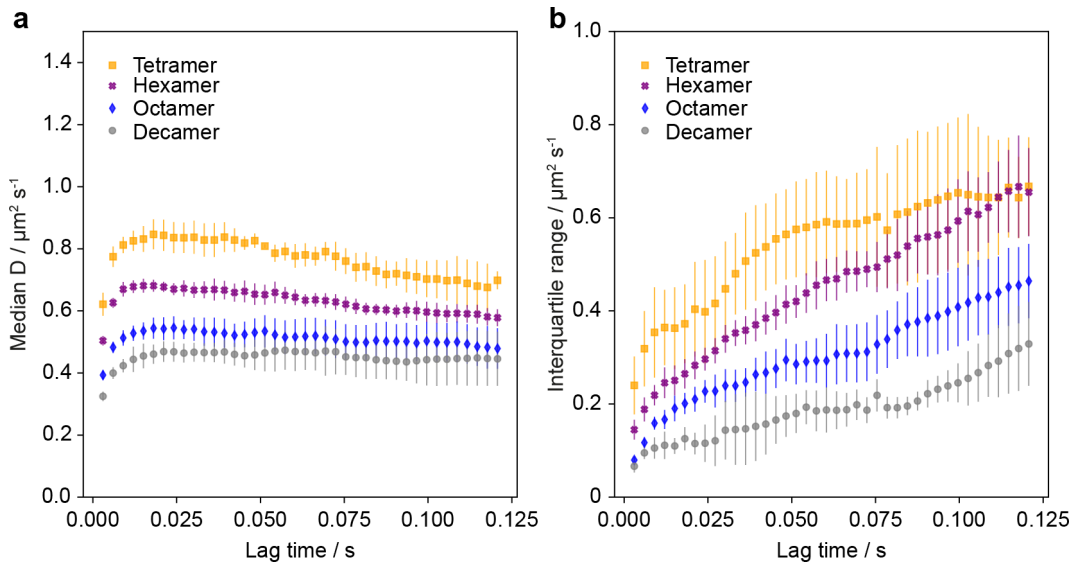


**Extended Data Fig. 6 | Effect of lag time on calculated diffusion coefficients. (a)** Average median diffusion coefficient and **(b)** corresponding interquartile range vs chosen lag time (*t*) for each oligomeric species from n = 4 independent ΔPRD measurements ($n_{tetramer}$ = 213, $n_{tetramer}$ = 937, $n_{hexamer}$ = 330, $n_{decamer}$ = 83; trajectories data shown in Supplementary Fig. 8-9). As the distribution of diffusion coefficients broadened significantly as the lag time increased, the diffusion coefficient of each oligomer was determined by taking the median of the distribution instead of Gaussian fitting. Each data point represents the mean diffusion coefficient from the median values determined from four repeats of ΔPRD measurements and the error bars are presented as mean values ± s.d..

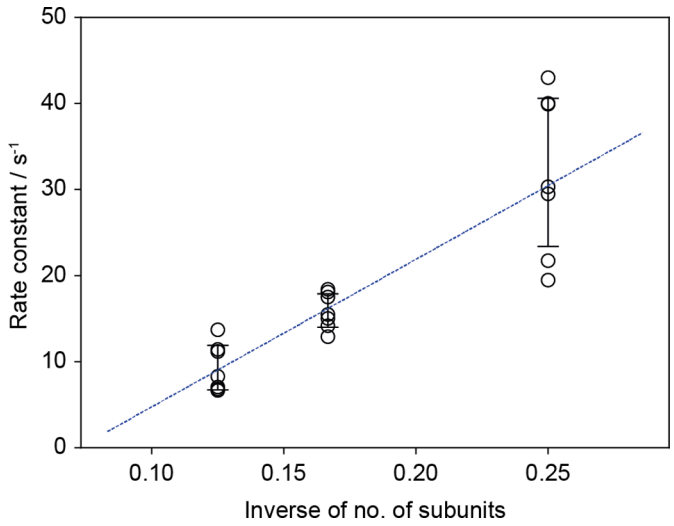


**Extended Data Fig. 7 | Dissociation constant vs inverse of number of subunits of WT oligomers.** Mean dissociation constant from the SLB of each oligomeric species of WT determined from n = 7 independent repeat measurements ($n_{tetramer}$ = 2263, $n_{hexamer}$ = 3264, $n_{octamer}$ = 203 trajectories; data shown in Supplementary Fig. 11) vs the inverse of the number of subunits of each oligomeric species and a corresponding weighted linear fit (blue dashed line). Error bars are presented as mean values ± s.d..

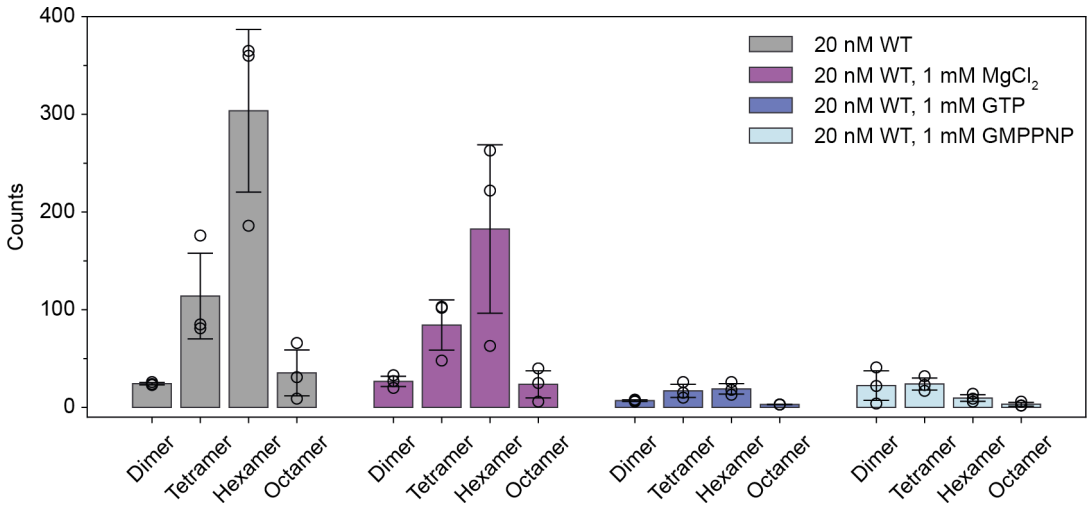


**Extended Data Fig. 8 | Effect of GTP and GMPPNP on the oligomeric distribution of WT.** Average oligomeric distribution of 20 nM WT in contact with an SLB in its apo-state, with 1 mM GTP, with 1 mM of GMPNP (non-hydrolysable GTP analogue) and with 1 mM $MgCl_2$ instead of 2 mM $MgCl_2$. The 1 mM $MgCl_2$ measurement was included as a control in case the presence of GTP/GMPNP results in a reduction in free $Mg^{2+}$, which could potentially affect the membrane affinity of WT dynamin oligomers. Each bar plot was generated by taking the mean oligomeric counts from n = 3 repeat measurements (1 min dynamic MP movie each). Error bars are presented as mean values ± s.d..

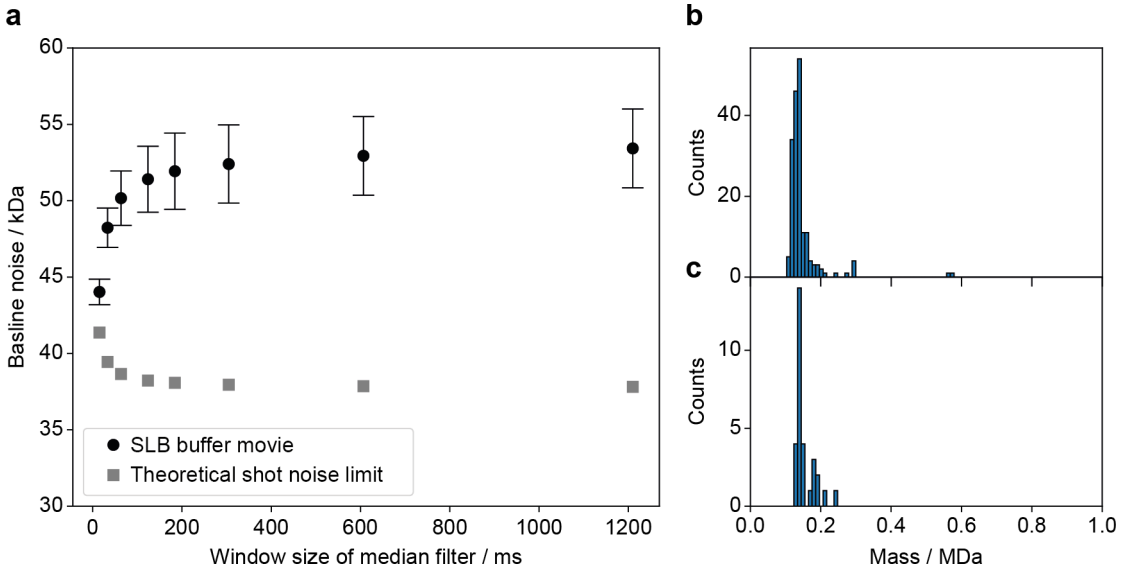


**Extended Data Fig. 9 | Analysis of background noise in dynamic MP movies. (a)** Mean baseline noise of the movie of HKS-100 buffer in contact with an SLB (black circles) shown in Supplementary Fig. 1 vs window size of the sliding median filter used to process the movie and the corresponding theoretical shot noise limit (grey squares). The error bars represent the mean baseline noise ± standard deviation across n = 4599 recorded frames. The inverse trend in baseline noise of the buffer movie compared to the theoretical shot noise is a result of particle-like background features in dynamic MP movies, which are subtracted out by the sliding median filter at short window sizes (for example 20-100 ms) but not at longer window sizes (> 200 ms). **(b-c)** Mass histogram of n = 182 and n = 30 trajectories, respectively, detected in a single SLB buffer movie processed with the same settings described in the Methods section, filtered for trajectories with a minimum length of 10 and 50 frames, respectively. The detected background features have contrasts corresponding to ~150 kDa, which prevented the detection of ΔPRD dimer and made reliable detection of WT dimer challenging.

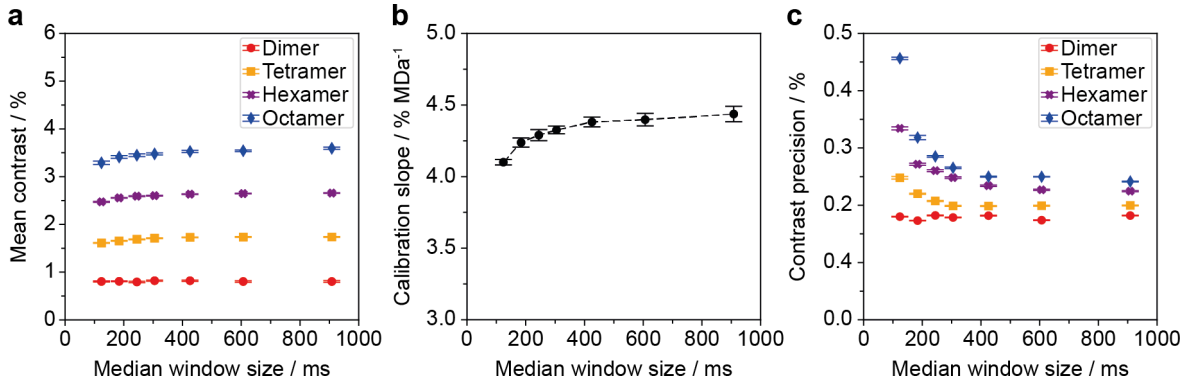


**Extended Data Fig. 10 | Effect of the window size of the sliding median filter on particle contrast. (a)** Mean contrast of WT dimer (red circles), tetramer (orange squares), hexamer (purple crosses) and octamer (blue diamonds) trajectories, **(b)** mean contrast vs mass calibration slope obtained from the dynamic MP movie in (a) vs single frame length after averaging and **(c)** contrast precision of our PSF-fitting procedure for each oligomer (same symbols as in (a)) all plotted vs total exposure time of 1 frame after averaging. The plots were obtained from the same movie of WT used in Figs. 1b-d and 2a (n = 1 movie (4 min) of 20 nM WT) with additional frame averaging of 1, 2, 3, 4 and 5 frames, which corresponds to frame lengths of 3.02, 6.04, 9.05, 12.07 and 15.09 ms or frame rates of 331, 166, 110, 83 and 66 Hz, respectively (see Supplementary Information). The data in (a) and (c) are presented as mean values ± s.e.m. for each oligomeric species. The data in (b) is presented as mean values ± s.d.. For these plots $n_{dimer}$ = 34, 51, 60, 52, 73, $N_{tetramer}$ = 82, 102, 98, 97, 94; $n_{hexamer}$ = 177, 229, 224, 208, 173; $n_{octamer}$ = 22, 29, 37, 38, 33 trajectories for total exposure times of 3.0, 6.0, 9.1, 12.1, 15.1 ms, respectively.

# Appendix B

# Supplementary Information for Chapter 4

This section includes the Supplementary Information of the publication Chapter 4 was adapted from: E.D.B. Foley, M.S. Kushwah, G. Young, P. Kukura, Mass photometry enables label-free tracking and mass measurement of single proteins on lipid bilayers, *Nature Methods*, 2021, **18**, 1247-1252.[120] Reprint permitted under the terms of the Creative Commons Attribution 4.0 International License. The publication including Supplementary Videos is also available online: https://doi.org/10.1038/s41592-021-01261-w.

nature portfolio

https://doi.org/10.1038/s41592-021-01261-w

## Supplementary information

# Mass photometry enables label-free tracking and mass measurement of single proteins on lipid bilayers

In the format provided by the authors and unedited

# Supplementary Information

# Mass photometry enables label-free tracking and mass measurement of single proteins on lipid bilayers

Eric D. B. Foley[#†], Manish S. Kushwah[#†], Gavin Young[†‡] and Philipp Kukura[†*]

[#]Equal contribution

[†]Physical and Theoretical Chemistry Laboratory, Department of Chemistry, University of Oxford, UK

[‡]Current address: Refeyn Ltd., Oxford, Oxfordshire, GB

*To whom correspondence should be addressed: philipp.kukura@chem.ox.ac.uk

# Contents

**Materials**

HEPES (H3375), KCl(P9541), Imidazole (I5513), DL-Dithiothreitol (DTT: D9779), Magnesium Chloride hexahydrate (M2670), Glycerol (G5516), Isopropyl-β-D-thiogalactoside (IPTG: I6758), Ampicillin (59349), Chloramphenicol (C0378), Protease inhibitor cocktail (4693159001; Roche), HiTrap®TALON® cobalt columns (GE28-9537-67), StrepTrap™ columns (GE28-9075-48), Grace Bio-Labs reusable CultureWell™ silicone gaskets (GBL103280), Chloroform (288306) and Desthiobiotin (71610-3) were purchased from Merck Life Science UK Limited. Glass coverslips (24x50 mm, Menzel Gläser, VWR 630-2603) were purchased from Thermo Fisher Scientific. 1,2-dioleoyl-sn-glycero-3-phosphocholine (DOPC; 850375P) and 1,2-dioleoyl-sn-glycero-3-phospho-L-serine (sodium salt) (DOPS; 840035P) were purchased from Avanti Polar Lipids. GTP (NU-1012) and GppNHp - Tetralithium salt (GMPPNP) (NU-401) were purchased from Jena Biosciences. BL21-CodonPlus and Terrific Broth were purchased from Agilent Technologies and Fisher Scientific, respectively. The ultrasonicator and plasma cleaner are from Sonics & Materials, Inc. and Diener electronic, respectively. The Dynamin1 wild type (WT) bacterial expression vector[1,2] was generously provided by Prof. Thomas Pucadyil (IISER Pune, India). ΔPRD ($Dyn1_{1-746}$) was generated in the lab using standard cloning procedures and confirmed using DNA sequencing.

HEPES, KCl, $MgCl_2$, and Imidazole, stocks were prepared in Milli-Q® water (18.2 MΩ·cm) (Milli-Q) and filtered using a 0.2 μm filters. Ampicillin, IPTG and DTT were prepared in degassed Milli-Q, aliquoted and stored at -20°C. GMPPNP (50 mM) was dissolved in degassed 20 mM HEPES (pH = 7.4). GTP solution and GMPPNP stocks were aliquoted and stored at -20°C. DOPC (25 mM) and DOPS (10 mM) stocks were prepared using chloroform and aliquoted and stored at -20°C under nitrogen.

**Buffer preparation**

Due to its label-free nature, dynamic mass photometry (MP) is sensitive to impurities originating from stock solutions used to prepare buffers, which can integrate into the SLBs and cause defects or additional background noise. Therefore, buffer stocks were prepared carefully. HEPES (1 M, pH = 7.7), KCl (3 M) and $MgCl_2$ (1 M) stocks were prepared in degassed Milli-Q water and filtered twice (0.2 μm, VWR international, 514-600) and stored at 4°C until use. Buffers were reconstituted form the stock solutions immediately before dynamic MP experiments with degassed Milli-Q water, and replaced every 2-3 hours to decrease the influence of reactive oxygen species during dynamic MP measurements.

**Protein expression and purification**

Bacterial expression vectors for WT and ΔPRD were transformed in BL21-CodonPlus and grown until $OD_{600}$ = 0.6 in Terrific Broth containing ampicillin (100 μg $ml^{-1}$) at 37°C. Protein production was induced with 0.1 mM IPTG, and bacterial cultures were grown for 12 hours at 18°C. Cells were harvested, and bacterial pellets were stored at -80°C. For purification, bacterial pellets were thawed on ice and dissolved in lysis buffer (20 mM HEPES, pH = 7.4, 300 mM KCl and 20 mM Imidazole) containing one tablet of protease inhibitor cocktail. Cells were lysed using a cell homogenizer, and lysate was spun at 20,000 g for 20 min at 4°C to remove insoluble cell debris. The supernatant was applied to a 5 ml HiTrap®TALON® column. The column was washed with 60 ml lysis buffer, followed by 60 ml wash buffer (20 mM HEPES, pH = 7.4, 150 mM KCl and 20 mM Imidazole). The protein was eluted with elution buffer (20 mM HEPES, pH = 8, 150 mM KCl, 200 mM Imidazole) and eluted protein was applied to a 5 ml StrepTrap™ column, which was pre-equilibrated with elution buffer, at 2 ml $min^{-1}$. The column was washed sequentially with 50 ml strep-1 buffer (20 mM HEPES, pH = 7.4, 300 mM KCl), 50 ml strep-2 buffer (20 mM HEPES, pH = 7.4, 300 mM KCl, 1 mM DTT) and 50 ml strep-3 buffer (20 mM HEPES, pH = 7.4, 150 mM KCl, 1 mM DTT). The protein was eluted with strep-elution buffer (20 mM HEPES, pH = 7.4, 150 mM KCl, 1mm DTT, 10% glycerol, 2.5 mM Desthiobiotin), flash frozen and stored at -80°C until use.

To prepare the protein for dynamic MP experiments, WT or ΔPRD were dialysed overnight at 4°C in degassed HKS-150 buffer (20 mM HEPES, pH = 7.4, 150 mM KCl) containing 1 mM DTT. After dialysis, the protein was spun at 20,000 g for 30 minutes at 4°C to remove aggregates. The supernatant was collected, and the concentration was estimated by measuring absorbance at $OD_{280}$ nm ($\varepsilon_{280}$ = 62,800 $M^{-1}$ $cm^{-1}$ and 54,300 $M^{-1}$ $cm^{-1}$ for WT and ΔPRD, respectively). Proteins were stored on ice during use. We determined that the protein stocks contained no misfolded or aggregated proteins by performing standard MP and dynamic MP measurements on protein samples that had been centrifuged at 20,000 g and 100,000 g (Supplementary Figure 13). Additionally, we purified our ΔPRD stock by size exclusion chromatography and again found no evidence of aggregation (Supplementary Fig. 14). Finally, the increase in membrane contact, with simultaneous decrease in diffusion coefficient and increase in membrane affinity as a function of increasing dynamin oligomerisation (Fig. 2b, d) also suggests that oligomers observed in our study are fully-folded, membrane-active oligomers.

**Size-exclusion chromatography and mass photometry measurements.**

Dynamin1-ΔPRD (13 µM; 1 ml) was thawed from -80°C (stored in 20 mM HEPES, pH = 7.4, 150 mM KCl, 10% glycerol, 1 mM DTT and 2.5 mM desthiobiotin) and applied to a Superdex 16/600 200 column which was equilibrated with degassed HKS-150 (20 mM HEPES, pH = 7.4, 150 mM KCl). 1 ml fractions were collected at 1 ml/min and 1 mM DTT was added to all fractions. The concentration of each fraction was measured using absorbance at $OD_{280}$ nm and 20 µl from each fraction was assessed by SDS-PAGE. All fractions were stored on ice until MP measurements. For standard MP measurements, each fraction was either diluted to 200 nM using HKS-150 supplemented with 1 mM $MgCl_2$ and 1 mM DTT or measured without any dilution (low protein concentration elutions). Diluted samples, were incubated for one minute at RT prior to measurement and for undiluted samples 200 µl of the elution was incubated at RT for 5 minutes and repeat measurements were taken from the 200 µl stock.

**Additional frame averaging and PSF fitting error of particle locations**

For every successful PSF-fitting operation, the error of the fit in x and y was estimated from the covariance of the parameters of the fit. To determine the mean fitting errors in 2 dimensions for each oligomeric species of WT, we examined the data shown in Fig. 1b-c at different effective imaging speeds by averaging together increasing numbers of consecutive frames (2, 3, 4 and 5, resulting in effective frame rates of 166 Hz, 100 Hz, 83 Hz and 66 Hz) of the dynamic MP movie after treatment with the sliding median filter. Trajectories were linked and filtered as described in the Methods section (with incrementally increasing offsets from 0.0015-0.0023 for frame rates from 331 Hz to 66 Hz). The median PSF fitting error in x and y was then determined for each trajectory that passed the filtering steps and a Gaussian was fit to the resulting distribution of median x and y errors of each oligomeric species to extract the mean localisation error and standard deviation. The fitting errors in 2D particle positions displayed in Fig. 1d were calculated from the means of these Gaussian fits. We note that this provides a lower bound on the localisation precision of dynamic MP at our operating frame rate. Trajectory linking parameters were adjusted for decreased effective frame rates (max search distance of 4, 6, 6, 7 and 8, and memory of 3, 2, 2, 1 and 1 for 331 Hz, 166 Hz, 100 Hz, 83 Hz and 66Hz, respectively).

**Trajectory filtering for residence time and GTP analysis**

*Residence time analysis*

To calculate the dissociation rate constants from the SLB of each oligomeric species, we slightly modified the trajectory filtering procedure described in the Methods section to limit the impact of background noise on measured trajectory lengths. First, we constructed spatial maps of the probability density of detected particle locations (scipy.stats.gaussian_kde) across the field of view for each movie to identify regions that showed anomalously high particle densities (probability density ≥ 0.008, often a sign of improperly bound or immobile particles). Trajectories that contained less than ten points (>33 ms in length) outside of these identified regions were discarded. Due to the reduced number of trajectory points in this analysis (≥ 10 points instead of ≥ 50 points), we determined the contrast of each trajectory by taking the median of all its contrast measurements instead of Gaussian fitting as described in the Methods section. Trajectories were then filtered using the interquartile range of their contrast in a similar way as described above (offset = 0.0025, Supplementary Fig. 17a-b). Additionally, trajectories that had coordinates within 5 pixels of the edge of the field of view or contained any gaps were discarded to ensure that trajectory lengths were as accurate as possible.

*Analysis of the effect of GTP and GMPPNP on the oligomeric distribution of dynamin*

For the analysis of the effect of GTP on the mass distribution of WT on the SLB (Fig. 2g, Extended Data Fig. 8) the trajectories were filtered as described in the residence time analysis section, except that a minimum trajectory length threshold of 20 instead of 10 frames was applied to limit the effect of transient background fluctuations on the count of dimeric particles. Additionally, trajectories containing gaps were not discarded. Mass histograms were plotted for the movie recorded immediately before GTP was added (last 1 min of acquisition before GTP addition) and the first movie recorded immediately after GTP addition (first minute of acquisition after addition). Trajectories were allocated to a particular oligomeric species if their mass, was within two standard deviations of the mean mass of that oligomer, which was determined from the entire set of 1 min movies up to GTP addition in each case by Gaussian fitting (Supplementary Fig. 6b-f). This procedure was used for five replicate measurements of WT-dynamin (10-20 nM to achieve satisfactory particle density) with GTP addition (1 mM) after 3-4 min of acquisition (Supplementary Fig. 12). We used the same approach for the data shown in Extended Data Fig. 8, except that GTP or GMPPNP were added together with WT at the beginning of the measurement rather than after a few minutes of data acquisition

**Simulation of dynamic MP movies**

The graphs in Supplementary Fig. 3 and Extended Data Fig. 3 were obtained from a set of simulated dynamic MP movies, which were generated by simulating PSFs onto raw images of HKS-100 buffer in contact with an SLB (20,000 frames recorded at 331 Hz for) and then processing the resulting images with the sliding median filter (window size = 201 frames, 607 ms). To simulate PSFs, we used the model described in Equation 2 ($a_1/a_2$ = -5.4315762370*,* $w_1$ = *2.1800050329*, $\sigma$ = 5.0012142342). This PSF model was scaled appropriately to obtain contrasts representative of WT dimer, tetramer, hexamer and octamer (1.0, 2.0, 3.0 and 4.0%, respectively). Diffusion and motion blur were simulated by moving the PSFs incrementally in x and y every 0.2 ms (or exactly between every frame for simulations without motion blur) by sampling x and y step sizes from a Gaussian distribution centred around 0 and with a standard deviation of 2Dt, where D is the diffusion coefficient of the corresponding WT species (Extended Data Fig. 5, Supplementary Table 4) and t the lag time (0.2 ms for motion blur and 3.0 ms in the absence of motion blur). Trajectory lengths were determined by sampling from an exponential distribution with a rate constant of 20 $s^{-1}$ and each oligomeric species was assigned an equal probability of appearing on the SLB. The resulting movies were analysed as described in the residence time analysis section but without spatial filtering for high particle density regions.

## Supplementary Figure 1

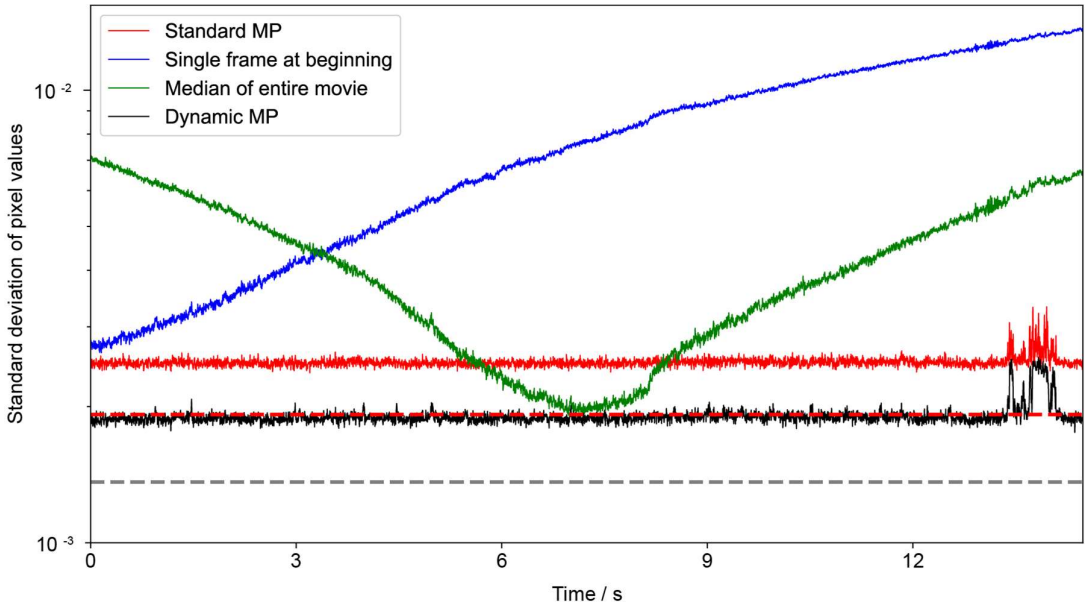


**Effect of background subtraction on baseline noise**

The baseline noise (the standard deviation of all pixel values in a given frame) of a dynamic MP movie of buffer solution on an SLB obtained with the background subtraction used in standard MP (red line), by subtracting the initial frame from all frames (blue line), subtracting the median of the entire movie from all frames (green line) and using the sliding median filter used for the dynamic MP experiments in this work (black line). The grey dashed line shows the theoretical shot noise limit when using the sliding median filter. The theoretical shot noise limit when using standard MP background subtraction (red dashed line) overlaps with the sliding median baseline noise (~0.002). The sliding median background subtraction results in lower background noise because the background is calculated from 200 additional frames compared to the background subtraction used in standard MP. Occasional spikes in background noise appear due to larger particles diffusing across the field of view.

## Supplementary Figure 2

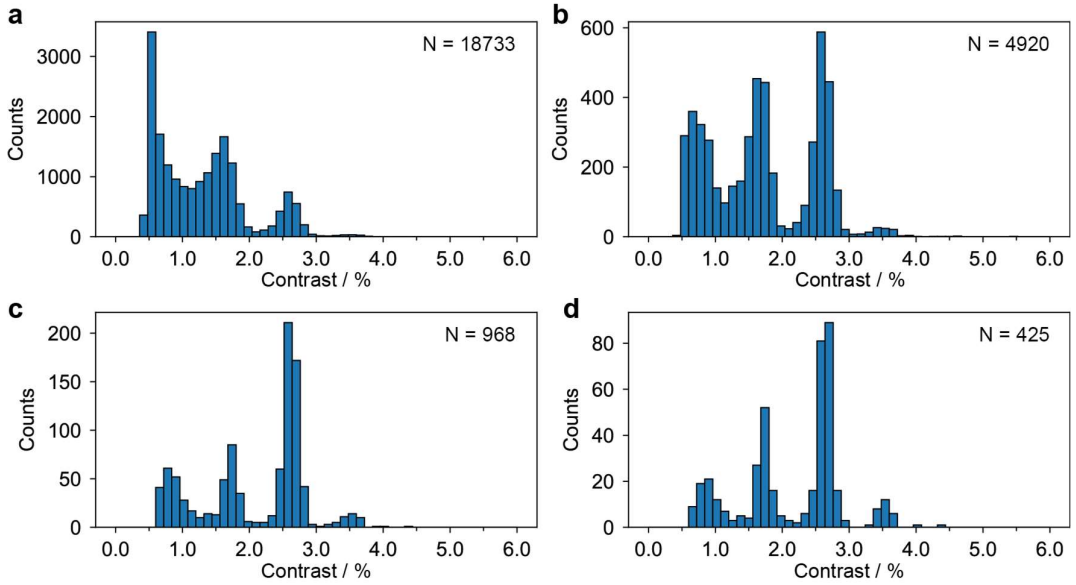


**Effect of filtering particle trajectories by their SLB residence times**

**(a)-(d)** Contrast histograms (bin width = 0.12%) obtained from the same dynamic MP movie of WT used in Fig. 1b-d and 2a after applying a minimum threshold of 5, 10, 30 and 50 frames (331 Hz) to the trajectory length, respectively. Particle trajectories that remained on the membrane for fewer frames than the specified threshold were discarded. Here, each data point corresponds to the median contrast of a trajectory. This length filtering procedure effectively improves the quality of the data and reduces background features that were incorrectly identified as particles and linked into short trajectories, resulting in an increase in contrast resolution.

## Supplementary Figure 3

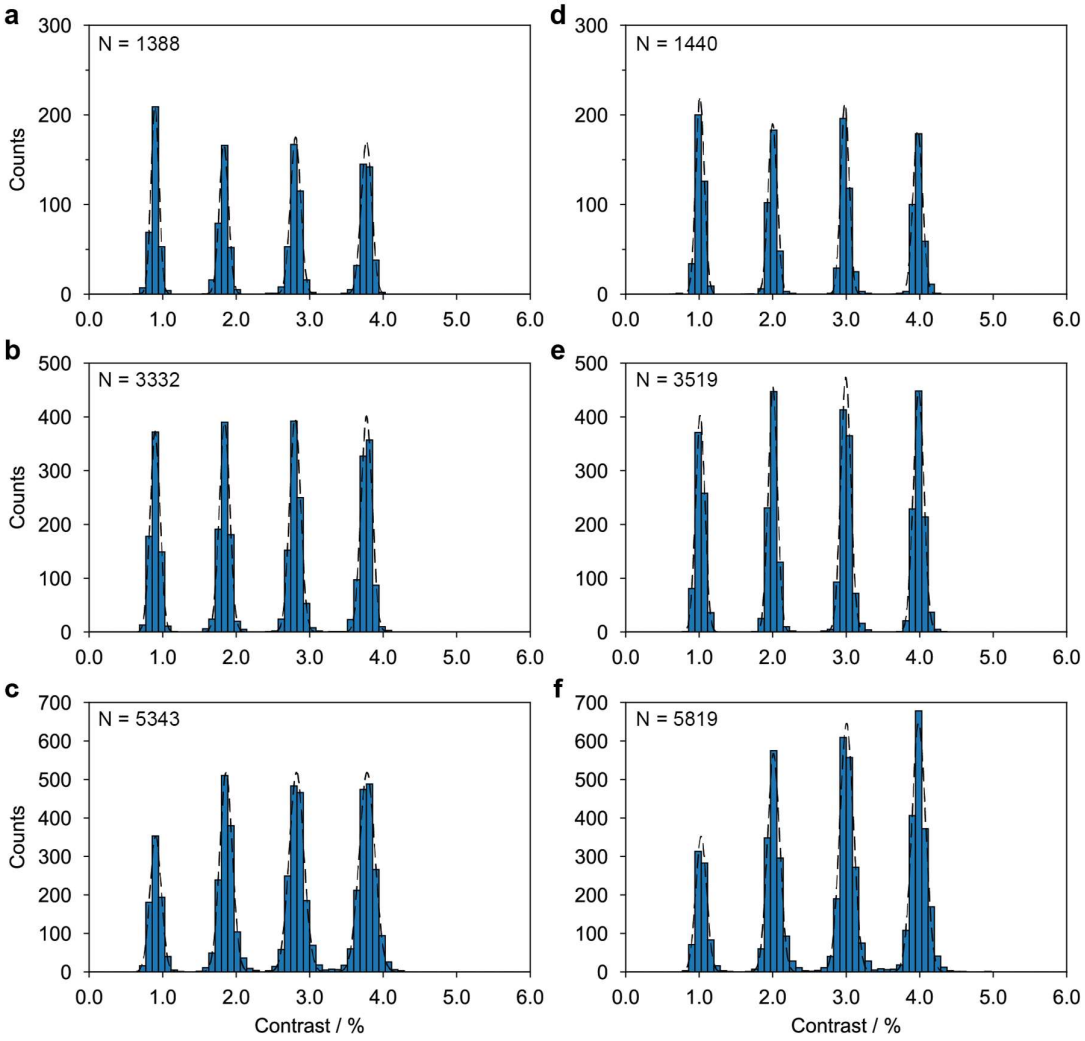


**Simulated effect of motion blur and particle density on particle contrast in dynamic MP**

**(a)-(c)** Contrast histograms generated from a movie of HKS-100 buffer in contact with a supported lipid bilayer (331 Hz) with point spread functions with contrasts of 1.0-4.0% roughly corresponding to WT dimer, tetramer, hexamer and octamer simulated with motion blur onto the raw images with mean particle densities of 0.13, 0.30 and 0.79 $\mu m^{-2}$, respectively. Motion blur was simulated by allowing the PSFs to move every 0.2 ms (~15 times in each image) based on the diffusion components measured for each species in dynamic MP experiments and each oligomeric species was assigned the same probability of appearing in the movie and the same membrane affinity (see methods) **(d)-(f)** Contrast histograms of dynamic MP movies with simulated PSFs generated in the same way as in (a)-(c) but without motion blur, *i.e.* particle movement occurred exactly in between acquired images. We note that at the highest particle density (c, f) there is a bias in the detection algorithm towards larger species and peak widths are larger than at lower particle densities. The increase in peak widths may be a consequence of the sliding median filter or decreased precision in particle fitting due to an increased amount of overlapping PSFs or simply due to less precise PSF fitting due to more crowded images. The dynamic MP experiments in this study exhibited particle densities around 0.3-0.5 $\mu m^{-2}$, *i.e.* similar to those in (b) and (e). Only trajectories that lasted at least 10 frames were used to generate this figure and the mean contrast and standard deviation for each species in these histograms are supplied in Supplementary Table 2. Black dashed lines represent Gaussian fits to the contrast histograms.

## Supplementary Figure 4

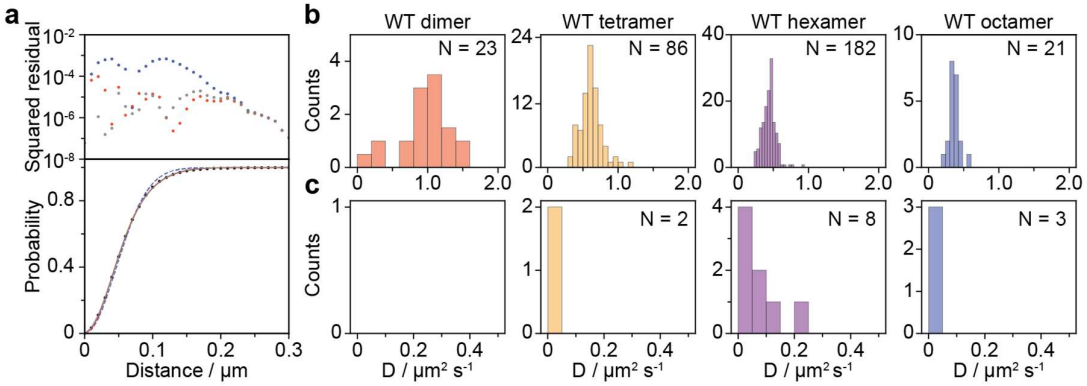


**Extraction of diffusion coefficients from trajectories**

**(a)** 1-(blue), 2-(red) and 3-(gray) component fits to the cumulative probability density of the distance moved during one frame (3 ms) by the particle shown in Fig. 1e-g (N = 6033 measurements of 1-frame displacements). **(b)** Distributions of the major diffusion component of WT dimer (red), tetramer (orange), hexamer (purple) and octamer (blue) particles for the same data used in Fig. 1b-d and 2a (n = 1, 4 min movie of the same sample). **(c)** Same as **(b)** for the minor diffusion component (if present). The vast majority of particles only exhibited one diffusion component (Supplementary Fig. 5).

## Supplementary Figure 5

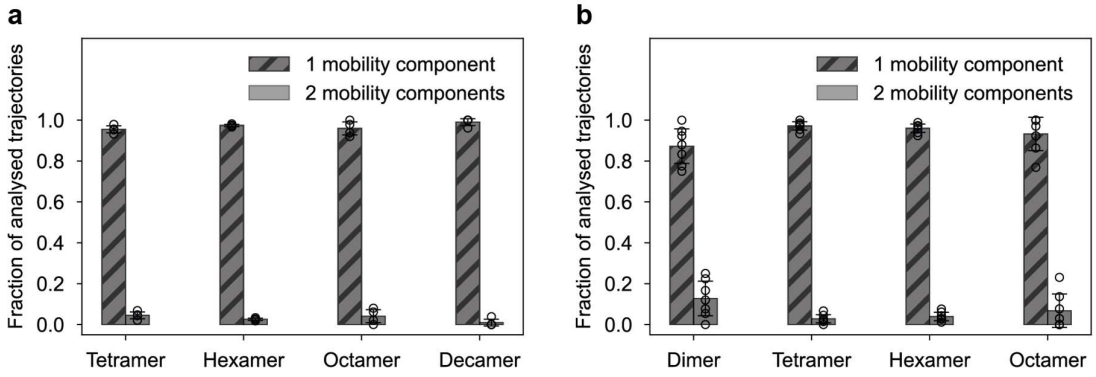


**Distribution of mobility components**

Mean fractions of one- and two-component diffusion of each oligomeric species of ΔPRD (n = 4 independent measurements with a total of $N_{tetramer}$ = 214, $N_{hexamer}$ = 937, $N_{octamer}$ = 330, $N_{decamer}$ = 83) **(a)** and of WT (n = 7 independent measurements with a total of $N_{dimer}$ = 197, $N_{tetramer}$ = 501, $N_{hexamer}$ = 1326, $N_{octamer}$ = 156) **(b)** based on fits to the cumulative probability density function of particle displacement with a lag time of 12 ms (see methods). Only trajectories that lasted at least 50 frames were considered for this plot. The contrast of WT dimer overlaps with the contrast of background features, which is most likely why it shows increased two-component diffusion compared to the other species. Due to its lower contrast, the ΔPRD dimer could not be detected and is thus not included in this plot. Error bars are presented as mean values ± standard deviation.

## Supplementary Figure 6

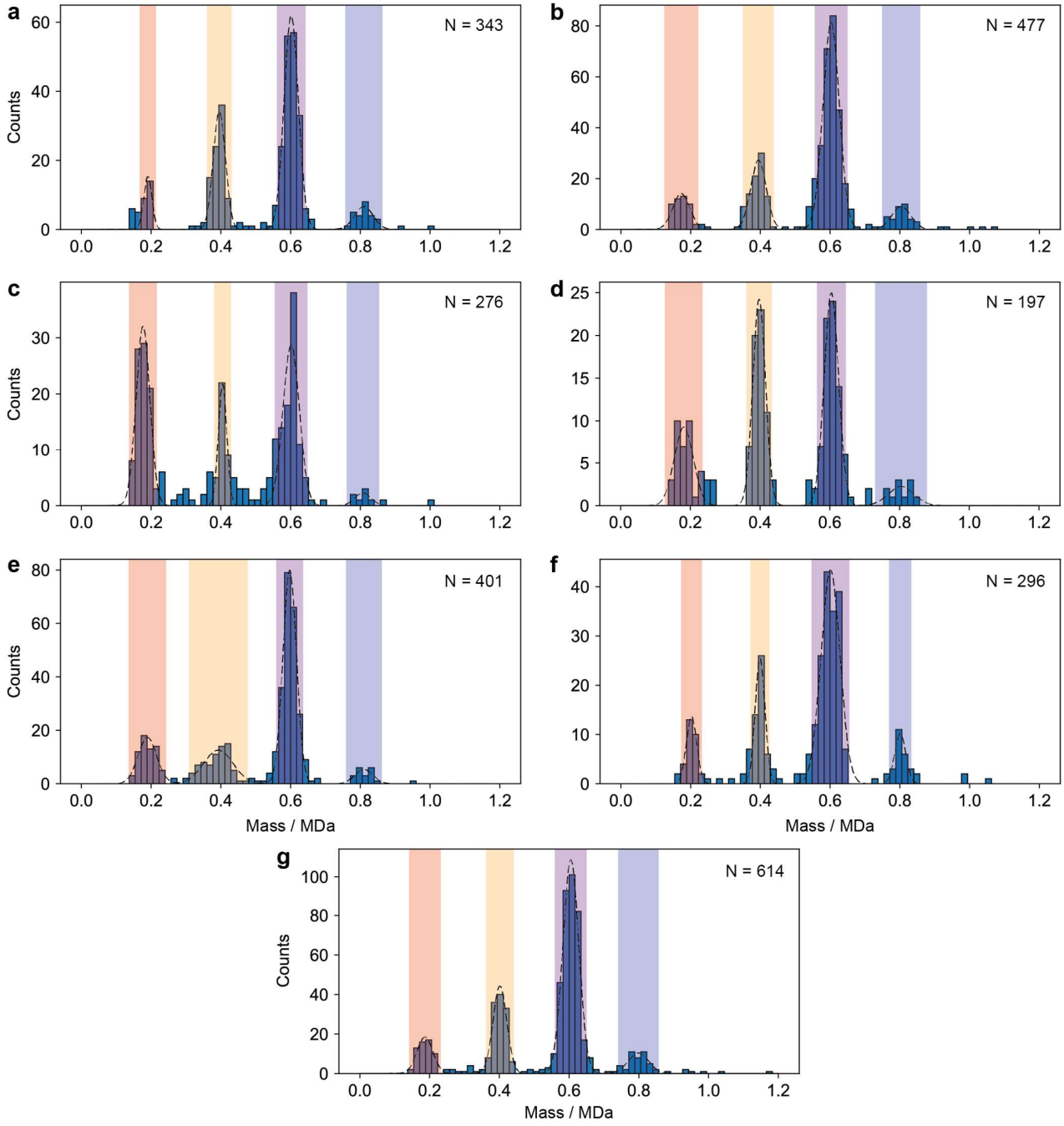


**Mass distribution of WT**

**(a-g)** Mass histograms obtained from seven repeats of dynamic MP measurements (4-5 min each) of WT (10-20 nM) in contact with an SLB. Each data point in the histograms represents the mean contrast of a trajectory as determined by Gaussian fitting, as described in the methods section. The black dashed lines represent Gaussian fits to the oligomeric peaks of WT. If a trajectory's mean contrast was within two standard deviations of the mean of these Gaussian fits, it was classified as that particular oligomeric species (red = dimer, orange = tetramer, purple = hexamer, blue = octamer). The number of bin width for all mass histograms was set to 0.017 MDa (70 bins) and the same initial guess for Gaussian fitting was used in each case. The dimer trajectories often overlapped in mass with background features (see also Extended Data Fig. 10b-c) and were thus difficult to distinguish from background noise.

## Supplementary Figure 7

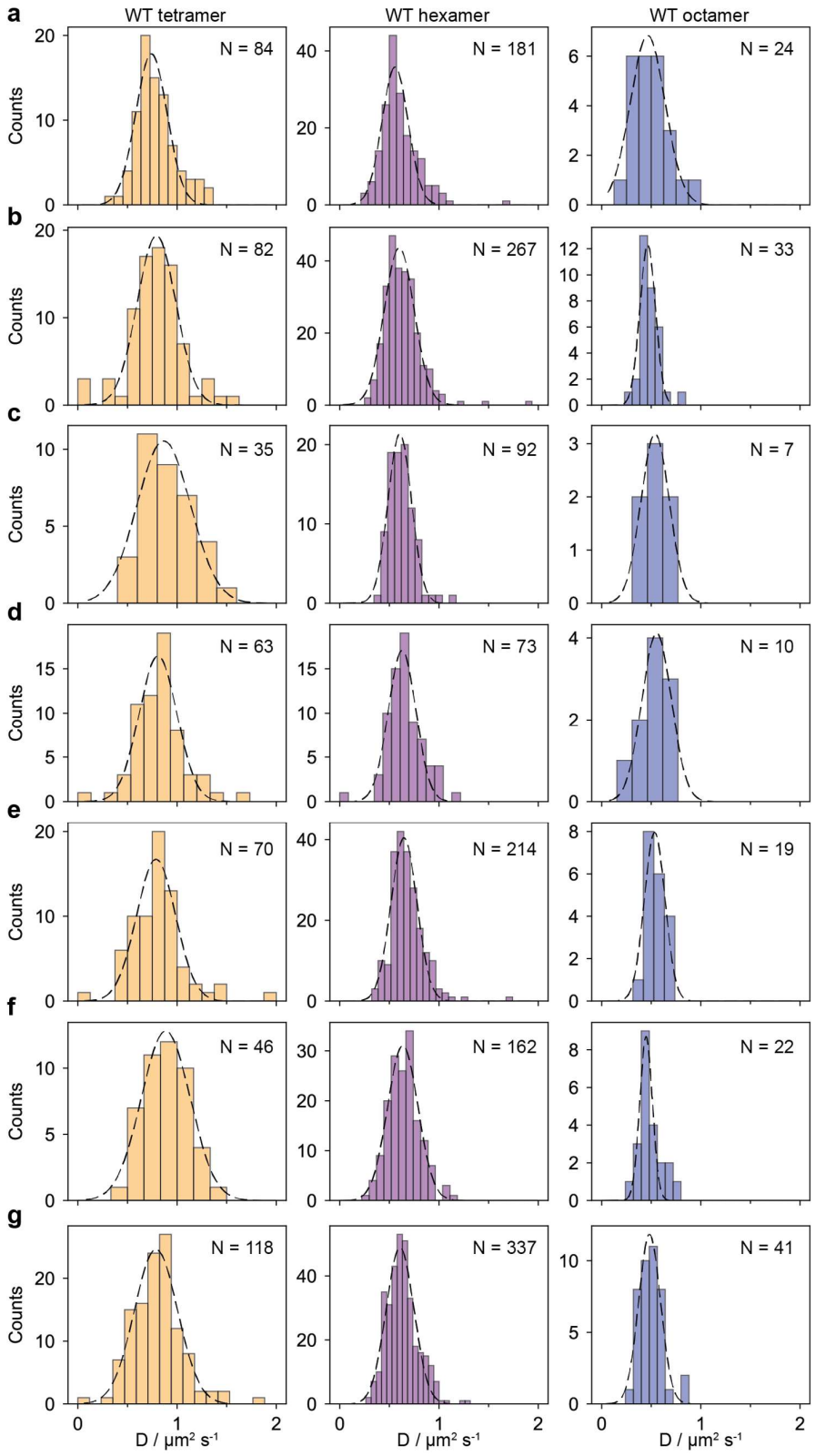


**Distributions of diffusion coefficients of WT oligomers**

**(a-g)** Diffusion coefficients calculated as described in the methods section for each oligomeric species (tetramer = orange, hexamer = purple, octamer = blue) detected in the WT measurements shown in Supplementary Fig. 6. The mean diffusion coefficients were determined by Gaussian fitting to these histograms (black dashed line). The number of bins in each histogram was chosen using the Freedman-Diaconis rule.

## Supplementary Figure 8

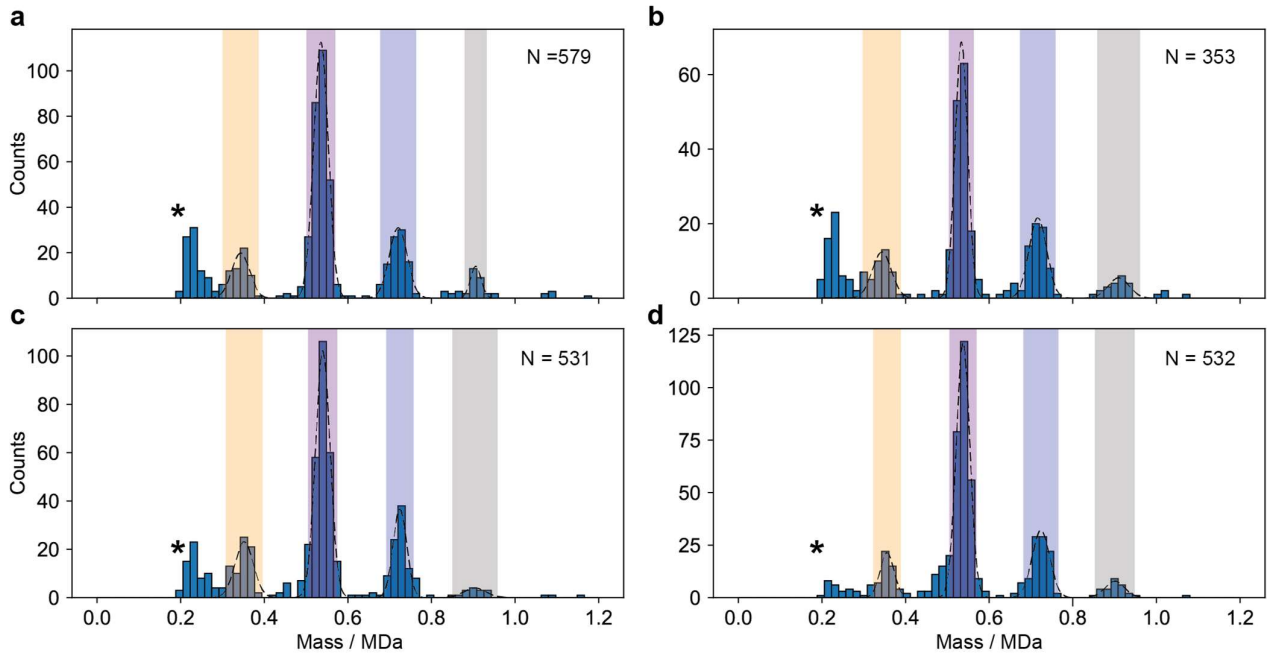


**Mass distribution of ΔPRD**

**(a-d)** Mass histograms obtained from four repeats of dynamic MP measurements (4-5 min each) of ΔPRD (10-20 nM) in contact with an SLB. Each data point in the histograms represents the mean contrast of a trajectory as determined by Gaussian fitting, as described in the methods section. The black dashed lines represent Gaussian fits to the oligomeric peaks of ΔPRD. If a trajectory's mean contrast fell within two standard deviations of the mean of these Gaussian fits, it was classified as that particular oligomeric species (orange = tetramer, purple = hexamer, blue = octamer, grey = decamer). The bin width in all histograms was set to 0.016 MDa and the same initial guess for Gaussian fitting was used in each case. *Detected events due to background noise representing the limit of detection in these measurements. As such, the ΔPRD dimer (180 kDa) could not be reliably detected.

## Supplementary Figure 9

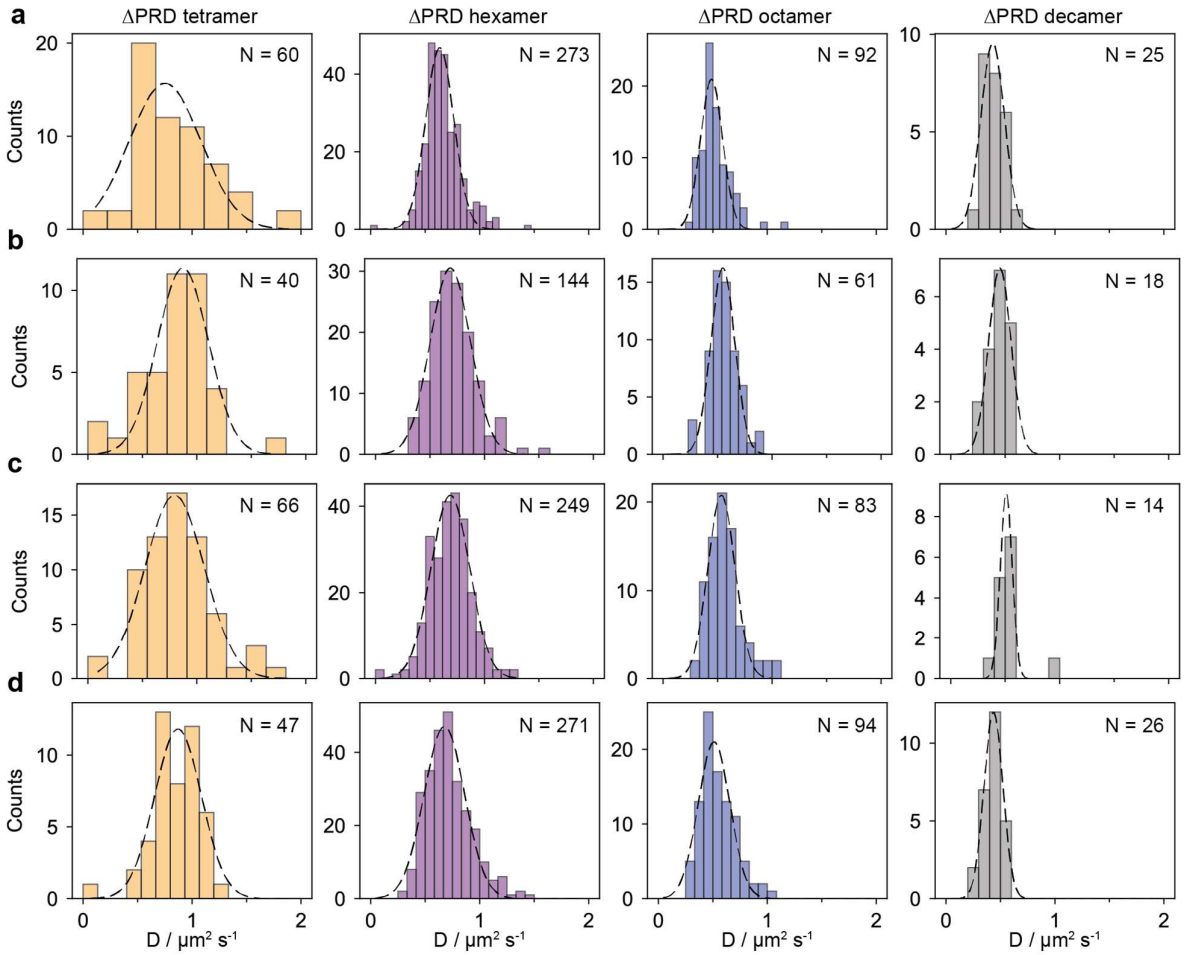


**Distribution of diffusion coefficients of ΔPRD oligomers**

**(a-d)** Diffusion coefficients calculated as described in the methods section for each oligomeric species (tetramer = orange, hexamer = purple, octamer = blue, decamer = gray) of the ΔPRD measurements shown in Supplementary Fig. 8. The mean diffusion coefficients were determined by Gaussian fitting (black dashed line) to the histograms. The number of bins in each histogram was chosen using the Freedman-Diaconis rule.

## Supplementary Figure 10

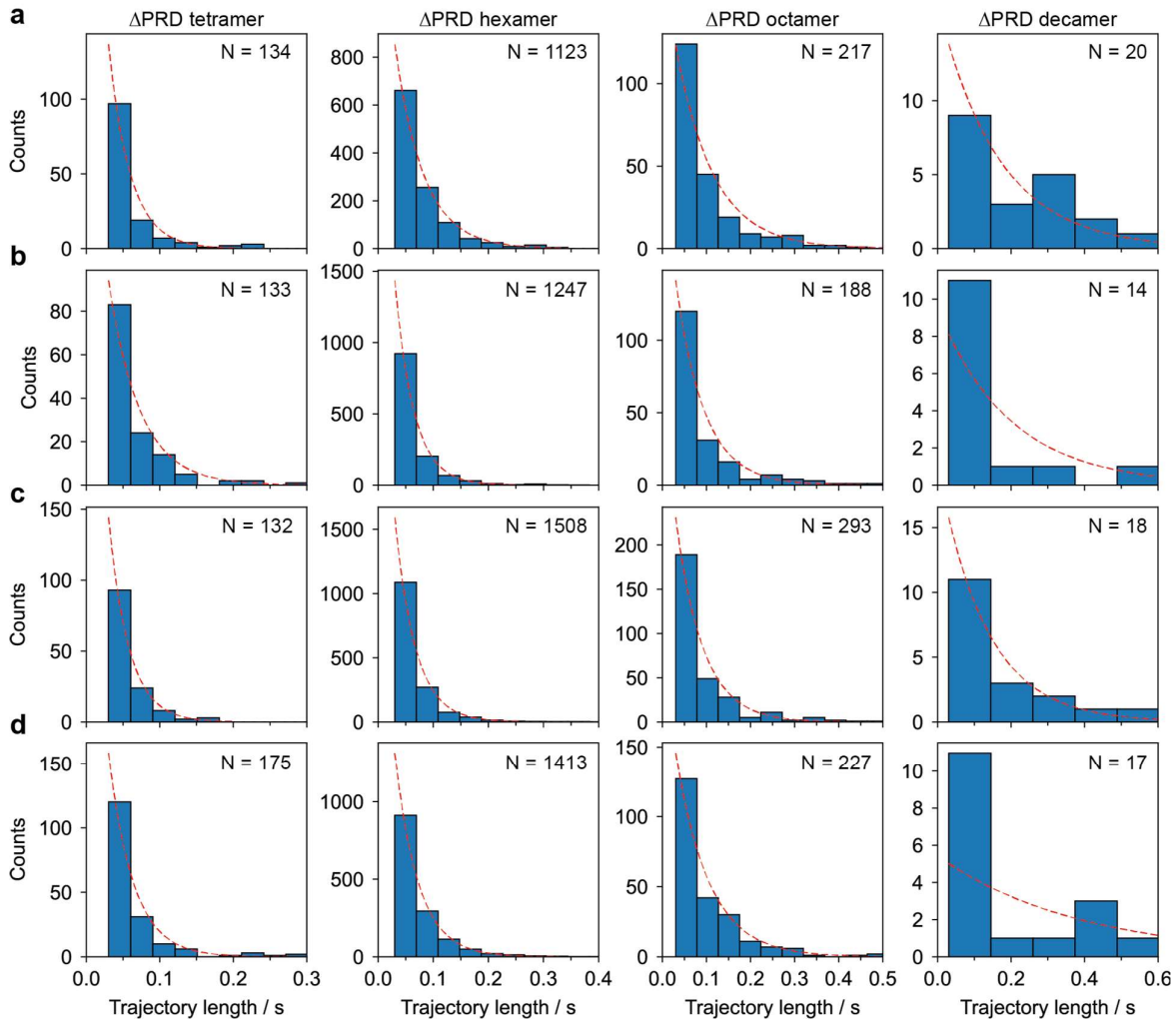


**Distribution of trajectory residence times of ΔPRD oligomers on the SLB**

**(a)-(d)** Histograms of counts vs trajectory lengths for each oligomeric species detected in the four repeats of ΔPRD measurements shown in Supplementary Fig. 8. Dissociation rate constants for unbinding from the SLB were calculated by maximum likelihood estimation using the unbinned data (see methods) and the resulting exponential distributions are plotted as red-dashed lines (appropriately scaled for display). The number of decamer trajectories (right column) was small in comparison to the other oligomeric species and thus sometimes resulted in poor fits. Only trajectories that lasted at least 10 frames and contained no gaps were considered.

## Supplementary Figure 11

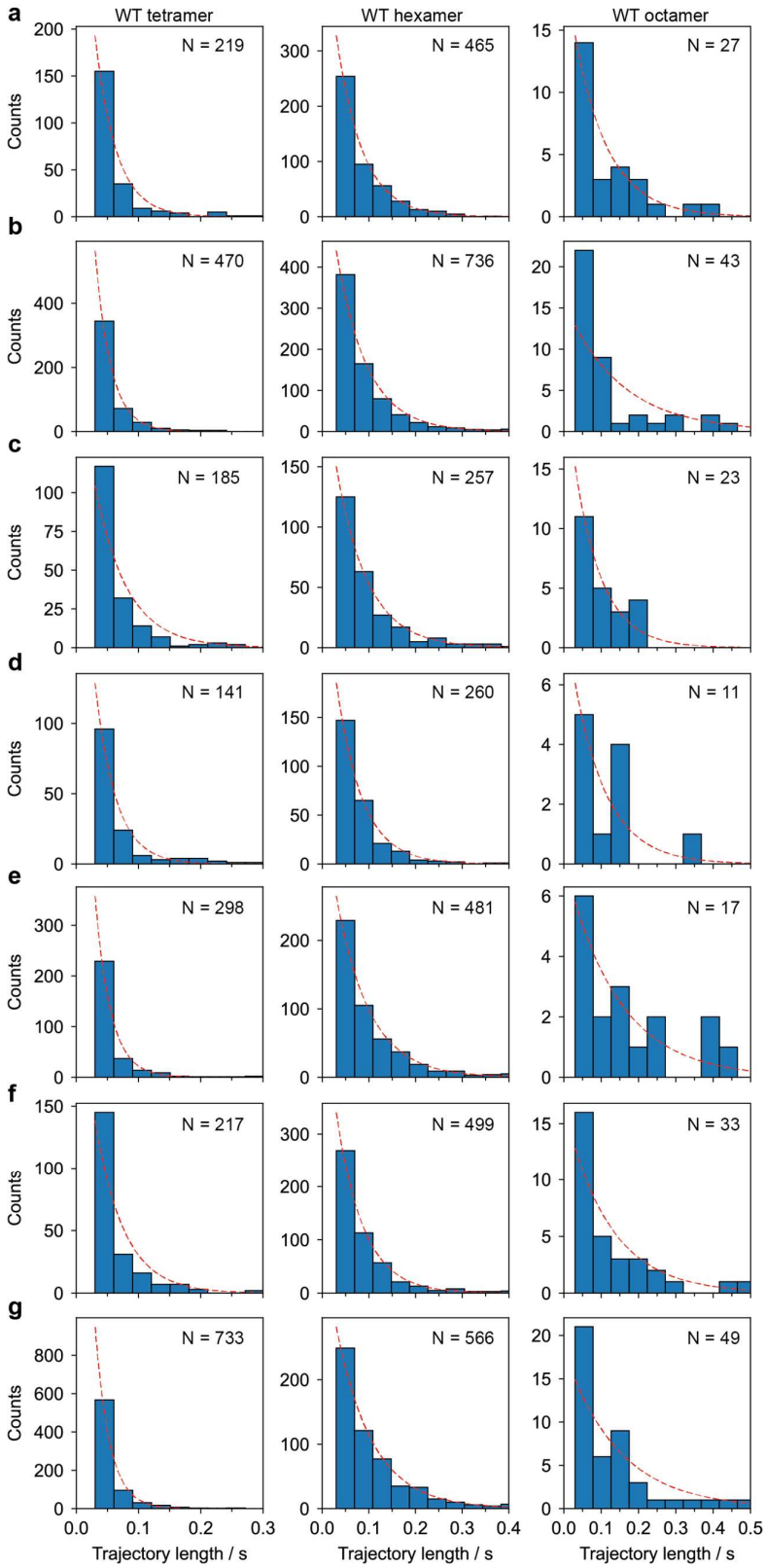


**Distribution of trajectory residence times of WT oligomers on the SLB**

**(a)-(d)** Counts vs trajectory length for each oligomeric species detected in the 7 replicate measurements of WT shown in Supplementary Fig. 6. Dissociation rate constants for unbinding from the SLB were calculated by maximum likelihood estimation using the unbinned data (see methods) and the resulting exponential distributions are plotted as red-dashed lines (appropriately scaled for display). The number of octamer trajectories (right column) was small in comparison to the other oligomeric species and thus sometimes resulted in poor fits. Only trajectories that lasted at least 10 frames and contained no gaps were considered.

## Supplementary Figure 12

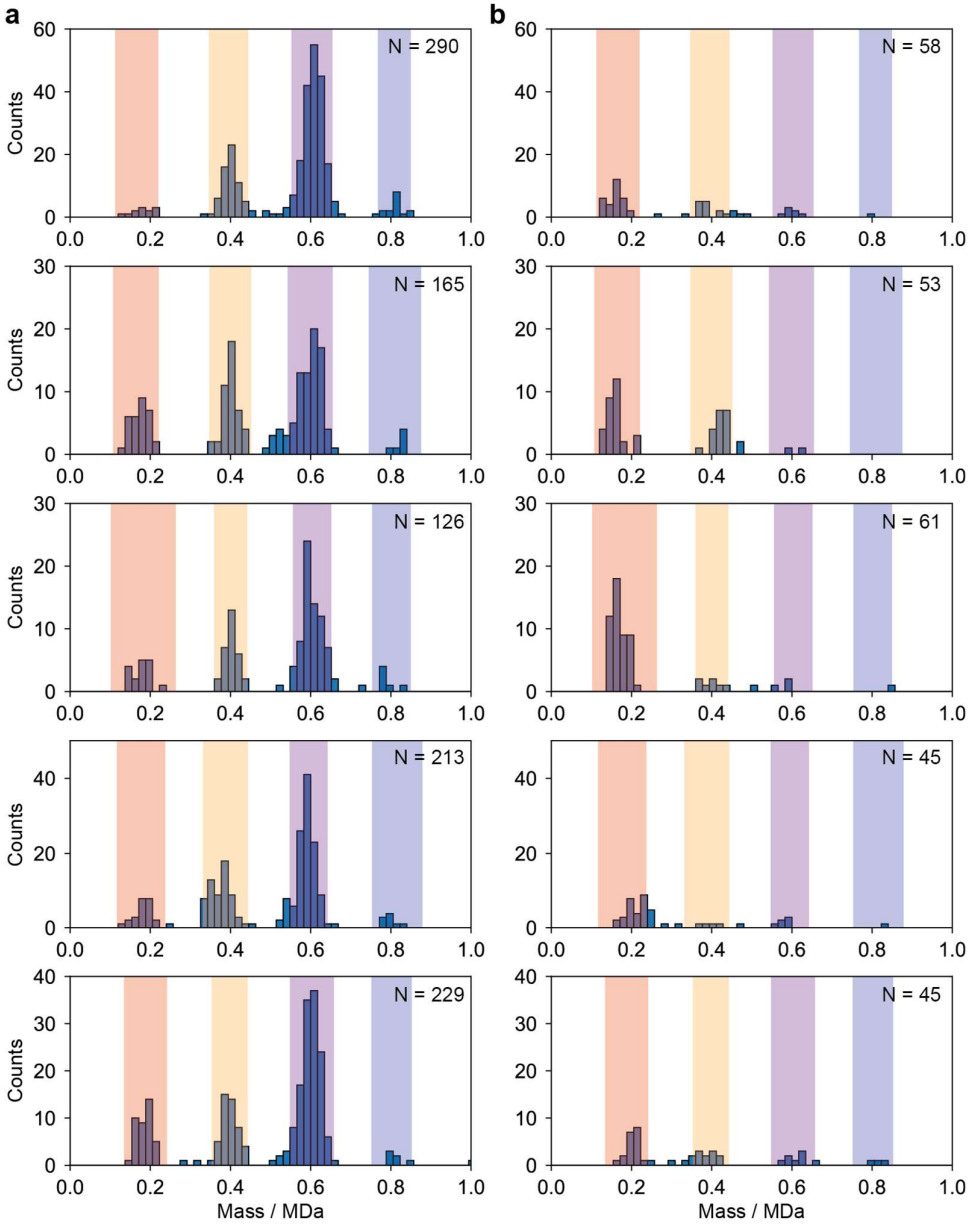


**Effect of GTP addition on the mass distribution of WT**

Mass distribution of five measurements of WT (10-20 nM) in contact with an SLB before (**a**) and after (**b**) addition of 1 mM GTP (1 min movie each). Shaded areas were used to classify trajectories as dimer (red), tetramer (orange), hexamer (purple) and octamer (blue) as described in the methods section. This data was used to generate the bar plot shown in Fig. 2g. Only trajectories that lasted at least 20 frames were considered.

## Supplementary Figure 13

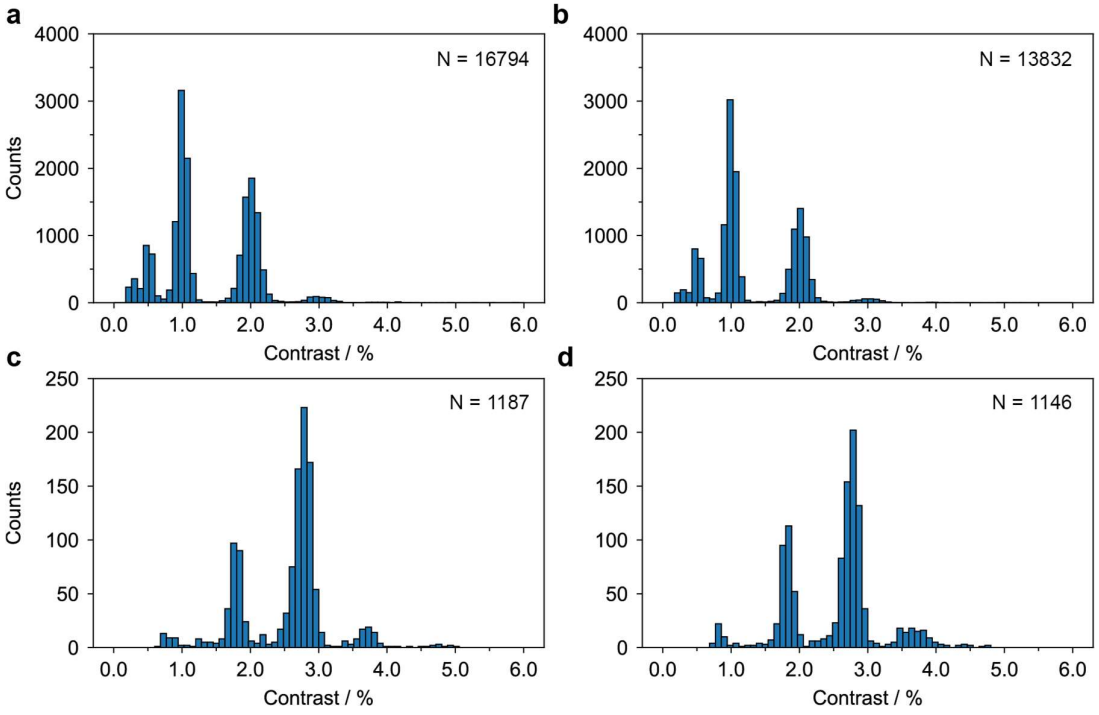


**Effect of ultracentrifugation on the measured oligomeric distribution of WT**

Contrast histograms obtained from standard MP measurements of 100 nM WT **(a-b)** and dynamic MP measurements of 10 nM WT on an SLB **(c-d)** after centrifugation of the stock solution at 20,000 g **(a, c)** and 100,000 g **(b, d)**. The standard MP histograms consist of four combined repeat measurements (1 min movie each) and the dynamic MP measurements consist of two combined 3 min movies each considering only trajectories that lasted at least 50 frames. The data in (c) is the same as in Extended Fig. 2d.

## Supplementary Figure 14

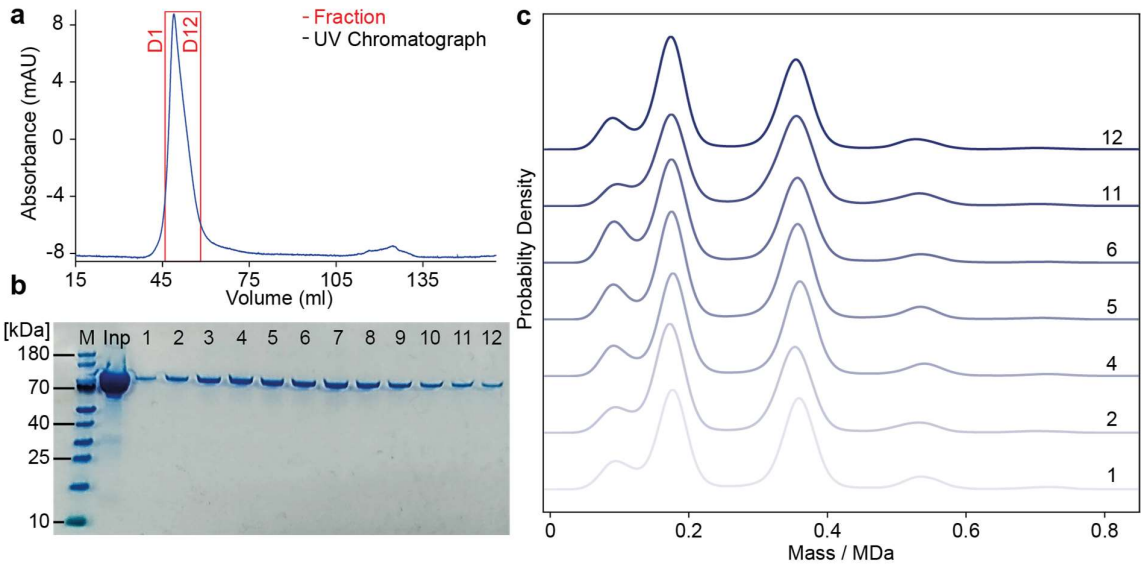


**Effect of size exclusion chromatography on the abundance of dynamin oligomers.**

**(a)** Size exclusion chromatography (SEC) elution profile of ΔPRD (13 μM). (**b)** SDS-PAGE of the ΔPRD SEC elution (n = 1 measurement). Input shows the initial concentration subjected to SEC purification. **(c)** Mass distribution of fractions obtained from the SEC elution (all diluted to 200 nM) measured by standard MP. Each histogram is a combination of 4 independent repeat measurements (total particle numbers: $N_{D1}$ = 39012, $N_{D2}$ = 47099, $N_{D4}$ = 70911, $N_{D5}$ = 73538, $N_{D6}$ = 71287, $N_{D11}$ = 73616, $N_{D12}$ = 45450).

## Supplementary Figure 15

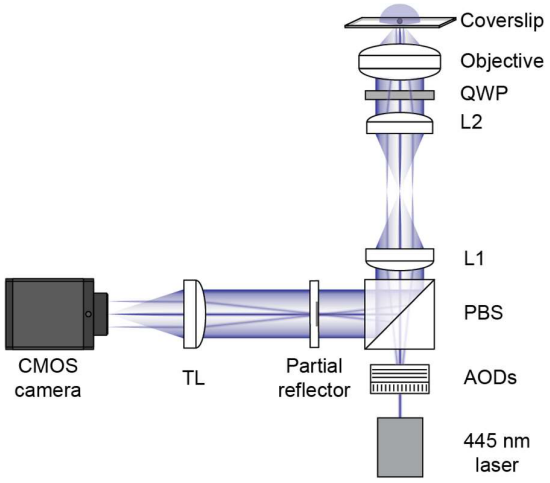


**Custom-built setup used in this study**

Layout of the custom-built mass photometer used to acquire the data shown in Fig. 1a, e-g and 2e-f, similar to that reported previously[3,4]. A collimated 445 nm laser beam (Lasertack) is directed through an orthogonal pair of acousto-optic deflectors (AODs; AA opto Electronic, DT SXY-400). After passing through a polarising beam splitter (PBS), two telecentric lenses (L1 and L2) direct the deflected beam through a quarter-wave-plate (QWP) and into the back focal plane of the objective (Olympus PlanApo N, 1.42 NA, 60x). This setup results in the beam being weakly focused and scanned across the sample to illuminate a 9.4 x 6.2 $\mu m^2$ field of view. The light reflected at the glass-water interface of the coverslip together with the light scattered by the sample is collected by the objective and travels through the same telecentric lens system that the incident light was passed through. Use of the QWP and PBS separates the collected light from the incident light and passes through a partial reflector, which is positioned in the reimaged back focal plane of the objective. This partial reflector is made of a 3.5 mm diameter layer of silver deposited onto a window and attenuates the reflected (at low NA) light by over two orders of magnitude compared to the light scattered by particles[3]. After passing through the partial reflector the light is imaged by a tube lens (TL) onto a CMOS camera (Point Grey, GS3-U3-23S6M-C) resulting in 250x magnification and a pixel size of 23.4 nm. Images are recorded at 1 kHz and then binned in groups of 3 by a custom LabVIEW software that also performs x and y pixel binning (generally 3 x 3) before saving the images for later analysis. Samples are mounted on a custom-built sample stage, with height adjustment provided by a micrometer translation stage (Optosigma) and piezoelectric actuator (Thorlabs AE0505D16F). Sample focus is maintained by an autofocus system (not shown) as follows: a diode laser (Lasertack) is coupled out of a single mode fiber with a 4x objective, and travels collimated into the imaging objective via a dichroic. The beam overfills the objective back aperture and high-NA components are totally internally reflected, causing the back-reflection of an annular beam from the sample. This annular beam is imaged onto a CMOS camera (Thorlabs DCC1545M). Custom labview code continuously measures the radius of this annular beam, and adjusts the piezoelectric actuator in the stage to maintain this radius at a set value. The sample stage and all the optics (except for coupling of the autofocus laser into the single mode fiber) are coupled to a 600x400x50mm aluminium breadboard, enclosed by 40mm thick aluminium walls and lid, which sits on a granite table.

## Supplementary Figure 16

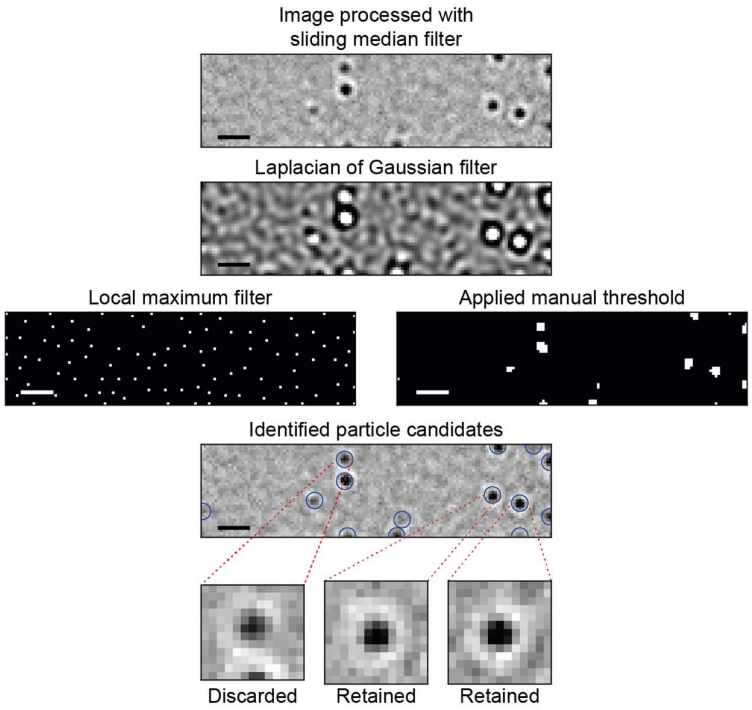


**Image processing for identification of particle candidates**

Background-subtracted images are filtered with a Laplacian of Gaussian kernel with a size to match the size of PSFs in the images (sigma = 1.5). Next, a manually set threshold and local maximum filter are applied to the filtered image. By combining the resulting binary maps, we obtain single pixels at the centre of potential parPticle candidates (circled in blue). From each of these pixels a 13x13 region of interest is constructed to which our PSF model is then applied for quantification of particle contrast and position. If the pixel candidate is too close to an edge of the field of view to construct a complete 13x13 region of interest, it is discarded, as shown in the example here. Scale bar = 1 μm. The images shown in this figure were obtained by applying our image processing pipeline to a snapshot from one dynamic MP movie. This approach produced similar results in all dynamic MP movies used in this study (n > 30).

## Supplementary Figure 17

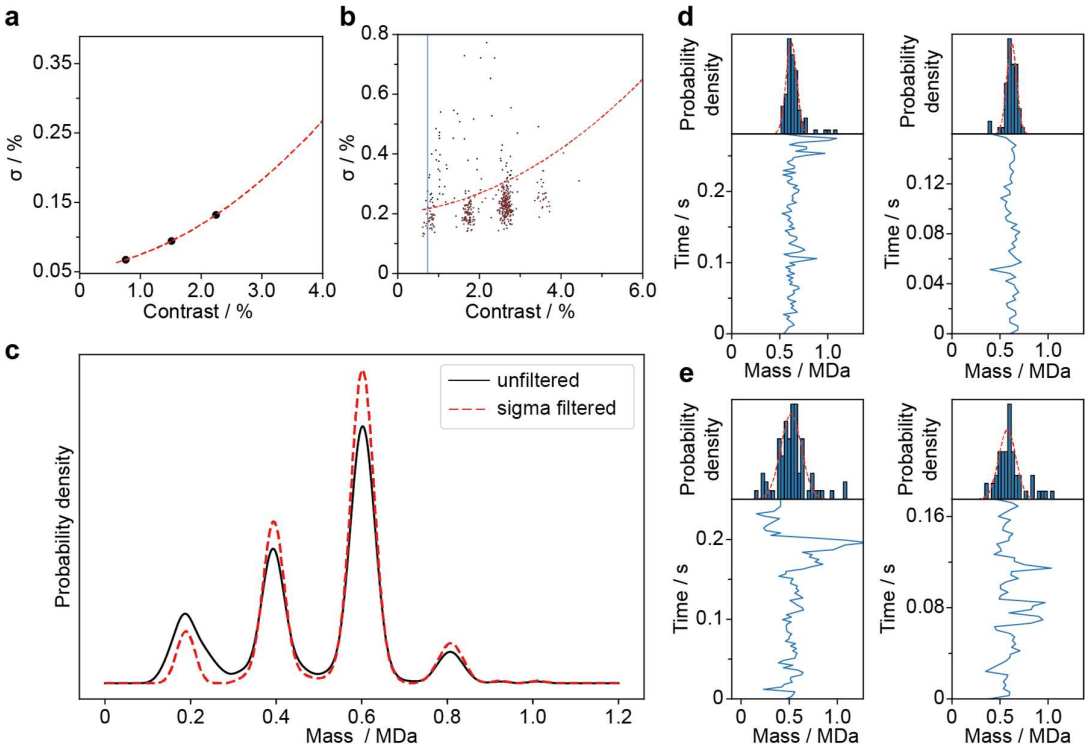


**Filtering of trajectories using the standard deviation of their contrast distributions**

**(a)** Standard deviation (σ) vs mass for WT oligomers obtained from standard MP experiments in solution. **(b)** Standard deviation vs mass scatter plot for the trajectories obtained from the dynamic MP measurement of WT shown in Fig. 1b-d and 2a (after length filtering). The solution-phase trend from (a) is applied with an appropriate offset as a threshold (here 0.15%). Trajectories below the threshold (red) are used for analysis. In this particular case, trajectories with a standard deviation in mass below 170 kDa (blue line) were not used to reduce the number of trajectories that likely result from background noise in the analysis. **(c)** Effect of the applied threshold on the mass distribution of trajectories. **(d)** Examples of trajectories that passed filtering. **(e)** Examples of trajectories that did not pass filtering.

## Supplementary Figure 18

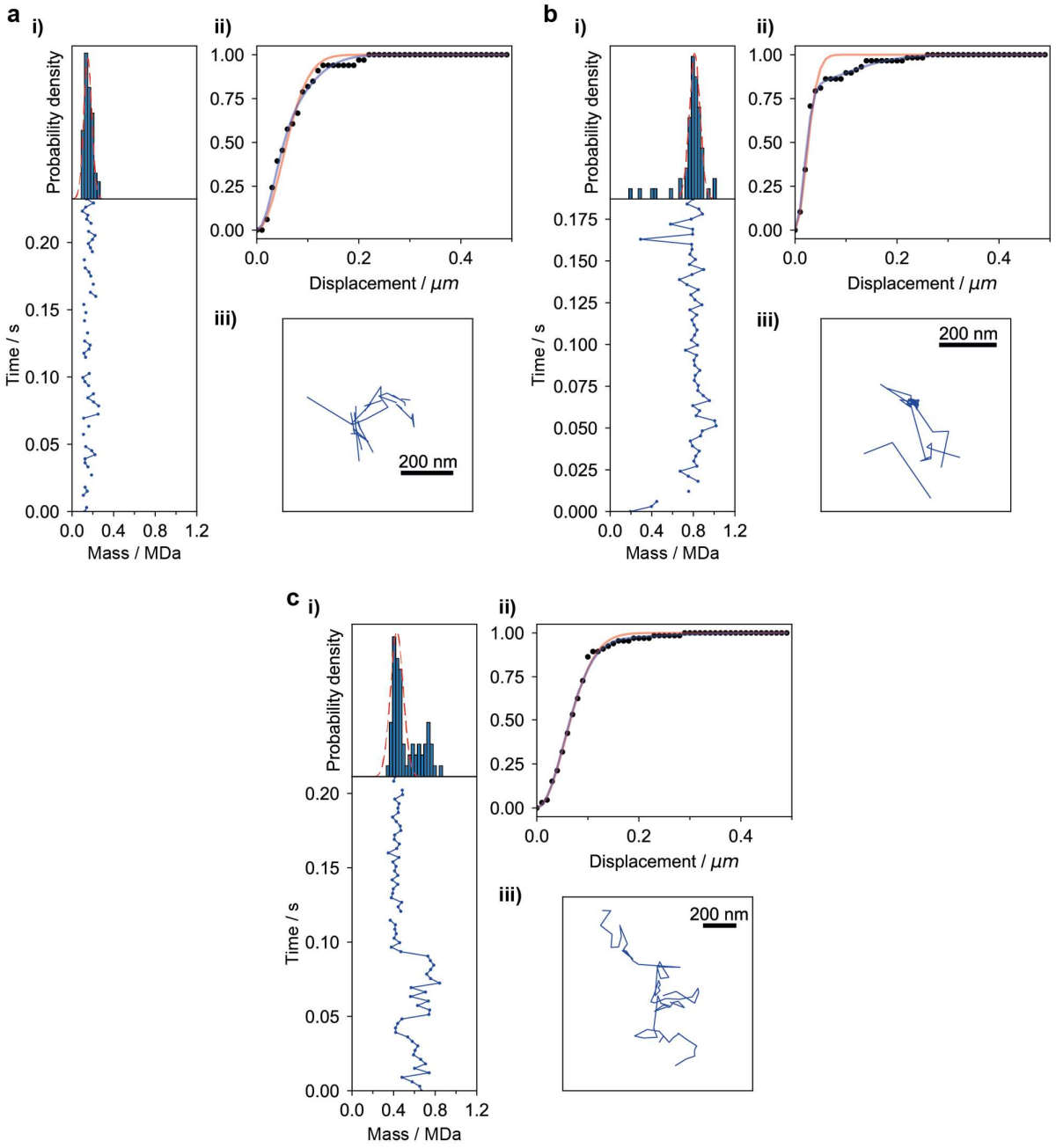


**Examples of particles that were excluded from the diffusion analysis**

**(a)** Mass trace (**i**), cumulative probability density distribution of 1-frame displacement with 1-and 2-component mobility fits in red and blue, respectively (**ii**), and trajectory in 2D space (**iii**) of a particle that was excluded from the diffusion analysis because it was above the set threshold of allowed trajectory gaps. **(b)** Same as (a) but for a particle that was excluded because it was determined to be too stationary during its time on the SLB. **(c)** same as (a) but for a particle with a mean mass that deviated too far from the mass determined by Gaussian fitting (red dashed line), which was usually a sign of an incorrectly linked trajectory. These examples of excluded particles were chosen from the data shown in Fig. 1b-c and 2a.

## Supplementary Tables

**Supplementary Table 1.** Mean contrast values ± standard deviation of WT measured with standard MP (MP; n = 3 independent measurements) and dynamic MP (DMP; n = 6 independent measurements)

| Oligomeric species | MP contrast / % | DMP contrast / % |
|---|---|---|
| Dimer | 1.00 ± 0.01 | 0.83 ± 0.05‡ |
| Tetramer | 2.01 ± 0.01 | 1.82 ± 0.01 |
| Hexamer | 3.03 ± 0.02 | 2.79 ± 0.02 |
| Octamer | 4.03† | 3.74 ± 0.04 |

†Extrapolated from calibration slope

‡Partially overlapped with background noise

**Supplementary Table 2.** Mean contrast values and standard deviations (in %) of trajectories obtained from a movie generated by simulating randomly diffusing point spread functions representative of oligomeric species of WT dynamin at different particle densities onto a dynamic MP movie of HKS-100 buffer in contact with a supported lipid bilayer (n = 1 simulated movie for each particle density). One set of simulations included simulating particle movement during image acquisition ('blurred') and one set did not simulate this effect ('static', *i.e.* particle movement occurs exactly in between frames). Point spread functions were simulated onto the raw images with contrast values of 1.00% (dimer), 2.00% (tetramer), 3.00% (hexamer) and 4.00% (octamer).

| Particle density / $\mu m^{-2}$ | Dimer (static) | Dimer (blurred) | Tetramer (static) | Tetramer (blurred) | Hexamer (static) | Hexamer (blurred) | Octamer (static) | Octamer (blurred) |
|---|---|---|---|---|---|---|---|---|
| 0.13 | 1.01 ± 0.06 | 0.90 ± 0.05 | 2.00 ± 0.06 | 1.83 ± 0.06 | 2.98 ± 0.06 | 2.81 ± 0.07 | 3.97 ± 0.07 | 3.77 ± 0.07 |
| 0.30 | 1.01 ± 0.06 | 0.90 ± 0.07 | 2.00 ± 0.06 | 1.84 ± 0.07 | 2.99 ± 0.07 | 2.80 ± 0.07 | 3.98 ± 0.07 | 3.77 ± 0.08 |
| 0.79 | 1.03 ± 0.07 | 0.90 ± 0.08 | 2.01 ± 0.08 | 1.86 ± 0.09 | 3.00 ± 0.09 | 2.82 ± 0.10 | 3.99 ± 0.09 | 3.78 ± 0.11 |

**Supplementary Table 3.** Mean contrast vs mass calibration slopes ± standard deviation obtained from the simulated dynamic MP movies shown in Supplementary Fig. 6 b,e (at 0.30 $\mu m^{-2}$ particle density, n = 1 movie for 'static' and 'blurred') and from n = 3 standard MP and n = 6 dynamic MP measurements of WT dynamin (Extended Data Fig. 2c-d).

| | Simulated data (static) | Simulated data (blurred) | Standard MP | Dynamic MP |
|---|---|---|---|---|
| Contrast vs mass slope / % $MDa^{-1}$ | 4.99 ± 0.01 | 4.68 ± 0.03 | 5.04 ± 0.01 | 4.63 ± 0.06 |

**Supplementary Table 4.** Mean diffusion coefficients (D), dissociation constants from the SLB (k) and mean trajectory lengths for WT dynamin (n = 7 repeat measurements; Extended Fig. 5, 7). Mean trajectory lengths were calculated from the dissociation constant of each species (mean = 1/k for one component exponential distributions) to avoid bias towards shorter trajectories (< 10 frames) due to background features being identified as particles.

| | Tetramer (0.40 MDa) | Hexamer (0.60 MDa) | Octamer (0.80 MDa) |
|---|---|---|---|
| D / $\mu m^2\ s^{-1}$ | 0.81 ± 0.05 | 0.61 ± 0.03 | 0.50 ± 0.04 |
| k / $s^{-1}$ | 32 ± 9 | 16 ± 2 | 9 ± 3 |
| Mean trajectory length / s | 0.03 ± 0.01 | 0.06 ± 0.01 | 0.11 ± 0.03 |

**Supplementary Table 5.** Mean diffusion coefficients (D), dissociation constants from the SLB (k) and mean trajectory lengths of ΔPRD (n = 4 repeat measurements; Fig. 2b, d). Mean trajectory lengths were calculated from the dissociation constant of each species (mean = 1/k for one component exponential distributions) to avoid bias towards shorter trajectories (< 10 frames) due to background features being identified as particles.

| | Tetramer (0.36 MDa) | Hexamer (0.54 MDa) | Octamer (0.72 MDa) | Decamer (0.90 MDa) |
|---|---|---|---|---|
| D / $\mu m^2\ s^{-1}$ | 0.82 ± 0.05 | 0.67 ± 0.02 | 0.52 ± 0.02 | 0.46 ± 0.03 |
| k / $s^{-1}$ | 31 ± 5 | 25 ± 4 | 14 ± 2 | 5 ± 2 |
| Mean trajectory length / s | 0.03 ± 0.01 | 0.04 ± 0.01 | 0.07 ± 0.01 | 0.19 ± 0.07 |

## References


1. Dar, S., Kamerkar, S. C. & Pucadyil, T. J. A high-throughput platform for real-time analysis of membrane fission reactions reveals dynamin function. *Nat. Cell Biol.* **17**, 1588–1596 (2015).

2. Deo, R. *et al.* ATP-dependent membrane remodeling links EHD1 functions to endocytic recycling. *Nat. Commun.* **9**, 5187 (2018).

3. Cole, D., Young, G., Weigel, A., Sebesta, A. & Kukura, P. Label-Free Single-Molecule Imaging with Numerical-Aperture-Shaped Interferometric Scattering Microscopy. *ACS Photonics* **4**, 211–216 (2017).

4. Young, G. *et al.* Quantitative mass imaging of single biological macromolecules. *Science* **360**, 423–427 (2018).